CONTENTS

Abstract iii

Acknowledgements v

Contents vii

List of Figures x

List of Tables xiv

Glossary of Acronyms xv

1 Introduction 1

1.1 Objectives . . . 2

1.2 Outline and Research Contributions . . . 2

2 Background 5

2.1 Role of Cardiac Tissue Stiffness . . . 5

2.2 Measuring Cardiac Tissue Stiffness . . . 5

2.2.1 *Ex vivo* Stiffness Measurements . . . 6

2.2.2 *In Vivo* Stiffness Measurements . . . 7

2.3 Elastography . . . 9

2.3.1 Ultrasound Elastography . . . 10

2.3.2 MR Elastography . . . 10

2.3.3 Inversion Algorithms . . . 12

2.3.4 Material Models . . . 18

2.3.4.1 Viscoelastic Parameter Estimation . . . 18

2.3.4.2 Isotropic Parameter Estimation . . . 19

2.3.4.3 Transversely Isotropic Parameter Estimation . . . 19

2.3.4.4 Orthotropic Parameter Estimation . . . 25

2.3.5 Muscle Elastography . . . 27

2.3.6 Cardiac Elastography . . . 28

2.4 Limitations and Gaps in Knowledge 32

3 Finite Element Model Update Method **35**
3.1 Finite Element Methods for Steady State Harmonic Problems 35
3.1.1 Principle of Virtual Work 35
3.1.2 Finite Element Method 36
3.1.3 Development of a First Order Hexahedral Mesh of a Canine Left Ventricle 37
3.1.4 Elements 42
3.1.5 Steady-State Harmonic Motion 44
3.2 FEMU Isotropic Method Validation 46
3.2.1 Isotropic Phantom MRE Experiment 46
3.2.2 Stiffness Estimate: FEMU 49
3.2.3 Stiffness Estimate: Directional Filter + LFE 51

4 Identifiability of Transversely Isotropic Material Properties from MRE **55**
4.1 Methods 56
4.1.1 Linear Elastic Constitutive Model 56
4.1.2 Finite Element Modelling and Simulations 58
4.1.3 Determinability of Material Parameters 59
4.2 Results 60
4.2.1 Isotropic Phantom 60
4.2.2 Anisotropic Left Ventricle Simulations 61
4.2.3 Anisotropic Parameter Estimation from the Isotropic Phantom . . 63
4.3 Discussion 65

5 Isotropic Virtual Fields Method **69**
5.1 Analytic Virtual Fields Method 69
5.1.1 Formulation 69
5.1.2 Results 72
5.1.2.1 Beam Simulations 73
5.1.2.2 Isotropic Phantom MRE 77
5.2 Optimised Virtual Fields Method 81
5.2.1 Formulation 81
5.2.2 Results 85
5.2.2.1 Beam Simulations 85
5.2.2.2 Isotropic Phantom MRE 95
5.2.2.3 Left Ventricle Simulations 96
5.3 Discussion 101

6 Anisotropic Optimised Virtual Fields Method **105**
6.1 Formulation and Implementation 106
6.1.1 Five Parameter Model 106
6.1.2 Three Parameter Model 110
6.1.3 Implementation 111
6.2 Results 114
6.2.1 Beam Simulations 114
6.2.2 Isotropic Phantom MRE 120
6.2.3 Left Ventricle Simulations 124
6.3 Discussion 134

7 Conclusions **139**
7.1 Summary 139
7.2 Contributions to the Field 141
7.3 Limitations 141
7.4 Future Work 142

A Finite Element Strain Formulations **143**

B Parameter Variance Matrices **151**

C Constraints on Virtual Displacements **161**

D Anisotropic Damping Coefficients **167**

References **177**

LIST OF FIGURES

2.1 PV loop 8
2.2 ”Family” of PV loops 8
2.3 MRE sequence example 10
2.4 MRE scanning setup 11
2.5 Example manual stiffness calculation 14
2.6 Transversely isotropic material 19
2.7 Transversely isotropic material parameters related to the material orientation . 21

3.1 Canine LV model from CIM 37
3.2 Element refinement directions 38
3.3 Canine LV model showing bunching of apical elements 38
3.4 Mesh refinement steps with apical derivative correction 40
3.5 Re-meshing the apex 41
3.6 Resulting element volumes before and after equipotential smoothing 41
3.7 LV model with varying element types 43
3.8 Hourglassing example 43
3.9 A graphical representation of the complex load/response. 45
3.10 MRE displacement encoding directions 47
3.11 Four phase offset images 48
3.12 Fitting a sine curve to the phase offsets 49
3.13 Two phantom meshes 50
3.14 Band pass Butterworth and directional filters 51
3.15 Band pass Butterworth and directional filters applied to phantom data 51
3.16 Phantom LFE stiffness map 52

4.1 LV finite element model 58
4.2 Phantom isotropic parameter sweep 61
4.3 LV time-discretised displacement map 61
4.4 LV objective function 62
4.5 LV results from Monte Carlo experiment 63
4.6 Anisotropic phantom parameter sweep 64

5.1 Beam: Simulated harmonic displacements in a cantilever beam model 73
5.2 Analytic VFM: Box plots of estimated parameters with varying wave numbers 74
5.3 Analytic VFM: Box plots of estimated parameters with varying Gaussian noise 75
5.4 FEMU method: results of varying amount of Gaussian noise 76
5.5 FEMU method: results of varying amount of Gaussian noise with fixed Poisson's ratio 77
5.6 Analytic VFM: Phantom virtual displacement field and measured displacement field 78
5.7 Analytic VFM: Phantom MRE results per image layer 79
5.8 Analytic VFM: Phantom shear moduli shown with measured displacement fields 80
5.9 Analytic VFM: Phantom damping coefficients shown with measured displacement fields 80
5.10 Example of optimised virtual displacement fields 86
5.11 Discretised Optimised VFM: Shear moduli from beam simulation 87
5.12 Discretised Optimised VFM: Shear moduli and viscoelastic damping from beam simulation 88
5.13 Discretised Optimised VFM: Box plots of displacements at discretised time points 89
5.14 Optimised VFM: Beam loading test 90
5.15 Optimised VFM: Beam loading test sensitivity 91
5.16 Optimised VFM: Resulting estimated shear moduli from a beam loading test with added Gaussian noise 92
5.17 Optimised VFM: Resulting estimated damping coefficients from a beam loading test with added Gaussian noise 93
5.18 Optimised VFM: Mean estimated moduli from the beam Monte Carlo experiment plotted versus normalised sensitivity values 94
5.19 Optimised VFM: Standard deviation of estimated moduli from the beam Monte Carlo experiment plotted versus normalised sensitivity values 95
5.20 Optimised VFM: Phantom MRE results 96
5.21 Optimised VFM: LV reference model with anterior and apical node sets . . . 97
5.22 Optimised VFM: LV loading test sensitivity 97
5.23 Optimised VFM: LV model results with noise 98
5.24 Optimised VFM: Mean estimated moduli from the Monte Carlo experiment plotted versus normalised sensitivity values 99
5.25 Optimised VFM: Standard deviation of estimated moduli from the Monte Carlo experiment plotted versus normalised sensitivity values 99
5.26 Optimised VFM: LV (loading case #60) results with varying amounts of noise 100
5.27 Optimised VFM: LV simulation (#58) results with varying amounts of noise . 100

5.28 Optimised VFM: LV model standard deviations plotted versus the amount of Gaussian noise added to reference displacements 101

6.1 Beam loading faces 112
6.2 Cylindrical phantom and two material orientations 113
6.3 LV finite element model illustrating a) anterior surface nodes, b) apical surface nodes and c) fibre field measured from histology. 114
6.4 Beam: Histogram of five parameters estimated from loading test 115
6.5 Beam: Histogram of three parameters estimated from loading test 115
6.6 Beam: Plot of normalised sensitivity values for the five-parameter formulation 116
6.7 Beam: Plot of normalised sensitivity values for the three-parameter formulation 117
6.8 Beam: Simulations used for noise analysis 118
6.9 Beam: Resulting estimated moduli from five-parameter estimation of Monte Carlo experiment 119
6.10 Beam: Resulting estimated moduli from three-parameter estimation of Monte Carlo experiment 120
6.11 Phantom: Resulting estimated moduli from five-parameter formulation applied to all phantom sub-regions 122
6.12 Phantom: Resulting estimated moduli from three-parameter formulation applied to all phantom sub-regions 122
6.13 Phantom: Plot of normalised sensitivity values for the five-parameter formulation 123
6.14 Phantom: Plot of normalised sensitivity values for the three-parameter formulation 123
6.15 LV: Plot of normalised sensitivity values for the five-parameter formulation . 125
6.16 LV: Plot of normalised sensitivity values for the three-parameter formulation . 125
6.17 LV: Simulations used for noise analysis 126
6.18 LV: Resulting estimated moduli from five-parameter estimation of Monte Carlo experiment 128
6.19 LV: Resulting estimated moduli from three-parameter estimation of Monte Carlo experiment 128
6.20 LV: Results from MC simulation with varying amounts of noise using five-parameter formulation 130
6.21 LV: Results from MC simulation with varying amounts of noise using three-parameter formulation 130
6.22 LV: Coefficients of variation compared for five- and three-parameter formulations 131
6.23 LV: Normalised parameter sensitivity versus excitation frequency 132
6.24 LV: Resulting estimated moduli from five-parameter estimation of Monte Carlo experiment over varying frequencies 134

6.25 LV: Resulting estimated moduli from three-parameter estimation of Monte Carlo experiment over varying frequencies 134

A.1 FEM Coordinate Systems 144
A.2 Phantom element type results 150

D.1 Beam: Histogram of damping coefficients estimated from loading test using five-parameter formulation 168
D.2 Beam: Histogram of damping coefficients estimated from loading test using three-parameter formulation 168
D.3 Beam: Estimated damping coefficients from five-parameter Monte Carlo simulation with Gaussian noise 169
D.4 Beam: Estimated damping coefficients from three-parameter Monte Carlo simulation with Gaussian noise 169
D.5 Phantom: Resulting damping coefficients from five-parameter formulation in phantom all subzones 170
D.6 Phantom: Resulting damping coefficients from three-parameter formulation in phantom all subzones 170
D.7 LV: Histogram of damping coefficients estimated from loading test using five-parameter formulation 171
D.8 LV: Histogram of damping coefficients estimated from loading test using three-parameter formulation 171
D.9 LV: Estimated damping coefficients from five-parameter Monte Carlo simulation with Gaussian noise 172
D.10 LV: Estimated damping results from three-parameter Monte Carlo simulation with Gaussian noise 172
D.11 LV: Estimated damping coefficients from Monte Carlo simulation with varying amounts of noise using five-parameter formulation 173
D.12 LV: Estimated damping coefficients from Monte Carlo simulation with varying amounts of noise using three-parameter formulation 173
D.13 LV: Coefficients of variation for damping coefficients compared for five- and three-parameter formulations 174
D.14 LV: Estimated damping coefficients from five-parameter estimation of Monte Carlo experiment over varying frequencies 174
D.15 LV: Estimated damping coefficients from three-parameter estimation of Monte Carlo experiment over varying frequencies 175

LIST OF TABLES

2.1 Anisotropic MRE studies 27
2.2 Cardiac elastography studies. ED: end-diastole, ES: end-systole, NA: Not applicable. 30

3.1 Phantom FEMU results 51

4.1 Summary of optimality criteria determined from the Hessian of the objective functions at the minimum. 64
4.2 Results from material parameter estimations 64

6.1 Beam: Number of converged Monte Carlo simulations 120
6.2 Phantom: Number of converged simulations 121
6.3 LV: Number of converged simulations 127
6.4 LV: Superimposed wave fields 129
6.5 LV: Three-parameter superimposed field results 129
6.6 LV: Five-parameter superimposed field results 129
6.7 LV: Number of converged simulations for varying frequencies 133

GLOSSARY OF ACRONYMS

MRE	Magnetic Resonance Elastography
MRI	Magnetic Resonance Imaging
DTMRI	Diffusion Tensor Magnetic Resonance Imaging
FEM	Finite Element Model
FEMU	Finite Element Model Update
DF-LFE	Direction Filter with Local Frequency Estimation
MMDI	Multi-Model Direct Inversion
VFM	Virtual Fields Method
LV	Left Ventricle

1

INTRODUCTION

MAGNETIC resonance elastography (MRE) is a means of non-invasively measuring the intrinsic stiffness of biological tissue [106]. MRE has been used to investigate the ”effective” stiffness of myocardium at various points in the cardiac cycle without the need for catheterisation [41–45, 78, 80, 82, 100, 138, 163]. Most of these studies, however, assumed that the myocardium is infinite and isotropic, even though myocardium is known to have anisotropic material properties [34]. By assuming an infinite material, reflection and absorption of waves can be ignored, which will affect the accuracy of stiffness estimates [91]. Anisotropic properties of materials have also been studied using MRE, primarily in skeletal muscle [57, 61, 75, 115, 126], brain [3, 47, 129, 130], a variety of phantoms [25, 109, 125, 139, 151] and simulations [149, 150]. In these studies, either two, three, or five parameters were estimated to describe the anisotropic material properties. Fibre directions were either assigned using rule-based methods or using diffusion tensor MRI (DTMRI). With the development of DTMRI to examine cardiac fibre architecture, fibre information can be used in conjunction with MRE displacements in order to assess the patient-specific anisotropic properties of cardiac tissue [100]. Accurate estimation of transversely isotropic material properties requires the existence of both fast and slow shear waves within the medium [135, 139], which presents challenges in cardiac tissue due to the variable fibre orientations throughout the myocardium. Additionally, the thin wall of the myocardium creates a wave-guide effect [140], which makes the assumption of an infinite medium false. Once inversion methods are identified that can surpass these challenges, cardiac MRE can then be applied to investigate the progression of pathologies such as hypertensive heart failure by comparing the anisotropic stiffness parameters at various points in the development of the disease in order to gain a better understanding of the structural changes that occur.

1.1 Objectives

The objectives of this thesis are threefold:

1. Implement and validate a boundary value finite element model update (FEMU) inversion method for identifying global anisotropic material properties

2. Develop and validate a virtual fields method (VFM) for identifying global isotropic and anisotropic material properties

3. Implement both methods with simulated harmonic displacements in a realistic left ventricle (LV) model as well as MRE data from an isotropic phantom

1.2 Outline and Research Contributions

This thesis is organised as follows:

Chapter 2 presents the state of knowledge on magnetic resonance elastography and various inversion algorithms. Additionally, studies that have estimated anisotropic properties as well as myocardial stiffness are discussed.

Chapter 3 describes the development of a finite element analysis method simulating steady-state harmonic motion, which models harmonic displacement fields as seen in MR elastography experiments. A pipeline to create an LV model geometry from MRI cine images is discussed. The model is used throughout Chapters 4, 5 and 6. A validation of the FEMU method was carried out, in which estimated stiffness of an isotropic phantom was compared with stiffness estimates from two other common MRE inversion methods: a directional filter + local frequency estimation (DF-LFE) and a multi-model direct inversion (MMDI).

Chapter 4 presents results from the estimation of transversely isotropic material properties using the FEMU method from simulated displacements in a realistic left ventricular geometry embedded with myocardial fibre orientations. Additionally, a parameter identifiability study was carried out with simulated harmonic displacements using a left ventricular model as well as with isotropic experimental phantom data. Relative identifiability of the various material parameters is discussed. To the researcher's knowledge, this is the first investigation of relative parameter identifiability of transversely isotropic material properties.

Chapter 5 investigates the use of the virtual fields method (VFM) to obtain a complex isotropic shear modulus from MRE displacement fields using both analytic as well

as optimised numeric virtual displacement fields. The method was tested with simulated harmonic displacements in a cantilever beam and left ventricular geometry. Varying amounts of Gaussian noise were added to the reference displacement fields. Then, both the analytic and optimised VFMs were applied with experimental MRE phantom displacement fields and results were compared with the results from the FEMU, DF-LFE and MMDI methods.

This chapter builds upon the methods implemented by Pierron et al. [117] and Connesson et al. [29]. In this chapter, the VFM is implemented with experimental MRE data with a clinically realistic image resolution (1 mm x 1 mm x 5 mm). Additionally, complex moduli, rather than time discretised viscoelastic parameters, are estimated, significantly reducing computation time and avoiding time dependency that was observed in both [117] and [29]. The method was tested with the complex LV geometry, illustrating its capability of solving the inverse problem in cardiac MRE experiments.

The influence of various loading conditions was tested with both the cantilever beam model and LV geometry. Parameter sensitivity values were used to quantify the relative sensitivity to noise of each loading configuration. It is shown that, even in the isotropic case, the accuracy in the estimation of a complex shear modulus and sensitivity to Gaussian noise, using the optimised VFM, is dependent on the loading configuration and waves present within the medium.

Chapter 6 presents two material model formulations thath represent a transversely isotropic material. Using the first, all five independent parameters of the elasticity matrix are estimated using the optimised VFM. With the second, only three parameters are estimated, avoiding the estimation of a bulk modulus. As in Chapter 5, the two implementations were tested in harmonic simulations using a cantilever beam and left ventricular geometry as well as MRE phantom displacement fields. It is shown that not all parameters are equally sensitive to noise. Again, a loading test was carried out for both the cantilever beam and LV models, illustrating the importance of the loading applied (and resulting displacement field) in the identification of transversely isotropic material properties. The impact of the complex LV geometry is also discussed. The anisotropic VFM was tested with the isotropic phantom MRE data with two different arbitrarily assigned material orientations.

This is the first application of the optimised VFM to identify anisotropic material properties from MRE displacement fields. Two different material model formulations have been implemented, which both have unique strengths and weaknesses due to their differences in formulation. Many MRE inversion methods assume incompressibility in order to simplify the wave equation. The second material model

formulation presented allows one to separate components of stress due to the bulk wave and the shear wave, respectively, without making an assumption of incompressibility.

Chapter 7 summarises the conclusions from the use of the FEMU and VFM inversion methods, contributions to the field and future directions stemming from this research.

2 BACKGROUND

THIS chapter provides the motivation of the thesis and covers background information necessary for understanding the work in subsequent chapters. Firstly, the role of cardiac tissue stiffness in heart disease is reviewed, focusing on its role in diastolic heart failure. Then, different methods of measuring properties of myocardium are discussed. Finally, a review of magnetic resonance elastography (MRE) is provided, including inversion methods, applications to anisotropic materials as well as studies investigating myocardial properties.

2.1 Role of Cardiac Tissue Stiffness

Myocardial stiffness is an important determinant of cardiac function, and significant increases in global myocardial stiffness are thought to be associated with pathologies such as diastolic heart failure [170] and hypertensive heart disease (HHD) [16]. Animal models of heart failure show an increase in fibrosis and loss of tissue anisotropy in the left ventricular (LV) myocardium [89]. Patients with heart failure with preserved ejection fraction (HFPEF) present with impaired filling, possibly due to increased myocardial stiffness. The two most common changes that occur with HHD are thickening of the LV wall, known as LV hypertrophy, and fibrosis [16]. Cardiac fibrosis is marked by collagen growth within the myocardium, leading to a tissue-level increase in stiffness [16]. Therefore, myocardial stiffness could be an important diagnostic marker or measurement of disease progression for pathologies such as diastolic heart failure and HHD.

2.2 Measuring Cardiac Tissue Stiffness

In any method for estimating material properties, the underlying assumption is that the mechanical properties constrain the patterns of deformation. Given enough information (i.e.

loading force and boundary conditions), the mechanical properties are deducible from the deformation field. This section introduces and discusses methods available for estimating material properties of myocardium.

2.2.1 *Ex vivo* Stiffness Measurements

Once excised from the body, known deformations can be applied to myocardial tissue samples in order to estimate intrinsic material properties.

Tensile Testing For example, after excising myocardium, tensile testing can be carried out by attaching (e.g. clamping, gluing, suturing) the material or tissue of interest between two fixed ends. A prescribed deformation is applied by stretching one end (either prescribing the displacement or force applied). A force transducer at the opposite end measures the resulting force (F) exerted by the material resisting the stretch. The stress (σ) is then calculated as:

$$\sigma = \frac{F}{A} \tag{2.1}$$

where A is the estimated cross-sectional area of the specimen. The strain (ϵ) is calculated as the ratio of the change in length (ΔL) to the original length (L_0).

$$\epsilon = \frac{\Delta L}{L_0} \tag{2.2}$$

The slope of the stress versus strain curve is related to the material stiffness. Tensile testing was performed in [5] to test the difference in material stiffness between healthy and infarcted myocardium. In a linear elastic material, the slope is referred to as the Young's modulus. In a hyperelastic material, such as myocardium, the stress-strain curve is non-linear and can be approximated by an exponential function. The slope (instantaneous stiffness) increases as the amount of strain applied increases. In tensile testing, a cyclic load can be applied to measure viscous effects of the material.

Anisotropic materials exhibit varying stiffness depending on the material direction. Biaxial tensile testing can be used to measure the stress-strain relationships in two directions, simultaneously, by clamping the material on four sides and stretching in two orthogonal directions. Biaxial tensile testing performed on *ex vivo* canine and porcine myocardium [32, 53, 168] has revealed an anisotropic tissue stiffness with greatest stiffness along the fibre (myocyte) direction.

Using tensile testing to estimate material stiffness presents a few challenges. Firstly, measuring the cross-sectional area of a tissue sample is a non-trivial problem. Likewise, since the tissue is often destructed in the area where it is attached, changes in length are measured in a small portion of the tissue far from any edges. Therefore, optical methods

are often used for measuring the change in length. Thirdly, the method by which the sample is attached can have a large impact on the resulting stiffness estimates. Clamping has been shown to increase the apparent stiffness. Conversely, sutures are time consuming and may cause the tissue to tear during the experiment [53]. Other attachment methods include needles as well as hooks.

Dynamic Mechanical Analysis Dynamic mechanical analysis (DMA) and dynamic shear testing (DST) are nondestructive dynamic material tests that can measure the complex stiffness modulus of a material over a given range of frequencies. DMA applies an oscillatory stress (σ) to a sample and measures the resulting strain (ϵ) and phase delay (ϕ). From the strain and phase delay, a complex-valued shear modulus (G^*) is obtained.

$$G^* = \frac{\sigma}{\epsilon}\cos\phi + i\frac{\sigma}{\epsilon}\sin\phi \tag{2.3}$$

DMA requires careful selection of testing parameters, including sample thickness, compressive clamping strain, shear strain amplitude and shear strain rate. It has been shown that as the thickness of a sample and testing frequency increase, the estimated shear modulus may erroneously increase due to non-uniform shear deformation throughout the thickness. Therefore, the choice of sample thickness is imperative for estimating accurate material properties [128]. Both tensile testing and DMA require myocardial tissue samples to be excised from the body. One additional challenge lies in keeping the tissue viable and oxygenated as it has been shown that as tissue becomes deoxygenated, it increases in stiffness [74].

2.2.2 *In Vivo* Stiffness Measurements

Using available imaging modalities, *in vivo* deformations can be measured. Then, material properties can be estimated without removing tissue from the body.

Strain Material properties can be reconstructed from measured strains under static loading given that the loading stress is known. However, without known stresses, strain is often used as a surrogate marker for myocardial properties. Myocardial strain can be measured clinically using magnetic resonance image (MRI) tagging [105], displacement encoding with stimulated echos (DENSE) MRI [2], echocardiography [40, 154], or feature tracking [8]. Strain has been correlated with myocardial contractility [1] as well as diastolic stiffness [119]. Strain, however, is dependent on the pre-load. A larger strain may be indicative of a lower compliance or, alternatively, a larger end-diastolic pressure. Therefore, strain alone does not give a complete understanding of intrinsic material properties.

Compliance Estimation from PV Loop The pressure-volume (PV) loop, is a plot of the LV cavity pressure versus LV volume at every point in the cardiac cycle. The four phases of the cardiac cycle, filling, isovolumetric contraction, ejection and isovolumetric relaxation, are shown in Figure 2.1.

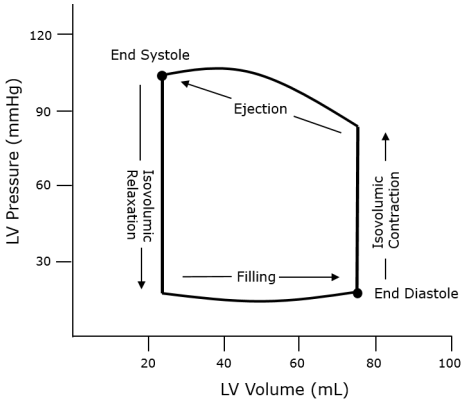

FIGURE 2.1: Pressure-volume loop over one cardiac cycle.

For a given cardiac cycle, there is one point which corresponds to end-diastole and one which corresponds to end-systole. Assuming a constant effective compliance and level of maximum contraction, multiple PV loops can be developed with varying loading conditions (e.g. increased end-diastolic volume). From this "family" of PV loops (Figure 2.2), the end-diastolic pressure volume relationship (EDPVR) and end-systolic pressure volume relationship (ESPVR) can be developed by drawing a curve which connects all end-diastolic points and end-systolic points, respectively.

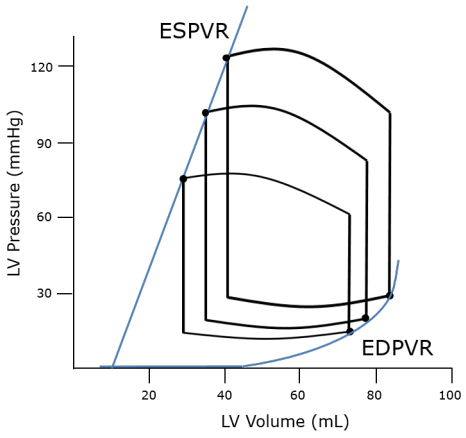

FIGURE 2.2: Multiple PV loops used to reconstruct the ESPVR and EDPVR curves

The EDPVR is non-linear and represents the passive physical properties of the LV chamber. Chamber stiffness (dP/dV) increases as end-diastolic pressure (or volume) increases. It is therefore dependent on pre-load. Conversely, the ESPVR is linear and characterises the properties of the chamber when the myocardium is maximally activated [20].

The slope of the ESPVR is called the end-systolic elastance.

Numerous studies have fitted curves (exponential, cubic or power law) to the EDPVR and used curve-fitting constants as measures of intrinsic properties of the myocardium. For example, investigating diastolic heart failure [122, 170], an exponential equation, $P = Ae^{\beta V}$, was fit to three PV points and β was reported as the stiffness constant. Shifts in EDPVR can be reflective of changes in intrinsic properties, physiological remodelling or pathological remodelling. However, the EDPVR reflects the net effect of material properties and chamber structural properties (including cavity dimension and wall thickness). Therefore, it is not a direct measure of intrinsic myocardial stiffness.

Finite Elasticity Simulation Method One method to measure intrinsic properties of myocardium has been patient-specific biomechanical modelling [7, 59, 83, 162, 165]. A patient-specific finite element (FE) model is created by fitting an LV geometry to endo- and epicardial contours from MR images. With an initial estimate of material properties, the model is inflated to a known LV pressure, which corresponds to a known time point during diastolic filling. The pressures are typically measured via catheter in the LV cavity. The passive material stiffness is iteratively optimised by minimising the error between the simulated model LV displacement (or strain) between diastasis and end-diastole and the true LV displacement between these two time points (obtained from MRI). This method takes into account the patient-specific geometry, fibre orientation (rule-based or DTI) and hyperelastic material behaviour of myocardium, and thus provides intrinsic material properties of the myocardium. The greatest disadvantage of this method is that it relies on invasive pressure measurements, which are used to define the pressure loading conditions. This is an active area of research and methods differ in their application of boundary conditions, objective functions and material models.

2.3 Elastography

Elastography, a method that has been developed over the last two and a half decades, provides a means of non-invasively measuring tissue stiffness through imaging. Elastography involves a) inducing low-frequency vibrations (10 Hz - 1 kHz) in the material of interest, b) measuring the displacements through ultrasound, MRI, optical or another type of imaging and c) converting displacement fields to stiffness information through an inversion algorithm. Thus far, elastography has been applied to the detection of liver fibrosis [68, 169], cancer in the breast [102, 141] and prostate [73] as well as diagnosis of diseases in the brain [84, 129], cardiac and cardiovascular system [41, 98, 99] and musculoskeletal system [137]. The following sections outline ultrasound and MRI methods, but other modalities, such as optical coherence tomography [71, 146], are also available.

2.3.1 Ultrasound Elastography

Ultrasound and magnetic resonance elastography (MRE) are two imaging modalities readily used in clinical environments, both of which are suitable means of measuring harmonic displacements for stiffness reconstruction. Ultrasound elastography, although inexpensive compared to MRE, is constrained by limited acoustic windows of observation, low signal-to-noise ratios and lateral resolution. Many ultrasound elastography studies, like MR elastography, utilise external drivers at lower frequencies [64, 153] and encode displacement with ultrasound. Ultrasound elastography papers are numerous and diverse. For conciseness, only a few papers have been included in this chapter, namely those that have estimated material properties of myocardium and transversely isotropic materials. The inversion methods presented in this thesis are not restricted for use with MR elastography and can also be applied to ultrasound elastography measured displacement fields in the future.

2.3.2 MR Elastography

The experimental data analysed in this thesis was collected using MRI. MRE utilises a gradient echo or spin echo pulse sequence in conjunction with motion-sensitizing gradients which are synchronised with the mechanical driving frequency. An example of a generic MRE sequence is shown in Figure 2.3 [107]. The frequency of the MR gradients acts as a filter, retaining motion at that frequency and filtering out other harmonic displacements.

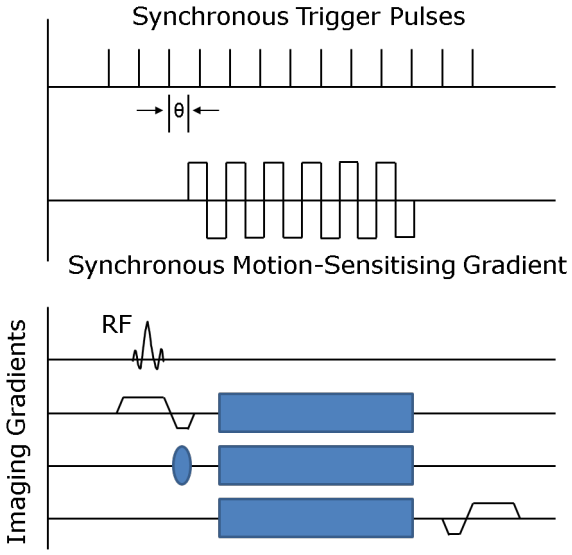

FIGURE 2.3: A simplified diagram of an MRE sequence with the timing of the motion-sensitising gradients aligned with the timing of the external driver.

During an MRE scan, a passive driver is placed over the tissue of interest and the MR receiver coil is placed over the driver. An active pneumatic driver, typically a large speaker,

is set up outside the scan room and attached to the passive driver through plastic tubing. The active driver causes oscillating pressure against the drum head of the passive driver (Figure 2.4).

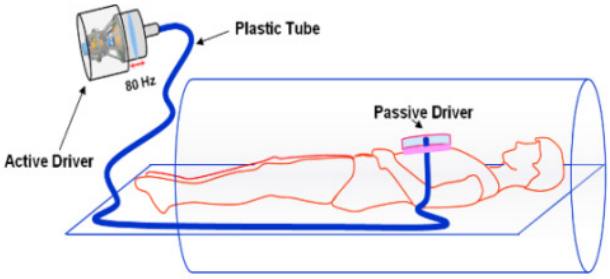

FIGURE 2.4: An illustration of an MRE setup showing a pig, MRI scanner, active driver and passive driver.

The physics underlying MR elastography was originally described [106] and tested in a phantom [107] by Muthupillai et al. In the presence of a magnetic gradient, the phase shift (caused by the motion of the proton H^1) can be described as [17]:

$$\Phi = \gamma \int_0^\tau G_r(t) \cdot r(t) dt \tag{2.4}$$

where γ is the gyromagnetic ratio (a characteristic of the nuclei); τ is the time duration of the gradients after excitation; $G_r(t)$ is a temporal function of the magnetic gradient; and $r(t)$ describes the position of the nuclear spin. If $r(t)$ describes describes linear motion (e.g. $r(t) = r_0 + v_0 t$), Equation (2.4) becomes a simple relationship between phase shift and the first gradient moment ($G_r(t) = G_x\hat{i} + G_y\hat{j} + G_z\hat{k}$).

Alternatively, complex motion can be noted as $r(t) = r_0 + \zeta(r,t)$ where r_0 is the mean position and $\zeta(r,t)$ describes the oscillating about the mean position. Simple harmonic motion of a proton relative to its mean position can be described as:

$$\zeta(r,t) = \zeta_0 \cos(k \cdot r - \omega t + \theta) \tag{2.5}$$

where k is the wave number (spatial frequency), ω is the frequency of mechanical excitation (temporal frequency), θ is the phase offset and ζ_0 is the amplitude of the displacement. It is useful to have a motion-sensitising gradient, which is alternated in polarity at the same frequency as the proton motion. This alternating polarity of the motion-sensitising gradient is illustrated in Figure 2.3. If τ is chosen such that $\int_0^\tau G_r(t)dt = 0$, then the resulting phase shift can be written as:

$$\Phi(r,\theta) = \frac{2\gamma NT(G \cdot \zeta_0)}{\pi} \sin(k \cdot r + \theta) \tag{2.6}$$

N is the number of gradient cycles and T is the period of the mechanical excitation. Consequently, the amplitude of the harmonic oscillation can be directly calculated given

the phase shift at several phase offsets at each pixel. In addition, as can be seen in Equation (2.6), the phase shift is proportional to the scalar product of $G \cdot \zeta_0$ and N. Therefore, if phase shifts are accumulated over multiple cycles of mechanical excitation (increasing N), higher sensitivity can be gained in order to detect small amplitude motion.

Through this means, the amplitude and phase of the wave travelling through the medium, induced by the external driver, are reconstructed by collecting images at multiple phase offsets with respect to the mechanical excitation [94]. This method was validated by comparing MRE measured displacements with displacements measured by laser optics (r^2 = 0.97) [107].

2.3.3 Inversion Algorithms

This section summarises several methods for calculating material stiffness from elastography data. The general approach is to derive equations relating shear stiffness to measurable quantities.

It is a good approximation to model biological tissue as linearly elastic under the small strains induced by MRE (the harmonic displacement are generally a few microns) [56]. The full elasticity matrix describing a linear elastic material has 21 independent constants. If one assumes that the material is isotropic, this number reduces to just two independent values (e.g. K and G) to characterise the tissue, where K represents the bulk modulus and G is the shear modulus. If local homogeneity is also assumed, the equation for harmonic motion can be written as:

$$G \bigtriangledown^2 \mathbf{u} + (\lambda + G) \bigtriangledown (\bigtriangledown \cdot \mathbf{u}) = -\rho\omega^2\mathbf{u} \tag{2.7}$$

where λ is the first Lamé parameter (= K - 2/3G), ρ is the density, ω is the angular frequency of the mechanical loading and $\mathbf{u}$ is the displacement field. The material constants, K and G, can be considered complex quantities where the imaginary component represents attenuation, or damping. It is apparent from this equation that wave propagation is solely dependent on inherent properties of the tissue (K and G). The shear modulus is associated with "shear waves" (i.e. distortional waves that do not involve a changes in material volume), whereas the bulk modulus is associated with "longitudinal waves" (i.e. dilatational waves including sound waves that involve local volume changes). If incompressibility is assumed, then Equation (2.7) reduces to the Helmholtz wave equation.

$$G \bigtriangledown^2 \mathbf{u} = -\rho\omega^2\mathbf{u} \tag{2.8}$$

An inversion algorithm is then used to solve Equation (2.8) for the shear modulus of the material. Most shear stiffness values estimated with elastography are seen as "effective" stiffnesses, which are accurate for a single frequency [68, 77, 79, 80, 93]. "Effective" or

relative values of tissue stiffness can be important for comparison of adjacent tissues in demarcating healthy from diseased tissue. Additionally, they can be useful in measuring disease progression in patients. In one study that plotted the linear regression of MRE stiffness versus dynamic mechanical analysis (DMA) measured stiffness, the non-zero y-intercept indicated systematic differences between the two measurement methods [128]. Variations in stiffness estimates arise from the a) differences in loading frequencies and b) assumptions made in each inversion algorithm. A large portion of the research investigating elastography has gone towards the development of inversion algorithms that produce accurate and repeatable stiffness estimates from elastography displacement fields.

Manual Estimation The simplest means of estimating shear stiffness assumes that the tissue is linearly elastic, locally homogeneous, isotropic, incompressible and non-viscous. In the case of a simple shear wave, the shear modulus (G) is simply a function of the shear wave speed (v_s) and density (ρ).

$$G = \rho v_s^2 \tag{2.9}$$

where wave speed can also be written as the product of the frequency (f) and wavelength (λ). If there is only one wave present, the shear modulus is calculated by manually measuring the wavelength, given that the frequency of excitation is known. In some studies, this manual method is implemented by drawing a line on a 2D image slice, marking the peaks and measuring the wavelength as the distance between two peaks [14, 86, 128, 139]. The method breaks down in wave fields that contain reflections or attenuation.

As an illustration, a line was drawn between two peaks in the MRE phase contrast image in Figure 2.5 and the wavelength (λ) was measured to be approximately 38 mm. If the frequency of excitation (f) is known to be 60 Hz, the shear modulus can be calculated as:

$$\begin{aligned} G =& \left(1.0^{-6}\ \text{kg/mm}^3\right)\left(30\ \text{mm} \cdot 60\text{s}^{-1}\right)^2 \\ G =& 5.2\ \text{kPa} \end{aligned} \tag{2.10}$$

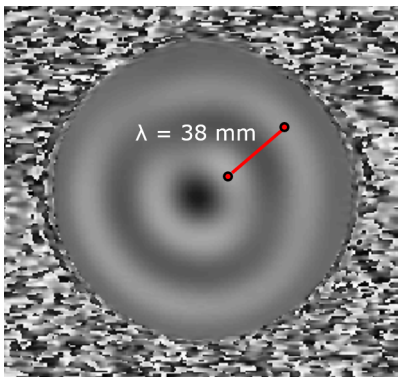

FIGURE 2.5: A phase contrast image encoding displacement in a cylindrical phantom is shown with a line drawn between two peaks, roughly measuring the wavelength (λ).

Local Frequency Estimation Local frequency estimation (LFE) is a commonly used algorithm for estimating spatial frequency ($1/\lambda$). LFE uses a set of lognormal quadrature wavelets to extract instantaneous spatial frequencies over several scales [76]. In concept, a pair of lognormal filters can be applied, which have appropriate bandwidths that contain the spatial frequencies of the wave image. Then, the local spatial frequency estimate is computed as the ratio of the two responses multiplied by the geometric mean of the two central frequencies of the filters. The estimation works well if the signal falls within the spectrum of frequencies included in the filters. A larger number of filter sets results in greater accuracy of the frequency estimate [94]. The shear modulus is then related to the temporal mechanical frequency (known) and estimated spatial frequency.

$$G = \rho \frac{f_t^2}{f_{sp}^2} \tag{2.11}$$

The LFE method is relatively insensitive to noise [94]. However, one major drawback is that the method has low resolution at boundary edges. Correct spatial frequencies are only reached half of a wavelength into a region. Therefore, in small objects where transverse wavelengths are much longer than the object of investigation, LFE will fail to accurately measure the local frequency of the propagating wave [93]. In addition, the LFE method assumes local homogeneity, incompressibility and no attenuation of waves. In one comparison of LFE and a direct inversion method [96], the LFE accurately reconstructed shear moduli, but inclusions were blurry, edges poorly defined and some artifacts were obvious. An additional disadvantage of the LFE inversion method is that a single real-valued shear modulus is estimated rather than a complex modulus, which contains information on the material damping.

However, LFE is advantageous since it allows material parameters to be estimated without utilising the equations of motion, which require second-order spatial derivatives [28]. Calculating derivatives of noisy data can result in inaccurate material parameter estimates.

Another advantage of the LFE method is that shear estimates can be obtained from a single image (i.e. displacements from a single encoding direction) or multiple images whereas other inversion methods often require displacements encoded in three orthogonal directions. The method, however, is also easily extended to 3D data sets.

Phase Gradient Method Another approach to deriving the spatial wavelength is known as the phase gradient (PG) method [167]. From MRE data, one has both amplitude and phase information from each pixel. The spatial change in phase (i.e. phase gradient) can then be converted into local spatial frequency or wave velocity [115]. Although simple in concept, this method is highly sensitive to noise. Additionally, it is inaccurate when two or more waves are superimposed (e.g. reflected waves) or when motion is complex and does not represent a single shear wave [93, 128]. In practice, the phase gradient method has been shown to overestimate shear moduli [128].

Direct Inversion Methods Direct inversion (DI) methods [61, 66, 93, 95, 96, 112, 114, 141, 143] invert the Helmholtz wave equation (Equation (2.8)) using the spatial Laplacian at each point. In practice, direct methods require data smoothing and accurate calculation of second derivatives from noisy data [93]. Data can be fit to polynomial functions which have analytic derivatives [112] to reduce the impact of noise in the signal on parameter estimates.

Matched Filter Matched filter (MF) algorithms use an adaptive smoothed matched filter and its second derivative to perform the division of the right-hand side of Equation (2.8) by the Laplacian described in the DI method above. A filter is chosen such that it minimises the variance of the conditional probability density function of the estimate for G in each region of interest [113]. Since filters are varied across the image, this method becomes computationally intensive.

Variational Method A variational formulation (also known as the virtual fields method) was introduced which multiplies the equation of motion by a sufficiently smooth test function, $\mathbf{v} = (v_1, v_2, v_3)$ [131, 132]. Setting the test function to zero on the boundaries eliminates the unknown traction term and permits one to solve for the material constants. This method avoids calculation of local second order derivatives of the noisy displacements. Only first order derivatives are required of the MRE displacement field and the smooth test function. Analytic and numerically derived test functions have been used to estimated isotropic shear moduli from MRE data [29, 118]. The optimised virtual fields method [9] will be discussed in greater detail in Chapters 5 and 6 as it applies to the estimation of isotropic and anisotropic material properties.

Helmholtz Decomposition The Helmholtz (or Helmholtz-Hodge) decomposition of smooth data states that every vector field can be written as the sum of a divergence-free part (u_T), a curl-free part (u_L) and a harmonic part (u_H), which is both divergence- and curl-free. In a nearly incompressible medium, the harmonic part becomes negligible and the displacement field can be written solely in terms of u_T and u_L. In many studies [101, 113, 114, 143], Helmholtz decomposition was used (through application of the curl) to remove the longitudinal component of the wave displacement. The curl of a 3D displacement field is computed as:

$$\bigtriangledown \times \mathbf{u} = \left(\frac{\partial \mathbf{u}_z}{\partial y} - \frac{\partial \mathbf{u}_y}{\partial z}\right)\hat{i} + \left(\frac{\partial \mathbf{u}_x}{\partial z} - \frac{\partial \mathbf{u}_z}{\partial x}\right)\hat{j} + \left(\frac{\partial \mathbf{u}_y}{\partial x} - \frac{\partial \mathbf{u}_x}{\partial y}\right)\hat{k} \tag{2.12}$$

Rather than assuming incompressibility, as was done to arrive at Equation (2.8), the longitudinal component is removed mathematically. After performing the curl, an inversion method (e.g. LFE, direct inversion, etc.) can be performed. One disadvantage of performing the Helmholtz decomposition is the extra order of derivative required through the curl operation. Additionally, the curl operator assumes local homogeneity which may not be an accurate assumption.

Finite Element Model Update Method The boundry value Finite Element Model Update (FEMU) method is an iterative approach to solving the inversion problem, originally suggested for estimation of elastic property distributions from ultrasound elastography displacements [69]. An initial estimate of material parameters is used as input to the forward problem along with boundary conditions applied from the measured elastography data. Then, the forward problem is solved, iteratively updating the material properties while minimising the difference between modelled and measured displacement fields. The FEMU method can be used to take into account the geometry, including boundaries, of the the structure being imaged, avoiding the assumption of waves travelling in an infinite medium.

A FEMU inversion method has been proposed previously [35, 36, 46, 49, 155, 157]. Van Houten et al. [155, 157] developed a moving-subzone approach to measure heterogeneous material properties of breast tissue. The FEMU method was also proposed to estimate the global shear modulus of an isotropic phantom by modeling the contact and pressure between a pneumatic driver and phantom surface [87]. Direct FEMU methods have been implemented and compared with the LFE and direct inversion methods [63–65]. Honarvar et al. implemented a direct FEMU method that directly solves for material properties, omitting the need for an iterative procedure. Additionally, the assumption of local homogeneity was circumvented by dicretising the shear modulus using a constant shape function and solving for the shear modulus at every point [66].

A mixed-FEMU method, solving for the shear modulus and a hydrostatic pressure term, was compared with a FEMU method which utilised the curl to omit the longitudinal wave displacements [64]. The methods were implemented with phantom MRE data with multiple inclusions as well as images of prostate tissue. The mixed-FEMU method was more computationally expensive since it solved for two parameters rather than just one. However, the curl-FEMU method deteriorated with increasing noise in the signal. These methods were also compared with a direct inversion as well as LFE methods. FEMU methods were more accurate than both the DI and LFE methods. Overall, boundary value FEMU methods are often more accurate than direct methods yet are much more computationally expensive since they require solving the forward problem multiple times.

Bounded Media One inversion method addressed the assumption of waves travelling in an infinite medium by taking into account the approximate geometry of the imaged object, thus incorporating the physical boundaries [81]. Material properties were estimated by inverting equations which describe waves travelling in specific simplified shapes such as beams, disks and thin plates [54]. Compared to LFE which becomes inaccurate near the boundaries, these bounded media inversions provided accurate estimates throughout the 2D shape.

For example, cardiac stiffness was estimated by assuming that the left ventricle (LV) was a thin, spherical shell [77, 82]. To derive the equation of motion, a number of assumptions were made: 1) motion is axisymmetric and non-torsional; 2) displacement of the shell is small in comparison to its thickness; 3) the thickness of the shell is small compared with the smallest radius of curvature; 4) elements of the shell initially perpendicular to the middle surface remain so after deformation and are not elongated; 5) and the normal stress acting on planes parallel to the shell middle surface is negligible in comparison with other stresses. Expressed in terms of polar coordinates, the equation for waves propagating in a thin, spherical shell was:

$$\begin{aligned}\beta^2\frac{\partial^2 u}{\partial\theta^2}+2\beta^2\cot\theta\frac{\partial^2 u}{\partial\theta^2}-[(1+\nu)(1+\beta^2)+\beta^2\cot\theta]\frac{\partial u}{\partial\theta}+\\ \cot\theta[(2-\nu-\cot^2\theta)\beta^2-(1+\nu)]u-\beta^2\frac{\partial^4 w}{\partial\theta^4}-2\beta^2\cot\theta\frac{\partial^2 w}{\partial\theta^2}+\\ \beta^2(1+\nu+\cot^2\theta)\frac{\partial^2 w}{\partial\theta^2}-\beta^2\cot\theta(2-\nu+\cot^2\theta)\frac{\partial w}{\partial\theta}-2(1+\nu)w-\frac{a^2\ddot{w}}{c_p^2}\\ =-p_a\frac{(1-\nu^2)a^2}{Eh}\end{aligned} \tag{2.13}$$

where a is the mean radius of the shell; u is the complex circumferential displacement; w is the complex radial displacement; c_p is the flexural plate wave speed ($c_p = E/(1-\nu^2)\rho$); $\beta = h^2/12a$; h is the thickness of the shell; θ is the angular position around the shell;

and p_a is the applied load. Resulting elastic moduli were compared with an established pressure-volume method for estimating myocardial stiffness [20, 72]. There was a strong correlation between the shear stiffness measured using the MRE bounded inversion method and the pressure-volume loop method.

Similar to other inversion methods discussed previously, the equations of motion require the calculation of high-order derivatives. When displacement data is noisy, these can be a potential source of error. Additionally, the bounded media inversions disregard through-plane motion which can lead to systematic errors. Although this bounded inversion method eliminated the assumption of an infinite medium, it still assumed 1) isotropy, 2) homogeneity and 3) negligible displacement due to longitudinal waves.

2.3.4 Material Models

2.3.4.1 Viscoelastic Parameter Estimation

Biological tissues are viscoelastic meaning that the apparent stiffness of the material changes depending on the frequency of the harmonic motion applied. Additionally, due to viscoelasticity, shear waves applied by external actuators are damped within the tissue. Many groups (e.g. [24, 28, 61, 91, 96, 112–114, 141, 142]) have applied previously discussed inversion methods to solve for elasticity using a viscoelastic material model. Many viscoelastic material models have been used to describe the dissipative behavior in biological tissue during elastography experiments such as the Voigt [123], Kelvin-Voigt [153] and Zener [148] models, for example. In MRE experiments, the longitudinal viscosity is often neglected since its effects are not apparent on the scale of MRE experiments. Often, the shear modulus can be re-written as a complex modulus with both storage and loss components:

$$G^* = G' + iG'' \tag{2.14}$$

The loss factor (η) (also known as the structural damping coefficient, s) is the ratio of G''/G'. The real component of the complex modulus is referred to as the storage modulus whereas the imaginary component is the loss modulus.

In one study [142] utilising a viscoelastic model to reconstruct shear moduli from MRE, both the shear modulus and shear viscosity terms were accurately reconstructed in simulations but the viscosity term showed high variance in real MRE data. Additionally, it has been shown that, in skeletal muscle, both stiffness and viscosity are anisotropic [52, 61]. One study utilising ultrasound elastography reported that the shear wave attenuation in canine myocardium was approximately two times larger along the fibre direction compared to perpendicular to the fibres [158].

Ignoring viscous components has been shown to over-estimate the elastic modulus [68]. However, some researchers [138] have chosen to perform MRE at low frequencies ($<$ 50 Hz) as a means of minimising error since viscous damping has a smaller impact at low frequencies. In MRE experiments investigating properties of biological tissues, though, a wide range of driving frequencies have been used, ranging from 24.3 Hz [138] to 10 kHz [132]. At high frequencies, attenuation can severely dampen the amplitude of the propagating wave [6].

2.3.4.2 Isotropic Parameter Estimation

The large majority of MRE research has been aimed at identifying a single isotropic shear modulus or a complex shear modulus. As discussed previously, an isotropic, linearly elastic material can be fully described by two parameters (e.g. K and G). A number of parameter combinations may be used to describe the material including: G and ν, where ν, Poisson's ratio, describes the compressibility of the material. However, most isotropic inversion methods assume that the material is incompressible ($\nu = 0.5$), thereby, reducing the number of estimated material parameters to one.

2.3.4.3 Transversely Isotropic Parameter Estimation

However, many biological tissues, such as muscles and tendons, are composed of fibres. Often, these materials are better described by transversely isotropic material laws which have a greater stiffness along the axis of symmetry (Figure 2.6. Tumors have also been shown to be highly anisotropic [142].

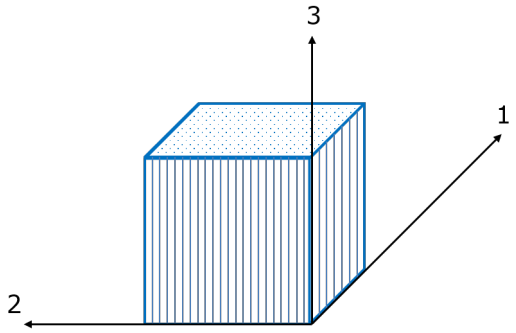

FIGURE 2.6: A transversely isotropic material with the fibre direction aligned with the [0 0 1] axis.

Numerous studies have estimated isotropic shear moduli of skeletal muscles [13, 14, 22, 26, 27, 37, 38, 58, 75, 92, 152]. The estimated parameters were either accepted to be a "mean" shear modulus which lies in between the stiffness parallel and perpendicular to the fibre direction or were reported for a specific direction relative to the fibre orientation. In one study, an isotropic MRE inversion was applied to MRE images of anisotropic structures in the brain, resulting in differences in estimated shear moduli up to 33% depending on the

loading condition (either parallel or perpendicular to the fibre direction) [3]. Therefore, an isotropic estimate of stiffness in an anisotropic medium is dependent on the imaging plane and does not necessarily represent the mean shear modulus. An appropriate material model is, therefore, necessary to accurately quantify the stiffness in the fibre direction as well as perpendicular to the fibres. Estimates of anisotropic shear moduli can be obtained using an isotropic inversion method by orientating the imaging plane to measure shear stiffness both parallel and perpendicular to the fibre direction [51, 52, 57, 85]. However, this method fails when the fibre structure becomes complex, such as in myocardium where the fibres are arranged in a helical pattern around the left ventricle.

An anisotropic linear elastic stiffness matrix, which relates the internal stress of the material to the strain, has 21 independent parameters. However, if the material is assumed to be transversely isotropic, the stiffness matrix is reduced to the following form:

$$\begin{Bmatrix} \sigma_1 \\ \sigma_2 \\ \sigma_3 \\ \sigma_4 \\ \sigma_5 \\ \sigma_6 \end{Bmatrix} = \begin{bmatrix} C_{11} & C_{12} & C_{13} & 0 & 0 & 0 \\ & C_{22} & C_{13} & 0 & 0 & 0 \\ & & C_{33} & 0 & 0 & 0 \\ & & & C_{44} & 0 & 0 \\ & sym & & & C_{66} & 0 \\ & & & & & C_{66} \end{bmatrix} \begin{Bmatrix} \epsilon_1 \\ \epsilon_2 \\ \epsilon_3 \\ \epsilon_4 \\ \epsilon_5 \\ \epsilon_6 \end{Bmatrix} \tag{2.15}$$

where $C_{12} = C_{11} - 2C_{44}$. Thus, there are five independent parameters: C_{11}, C_{33}, C_{13}, C_{44} and C_{66}. Engineering constants (Young's moduli, shear moduli and Poisson's ratios) can be calculated from the compliance matrix, which is the inverse of the elastic stiffness matrix.

$$\begin{bmatrix} C_{11} & C_{12} & C_{13} & 0 & 0 & 0 \\ C_{12} & C_{22} & C_{13} & 0 & 0 & 0 \\ C_{13} & C_{13} & C_{33} & 0 & 0 & 0 \\ 0 & 0 & 0 & C_{44} & 0 & 0 \\ 0 & 0 & 0 & 0 & C_{66} & 0 \\ 0 & 0 & 0 & 0 & 0 & C_{66} \end{bmatrix}^{-1} = \begin{bmatrix} \frac{1}{E_1} & \frac{-v_{12}}{E_1} & \frac{-v_{31}}{E_3} & 0 & 0 & 0 \\ \frac{-v_{12}}{E_1} & \frac{1}{E_1} & \frac{-v_{31}}{E_3} & 0 & 0 & 0 \\ \frac{-v_{13}}{E_1} & \frac{-v_{13}}{E_1} & \frac{1}{E_3} & 0 & 0 & 0 \\ 0 & 0 & 0 & \frac{1}{G_{12}} & 0 & 0 \\ 0 & 0 & 0 & 0 & \frac{1}{G_{13}} & 0 \\ 0 & 0 & 0 & 0 & 0 & \frac{1}{G_{13}} \end{bmatrix} \tag{2.16}$$

Five engineering constants are needed to define a transversely isotropic response: elastic parameters E_1 $(= E_2)$, E_3, G_{13} $(= G_{23})$, and Poisson's ratios ν_{12} and ν_{13} $(= \nu_{23})$, assuming a fibre direction aligned with the $[0\ 0\ 1]^T$ axis. Other combinations of parameters can be chosen (e.g. E_1, E_3, G_{12}, G_{13} and ν_{31}).

For transversely isotropic materials, inversion algorithms discussed previously (i.e. manual, LFE, PG, FEMU) have been applied to the identification of two [24, 28, 57, 75, 108, 115, 124, 126, 141], three [61, 116, 139, 143, 150, 151] or five parameters [129, 136], depending on the number of assumptions made. Some methods require the knowledge of

fibre directions (e.g. from DTI or *a priori* information) and others use MRE displacements themselves to identify the fibre orientation.

In a transversely isotropic material, the Young's moduli and shear moduli are related to the stress and strain induced relative to the fibre direction as shown in Figure 2.7.

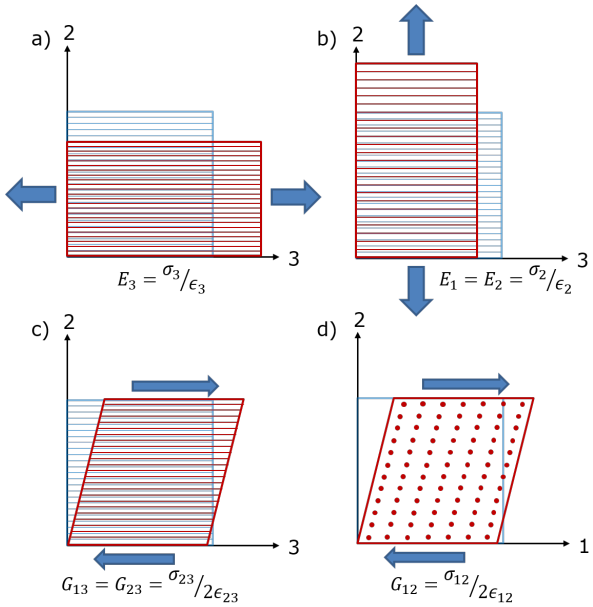

FIGURE 2.7: Tensile moduli are obtained by stretching the material in the a) fibre direction (E_3) and b) transverse direction - perpendicular to the fibres ($E_1 = E_2$). Shear moduli are described by deformation in planes c) parallel ($G_{13} = G_{23}$) and d) perpendicular (G_{12}) to the fibres. Blue lines indicate the undeformed state.

Under harmonic loading, a complex wave is composed of three independent waves: 1) a longitudinal wave, dependent on the bulk modulus of the material, 2) a slow shear wave, dependent on the shear moduli and 3) a fast shear wave, dependent on the shear and tensile moduli. Each of these three independent waves travels at a unique speed.

In an incompressible material, the longitudinal wave speed approaches infinity. Slow shear waves do not induce fibre stretching and so only provide information regarding the two shear moduli (G_{12} and G_{13}). The polarisation direction of the slow shear wave ($\mathbf{m_s}$) is perpendicular to both the fibre direction ($\mathbf{a}$) and the wave propagation direction ($\mathbf{n}$), induced by a shear similar to that shown in Figure 2.7d. Conversely, fast shear waves induce fibre stretching and so its speed is dependent on the two tensile moduli of the material (Figure 2.7c). Fast shear waves are polarised in the plane defined by the fibre and propagation directions. The polarisation direction ($\mathbf{m_f}$) is perpendicular to the wave propagation direction and the slow shear wave polarisation direction. In elastography, the resulting complex wave is a combination of these two independent shear waves traveling in the same direction at different speeds along with the longitudinal wave. The wave polarisation

directions can be written as:

$$\mathbf{m_s} = \frac{\mathbf{n} \times \mathbf{a}}{|\mathbf{n} \times \mathbf{a}|} \qquad \mathbf{m_f} = \mathbf{n} \times \mathbf{m_s} \tag{2.17}$$

Slow and fast shear wave speeds were measured using ultrasound elastography by applying an external vibration (100 Hz) parallel and perpendicular to the fibre direction [51]. In excised bovine muscle, fast shear waves were approximately three times faster than slow; and in *in vivo* human biceps, the fast shear wave speed was four times that of the slow wave.

Five Parameter Estimation Only one study [136], to the author's knowledge, estimated all five parameters and reported the anisotropic Young's moduli (E_1 and E_3) and shear moduli (G_{12} and G_{13}) from ultrasonic shear wave measurements. However, due to large errors in the estimation of C_{13}, the subsequent estimation of the fibre Young's modulus (E_3) failed.

Three Parameter Estimation If the transversely isotropic material is assumed to be incompressible, the number of independent material constants is reduced from five to three (e.g. G_{12}, G_{13} and E_3). In one study, G_{12}, G_{13} and E_1/E_3 were estimated from MRE displacements using a phase gradient inversion method [115]. However, displacements were only acquired from one encoding direction and thus, E_3/E_1 could not be deduced due to lack of information describing the fast shear wave propagation. In a later study [143], three parameters were estimated: G_{12}, G_{13} and $G_\beta = 4 \cdot G_{12}E_3/E_1$ using a direct inversion method which decomposed the stress tensor into the longitudinal and transverse components. Applied to simulated harmonic displacement data with no added noise, the relative L^2-errors in estimated values were 36.7%, 39.5% and 58.0%, respectively, illustrating that the method was not robust.

A four parameter model to describe transversely isotropic, linear elastic materials was derived from a transversely isotropic hyperleastic material law at the reference state [47]. The model is valid for the assumption of small strain.

$$\begin{aligned} \kappa &= K & \phi &= \frac{G_{13}}{G_{12}} - 1 \\ \mu &= G_{12} & \zeta &= \frac{E_3}{E_1} - 1 \end{aligned} \tag{2.18}$$

Assuming incompressibility ($\kappa \to \inf$), the model reduces to three parameters: μ, the shear modulus in the isotropic plane, ϕ, related to the shear anisotropy and ζ, related to the tensile anisotropy. The three parameters can be restated in many forms. However written, two relate to the two shear moduli and one relates to the tensile anisotropy.

Building upon this model, simulation studies by Tweten et al. [150] characterised the role of each parameter on the three wave speeds. θ was defined as the angle between the fibre vector, $\mathbf{a}$, and the wave propagation direction, $\mathbf{n}$. At $\theta = 0°$ and $\theta = 90°$, the fast wave speed was zero. An increase in ζ led to an increase in the fast shear wave speed but had no effect on the slow shear wave speed. Simulations also showed that slow and fast shear wave speeds were unaffected by the bulk modulus, illustrated by sweeping over values of κ.

In this and successive studies [139, 150, 151], directional filters were used to filter the fast and slow shear waves by performing a dot product between the displacement field and the normalised slow and fast shear wave polarisation directions, respectively. The second step was to isolate the propagation direction ($\mathbf{n}$) by filtering the polarised data in Fourier space [97]. LFE was used to estimate the wave speed at each voxel and a weighted least squares method was used to estimate the material properties. Relative displacement amplitudes at each voxel were used as weights in the weighted least squares method.

Results from a simulation study [150] showed that local estimates of the material properties depended on the location (i.e. near or far from boundaries). For global estimation, a Monte-Carlo experiment (n = 30) was carried out for each simulation with and without Gaussian noise added to the simulated displacements (SNR = 10) prior to processing. For the case with noise, mean global estimates of μ and ϕ were within 25% of the true values. However, the mean global estimate of ζ was always underestimated and erred by up to 40%.

In a subsequent study [139], turkey breast was embedded in gelatin in cylindrical and cubic containers and vibrated (800 Hz). The cylinder was vibrated from a rod through the centre of the container so that waves propagated radially. The cubic specimen was vibrated with varying actuations. Fibre orientations of the muscle tissue were measured using DTI and an average fibre orientation was assumed to be homogeneous throughout the sample. A fibrin aligned gel [108] was also excited at 200 Hz in a cylindrical container and 600 Hz in a cubic container. Displacements were quantified and a directional filter was used to separate the slow and fast waves travelling through the material in 16 different propagation directions. In contrast to the LFE method used previously, wavelengths were estimated by manually selecting peaks and valleys in each filtered displacement direction. Anisotropy was estimated as the ratio between slow and fast shear wave speeds.

In the cylindrical phantoms, researchers were able to measure μ and ϕ since only slow shear waves were excited. In the cubic phantom, fast shear waves were induced and then μ and ζ were measured. However, during no experiment were all three parameters identified simultaneously. Results were compared to complex shear moduli measured through dynamic shear testing (DST) between 30 Hz - 40 Hz. Values were not directly comparable due to the difference in frequency between the MRE and DST experiments. However,

overall, values appeared to be acceptably similar and only qualitative comparisons were made.

Three inversion methods, each estimating either three or four parameters, were tested with simulated harmonic motion in a finite element cube model [149]. Three parameters estimated were: μ, ϕ and ζ, describing the shear, shear anisotropy and tensile anisotropy, and four parameters included a loss factor η. Two directional filter inversion (DFI) methods were compared, one using LFE and the other using a local direct inversion (LDI) [111], to a curl inversion method, separating the longitudinal from transverse waves. Identification of parameters was compared with 1) slow waves only, 2) fast waves only and 3) slow and fast shear waves as well as with varying amounts of noise (SNR = 1 - ∞). With both fast and slow shear waves present in the noise-free simulation, only the isotropic shear modulus was accurately estimated (to within 25% of the true value) using each inversion method. The curl method accurately estimated ϕ and the DFI-LFE method accurately estimated ζ. However, no method accurately estimated all three parameters. When Gaussian noise was applied, isotropic shear and the loss factor η were the only parameters which were accurately estimated at SNR $\geq$ 5.

Three parameters, G_{13}, G_{12} and E_3, were also identified in the soleus, gastrocnemius and tibialis muscles of the lower leg using multi-frequency MRE and a direct inversion method (applied to the curl of the displacement field) [61]. Complex moduli were estimated which were composed of the storage (real part) and loss (imaginary part) moduli. The loss factor (a ratio of the loss modulus to the storage modulus) was greater for the G_{13} than for the G_{12} parameter, indicating that damping in skeletal muscle may also be anisotropic. This method was not tested with phantom or simulated data with known parameters. It should be reiterated that the studies mentioned in this section have all either assumed that the material is incompressible or removed the longitudinal wave displacemnts with the curl of the wave field, which allows the number of independent parameters to be reduced to three.

Two-parameter estimation Other studies have estimated only two parameters, generally two shear moduli, which provide information on the shear stiffness and anisotropy of the material, which requires the assumption of at least one other parameter.

The methods discussed previously require prior knowledge of the fibre orientation, either via DTI, histology or simply *a priori* information. However, other methods have used displacement information to additionally estimate Euler angles defining fibre directions [24, 28, 141]. For example, Chatelin et al. [24] used only one displacement encoding direction to estimate the G_{13} and G_{12} shear parameters. An ultrasound probe was used as the driver (frequencies = 100 Hz and 200 Hz) and MRI was used to measure displacements. Displacements were first converted to a polar coordinate system and the Green formula-

tion, which describes a wave travelling from a point source, was used to derive analytic displacement fields from an initial guess of the shear modulus. Then, displacements were directionally filtered at 36 different directions within the image plane and a shear modulus was estimated, using an iterative minimisation of a cost function, for each individual direction. The elasticity matrix was then fit to the 36 shear parameters, aligning the third Cartesian direction along the fibre orientation. The method was tested with numerical (simulated) results with added Gaussian noise, an isotropic gel phantom, an anisotropic PVA phantom [25] and ovine back muscle. In each case, the results were consistent with stiffness values measured from dynamic mechanical analysis (despite measuring at different frequencies). One limitation of this study was that multiple parameters were assumed, including C_{11} in the stiffness tensor and Poisson's ratio. Additionally, attenuation was not included. Another limitation is that the method is only valid for a homogeneous fibre orientation within the region of interest. The benefits of this method were the speed of the analysis (requiring only 2 seconds per direction) and lack of requirement of prior knowledge of fibre orientations.

Similarly, in an earlier study, an LFE inversion algorithm was used to calculate viscoelastic shear moduli (a shear modulus, G, and a loss factor, $\eta = G"/G'$) in 32 planar directions from the curl of the displacement field [28]. The 32 shear moduli were then used to estimate the anisotropic shear moduli (G_{13} and G_{12}). The method was tested with simulated displacements with added Gaussian noise ($\sigma = N\% \cdot \overline{d}$, N = [0, 25, 50]). For the anisotropic shear estimation, G_{12} and η, which describes damping, were consistently underestimated for by at least 12% and 10%, respectively, including the case with no noise (N = 0). G_{13} was accurately estimated (to within 7%) for each noise case. The fibre direction was assumed to be known and waves were only polarised perpendicular to the fibre direction.

2.3.4.4 Orthotropic Parameter Estimation

Only one group, to our knowledge, has estimated orthotropic material parameters from MRE displacement data. In an orthotropic material, there are nine independent parameters in the elasticity matrix. A waveguide inversion method has been proposed which utilised knowledge of fibre directions to estimate all nine independent parameters [129, 130, 133]. The method combined DTI, MRE, spatial-spectral filtering, a Helmholtz decomposition and a direct inversion to estimate nine independent constants of the elasticity matrix. From the fibre direction (obtained from DTI), a rotating reference frame was calculated at each point, which was composed of one vector tangent to the waveguide (fibres) and two orthogonal vectors. A Helmholtz decomposition was used to separate the longitudinal and transverse waves and a transform was used to extract only the component of the wave displacement travelling tangential to the fibre direction. A dot product projection of the

tangential wave displacement with the local reference frame yielded the displacement contributions to wave propagation along the local fibre direction.

Parameters in the elasticity matrix were calculated directly by inserting either the longitudinal (u_L) or transverse (u_T) wave displacements travelling in one of the three orthogonal directions (n_1, n_2 and n_3) into the Helmholtz wave equation (Equation (2.8)). For example, C_{11} was solved as:

$$C_{11}\frac{\partial^2 u_1^L(n_1)}{\partial x_1^2} = -\rho\omega^2 u_1^L(n_1) \tag{2.19}$$

This method was tested in cerebral nerve fibres in healthy and diseased patients [129, 130]. Although nine parameters were estimated for the cerebro-spinal tracts in healthy volunteers [130], there were no significant differences between C_{11}, C_{22} and C_{33} values, nor between values of C_{44}, C_{55} and C_{66} suggesting none or potentially weak anisotropy. In the comparison between healthy volunteers and patients with amyotrophic lateral sclerosis (ALS), C_{33}, C_{44} and C_{66} were compared. The two shear terms, C_{44} and C_{66}, were significantly decreased in disease patients whereas C_{33} (related to the fibre stiffness) showed no difference.

Although this method was tested with MRE data, it is dependent on the the shape of the waveguides (fibre tracts) and boundary conditions. Additionally, the inversion requires calculation of second-order derivatives of the displacement field, which in MRE, is subject to noise. To date, this has not been tested with simulated data or phantom experiments.

Table 2.1 lists studies which identified anisotropic material properties from MRE displacement fields as well as the medium which was used and the parameters identified.

TABLE 2.1: Previous studies identifying anisotropic material properties from MRE. *In the first study by Romano et al., nine parameters were estimated, yet results were only presented for two parameters.

Reference	Medium	Parameters Estimated
[133]	Celery	C_{11}, C_{22}, C_{33}, C_{13}, C_{23}, C_{12}, C_{44}, C_{55}, C_{66}*
[141]	Breast tissue	G_{12}, G_{13}
[115]	Muscle tissue	G_{12}, G_{13}
[109]	Aligned fibrin gels	G_{12}, G_{13}
[143]	Muscle tissue	G_{12}, G_{13}, t
[130]	Brain tissue - white matter	C_{11}, C_{22}, C_{33}, C_{13}, C_{23}, C_{12}, C_{44}, C_{55}, C_{66}
[57]	Muscle tissue	G_{12}, G_{13}
[125]	Anisotropic phantom	G_{12}, G_{13}
[28]	Isotropic phantom and simulated data	G_{12}, G_{13}
[126]	Muscle tissue	G_{12}, G_{13}
[129]	Brain tissue - white matter	C_{11}, C_{33}, C_{13}, C_{44}, C_{66}
[61]	Muscle tissue	E_3, G_{12}, G_{13}
[151]	Turkey breast	μ, ϕ, ζ
[150]	Simulated data	μ, ϕ, ζ
[139]	Turkey breast	μ, ϕ, ζ
[24]	Isotropic phantom, anisotropic phantom, simulated data, muscle tissue	G_{12}, G_{13}
[149]	Simulated data	μ, ϕ, ζ

2.3.5 Muscle Elastography

Muscle is anisotropic with the a greater stiffness along the fibre direction compared to the transverse direction [24, 52, 57, 61, 85, 115, 116, 126, 139]. Therefore, an assumption of material isotropy is no longer accurate. Additionally, whereas tissue stiffness values can change as a result of pathology, the effective stiffness of skeletal muscle tissue can also change, as measured by elastography, with active contraction and passive stretching [13–15, 37, 38, 52, 127], adding to the complexity in measuring and interpreting the results.

2.3.6 Cardiac Elastography

Cardiac elastography presents unique challenges compared with skeletal muscle since, in addition to being anisotropic, the muscle is never in a fully relaxed state. Effective shear moduli measured with MRE at individual time points are a combination of chamber properties that vary with pressure loading as well as intrinsic properties such as myocardial activation during systole. Kolipaka et al. [78] showed a linear relationship between both shear stiffness and left ventricular pressure as well as [80] shear stiffness and contractility. Additionally, cardiac tissue stiffness is on the order of 10 kPa and the left ventricular wall in humans is between 1-2 cm. Applying shear waves using an external actuator requires the use of low frequency mechanical waves (< 100 Hz) in order to achieve adequate wave amplitudes. However, waves at these low frequencies are impacted by waveguide effects. Therefore, the geometry of the heart should be taken into account when performing an inversion of the harmonic displacements [140]. To incorporate boundary effects, Kolipaka et al. modelled the left ventricle (LV) as a thin spherical shell in order to perform inversions of the wave equation [79].

Wassenaar et al. [163] carried out a study of healthy human volunteers, estimating isotropic shear moduli using MRE with an LFE inversion method. One short-axis slice was used to estimate stiffness at 8 cardiac phases in 29 healthy volunteers. Effective shear moduli were not normalised for LV pressure, making comparisons between patients difficult. An apparent increase in stiffness with age could have simply been due to an increase in afterload resulting from arterial wall stiffening.

Cardiac MRE was also used to measure the mean LV myocardial stiffness in eight hypertensive pigs [99]. Results showed an increase in wall stiffness at end-diastole throughout the progression of diastolic heart failure. End-systolic mean LV wall stiffness initially increased but then stagnated. Similar cardiac MRE data were collected for seven pigs before and after inducing myocardial infarctions [98]. Results showed a greater mean shear in the infarct region at both end-diastole and end-systole compared with the remote region. The MRE measured shear was also strongly correlated with mechanical-testing derived stiffness measured on excised tissue samples. Cardiac MRE, therefore, has the potential to quantify both pathological tissue as well as disease progression. However, as mentioned, these studies have estimated an effective shear modulus that is dependent on both the loading and intrinsic properties of myocardium. A potential contribution to this field would be to separate the loading effects on estimated properties in order to determine solely the intrinsic properties of the myocardium.

Additionally, all studies investigating properties of myocardium mentioned to this point assume an isotropic material. Only one study [134] (unpublished), to this point, has estimated anisotropic shear properties of myocardium from MRE displacement fields. With knowledge of fibre orientations, measured by DTI, displacements at specific angles rela-

tive to the local fibre orientation were measured and used to estimate nine parameters of an orthotropic, linear elastic material model. Only two shear moduli (C_{44} and C_{66}), which describe shear in the fibre direction and transverse plane, were reported in the results and were not statistically different. Couade et al. [31] measured shear stiffness in both the longitudinal and short axis planes at the midwall of the LV, noting larger moduli in the short axis than the long axis. This can be explained since, at the midwall of the LV, fibres, which have a greater stiffness, are oriented approximately circumferentially in the short axis plane. Conversely, when the probe was oriented longitudinally, the shear stiffness was measured orthogonal to the fibre direction, which is known to be less stiff than the fibre direction.

Table 2.2 below lists a selection of cardiac elastography studies, using both ultrasound (US) and MR imaging modalities. For consistency, values in the table only report baseline (healthy) stiffness estimates when pathologies were examined, such as in [98, 99]. For loading frequencies less than 400 Hz, shear moduli ranged between 1 - 38.7 kPa. Studies that reported shear moduli *in vivo* at multiple time points in the cardiac cycle reported diastolic stiffness values between 1 - 15 kPa whereas systolic shear moduli varied between 5.1 - 38.7 kPa. For example, in [153], systolic shear stiffness values ranged between approximately 10 - 35 kPa, while estimated diastolic stiffness showed less variance, ranging between 1.0 - 3.5 kPa for the eight pigs imaged. Conversely, [98] estimated effective shear moduli within a narrow range (3.2 - 6.0 kPa) over the entire cardiac cycle at 80 Hz loading frequency. The discrepancy between estimated values of shear moduli between the studies listed in Table 2.2 is due to the frequency applied as well as the inversion methods used. However, generally, a greater effective stiffness is observed at end-systole than end-diastole.

Table 2.2: Cardiac elastography studies. ED: end-diastole, ES: end-systole, NA: Not applicable.

Reference	Imaging Modality	Shear Modulus (kPa)	Frequency (Hz)	Specimen	Cardiac Time Point
[70]	US	30	10-90	human	ES
[79]	MRI	5.1 - 9.89	80	porcine	20 cardiac time points
[78]	MRI	7.1 - 15	80	porcine	Varying end-diastolic pressures
[80]	MRI	5.1 - 14.0	80	porcine	Varying levels of systolic contraction
[163]	MRI	4.0 - 11.0	80	human	8 cardiac time points
[99]	MRI	3.2 - 6	80	porcine	8 cardiac time points
[98]	MRI	3.2 - 6	80	porcine	8 cardiac time points
[5]	MRI	3.0	140	porcine	ED
[4]	MRI	2.0 - 4.3	80, 100, 140, 180 and 220	human	trigger point: 100 ms after R-wave peak
[144]	US	1.66 - 3.84	50 - 300	human	Late-diastole
[153]	US	1 - 3.5 / 10 - 35	50 - 400	porcine	ED/ES
[31]	US	2.17 - 3.5 / 24.9 - 38.7	100 - 400	ovine	ED/ES

There have been numerous studies[41–45, 138] using cardiac MRE to measure shear wave amplitude, rather than effective shear stiffness. In noisy images, increasing the number of waves present in the tissue reduces the impact of noise and improves identification of shear properties. However, due to the viscous nature of myocardium, shear waves at high amplitudes are damped out. At a loading frequency of 50 Hz and an assumed isotropic shear modulus of 30 kPa [70], the wavelength would be approximately 10 cm, which is much larger than the heart. Therefore, rather than estimate shear stiffness from potentially few wavelengths, researchers have used shear wave amplitude (SWA) as a surrogate measurement of intrinsic properties of myocardium.

SWA MRE is based on the fundamental concept that energy flow through the heart is characterised by a constant flux of elastic wave energy. For a steady-state harmonic oscillation, the energy flux (F) can be written as:

$$F = \frac{1}{2}\rho\omega^2 U^2 c \tag{2.20}$$

where U is the scalar magnitude of displacement in the three Cartesian directions ($U = \sum_j U_j^2$, j = [1, 2, 3]), ρ is the density, ω is the angular frequency and c is the shear wave speed. Since the flux is constant, the ratio of the magnitude of displacement at two time points during one cardiac cycle (t_1 and t_2) can be written as:

$$\frac{U(t_1)}{U(t_2)} = \sqrt{\frac{c(t_2)}{c(t_1)}} \tag{2.21}$$

When a material is nearly incompressible, there is no change in wave amplitude due to a change in longitudinal wave speed. However, a change in shear stiffness has a power law relationship with the change in SWA. Utilising Equation (2.9), the ratio between SWA at two time points in the cardiac cycle can be written as:

$$\frac{U(t_1)}{U(t_2)} = \left(\frac{G(t_2)}{G(t_1)}\right)^{\frac{1}{4}} \tag{2.22}$$

Conversely, the equation can be written in terms of the ratio of shear moduli: $G(t_1)/G(t_2) = (U(t_2)/U(t_1))^4$. This equation allows for the measurement of changes in shear modulus by comparing changes in SWA [138]. When testing this method in six healthy volunteers with a 24.3 Hz external vibration applied, the ratio of shear between $t_{systole}$ and $t_{diastole}$ was 6.3 $\pm$ 0.9. Additionally, it was seen that changes in shear ratios preceded geometric changes in the heart, signifying isovolumetric contraction and isometric relaxation. Like shear modulus, SWA was shown to be correlated with LV pressures (R^2 = 0.89) [42].

This method was applied to compare isovolumetric relaxation (IVR) and isovolumetric contraction (IVC) times in healthy volunteers and patients with mild diastolic dysfunction (n=11) [43]. Duration times of isometric contraction were not different between the two groups whereas patients with diastolic dysfunction had significantly longer times of

isometric relaxation ($P < 0.01$). Additionally, measurements of SWA were shown to be significantly less in patients with diastolic dysfunction compared with healthy young volunteers and age-matched healthy volunteers [41, 44]. The same research group utilised low frequency harmonic loading to induce high amplitude wave oscillations in myocardium that were imaged using a standard cine ssfp MRI sequence rather than phase contrast (displacement encoding) sequence [45]. Shear wave amplitudes were measured by drawing a line from the anterior chest wall to the centre of the LV cavity and measuring the average peak height in the myocardium. Results were normalised by SWA's measured from a region of interest in the anterior chest wall. Similar to [43], IVR and IVC times were measured using the vibration synchronised MRI sequence. Resulting amplitudes measured using standard cine ssfp imaging were not significantly different from those measured using phase contrast MRE, indicating that information on relative stiffness of myocardium could be obtained during a typical cardiac MRI scan without the need for a longer scan time.

Using SWA's to assess properties of myocardium has the distinct advantage of bypassing the need for inversion methods. Therefore, low frequency mechanical loading can be used in order to achieve large amplitude waves (1 mm) since the number of wavelengths in the region of interest is not an issue. However, one goal of estimating absolute material properties of myocardium is to use the values as input to patient-specific finite element models, which are then used to accurately model cardiac mechanics. Therefore, although SWA may be a useful diagnostic tool in itself, it does not measure intrinsic properties, which would contribute to the overall understanding of patient-specific mechanics and myocardial function.

2.4 Limitations and Gaps in Knowledge

To summarise, stiffness is an important determinant of cardiac function and may be a useful diagnostic marker of cardiac pathologies, including hypertensive heart disease and diastolic dysfunction. However, most methods of estimating myocardial stiffness either provide relative (or surrogate) measurements. The finite elasticity simulation method [7, 160] estimates absolute stiffness values, yet still requires invasive pressure measurements. MRE avoids this requirement by including accelerations due to the harmonic motion, rather than requiring force boundary conditions. Therefore, MRE is advantageous in that it provides a direct, non-invasive measurement of myocardial stiffness.

Within the field of MRE, numerous inversion methods are used. Some of the common assumptions made in various inversion methods include:

- media is unbounded

- tissue is homogeneous
- material is isotropic
- displacements due to the longitudinal wave are negligible

Various inversion algorithms have aimed to address one or more of these assumptions. One group has used the shear wave amplitude itself, rather than stiffness, to avoid need for an inversion algorithm. Most inversion methods estimate an isotropic shear modulus, which is not sufficient when describing material properties of tissues such as myocardium, due to its fibrous nature. Studies that have estimated anisotropic material properties, generally estimated two (G_{12} and G_{13}) or three parameters (e.g. G_{12}, G_{13} and E_3) and assumed that the tissue was incompressible. Additionally, all published studies investigating MRE-derived material properties of myocardium have assumed that the tissue is isotropic. Therefore, this thesis is an extension of the large body of research on MRE and is aimed at investigating transversely isotropic material properties of myocardium. In Chapters 3 and 4, the boundary value FEMU method is investigated, which takes into account the geometry of the left ventricle, incorporates an anisotropic material model with realistic fibre orientations and does not assume negligible longitudinal waves.

3

FINITE ELEMENT MODEL UPDATE METHOD

THE boundary value finite element model update (FEMU) method is an iterative, inverse method estimating material parameters by computing multiple forward solutions of a finite element problem, updating the material properties at each iteration, to minimise the difference between some output from the model (ϵ, $\mathbf{u}$, etc.) and some associated experimental data. In this thesis, a FEMU method was implemented to estimate global material parameters for a homogeneous material. This chapter outlines the development of the method, including the construction of a finite element model of the left ventricle, and the simulation using Abaqus of harmonic motion assumed to occur during elastography experiments. Then, the FEMU method was validated by estimating isotropic parameters using experimental MRE phantom data, compared with two established MRE inversion methods.

3.1 Finite Element Methods for Steady State Harmonic Problems

3.1.1 Principle of Virtual Work

The force and momentum equations of equilibrium require that, for any object, the internal forces must be in equilibrium with the external forces acting on the object and its acceleration. The principle of virtual work is a ”weak form” of the equilibrium equations and it generally states that ”a continuous body is at equilibrium if the virtual work of all forces acting on the body is null for any kinematically admissible virtual displacement” [118].

$$-\int_V \boldsymbol{\sigma} : \delta\boldsymbol{\epsilon} dV + \int_S \mathbf{T} \cdot \delta\mathbf{u} dS + \int_V \mathbf{b} \cdot \delta\mathbf{u} dV = \int_V \rho\mathbf{a} \cdot \delta\mathbf{u} dV \tag{3.1}$$

where $\delta\boldsymbol{\epsilon}$ is the virtual strain field and $\delta\mathbf{u}$ is the virtual displacement field. These can be considered as test functions, which are multiplied by the terms of the equilibrium equation. $\boldsymbol{\sigma}$ is the Cauchy stress tensor, which carries in it the material properties, $\mathbf{T}$ represents external traction forces on the surface S, $\mathbf{b}$ represents body forces (such as gravity) in the volume V, ρ stands for density and $\mathbf{a}$ is the acceleration. The first term describes the internal virtual work due to inherent elastic properties of the material. The second and third terms describe the external virtual work due to the traction forces on the boundaries and the body forces, respectively. The right hand side of the equation describes the virtual work due to acceleration. The test functions are arbitrary but must be consistent with all kinematic boundary conditions of the problem. Given the traction forces and body forces applied on an object as well as its acceleration and material properties, the principle of virtual work can be used to solve for resulting displacements of an object.

3.1.2 Finite Element Method

In this thesis, Abaqus 6.13 (Dassault Systèmes Simulia Corp., Providence, USA), a finite element analysis software, was used to solve for the resulting displacement field given a harmonic load, as is the case in MRE. Abaqus utilises the Galerkin finite element method, which is a common way of calculating a numeric solution to a complex set of differential equations. The exact solution to the harmonic problem requires that force and momentum be in equilibrium at all times throughout the entire geometry. However, in the FEM, the equilibrium equations are approximated by replacing them with a weaker requirement, that equilibrium must be maintained in an average sense over a finite number of divisions of the volume. Therefore, the underlying principle of FEM is that a non-regular geometry is subdivided into smaller, non-overlapping regions, referred to as elements, and the solution is approximated by satisfying the equilibrium equations for each element, often using low-order polynomial interpolation functions to approximate the displacement fields. The Galerkin method uses these approximating polynomial functions as the test functions using the principle of virtual work and enforces orthogonality between the test function and equation residual. The equation residual represents the error between the true solution and the numerical approximation. In this approach, the virtual displacements cancel through and the resulting equations are solved numerically for the displacement given the boundary conditions and estimated material properties.

Displacement field values are typically approximated within an element with respect to parameters defined at vertices, called nodes, and a mapping is used to relate global (nodal) parameters to local (element) parameters. A greater level of accuracy in the solution can

be achieved by increasing the number of nodal parameters. This can be done by refining the mesh (i.e. adding more nodes/elements) or by introducing higher order elements (i.e. cubic elements versus linear). However, as the number of parameters increases, so does the computational cost. Therefore, the number of parameters should be chosen such that the necessary level of accuracy is obtained while minimising the computational cost.

3.1.3 Development of a First Order Hexahedral Mesh of a Canine Left Ventricle

The first step in the finite element method is to discretise the problem into elements. The steps for creating a first order hexahedral mesh of a canine left ventricle (LV) are presented in this section. Using Cardiac Image Modeller (CIM v8.1.5, University of Auckland), an in-house software, the initial model was created by fitting a 16 element prolate-spheroidal mesh described by bi-cubic Bézier shape functions to endocardial and epicardial contours of the LV at every cardiac time point (Figure 3.1).

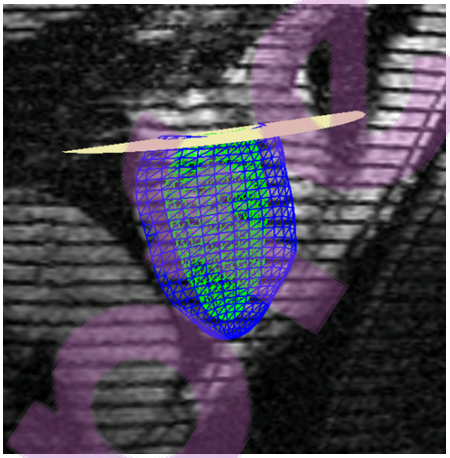

FIGURE 3.1: LV model created using CIM software. The yellow plane denotes the base plane of the LV.

Then, the model at one time point (diastasis) was converted to a tri-cubic Hermite mesh for refinement in CMISS (Continuum Mechanics, Image analysis, Signal processing and System identification), an in-house finite element software (www.cmiss.org). Within CMISS, the high-order mesh was refined three times in the circumferential (ξ_1) and longitudinal (ξ_2) directions and twice in the radial (ξ_3) direction (Figure 3.2). The derivatives were discarded in order to generate a first order mesh of hexahedral elements that could be imported into Abaqus. In the original tri-cubic Hermite mesh, there was one node at the apex, which was shared by four elements. These four elements at the apex had one collapsed edge.

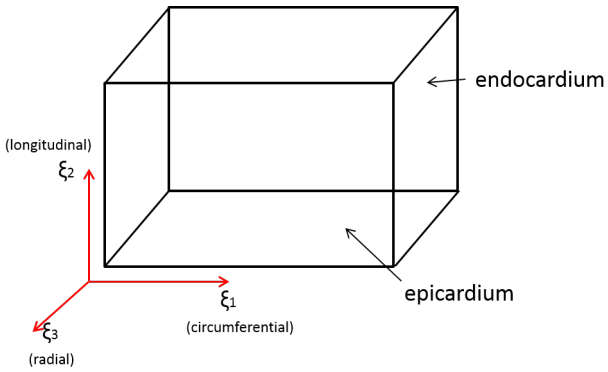

FIGURE 3.2: Hexahedral element showing the element directions (ξ_1, ξ_2 and ξ_3) with respect to left ventricular directions (circumferential, longitudinal and radial)

Initially, wedge elements, with six nodes, were defined at the apex to avoid using elements with collapsed edges. However, as is apparent in Figure 3.3, the mesh quality at the apex was poor due to some elements having very small volumes. During a simulation, these elements at the apex would quickly become distorted, resulting in negative Jacobian values (negative volumes) and unrealistic stress concentrations. There were two main problems with the mesh at the apex: 1) bunching or rippling of elements and 2) convergence of elements to a single point. Therefore, this section describes the steps that were taken to create a high quality LV mesh, utilising only linear hexahedral elements.

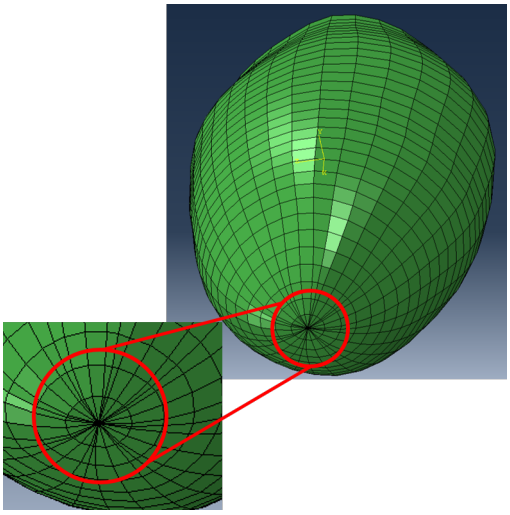

FIGURE 3.3: LV model in Abaqus illustrating bunching of wedge elements at the apex of the mesh.

In order to avoid the problem of element bunching, the original tri-cubic Hermite mesh was first refined three times in the ξ_1 direction (circumferentially). Then, a derivative correction was applied at apical nodes for which the spatial derivatives: $\partial y/\partial \xi_2$, $\partial^2 y/\partial \xi_1 \xi_2$, $\partial z/\partial \xi_2$, $\partial^2 z/\partial \xi_1 \xi_2$ were set to values that only depended on the circumferential position, defined by θ, and a constant, β (Equation (3.2)).

$$\frac{\partial y}{\partial \xi_2} = \cos\theta \qquad \frac{\partial z}{\partial \xi_2} = \sin\theta$$
$$\frac{\partial^2 y}{\partial \xi_2 \xi_1} = -\beta \sin\theta \qquad \frac{\partial^2 z}{\partial \xi_2 \xi_1} = -\beta \sin\theta \tag{3.2}$$

where $\beta = 2\pi/n$ and n is the number of nodes in the circumferential direction after the first refinement step.

Then, the mesh was refined three times in the ξ_2 (longitudinal) direction and twice in the ξ_3 (radial) direction and the derivatives were removed. The resulting first-order mesh had more uniform element sizes and nodal spacing at the apex and thus solved the first problem of element bunching (Figure 3.4).

To tackle the second issue, wedge elements at the apex were removed, creating a hole in the LV mesh at the apex (Figure 3.5a). Then, the nodes which surrounded this hole were extracted (Figure 3.5b). A volume was created by connecting nodes in each contour to create splines and lofting the contours together. The volume was meshed, adding a constraint that the original nodes to create the volume must be included in the mesh nodes (Figure 3.5c). The apical mesh was then ”inserted” back into the LV model (Figure 3.5d). And finally, equipotential smoothing was used to smooth the mesh (Figure 3.5e) by attempting to equalise element volumes [147].

Equipotential smoothing attempts to equalise the volume of elements attached to each node by adjusting nodal locations. Since it allows movement of external nodes, the meshed volume of the LV changed by 0.0347 mL, corresponding to 0.08% of the total volume. This amount of volume change was considered acceptable. Figure 3.6 illustrates the effect of equipotential smoothing by plotting the LV mesh where the colour represents the element volume. Prior to smoothing, element volumes ranged from 0.0661 mL (at the apex) to 25.3 mL. After smoothing, element volumes ranged from 2.36 - 16.7 mL. Additionally, as expected, the surface at the apex became smoother, eliminating the sharp transition between the LV and apical meshes. The equipotential smoothing method is known to ”pull in” badly shaped meshes while equalising element volumes. Smoothness was not quantified but was judged visually. Element volumes were used to determine the amount of smoothness applied since the primary purpose of the apical re-meshing steps was to avoid distorted and negative volume elements.

A bullseye layout is apparent in the element volume maps both before and after smoothing in Figure 3.6. This is due to the differences in wall thickness in different regions of the LV. The number of refinements transmurally is the same throughout the entire model. However, the wall thickness is not constant. Therefore, there is a regular pattern which shows the region of greatest wall thickness (blue) and least wall thickness (pink).

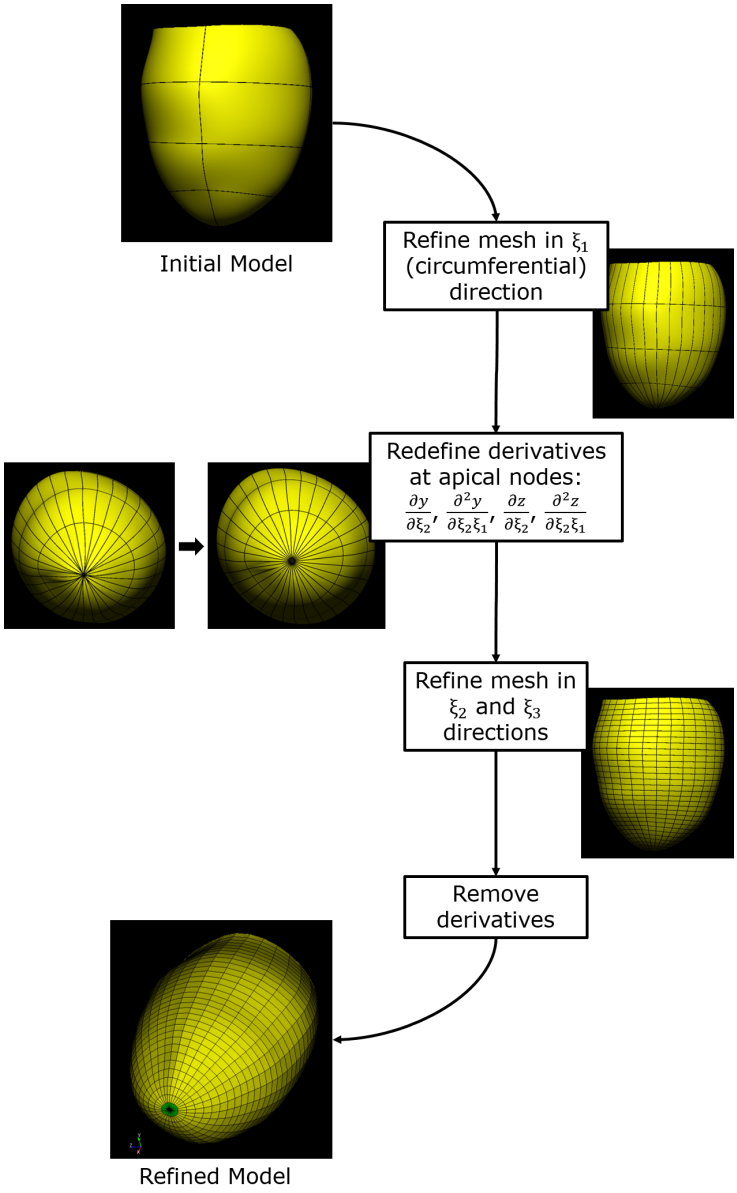

FIGURE 3.4: Mesh refinement steps with apical derivative correction.

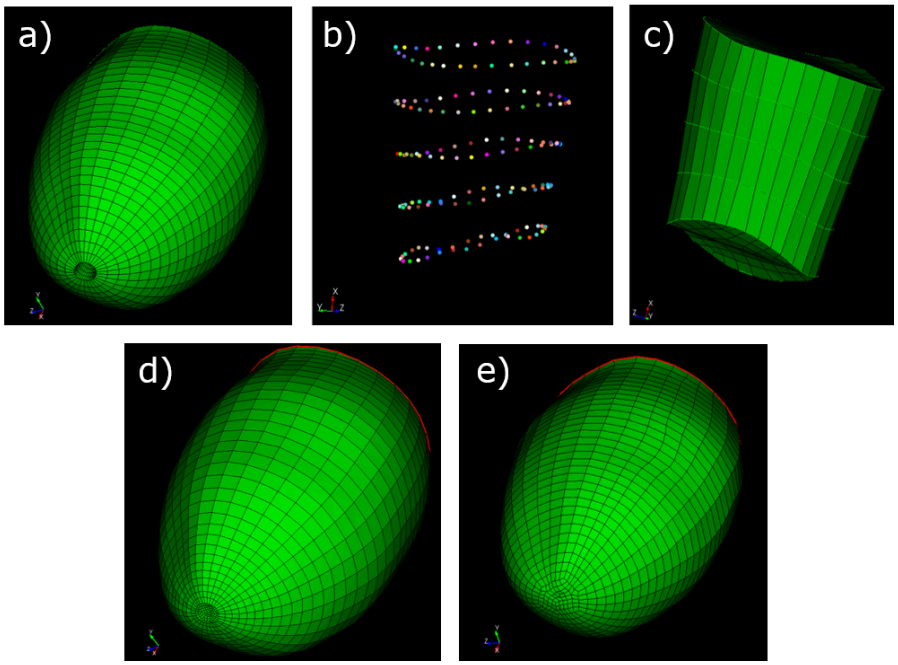

FIGURE 3.5: a) LV mesh with apical nodes removed, b) apical nodes, c) apical mesh, d) LV mesh with apical elements inserted and e) final smoothed LV mesh

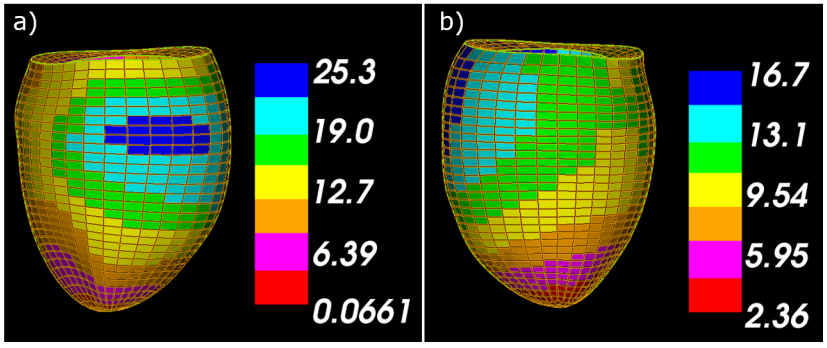

FIGURE 3.6: Plots of element volumes (mL) in the LV a) before (10.00 $\pm$ 5.85 mL) and b) after (9.85 $\pm$ 3.64 mL) equipotential smoothing was applied.

The resulting model contained 5490 nodes and 4320 first-order hexahedral elements.

3.1.4 Elements

With the final model of the LV, three different Abaqus element types were examined: C3D8, C3D8R and C3D8H. 'C' signifies a continuum element; '3D' means that the element is three-dimensional; and '8' implies that there are eight nodes which define the element. The 'R' stands for "reduced integration" and 'H' stands for "hybrid".

Shear locking, or overly stiff behaviour due to non-physical shear, can be a problem with fully integrated elements, when they are subjected to bending. Reduced integration elements (C3D8R) eliminate shear locking and can save computation time. Reduced integration elements in Abaqus do not compute strain at one integration point, but rather use an averaged strain-displacement matrix over the element volume (see Appendix A), thus ensuring constant strain over the entire element [48]. In reduced integration elements, elements exhibit no shear stiffening at all, introducing zero-energy deformation modes, or non-zero deformation with zero strain at the element centroid. This phenomenon is known as hourglassing.

An additional problem introduced with incompressible or nearly incompressible materials, such as biological tissues, is known as volumetric locking. In an incompressible material, the volume at each integration point is constrained, introducing eight constraints per element in fully integrated hexahedra. The problem arises in that there are only three degrees of freedom at each integration point to satisfy the volume constraints. Thus, the mesh is over-constrained and exhibits overly-stiff behaviour. Volumetric locking is less pronounced in reduced integration elements since they have fewer volumetric constraints.

In order to reduce the effect of volumetric locking, C3D8 elements in Abaqus use a "selectively reduced" integration scheme (see Appendix A). Full integration is used to calculate the deviatoric, or shear, stress and the uniform strain formulation, identical to that used for C3D8R elements, is used to compute the dilatational stress.

"Hybrid" elements are also available to use in fully or nearly incompressible materials modelled with solid elements. With this element type, the hydrostatic stress is described by an independent set of parameters (degrees of freedom to be determined during the solution procedure), and is coupled to the displacement solution through the stress equilibrium and constitutive equations. In Abaqus hybrid elements, the modified Cauchy stress is written as (Abaqus Theory Manual, v6.13):

$$\overline{\boldsymbol{\sigma}} = \boldsymbol{\sigma} + (1-\rho)\mathbf{I}\big(-\frac{1}{3}Tr(\sigma) - \hat{p}\big) \tag{3.3}$$

where $\boldsymbol{\sigma}$ is the stress tensor, $1/3\mathrm{Tr}(\boldsymbol{\sigma})$ is the hydrostatic stress and $\hat{p}$ is the independent hydrostatic pressure field. In Abaqus, ρ was chosen to be $1e10^{-9}$, since it is sufficiently close to zero without causing equation solver difficulties. Hybrid elements solve the problem

of volumetric locking in incompressible materials yet are more computationally expensive than C3D8 elements.

The three different element types, C3D8, C3D8R and C3D8H were tested with the canine left ventricular (LV) mesh. A harmonic displacement (f = 80 Hz) 0f 0.2 mm was applied to the anterior epicardial face of the LV and the basal epicardial nodes were fixed. Displacement maps encoding magnitude ($\sqrt{x^2 + y^2 + z^2}$) are shown in Figure 3.7. The Poisson's ratio, controlling incompressibility, was set to 0.49999999.

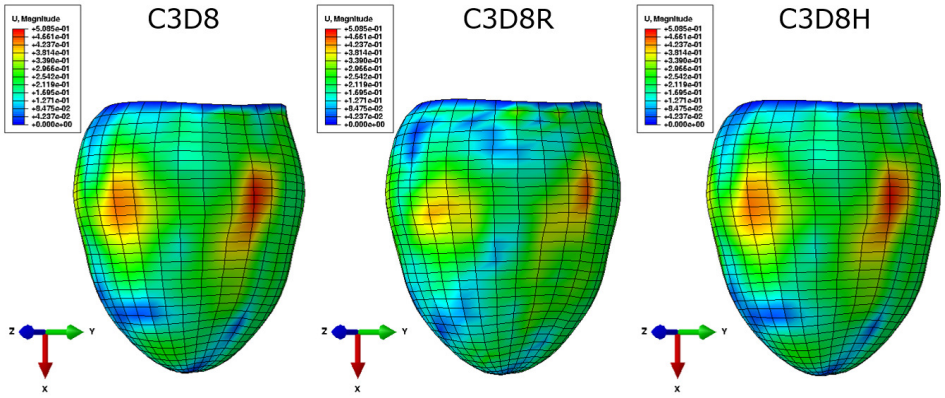

FIGURE 3.7: LV model simulation results (magnitude of displacement) for C3D8, C3D8R and C3D8H elements.

The displacement maps of the C3D8 and C3D8H elements look similar whereas slight differences can be seen in the C3D8R model displacement field. When the scale factor was increased 10x, hourglassing is apparent in the C3D8R model, particularly near the base and apex, while the C3D8H and C3D8 model elements show smooth transitions between regions (Figure 3.8).

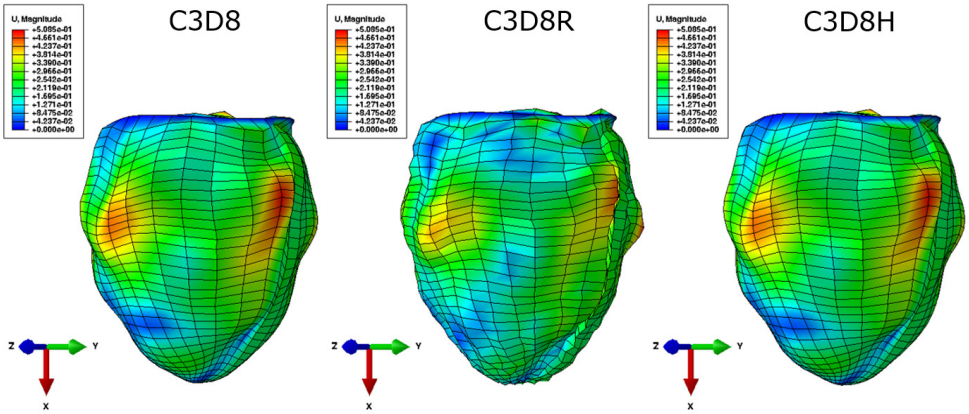

FIGURE 3.8: LV model simulation results (magnitude of displacement) for C3D8, C3D8R and C3D8H element types. Displacement magnitudes scaled 10x.

To quantify the differences in nodal displacements, the root mean squared difference

was calculated between: C3D8H vs C3D8R, C3D8H vs. C3D8 and C3D8R vs C3D8 models. Utilising both the real and imaginary components of the resulting harmonic displacement fields, the root mean squared differences were 1.747e-6 mm, 0.1133 mm and 0.1133 mm, respectively. Therefore, the displacement fields calculated with the C3D8 and C3D8H elements were nearly identical. Although C3D8 elements could have been used, C3D8H elements were chosen since most biological tissue is nearly incompressible and C3D8H elements avoid volumetric locking entirely.

3.1.5 Steady-State Harmonic Motion

The direct steady-state dynamic analysis procedure in Abaqus 6.13 (Dassault Systèmes Simulia Corp., Providence, USA) was used to simulate MRE displacements. This is a perturbation procedure in which the response of a model to an applied harmonic load is calculated about the base state. The result is a set of complex harmonic nodal displacements, $\mathbf{u}$. It was assumed that, in MRE experiments, steady-state harmonic motion has been achieved by the time that phase images are collected. The transient vibrations, which occur at the beginning of the excitation, are not accounted for in a harmonic response analysis. Generally, steady-state dynamic analysis procedures provide a solution to the linear equations of motion when the loading is harmonic, which has the trigonometric form:

$$P(t) = u_{mag} \cos(\omega t + \theta) \tag{3.4}$$

and the equivalent complex form:

$$S(t) = u e^{i\omega t} \tag{3.5}$$

where ω is the angular frequency ($= 2\pi f$). A phase angle (θ) allows the loading to be described relative to a reference time point (t = 0). The frequency of the steady-state response is assumed to be the same frequency of the applied harmonic load. The trigonometric form of the response (vector, tensor components) is thus described by the real part of the complex form.

Steady-state dynamic procedures result in frequency domain solutions that represent a single complete cycle of harmonic response. They provide solutions at the excitation frequency specified. Excitation input and response can be written in two parts, corresponding to the magnitude and phase angle, which are related to the complex form by:

$$\begin{aligned} u &= u_{Re} + i u_{Im} \\ u_{Re} &= u_{mag} \cos(\theta) \\ u_{Im} &= u_{mag} \sin(\theta) \end{aligned} \tag{3.6}$$

These equations are shown graphically in Figure 3.9.

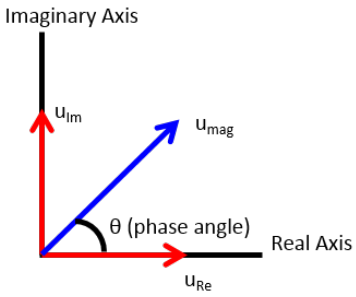

FIGURE 3.9: A graphical representation of the complex load/response.

The principle of virtual work can be written in its discretised form to solve for steady-state harmonic displacements. The first term of Equation (3.1), representing internal work, can be separated into internal work done by stiffness ($\mathbf{K}$) and that done by damping ($\mathbf{C}$). Assuming body forces such as gravity are negligible, Equation (3.1) can be rearranged and written as:

$$-\mathbf{M}\ddot{\mathbf{u}} + \mathbf{C}\dot{\mathbf{u}} + \mathbf{K}\mathbf{u} = \mathbf{P} \tag{3.7}$$

where $\mathbf{u}$ is the complex nodal displacement, incorporating both the real and imaginary components of displacement, $\mathbf{M}$ is the mass matrix, $\mathbf{C}$ is the damping matrix and $\mathbf{K}$ is the stiffness matrix. The test, or weighting, functions are equivalent to the shape functions used to describe each element and are carried in the discretised matrices: $\mathbf{M}$, $\mathbf{C}$, $\mathbf{K}$ and $\mathbf{P}$. Acceleration ($\ddot{\mathbf{u}}$) and velocity ($\dot{\mathbf{u}}$) are related to the angular frequency and complex displacement (cancelling the $e^{i\omega t}$ term) as:

$$\begin{aligned} \ddot{\mathbf{u}} &= -\omega^2\mathbf{u} \\ \dot{\mathbf{u}} &= i\omega\mathbf{u} \end{aligned} \tag{3.8}$$

Therefore, Equation (3.7) can be rewritten as:

$$-\omega^2\mathbf{M}\mathbf{u} + i\omega\mathbf{C}\mathbf{u} + \mathbf{K}\mathbf{u} = \mathbf{P} \tag{3.9}$$

Mass proportional damping C was not included in the model. However, structural damping was included to model realistic energy loss from the system in a vibrating structure. The structural damping forms the imaginary part of the stiffness matrix, which is also known as the structural damping matrix. Structural damping forces are proportional to displacement and are in phase with velocity. Without damping, the solution would become unbounded when ω is equal to natural frequencies of the system. With structural damping included in the material model and without mass proportional damping, Equation 3.9 now becomes:

$$-\omega^2\mathbf{M}\mathbf{u} + i\mathbf{K_L}\mathbf{u} + \mathbf{K_s}\mathbf{u} = \mathbf{P} \tag{3.10}$$

and

$$\mathbf{K} = i\mathbf{K_L} + \mathbf{K_S} = \mathbf{K_S}(is + 1) \tag{3.11}$$

This equation is more often written in terms of the structural damping coefficient (s) as:

$$-\omega^2\mathbf{M}\mathbf{u} + (is + 1)\mathbf{K_s}\mathbf{u} = \mathbf{P} \tag{3.12}$$

In this formulation, $\mathbf{K_s}\mathbf{u}$ is in phase with the displacement and $is\mathbf{K_s}\mathbf{u}$ is in phase with the velocity [145]. The damping coefficient is a general way of describing energy loss in a system [21]. It directly measures energy dissipation with no reference to the mechanisms involved. The structural damping coefficient can be related to viscous damping:

$$\zeta = s \cdot \frac{\omega_n}{\omega} \tag{3.13}$$

where ζ is the fractional damping coefficient (a ratio of the real damping over critical damping of the system), ω_n is the natural frequency of the system and ω is the forcing frequency. In the FEMU method, the structural damping coefficient (s) was included in the parameters to be identified since it has been shown that omitting damping in elastography inversion methods can result in estimation errors up to 25$\%$ (at 67.5 Hz) [49].

3.2 FEMU Isotropic Method Validation

The finite element model update (FEMU) method was used to estimate the linear elastic isotropic shear stiffness in a cylindrical phantom using experimental MRE displacements. The results were compared with shear moduli estimated from the same phantom using two other common MRE inversion methods: 1) directional filtering with local frequency estimation (DF-LFE) and 2) multi-model direct inversion (MMDI).

3.2.1 Isotropic Phantom MRE Experiment

Magnetic resonance elastography images of a PVC cylindrical gel phantom (radius = 76.2 mm, height = 127 mm) were collected using a Siemens Trio MR scanner (TR = 25 ms, TE = 21.27 ms) and a gradient recalled echo imaging sequence [23]. A pneumatic driver was used to apply a harmonic load to the phantom at 60 Hz with a 5% power setting. Phase contrast images (native resolution = 128 voxel x 64 voxel , reconstructed resolution = 256 voxel x 256 voxel) were collected at 16 axial locations in the mid-region of the

phantom. At each location, three images were collected, which encoded phase in three orthogonal directions (Figure 3.10). The through-plane displacement was encoded in the slice direction and is referred to as the z-direction. The phase (R-L) and readout (A-P) encoding directions are called the x and y directions, respectively. Images were collected with 5 mm slice thickness and 5 mm spacing between slice centres.

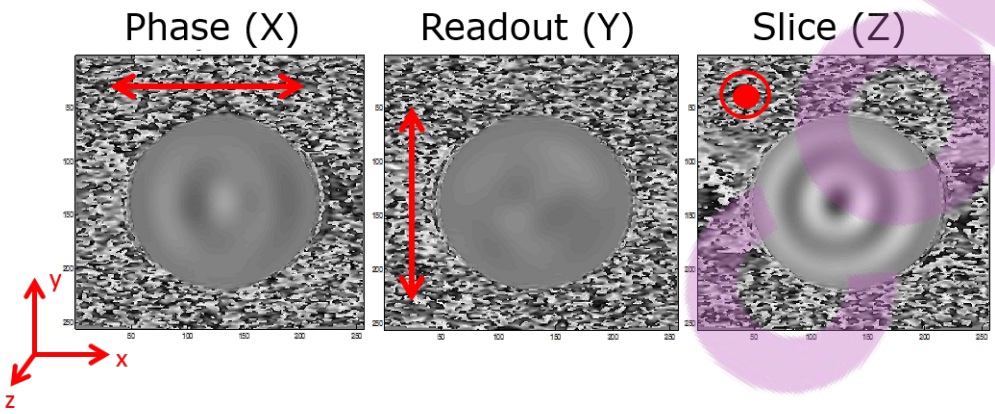

FIGURE 3.10: The three phase images show displacement encoded in the phase, readout and slice directions, respectively.

Each phase image collected is known as a wave image and is equivalent to imaging the dynamic displacement at one time point. Data were then collected at different time points by changing the timing of the motion encoding gradient (MEG) with respect to the motion timing. Each of these points in time is known as a phase offset. In this experiment, images were collected at four phase offsets during the time-harmonic cycle (Figure 3.11). In the imaging protocol, a trigger was sent from the scanner to the external pneumatic driver. Typically in MRE, anywhere between two and eight phase offset images are collected.

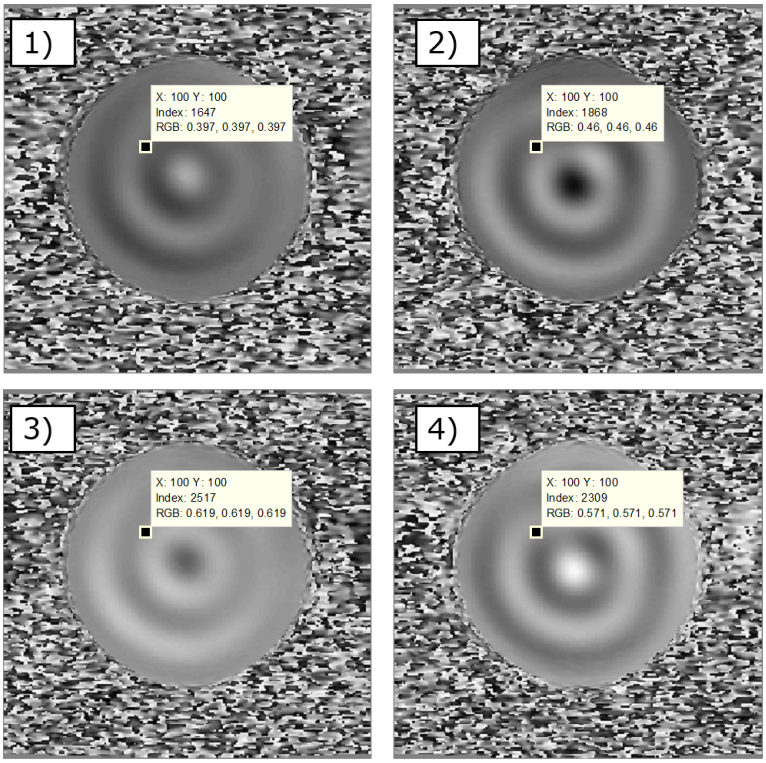

FIGURE 3.11: Phase images at four phase offsets in the cylindrical phantom. One pixel (100,100) is highlighted.

A Fourier transform was used to fit a sine wave to the four phase offsets. To illustrate this process, Figure 3.11 shows four phase offset images from one image plane encoding displacements in the through-plane direction. One pixel (100,100) has been marked on each image.

Taking the Fast Fourier Transform (FFT) of these four data points results in four numbers. The first of which is the DC component of the signal whereas the second, third and fourth values are the first, second and third harmonic amplitudes, respectively. The result of the FFT is symmetric such that only the first half of the points has unique magnitudes and the rest are symmetrically redundant. In this case, the first harmonic (FH) represents the primary harmonic component found in the MRE signal. The amplitude of the harmonic is equal to the amplitude of the FH divided by the number of sampling points (N) and multiplied by two to account for the symmetric redundancy of the resulting FFT output. Assuming that the frequency of displacement is the same as the frequency of the pneumatic driver (60 Hz), the FH amplitude, a complex value, can be used to describe the sine wave which fits the four data points. The four values from the marked pixel (100,100) in Figure 3.11 have been plotted in the graph along with the fitted sine wave on an arbitrary time scale in Figure 3.12b.

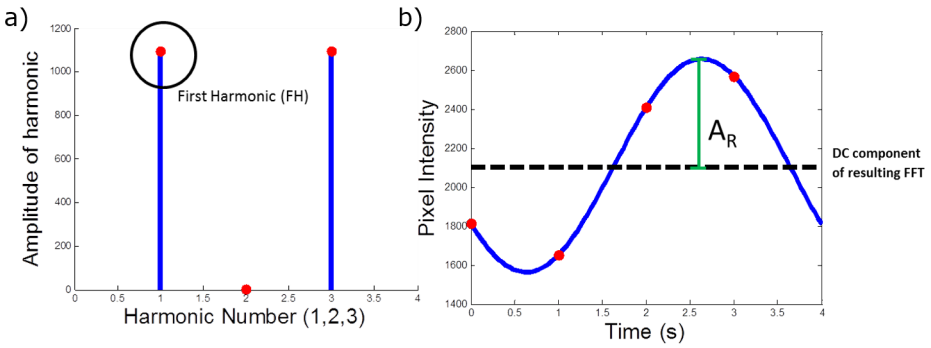

FIGURE 3.12: a) Resulting (real component of) harmonic amplitudes from FFT of four phase data points highlighted in Figure 3.11 and b) the sine wave, described by the complex first harmonic amplitude, fitted to the four phase data points.

Then, the complex amplitudes were converted to complex displacements with units of μm by first converting the pixel magnitude, which ranged from [0, 4096], to radians. Then, the amplitude in radians was related to μm via the motion encoding coefficient (MENC) which has units of μm/rad. In the phantom experiment, the MENC value for 60 Hz excitation and 60 Hz encoding gradient was 13.3 μm/rad for a Tim Trio system with gradients of 27 mT/m (2.7 G/cm) and a slew rate of 164 μs.

$$d = A \cdot \left(\frac{2\pi}{4096}\right) \cdot MENC \tag{3.14}$$

3.2.2 Stiffness Estimate: FEMU

A finite element model was developed that represents the geometry of the imaged portion of the cylinder. The actual cylindrical phantom had a diameter of 76.2 mm and a height of 127 mm. However, the 16 slices were acquired from the mid-region of the cylinder and covered 80 mm of the total height. Therefore, the finite element model of the phantom was defined to have a diameter of 76.2 mm and a height of 80 mm. Two different mesh resolutions were used to estimate the isotropic elastic parameters of the phantom. Mesh #1 had 236652 nodes and 232070 elements and Mesh #2, with a more coarse mesh, had 31563 nodes and 28840 elements, as illustrated in Figure 3.13.

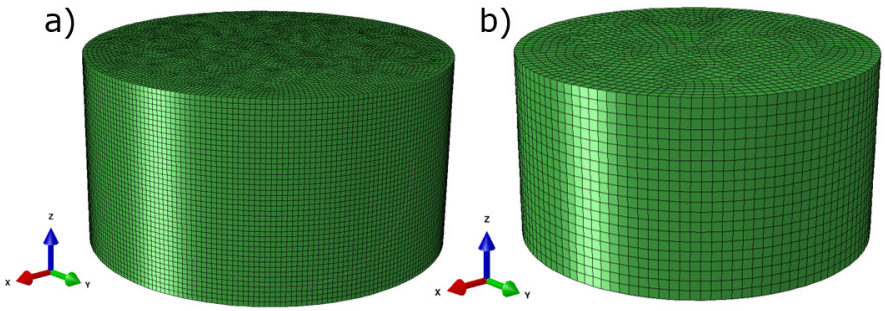

FIGURE 3.13: Two finite element models of the same phantom geometry with differing mesh resolutions: a) Mesh #1, b) Mesh #2.

Displacement data was interpolated at the nodes using a cubic spline interpolation. The interpolated displacements were either used as boundary conditions or reference displacements in the FEMU objective function. Displacements were constrained on the top and bottom slices as well as the surface nodes of the phantom model. The remaining internal nodes were used in the objective function.

The objective function to be minimised, $\%RMSE(\mathbf{u})$, was calculated as the root mean square of the Euclidean distances between nodal displacements generated from model predictions and ground truth displacements from the MRE phantom data, and expressed as a percentage of the root mean squared ground truth displacements.

$$\%RMSE(u) = \frac{\sqrt{\sum^{N}\sum^{x,y,z}(u_{MRE} - u_{FEM})^2}}{\sqrt{\sum^{N}\sum^{x,y,z}(u_{MRE})^2}} \tag{3.15}$$

An optimisation algorithm, *fmin-cobyla*, provided in the *Scipy* optimisation package of Python, was used to estimate the material parameters by minimising Equation 3.15. This is a nonlinear constrained optimisation method that does not require knowledge of derivatives [121]. Each iteration forms a linear approximation to the objective and constraint functions by interpolation at the vertices of a simplex.

An isotropic parameter estimation was run with three independent parameters to be identified: structural damping (s), Young's modulus (E) and Poisson's ratio (ν). The initial estimates for each were 0.1, 16 kPa and 0.499, respectively. An initial step size of 5 was used and the optimisation finished when the trust region radius was smaller than 1e-2 [120]. The damping coefficient and Poisson's ratio were scaled so that step sizes reflected a physically reasonable amount of change in each parameter: [100·s, E, 1000·ν] The resulting parameter estimates, final %RMSE and number of iterations required for convergence are shown in Table 3.1.

TABLE 3.1: Results from FEMU applied to experimental MRE phantom data using two different mesh resolutions.

Mesh	E (kPa)	s	ν	% RMSE	Iterations
1	16.655	0.100	0.500	16.46%	366
2	16.933	0.100	0.499	16.11%	77

3.2.3 Stiffness Estimate: Directional Filter + LFE

As a comparison, an established directional filtering + local frequency estimation (DF-LFE) method [97] was applied to the phantom data. A directional Butterworth band pass filter (4th order, [4,40] waves/FOV) was used to filter the displacements in eight directions in frequency space, thus removing any bulk motion and high-frequency noise. Figure 3.14 illustrates the combination of the Butterworth band pass filter and directional filter in k-space and Figure 3.15 illustrates the resulting phantom displacements from each of the eight directional filters for one slice.

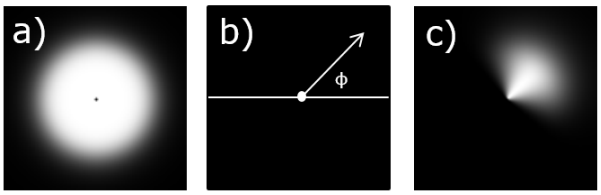

FIGURE 3.14: a) Butterworth band pass filter, b) filter direction and c) half of the resulting directional band pass filter applied to the phase data in k-space.

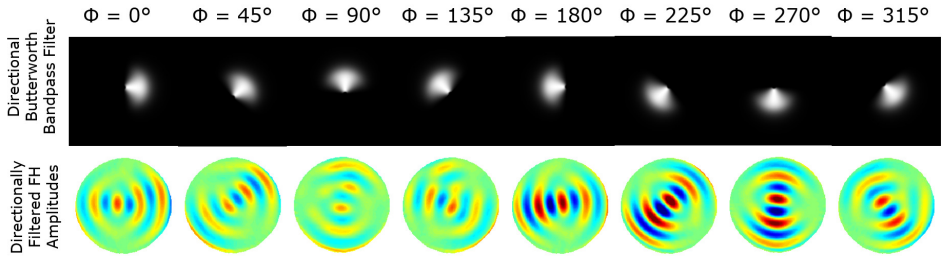

FIGURE 3.15: Butterworth band pass filters applied in eight directions and the resulting filtered first harmonic (FH) amplitudes in one slice of the phantom. FH amplitudes shown are the real component only of displacements in the slice (through-plane) direction. Filtered FH amplitudes range between: [-500,500].

Then, the directionally filtered data were re-interpolated at four equally spaced time points, or phase offsets, and LFE (using MRE/Wave, Mayo Clinic, Rochester, USA) was used to estimate the shear stiffness using the new filtered phase offset data [76]. The

resulting stiffness maps were then weighted by the first harmonic (FH) amplitude in each direction, producing a final weighted stiffness map for each image slice. Stiffness maps were weighted in order to give a greater weight to pixels with more signal (larger displacements) than those with lower signal. The weighting for each displacement direction (x, y, z) as well as each filter direction (i = 1:8) was written as:

$$w = \frac{FH_{di}^2}{\sum_{d}^{x,y,z} \sum_{i=1}^{8} FH_{di}^2} \tag{3.16}$$

Figure 3.16 shows a stiffness map from the first slice of the phantom image data. As mentioned in Chapter 2, the LFE method performs poorly at image boundaries as can be seen by the low shear estimates around the border of the phantom in Figure 3.16a. Additionally, previous studies have shown that the correct stiffness estimate is only reached one half a wavelength from the boundary of a region [94]. In one axial slice, there are approximately two wavelengths radially. Given a radius of 76.2 mm and a pixel resolution of 1 mm x 1 mm, half of one wavelength is approximately 19 pixels. Therefore, to omit the poorly estimated regions, the phantom mask was eroded by 19 pixel layers in all 16 slices of the phantom using the Matlab (2012b) function *bwmorph*. The heterogeneity of the stiffness estimates in the slice shown, and all slices, may be due to small inhomogeneities within the gel phantom that give rise to variations in estimated shear moduli.

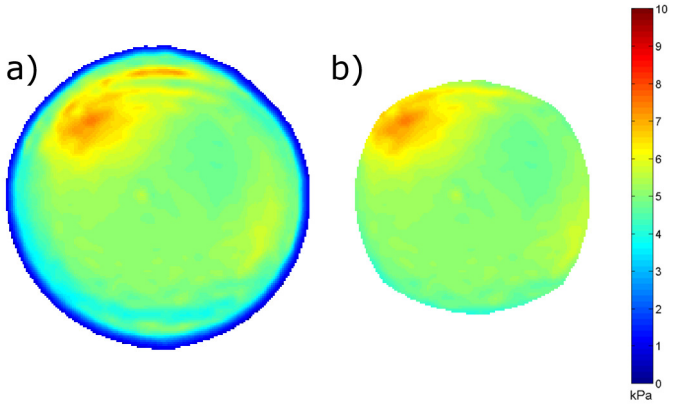

FIGURE 3.16: Resulting map of shear stiffness for one slice of the phantom data a) without and b) with boundaries omitted.

The mean shear stiffness over the entire phantom, within the eroded mask, was calculated to be 5.34 $\pm$ 0.37 kPa. Since the PVC gel phantom can be assumed to be isotropic, shear stiffness is related to Young's modulus by:

$$G_{12} = \frac{E_1}{2(1+\nu)} \tag{3.17}$$

Assuming incompressibility (ν = 0.5), this equates to a Young's modulus of 16.02 kPa. The resulting Young's moduli from the FEMU method using both mesh refinements, listed

in Table 3.1, differ from the resulting LFE estimated Young's modulus by approximately 4.0% and 5.7%.

A third method, a multi-model direct inversion method (MMDI), was used by a collaborating group to estimate the shear modulus of the same phantom, which uses direct inversion of the Helmholtz wave equation. This method requires the calculation of high-order derivatives. The MMDI method resulted in a shear modulus of 5.45 kPa (E = 16.35 kPa). The FEMU results are slightly higher than both the DF-LFE and MMDI methods, but all mean shear moduli differ by less than 0.25 kPa. Overall, the FEMU method provides an estimate of isotropic material properties that are comparable to shear stiffness values measured from two other common MRE inversion methods. No other stiffness estimates (e.g. dynamic mechanical analysis) were available for the phantom.

This chapter validates the FEMU method as a way to estimate global isotropic material properties from an elastography displacement field and also discussed steps taken to create a first-order hexahedral mesh of a canine LV geometry. This method is expanded in Chapter 4 to identify anisotropic material properties from simulated harmonic displacement fields in the LV model as well as experimental MRE displacements from the cylindrical phantom.

4

Identifiability of Transversely Isotropic Material Properties from MRE

Aspects of this chapter have been published in:

1. Miller R, Jiang H, Mazumder R, Cowan BR, Nash MP, Kolipaka A, Young AA. Determining anisotropic myocardial stiffness from magnetic resonance elastography: A simulation study. In: Functional Imaging and Modeling of the Heart. 2015. p. 346-354.

2. Miller R, Kolipaka A, Nash MP, Young AA. Relative identifiability of anisotropic properties from magnetic resonance elastography. NMR in Biomedicine. *Accepted Manuscript.*; 2017.

Validation of the use of the finite element model update (FEMU) method to estimate isotropic shear stiffness from phantom MRE data was presented in Chapter 3. In this chapter, the FEMU method was implemented to identify transversely isotropic material properties in an isotropic gel phantom and using simulations of harmonic motion in an LV model with a histology-derived fibre field. Then, Gaussian noise was added to the reference displacement fields and material parameter estimations were performed. The relative identifiability of each transversely isotropic material parameter was investigated, in order to demonstrate the ability of iterative FEMU inversion methods to accurately estimate global material parameters and to determine whether this is a well-posed inverse problem for which all material parameters can be uniquely determined. Constitutive parameter sweeps were analysed and characteristics of the Hessian matrix at the optimal solution were used to evaluate the determinability of each constitutive parameter. Four out of five constitutive

parameters (Young's moduli E_1 and E_3, shear modulus G_{13} and damping coefficient s), which describe a transversely isotropic linear elastic material, were well-determined from the MRE displacement field using an iterative FEMU inversion method. The remaining parameter, Poisson's ratio, was least identifiable. Young's moduli, shear moduli and the damping coefficient are well-determined from MRE data whereas Poisson's ratio is not as well-determined and should potentially be set to a reasonable value for biological tissue (close to 0.5).

4.1 Methods

4.1.1 Linear Elastic Constitutive Model

Myocardial stiffness is anisotropic due to its fibrous and layered architecture [88] with greatest stiffness in the fibre direction, intermediate stiffness transverse to the fibres in the plane of the layer, and least stiffness orthogonal to the layers [34]. However, secondary (sheet) and tertiary (sheet-normal) material orientations are difficult to determine using DTMRI [18] and there is currently controversy over whether material properties of myocardial laminae can be personalised [161]. Following many previous studies [50, 159, 162], a transversely isotropic material model was used in this thesis to describe the material behavior of myocardium.

At large strains, myocardium is hyperelastic, exhibiting non-linear elasticity. However, at small strains induced by elastography, a linear elastic material model was used to approximate the slope of the stress-strain curve at the current deformed state of the myocardium. An anisotropic linear elastic stiffness matrix, $\mathbf{E}$, which relates the internal stress of the material to the strain, has 21 independent parameters. However, if the material is assumed to be transversely isotropic, the stiffness matrix is reduced to the following form.

$$\begin{Bmatrix} \sigma_1 \\ \sigma_2 \\ \sigma_3 \\ \sigma_4 \\ \sigma_5 \\ \sigma_6 \end{Bmatrix} = \begin{bmatrix} C_{11} & C_{12} & C_{13} & 0 & 0 & 0 \\ & C_{22} & C_{13} & 0 & 0 & 0 \\ & & C_{33} & 0 & 0 & 0 \\ & & & C_{44} & 0 & 0 \\ & sym & & & C_{66} & 0 \\ & & & & & C_{66} \end{bmatrix} \begin{Bmatrix} \epsilon_1 \\ \epsilon_2 \\ \epsilon_3 \\ \epsilon_4 \\ \epsilon_5 \\ \epsilon_6 \end{Bmatrix} \tag{4.1}$$

where $C_{12} = C_{11} - 2C_{44}$. Thus, there are five independent parameters: C_{11}, C_{33}, C_{13}, C_{44} and C_{66}. Note that Abaqus and the methods implemented in this thesis use a modified Voigt notation for the stiffness tensor (and calculated strains and stresses), i.e. $\epsilon_4 = \epsilon_{12}$, $\epsilon_5 = \epsilon_{13}$ and $\epsilon_6 = \epsilon_{23}$.

Engineering constants (Young's moduli, shear moduli and Poisson's ratios) can be calculated from the compliance matrix, which is the inverse of the elastic stiffness matrix ($C = E^{-1}$).

$$\begin{bmatrix} C_{11} & C_{12} & C_{13} & 0 & 0 & 0 \\ C_{12} & C_{22} & C_{13} & 0 & 0 & 0 \\ C_{13} & C_{13} & C_{33} & 0 & 0 & 0 \\ 0 & 0 & 0 & C_{44} & 0 & 0 \\ 0 & 0 & 0 & 0 & C_{66} & 0 \\ 0 & 0 & 0 & 0 & 0 & C_{66} \end{bmatrix}^{-1} = \begin{bmatrix} \frac{1}{E_1} & \frac{-v_{12}}{E_1} & \frac{-v_{31}}{E_3} & 0 & 0 & 0 \\ \frac{-v_{12}}{E_1} & \frac{1}{E_1} & \frac{-v_{31}}{E_3} & 0 & 0 & 0 \\ \frac{-v_{13}}{E_1} & \frac{-v_{13}}{E_1} & \frac{1}{E_3} & 0 & 0 & 0 \\ 0 & 0 & 0 & \frac{1}{G_{12}} & 0 & 0 \\ 0 & 0 & 0 & 0 & \frac{1}{G_{13}} & 0 \\ 0 & 0 & 0 & 0 & 0 & \frac{1}{G_{13}} \end{bmatrix} \tag{4.2}$$

The five engineering constants needed to define a transversely isotropic response are: elastic parameters E_1 ($= E_2$), E_3, shear parameters G_{13} ($= G_{23}$), and Poisson's ratios ν_{12} and ν_{13} ($= \nu_{23}$), assuming a fibre direction aligned with the $[0\ 0\ 1]^T$ axis. Various combinations of these parameters can be used. In nearly incompressible materials, the Poisson's ratio in the isotropic plane, ν_{12}, is related to the Poisson's ratio describing the fibre direction, ν_{13}, by $\nu_{12} = 1-(\nu_{13}+\epsilon)$. Since biological tissue is nearly incompressible, the constraint, $\nu_{12} = 1 - \nu_{13}$, was utilised, thereby reducing the number of parameters to four. The Poisson's ratios in the transverse-fibre directions (1-3, 2-3) are related to the Young's moduli and the Poisson's ratio in the fibre-transverse direction according to the following equation [90]:

$$\frac{\nu_{ij}}{E_i} = \frac{\nu_{ji}}{E_j} \tag{4.3}$$

In this study, the structural damping coefficient (s) was included in the parameters to be identified since it has been shown that omitting damping in elastography inversions can result in estimation errors up to 25% (at 67.5 Hz) [49]. Many studies have set a value for Poisson's ratio under the assumption that any error in Poisson's ratio will not affect the shear modulus significantly since the longitudinal wavelength (affected by Poisson's ratio) is much longer than the shear wavelength [61, 139, 150]. However, other studies suggest that even small changes in Poisson's ratio near the incompressible limit can result in large deviations in stress within the material [33]. Therefore, five parameters were investigated in this study: s, E_1, E_3, G_{13} and ν_{31}.

Transversely isotropic parameters were identified from simulated harmonic displacements in an LV model as well as from experimental MRE displacements in an isotropic phantom. The phantom experiment described in Chapter 3 was analysed again in this chapter utilising the less refined mesh (Mesh #2). Both isotropic and transversely isotropic linear elastic constitutive relations were used. In the isotropic model, only three parameters were estimated: s, E and ν. In the estimation of transversely isotropic material properties,

the material was arbitrarily aligned through the bore of the cylinder and the resulting fibre and cross-fibre stiffness values were expected to be the same.

4.1.2 Finite Element Modelling and Simulations

In the LV model, steady-state harmonic motion was simulated in an anatomically accurate canine left ventricular geometry. Physiologically realistic helical fibres [88] measured from histology were embedded using finite element interpolation of nodal parameters. Fibre angles measured with respect to the short axis plane varied from approximately -60 degrees to +60 degrees transmurally from epicardium to endocardium, respectively. The epicardial basal nodes were fixed and a sinusoidal displacement with an amplitude of 0.2 mm at 80 Hz was prescribed at 41 epicardial nodes at the apex (Figure 4.1b).

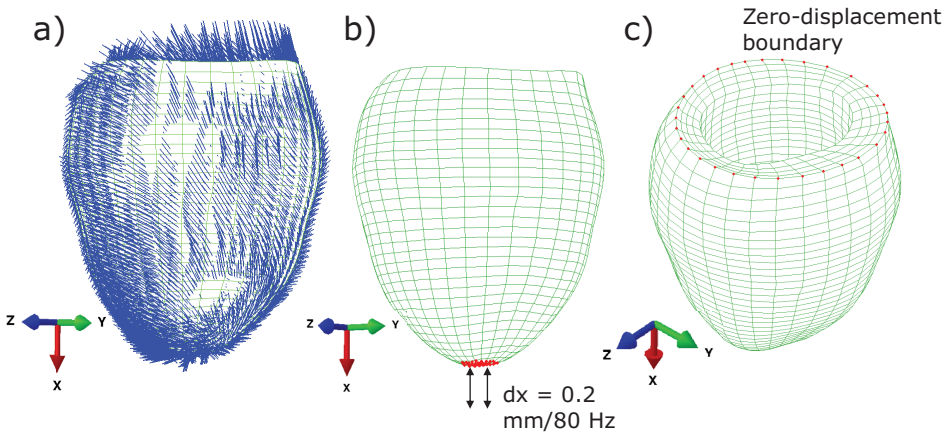

FIGURE 4.1: a) LV model showing embedded fibres as blue line segments b) boundary conditions at apical nodes in red, which were displaced 0.2 mm/80 Hz in the x-direction and 3) epicardial basal nodes in red that were fixed (right).

A local orientation was defined within each element where the local $[0\ 0\ 1]^T$ axis was designated to be aligned with the fibre direction. Stiffness values were defined based on cardiac anisotropic shear moduli measured from ultrasound elastography [31] which were derived from mechanical shear waves between 100 Hz- 400 Hz. Despite the difference in loading frequency from this study, values were comparable to anisotropic MRE measurements of skeletal muscle measured in [61] between 30 Hz - 60 Hz. The fibre direction was assigned a Young's modulus (E_3) of 10.5 kPa, moduli in the transverse directions (E_1, E_2) were set to 6.5 kPa and the fibre shear moduli (G_{13}, G_{23}) were set to 2.5 kPa. The structural damping coefficient was assigned a value of 0.1; the Poisson's ratio was set to 0.49999999 as cardiac tissue is largely incompressible; and a density of 1.06 g/cm^3 was assumed.

Gaussian noise was added to the real and imaginary components of the reference displacement field prior to estimation of the material parameters. According to Gudbjartsson et al, noise in MR images can be adequately modelled using a Gaussian distribution, given

that the signal-to-noise ratio (SNR) is above three [60]. Epicardial displacements from the ground truth case with added noise were prescribed on the outer surface. The Gaussian distributions of noise were computed for the x, y and z directions independently, with each having a mean of zero and standard deviation computed as:

$$\sigma_{noise} = 15\% \cdot \sigma_{disp} \tag{4.4}$$

where σ_{disp} was the standard deviation of the ground truth displacement field. The scaling factor of 15% was chosen following other MRE simulation studies [156] which corresponds to an SNR of approximately five. A Monte Carlo simulation was run (30 repeated simulations) with random Gaussian noise added to the boundary conditions re-generated at each run. Initial estimates for the optimisations were randomly assigned from a normal distribution with the reference (or true) value as the mean and 20% of the reference parameter as the standard deviation, which was arbitrarily chosen. A second Monte Carlo simulation was run in which the initial estimates were similarly varied except the Poisson's ratio was fixed (ν_{31} = 0.49999999).

4.1.3 Determinability of Material Parameters

Three criteria were evaluated in order to assess the determinability of the material parameters from the Hessian matrix, $\mathbf{H}$, computed at the minimum of the objective function [12, 110].

D-Optimality Criterion. This is related to the volume of the indifference region, defined by the hyperellipsoid with size determined by the eigenvalues of the Hessian matrix. The area is called the indifference region since varying the material parameters within this region doesn't affect the error function significantly. Since this volume is inversely proportional to the determinant of the Hessian, a D-optimal design would maximise $\det(\mathbf{H})$.

Eccentricity Criterion. The eccentricity, or ratio of the longest to shortest axis of the ellipsoid describing the region of indifference, is a measure of the discrepancy between the least- and best-determined parameters. The ratio of the largest eigenvalue to the smallest eigenvalue reflects the ellipsoidal eccentricity. An eccentric-optimal design would minimise $\mathrm{cond}(\mathbf{H})$. Since the five parameters evaluated in this study are of different scales (by three orders of magnitude), the eccentricity criterion was evaluated from a Hessian computed using parameter vectors that were normalised to have equal magnitude, $\mathbf{H}_{norm}$.

M-Optimality Criterion. The third criterion relates to the interaction between material parameters. An ellipsoid axis, which lies at some angle with respect to parameter axes, indicates a correlation between parameters. Interaction between parameters is minimal when the determinant of the scaled Hessian matrix, $M = \det(\tilde{\mathbf{H}})$, is equal to one. The (i, j) entry of $\tilde{\mathbf{H}}$ can be written as:

$$\tilde{h}_{ij} = \frac{h_{ij}}{\sqrt{h_{ii}h_{jj}}} \tag{4.5}$$

where i and j range over the number of parameters in the optimisation.

4.2 Results

4.2.1 Isotropic Phantom

The resulting material properties from the isotropic parameter estimation in the gel phantom were: s = 0.100, E = 16.655 kPa and ν = 0.500 (RMSE = 16.46%). Figure 4.2 shows the objective function plotted from the parameter sweep using the phantom model. The objective function shows a clear minimum in the Young's Modulus (E) direction but large valleys along the Poisson's ratio and structural damping directions. The D-optimality value ($\det(\mathbf{H})$) for identifiability was 1.028e12; the eccentricity value ($\mathrm{cond}(\mathbf{H}_{norm})$) was 26.19; and the M-optimality ($\det(\tilde{\mathbf{H}})$) value was 0.901.

The parameters are largely independent since $\det(\tilde{\mathbf{H}})$ is close to 1. The parameter independence can also be understood by observing the eigenvectors, which are each aligned primarily along one parameter axis. Overall identifiability is described by the D-optimality criterion, which is the $\det(\mathbf{H})$. A larger $\det(\mathbf{H})$ indicates a smaller indifference region and greater identifiability. A larger gradient along any one individual direction results in a larger D-optimality criterion. When the Hessian matrix is non-singular, its determinant can be written as the product of the eigenvalues. Therefore, in the case when the parameters are independent of one another, the eigenvalues from the scaled Hessian can be used to describe the relative identifiability of each parameter.

There was a large difference between the identifiability of the Young's modulus compared to the structural damping coefficient and Poisson's ratio (Eccentricity > 1). The structural damping coefficient was least identifiable (eigenvalue = 1.027), followed by the Poisson's ratio (eigenvalue = 3.720), leaving Young's modulus as the most identifiable parameter (eigenvalue = 26.89).

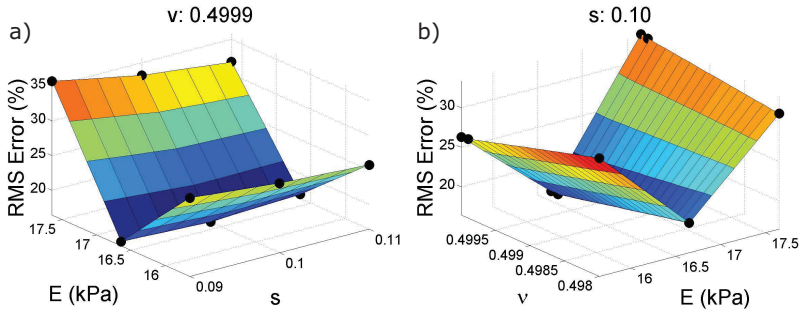

FIGURE 4.2: RMSE (%) for a) E and s and b) ν and E. Plots are shown with additional interpolated data points; black spheres indicate points at which error values were calculated.

4.2.2 Anisotropic Left Ventricle Simulations

Figure 4.3 shows the LV ground truth displacement maps and Figure 4.4 shows the objective function plots for the LV parameter sweep. When all five parameters were estimated using the ground truth values as the initial estimates and no Gaussian noise was added, the resulting parameters were: s = 0.100, E_1 = 6.501 kPa, E_3 = 10.490 kPa, G_{13} = 2.501 kPa and ν_{31} = 0.4999. Based on the Hessian at the minimum of the objective function for the LV parameter sweep, the D-optimality criterion ($\det(\mathbf{H})$) for identifiability was 6.730e21; the eccentricity value ($\mathrm{cond}(\mathbf{H}_{norm})$) was 256.34; and the M-optimality ($\det(\tilde{\mathbf{H}})$) value was 0.943. The parameters in order from least identifiable to most identifiable for the LV model were: ν_{31}, E_3, s, G_{13} and E_1. The eccentricity was very high indicating that there was a large discrepancy between the identifiability of the most identifiable parameter (E_1) and the least identifiable parameter (ν_{31}). The M-optimality value (0.943) close to one indicates weak dependence between parameters in the LV model.

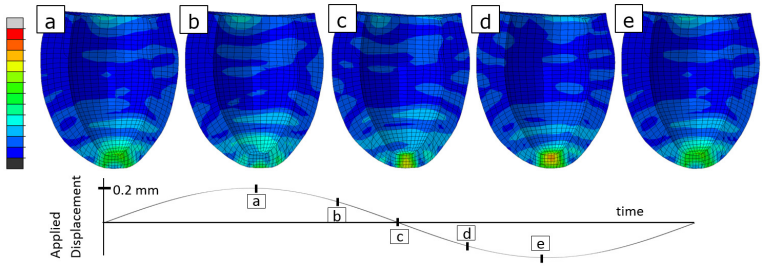

FIGURE 4.3: a) Displacement maps at five points (a-e) during one harmonic cycle in the ground truth FE LV model. Panels a-e show a section through the long axis of the LV and the color maps represent magnitude of the displacement ($\sqrt{x^2+y^2+z^2}$); red: +0.2 mm, blue: 0 mm.

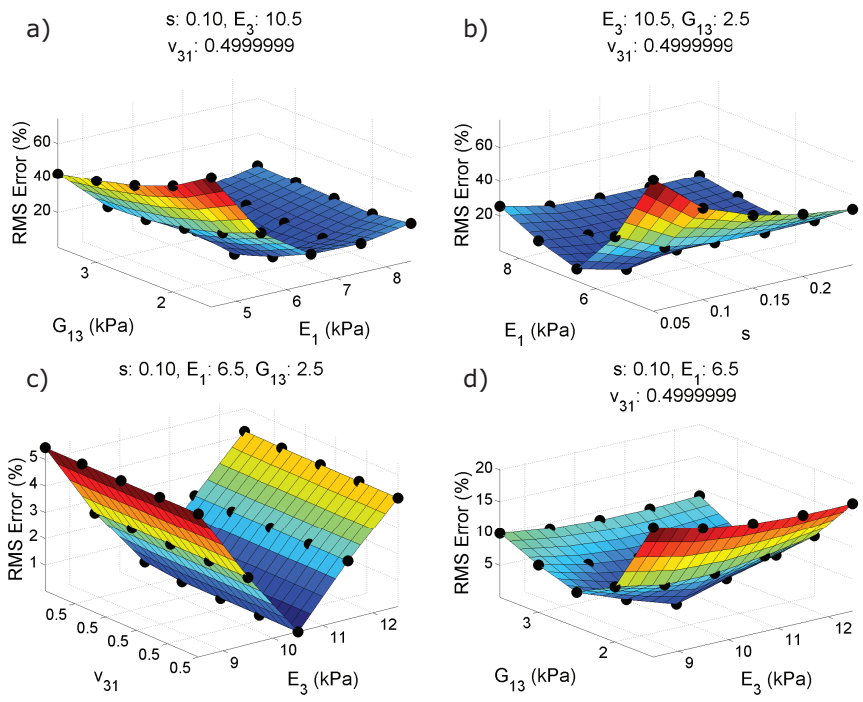

FIGURE 4.4: A representative example of plots of the objective function. Percent RMSE is plotted for parameters: a) G_{13} vs. E_1, b) E_1 vs. s, c) ν_{31} vs. E_3 and d) G_{13} vs. E_3; black spheres indicate points at which error values were calculated. Note the difference in scales between the plots.

Parameter values resulting from the 30 material parameter estimations with simulated noise were: s = 0.118 $\pm$ 0.011, E_1 = 6.555 $\pm$ 0.214 kPa, E_3 = 10.459 $\pm$ 1.014 kPa, G_{13} = 2.513 $\pm$ 0.077 kPa and ν_{31} = 0.464 $\pm$ 0.053. The optimisation was then repeated while fixing Poisson's ratio and only s, E_1, E_3 and G_{13} were estimated. The resulting parameters when Poisson's ratio was fixed were: s = 0.120 $\pm$ 0.015, E_1 = 6.538 $\pm$ 0.054 kPa, E_3 = 11.027 $\pm$ 0.628 kPa and G_{13} = 2.526 $\pm$ 0.054. Box plots in Figure 4.5 show the spread of identified parameters when Poisson's ratio was estimated and when it was fixed. The damping coefficient was consistently overestimated (true parameter = 0.1).

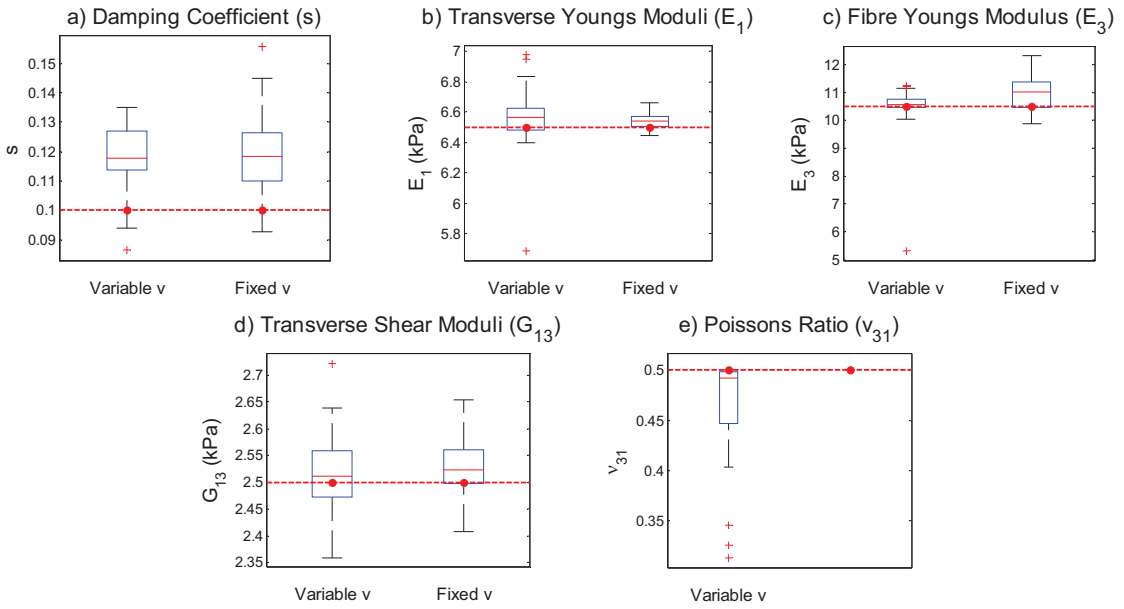

FIGURE 4.5: Box plots of material parameter estimation results for the a) damping coefficient, b) transverse Young's modulus, c) fibre Young's modulus, d) fibre shear modulus and e) Poisson's ratio. Boxplots show results from optimisations when varying Poisson's ratio ("Variable ν") and when fixing Poisson's ratio in the fibre-transverse direction ("Fixed ν"). Both Monte Carlo simulations (n=30) used varying initial estimates.

4.2.3 Anisotropic Parameter Estimation from the Isotropic Phantom

The anisotropic estimation applied to the isotropic phantom MRE displacements resulted in the following material parameter estimates: s = 0.10, E_1 = 16.75 kPa, E_3 = 16.75 kPa, G_{13} = 5.65 and ν_{31} = 0.50 (RMSE = 16.20%). Figure 4.6 shows the objective function plots from the anisotropic parameter sweep for the model of the phantom. The plots of the surfaces of the objective function show clear minima in some but not all parameters. It is noticeable, simply from the existence of valleys in the objective function, that not all parameters are equally identifiable.

The D-optimality value ($\det(\mathbf{H})$) for identifiability was 3.521e12; the eccentricity value ($\mathrm{cond}(\mathbf{H}_{norm})$) was 77.82; and the M-optimality ($\det(\tilde{\mathbf{H}})$) value was 0.811. Since the phantom material was isotropic, there was interaction between the parameters E_1 and E_3, which then resulted in the lower M-optimality value ($<$1). However, the eigenvectors showed little to no interaction between the Young's moduli, shear modulus and Poisson's ratio. The eigenvectors also showed slight interaction between the Young's moduli and the structural damping coefficient. The parameters in order from least to most identifiable (magnitude of eigenvalue) were: s, ν_{31}, E_3, E_1 and G_{13}. The shear parameter was much more identifiable than all other parameters, since the eigenvalue was more than 25x greater than that of the next biggest eigenvalue (E_1).

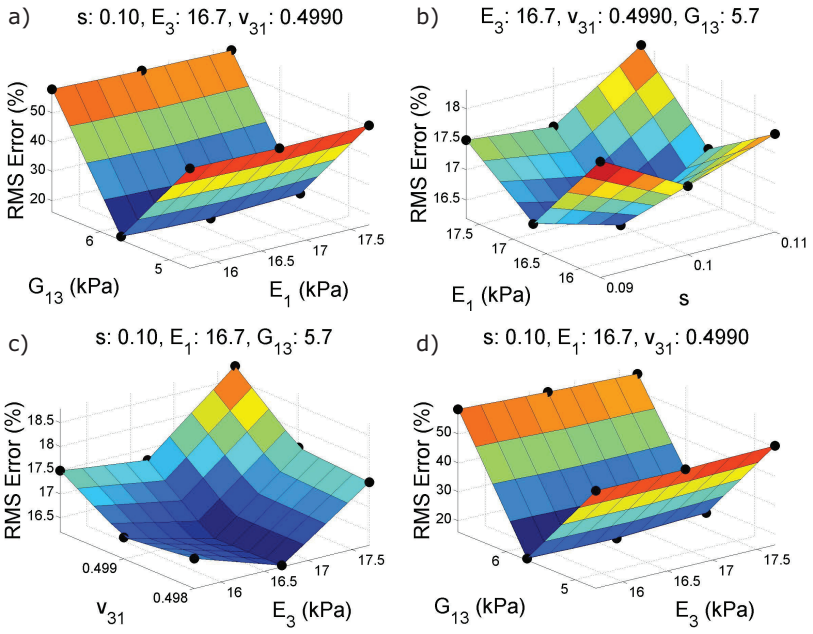

FIGURE 4.6: RMSE (%) is plotted for parameters: a) G_{13} vs. E_1, b) E_1 vs. s, c) ν_{31} vs. E_3 and d) G_{13} vs. E_3; black spheres indicate points at which error values were calculated.

TABLE 4.1: Summary of optimality criteria determined from the Hessian of the objective functions at the minimum.

	D-Opt	Eccentricity	M-Opt
LV	6.730e21	256.34	0.943
Phantom-Iso	1.028e12	26.19	0.901
Phantom-Aniso	3.521e12	77.82	0.811

TABLE 4.2: Results from material parameter estimations

	Damping (s)	Transverse Young's Modulus (E_1)	Fibre Young's Modulus (E_3)	Fibre Shear Modulus (G_{13})	Poisson's Ratio (ν_{31})
Phantom Anisotropic	0.10	16.75 kPa	16.75 kPa	5.65 kPa	0.499
LV	0.118 $\pm$ 0.011	6.555 $\pm$ 0.214 kPa	10.459 $\pm$ 1.014 kPa	2.513 $\pm$ 0.077 kPa	0.464 $\pm$ 0.053
LV (fixed ν)	0.120 $\pm$ 0.015	6.538 $\pm$ 0.054 kPa	11.027 $\pm$ 0.628 kPa	2.526 $\pm$ 0.054 kPa	$\equiv$ 0.49999999

4.3 Discussion

Myocardium is known to have anisotropic material properties, which has been shown to be important in the efficient mechanical performance of the heart [67]. Results from the LV simulations demonstrated the identifiability of fibre and cross-fibre material parameters based solely on the displacement field of a distortional wave as obtained in MRE.

High eccentricity values for the LV model and phantom indicate that some parameters were more identifiable than others. More specifically, from the eigenvectors and eigenvalues, the Poisson's ratio was the least identifiable parameter in the LV anisotropic inversion whereas the Young's modulus in the transverse direction (E_1) and the fibre shear modulus (G_{13}) were the most identifiable parameters. From the anisotropic parameter sweep of the phantom, the structural damping coefficient, s was the least identifiable parameter while G_{13} was the most identifiable. The lack of identifiability of the Poisson's ratio can be understood visually based on the large valley seen along the direction of the Poisson's ratio in the plots of the objective function from the parameter sweeps in Figure 4.2 and Figure 4.4. The valleys indicate that changing the Poisson's ratio close to 0.5 had little to no effect on the wave propagation in the simulated harmonic data. Additional experimental simulations were run (data not shown) where reference values of 0.4999 and 0.495 were chosen for Poisson's ratios. Around 0.4999, the Poisson's ratio was still not identifiable, indicated by a valley in the objective function and small associated eigenvalue. However, at $\nu = 0.495$, changes in Poisson's ratio had a greater effect on the wave propagation on the scale of the LV model and, consequently, the objective function. However, since values of Poisson's ratio closer to 0.5 are more physiologically realistic, this chapter investigated the identifiability of a value closer to 0.5.

For the LV model, the transversely isotropic material parameter estimations resulted in mean values close to the true parameters. Only the structural damping coefficient was systematically overestimated. This experiment validated the relative identifiability of the parameters shown by the parameter sweeps. The E_1 and G_{13} parameters were best identified, whereas E_3 showed larger variance (Figure 4.5). Using this optimisation algorithm, ν_{31} was not well identified in the LV model.

Overall, this work indicates that using displacement data from MRE to identify the shear modulus and Young's moduli is a well-posed problem. However, the parameters are not equally identifiable. As well as providing information on the relative identifiability of anisotropic parameters from MRE displacement data, this method also provides a way of measuring global anisotropic properties in patient-specific models that does not assume an infinite medium or lack of wave reflections and attenuation. However, due to the lack of identifiability of a Poisson's ratio close 0.5, when using the boundary value FEMU method, future studies should set a reasonable value and not optimise for this parameter.

Limitations of this study include the assumptions made in the constitutive equation.

Although myocardium is known to be non-linearly hyperelastic under large deformations, linear elasticity is considered to be adequate in the current application, given the small strains induced by MRE. In practice, MRE data can be acquired at different time points in the cardiac cycle in order to estimate the nonlinear variation in stiffness throughout the cycle. There is evidence that myocardium is fully orthotropic with different stiffnesses in fibre, cross-fibre, and laminar directions [34]. However, there is controversy about whether more than one family of laminae are present [62] and many groups have therefore employed transversely isotropic constitutive equations [162]. Since DTMRI measurement of secondary and tertiary material structure orientations is difficult [18], we restricted our analysis to transversely isotropic materials.

Another limitation of this model is the fact that the damping coefficient is considered isotropic. In one study [61] identifying three complex moduli (E_3^*, G_{12}^* and G_{13}^*) to describe a transversely isotropic material, the structural damping coefficient (also called the loss factor) was greater for the fibre shear (G_{13}) than for the shear in the isotropic plane (G_{12}), indicating that damping in skeletal muscle may be anisotropic. Future studies could include anisotropic damping. However, whether or not the damping coefficient provides clinically relevant information is controversial and may depend on the type of tissue being imaged. Some studies have reported correlations between inflammation and changes in viscoelastic parameters (e.g. [164]), such as the loss modulus, while others have observed no relationship (e.g. [104]). Stiffness (particularly in the fibre and cross-fibre directions) has tangible meaning as it gives insight into changes in muscle fibres (fibre direction) as well as collagen in-growth (cross-fibre direction). Additionally, the value chosen for the damping coefficient in the LV model (s = 0.1) was less than values often measured in biological tissue (e.g. [61]) and was closer to damping coefficients measured in agar phantoms. It was assumed, however, that this difference would not affect the parameter identifiability and overall results.

Isotropic myocardial shear stiffness has successfully been measured from MRE experiments [43, 44, 77, 79, 80, 99] and so it is assumed that sufficient wave propagation can be achieved experimentally. However, the loading applied to the LV model in this experiment is idealised and does not necessarily represent the true harmonic motion that would occur in the left ventricle during cardiac MRE. In the future, various loading conditions should be tested to evaluate their effect on parameter identifiability in an LV model.

One open question is whether an anisotropic model provides substantively better results, over an isotropic model, given a set of MRE data. As a simple test, an isotropic shear modulus was also estimated for the LV model reference displacements, which were generated using the transversely isotropic material model. Estimating a single shear modulus (along with a damping coefficient and isotropic Poisson's ratio), without Gaussian noise but varying the initial parameter estimate, resulted in an average %RMSE of 14% (n

= 10) compared with an average %RMSE of 1% (n = 10) when estimating five material parameters in the anisotropic model. Therefore, the use of a transversely isotropic material model greatly improved the ability to accurately model wave propagation in a transversely isotropic medium, as noted by the smaller %RMSE. However, in future, the Akaike information criterion (AIC) [19] should be investigated to determine whether an anisotropic shear modulus adds additional benefit over an isotropic model in a given application. The AIC takes into account both the %RMSE and the simplicity (number of parameters) in the model.

This study demonstrates that, in a nearly incompressible medium, four (s, E_1, E_3, G_{13}) out of five material properties used to describe a transversely isotropic linear elastic material are uniquely identifiable from simulated MRE displacement fields using a FEA model of harmonic steady-state wave propagation. As a material diverges from incompressibility (the Poisson's ratio decreases), the Poisson's ratio becomes more identifiable. When Gaussian noise was added to the LV optimisations, the solution was more dependent on the initial estimate. However, fixing Poisson's ratio only improved estimation of E_1. In a transversely-isotropic model, there is a reasonable degree of confidence when predicting the transverse Young's modulus (E_1) as well as the fibre shear (G_{13}) using this method; however, less confidence in the prediction of the fibre Young's modulus (E_3) and the damping coefficient (s). These results are consistent with a previous Monte Carlo simulation study (n = 30) [150] which identified three parameters to describe a transversely isotropic linear elastic material: μ, the shear modulus in the isotropic plane, ϕ, related to the shear anisotropy and ζ, related to the tensile anisotropy. From the estimations with added Gaussian noise (SNR = 10), mean global estimates of μ and ϕ were within 25% of the true values. However, the mean global estimate of ζ was always underestimated and varied by 40%. Estimating E_3 necessitates the existence of fast shear waves [139, 149–151], which induce fibre stretching, in the MRE displacement field. In the LV simulations in this study, a lack of adequate fast shear waves may account for the fact that E_3 was consistently less identifiable than E_1 and G_{13}. As has been presented in these recent studies investigating transversely isotropic properties estimated from MRE, other loading configurations should also be tested, which may improve the identifiability of the fibre Young's modulus.

The methodology proposed in this chapter builds upon previous FEA methods discussed in Chapter 2 by using displacements from MRE as boundary conditions along with the true geometry and fibre architecture of the heart to estimate transversely isotropic material properties. By incorporating data from three MR imaging modalities, cine SSFP, phase-contrast MRE, and DTMRI, this method aims to avoid assumptions of an infinite medium and material isotropy, in order to accurately model the geometry and mechanics of the heart during MRE and subsequently identify anisotropic material properties.

There are three inherent limitations of the boundary value FEMU method. Firstly, it

preferentially weights nodes where boundary conditions are applied since they are treated as ”more accurate” than nodes used in the objective function. Boundary conditions are chosen somewhat arbitrarily from the set of measured displacements which creates bias since each voxel is subject to the same degree of noise. Additionally, the FEMU method implemented in this thesis necessitates that Poisson's ratio either be estimated or set to a value. MRE displacement fields do not provide enough information to confidently estimate Poisson's ratio since the longitudinal wavelength is much longer than the imaged region. However, setting Poisson's ratio to an incorrect value may also lead to errors in parameter estimates, particularly E_1 and E_3. Finally, the boundary value FEMU method is iterative and therefore computationally expensive. A direct method, known as the virtual fields method, therefore, will be explored in Chapters 5 and 6. It uses all data points equally and, thus, does not preferentially weight some voxels over others. It also allows one to only solve for the deviatoric components without setting Poisson's ratio or solving for it.

5

ISOTROPIC VIRTUAL FIELDS METHOD

IN this chapter, both analytic and optimised (numeric) versions of the isotropic virtual fields method are implemented to estimate a complex shear modulus, containing both real and imaginary components, from a 3D harmonic displacement field. The method requires a set of measured full-field displacements to directly solve for material properties. The primary advantage of this method over the boundary value FEMU method is that the subjective choice of boundary conditions is not required and all data points are weighted equally. Additionally, it is a direct (non-iterative) method, which is less computationally intensive than the FEMU method. The method was implemented with simulated displacements in an isotropic beam and left ventricular model. Further, the method was tested with MR elastography data collected from an isotropic phantom.

5.1 Analytic Virtual Fields Method

5.1.1 Formulation

The virtual fields method (VFM) was developed by Grédiac et al. [55] as a method for the identification of material properties from mechanical tests using imaging data. The advantage of the VFM approach is that image data are used throughout the domain, resulting in a more direct estimation procedure compared with the traditional method of solving boundary value problems. The VFM utilises the principle of virtual work, which generally states that "a continuous body is at equilibrium if the virtual work of all forces acting on the body is null for any kinematically admissible virtual displacement" [118]. The principle of virtual work, identical to Equation 3.1, is written in this chapter denoting the virtual displacement field as $\mathbf{u}^*$ to be consistent with other VFM papers.

$$-\int_V \boldsymbol{\sigma} : \boldsymbol{\epsilon}^* dV + \int_S \mathbf{t} \cdot \mathbf{u}^* dS + \int_V \mathbf{b} \cdot \mathbf{u}^* dV = \int_V \rho \mathbf{a} \cdot \mathbf{u}^* dV \tag{5.1}$$

$\boldsymbol{\sigma}$ are the internal stresses, $\mathbf{t}$ are the applied traction forces, $\mathbf{b}$ are the body forces, ρ is the density and $\mathbf{a}$ is the acceleration. $\boldsymbol{\epsilon}^*$ and $\mathbf{u}^*$ are the virtual strains and virtual displacements, respectively. The first term represents the virtual work done by internal forces; the second and third terms represent virtual work done by external forces; and the right-hand side term represents the virtual work done by acceleration. The virtual fields must be 1) kinematically admissible (i.e. consistent with the boundary conditions of the problem) and 2) piecewise-C^0 continuous. In biological tissue, body forces such as gravity are in equilibrium with reaction forces imposed by surrounding tissue. For most MRE problems, the body forces, $\mathbf{b}$, can be assumed to be negligible since we assume that they don't cause a resulting displacement, particularly in the time scale measured during one harmonic cycle.

$$-\int_V \boldsymbol{\sigma} : \boldsymbol{\epsilon}^* dV + \int_S \mathbf{T} \cdot \mathbf{u}^* dS = \int_V \rho \mathbf{a} \cdot \mathbf{u}^* dV \tag{5.2}$$

Additionally, one common strategy is to set the virtual displacement field to zero at any locations where the boundary traction forces are unknown, thereby eliminating the second term of the equation. In harmonic problems involving linear elastic media (such as elastography), the resultant displacement frequency is the same as the load frequency. The acceleration can be written as the product of the angular frequency squared and measured displacement field ($\omega^2\mathbf{u}$).

$$-\int_V \boldsymbol{\sigma} : \boldsymbol{\epsilon}^* dV = \int_V \rho\omega^2 \mathbf{u} \cdot \mathbf{u}^* dV \tag{5.3}$$

where $\omega = 2\pi f$ and f is the frequency of excitation in Hz. Equation (5.3) relies on four measurements: the internal stress field (which carries in it the unknown material parameters), density, angular frequency and the resulting displacement field.

The VFM was initially used to estimate material properties from MR elastography displacements by implementing analytic virtual displacement fields [117, 132]. Sinusoidal analytic virtual fields were applied to simulations of harmonic displacements in a cylindrical geometry and Lamé parameters were estimated (normalised by density ρ), λ/ρ and μ/ρ. It was shown that the method was accurate except at interfaces between different materials within the cylinder [132]. In another study, analytic virtual displacement fields were strategically chosen such that the bulk component of the internal stress term was zero, eliminating the need to estimate the longitudinal wavelength [117]. Additionally, different analytic virtual displacement fields were investigated, which varied by k, the virtual wave number. The methods in [117] are outlined below and were implemented similarly to validate the method in a cantilever beam model in this thesis.

An isotropic linear elastic material law was used to describe the constitutive behaviour:

$$\boldsymbol{\sigma} = K\mathrm{Tr}(\boldsymbol{\epsilon})\mathbf{I} + 2G[\boldsymbol{\epsilon} - \frac{1}{3}\mathrm{Tr}(\boldsymbol{\epsilon})\mathbf{I}] \tag{5.4}$$

where K represents the bulk modulus and G, the shear modulus. By substituting the constitutive equation into the left hand side of the principle of virtual work (Equation (5.3)), the term for internal stress can be written as:

$$\int_V \boldsymbol{\sigma} : \boldsymbol{\epsilon}^* dV = K \int_V \mathrm{Tr}(\boldsymbol{\epsilon})\mathrm{Tr}(\boldsymbol{\epsilon}^*) dV + 2G \int_V (\boldsymbol{\epsilon} : \boldsymbol{\epsilon}^* - \frac{1}{3}\mathrm{Tr}(\boldsymbol{\epsilon})\mathrm{Tr}(\boldsymbol{\epsilon}^*)) dV \tag{5.5}$$

K is dependent on the Poisson's ratio ν, and consequently, the longitudinal wavelength. In elastography experiments, the longitudinal wavelength is much longer (approximately 300x) than the shear wavelength, and is therefore difficult to estimate since the geometry being imaged is much smaller than the longitudinal wavelength. Equation (5.4) is of a form that is advantageous in VFM applications since the internal stress is written as a linear combination of the bulk (K) and shear (G) components.

With the VFM, a virtual displacement field can be chosen such that the internal virtual stress due to the bulk modulus is negligible. This condition was easily met for a simple rectangular geometry by ensuring that the trace of the virtual strain field was zero ($\mathrm{Tr}(\boldsymbol{\epsilon}^*) = 0$).

$$\int_V \mathrm{Tr}(\boldsymbol{\epsilon})\mathrm{Tr}(\boldsymbol{\epsilon}^*) dV = 0 \tag{5.6}$$

In [117], this was done by only including one shear term in the virtual displacement field which ensured that ϵ^*_{11}, ϵ^*_{22} and ϵ^*_{33} were zero so that $\mathrm{Tr}(\boldsymbol{\epsilon}^*) = \epsilon^*_{11} + \epsilon^*_{22} + \epsilon^*_{33} = 0$. In the cube geometric model in [117], the resulting virtual displacement field applied was:

$$u^*_1 = (y - L_y) \sin\left(\frac{2k\pi}{L_y} y\right) \qquad u^*_2 = 0 \qquad u^*_3 = 0 \tag{5.7}$$

where L_y was the length of the cube, y was the position in the y-direction and k was the virtual wave number, which controlled the spatial frequency. A sine function, polarised in the x-direction, was used since it closely matched the harmonic displacement field measured experimentally, in which an x-displacement was applied on one face of the cube. The only non-zero component of the resulting virtual strain field was:

$$2\boldsymbol{\epsilon}^*_{12} = \sin\left(\frac{2k\pi}{L_y} y\right) + \frac{2k\pi}{L_y}(y - L_y) \cos\left(\frac{2k\pi}{L_y} y\right) \tag{5.8}$$

With the chosen virtual displacement field, Equation (5.5) was then simplified to:

$$-2G \int_V \epsilon_{12} \epsilon^*_{12} dV = -\rho\omega^2 \int_V u_1 u^*_1 dV \tag{5.9}$$

A discrete sum was used to approximate the integrals in the equation of virtual work. Equations (5.8) and (5.7) were substituted into (5.9) and the equation was written in terms of the homogeneous shear modulus, G.

$$G = \frac{\rho\omega[\overline{u_1(y - L_y)\sin\left(\frac{2k\pi}{L_y}y\right)}]}{2\boldsymbol{\epsilon}_{12}[\overline{\sin\left(\frac{2k\pi}{L_y}y\right) + \frac{2k\pi}{L_y}(y - L_y)\cos\left(\frac{2k\pi}{L_y}y\right)}]} = \frac{a}{b} \tag{5.10}$$

Overbars indicate spatial averaging. In [117], k was chosen to be six since there were approximately six wavelengths in the y-direction. An index of the sensitivity of the method to accurately estimate shear modulus from shear wave propagation was defined as the product of a and b, the numerator and denominator in Equation (5.10). At low sensitivities, the estimated shear moduli showed large variations. High sensitivity values indicated that the analytic virtual displacement field applied on the measured field at time point n_i provided adequate information with which to estimate the shear wavelength. Spatial averages were computed for regions with sensitivity above specified thresholds. Testing thresholds between $0.1 \cdot \max(a \cdot b)$ and $0.9 \cdot \max(a \cdot b)$ resulted in shear moduli ranging between 1647 Pa - 1693 Pa. These initial studies showed promising results for a fast inversion method which does not rely on multiple iterations or application of boundary conditions in order to determine material properties from MRE data. Analytic virtual fields that a) enforce zero virtual displacement on the boundaries as well as b) dissociate shear from bulk stress can easily be developed in regular geometries.

5.1.2 Results

The analytic virtual fields method was implemented with a cantilever beam model as well as isotropic phantom MRE data and the method was compared to results from the boundary value finite element model update (FEMU) method presented in previous chapters. A major point of difference between this work and previous studies using the analytic VFM to estimate parameters from elastography data is that, in this thesis, complex displacement fields, which describe amplitude and phase of the harmonic motion of each pixel/data point, were used as input rather than time discretised displacement fields as in [117]. The resulting estimated shear modulus is then complex; the real part is often called the storage modulus and the imaginary part is the loss modulus. The ratio of the imaginary to the real part is the loss factor or damping coefficient. Therefore, by solving the complex problem once, two material properties can be obtained. In this chapter, results will be reported as a single shear modulus (which is the storage modulus) and the damping coefficient (s). Previous studies have discretised the complex displacement field at numerous (e.g. n = 50) time points and solved the VF equations for both storage and loss moduli at each discretised time point using a viscoelastic formulation [29]. However, this method uses complex displacement fields to avoid the estimation of parameters at each discretised time point, thus saving computation time.

5.1.2.1 Beam Simulations

An ideal simulation of wave propagation in a finite element cantilever beam model was used to test and develop isotropic VFM inversion methods for application to MRE data. The beam model (50 mm x 50 mm x 200 mm) was vibrated in the y-direction on the left hand end (+z) of the beam. The nodes on the right hand end were pinned (dx = dy = dz = 0).

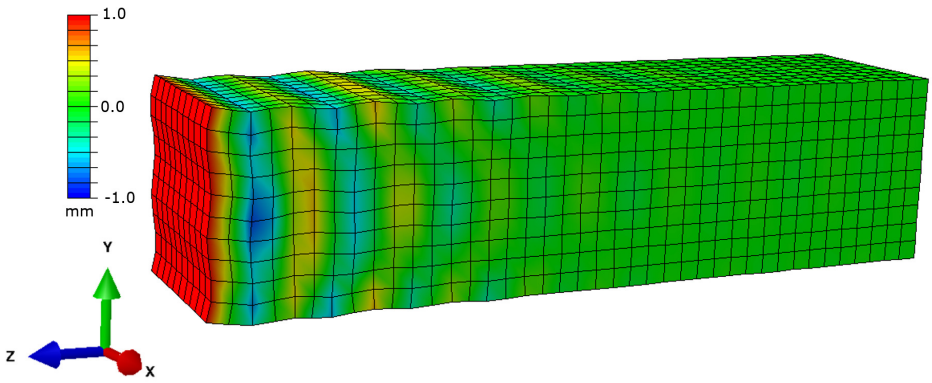

FIGURE 5.1: Finite element model simulating wave propagation in a cantilever beam geometry. The colour scale encodes y-displacements.

In the beam model, the shear modulus, damping coefficient, Poisson's ratio and density were set to 4.0003 kPa, 0.1, 0.4999 and 1.0e-6 kg/mm^3, respectively, and linear hexahedral (C3D8) elements were used. The analytic VFM was implemented as described above and, without any Gaussian noise added to the ground truth displacements, the resulting complex shear modulus was 4.0003 + 0.4000i kPa, which equates to G = 4.0003 kPa and s = 0.1. These resulting values were precisely the same as those input to the model.

To investigate the impact of noise, various amounts of Gaussian noise were added to the reference displacement field. The analytic VFM and the FEMU method, were used to determine the shear modulus of the beam for a Monte Carlo simulation (n = 30) for each amount of Gaussian noise. In both methods, the only assumed/known parameters were density (1.0e-6 kg/mm^2) and the frequency of excitation (80 Hz). For the VFM, the virtual wave number, k, was varied between 5 - 14 since there were approximately 9 wavelengths along the z-axis of the beam. For the FEMU method, the initial material parameters for the optimisation were chosen randomly from a Gaussian distribution centered at the true values (of damping, Young's modulus and Poisson's ratio) with a standard deviation of 25% of the true value.

The standard deviation of Gaussian noise (σ_{noise}) added to the reference displacements was:

$$\sigma_{noise} = N\% \cdot \sigma_{disp} \tag{5.11}$$

where N was varied between 15% - 50% and σ_{disp} was the standard deviation of measured displacements. For one noise case (N = 15%), box plots are shown in Figure 5.2 for the resulting estimated shear moduli, damping coefficients and sensitivity values ($a \cdot b$) versus the virtual wave numbers, k.

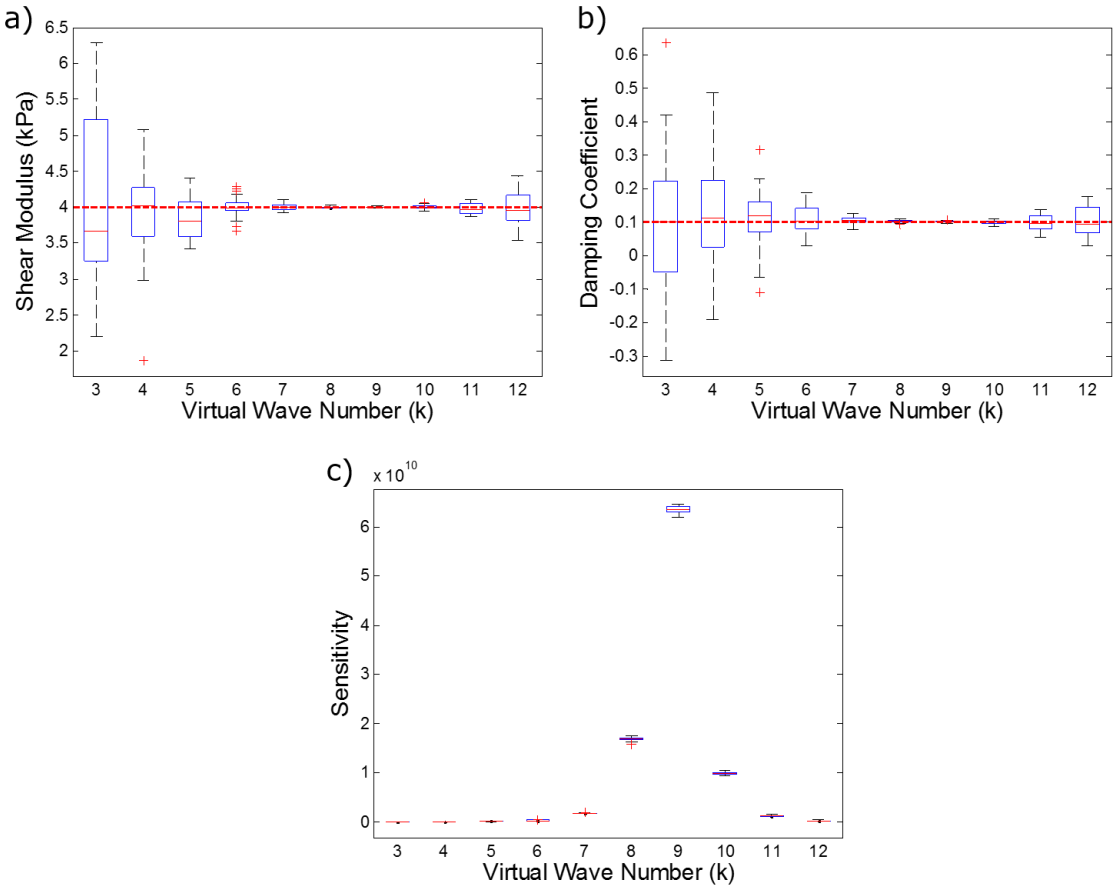

FIGURE 5.2: Box plots (n = 30) show a) shear moduli (kPa) b) structural damping coefficient and c) sensitivity versus the virtual wave number (k) using an analytic virtual field described by Equation (5.7). Results are shown for N = 15%.

Figure 5.2c shows that the sensitivity is greatest when the virtual wave number was equal to the approximate number of wavelengths along the length of the beam (k = 9). Both Figures 5.2a and 5.2b illustrate that as virtual wave numbers deviated from nine, the variance in both the estimated shear modulus and damping coefficient became large. Additionally, mean estimated shear moduli and damping coefficients were most accurate (i.e. closer to 4.0003 kPa and 0.1, respectively) when k = 9. Similarly, sensitivity of the method to estimate a complex shear modulus was greatest when k = 9. Therefore, with this particular analytic virtual displacement field, the estimated shear modulus was highly dependent on the choice of the virtual wave number. Plots for all other amounts of noise (N = 15% - 50%) were similar to Figure 5.2.

Figure 5.3 shows the estimated shear moduli and damping coefficients using the ana-

lytic VFM from the Monte Carlo simulation with k = 9, for the different specified values of noise, N.

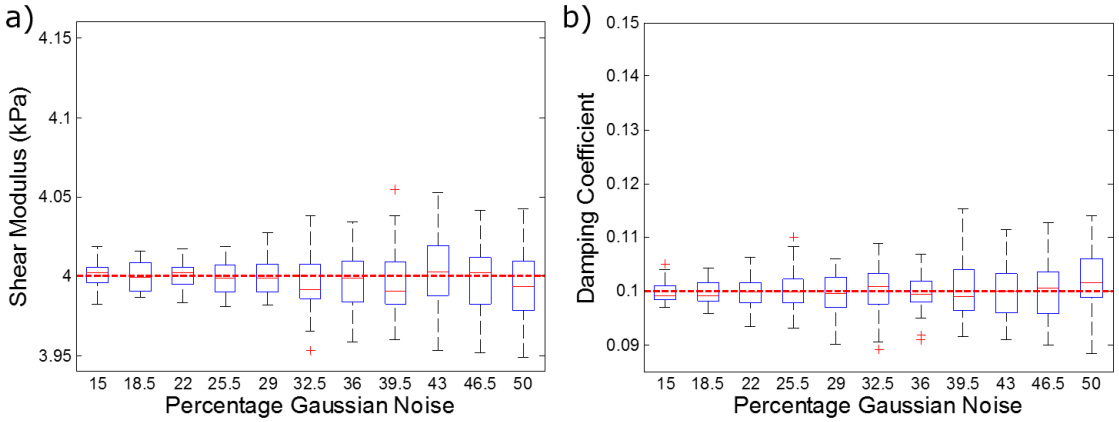

FIGURE 5.3: a) Shear moduli and b) damping coefficients (n = 30) estimated with the analytic VFM for each amount of Gaussian noise (N = 15% - 50%) applied to the simulated ground truth displacements. Results are shown for k = 9.

Figure 5.3 illustrates that with an appropriate virtual displacement field (k = 9) and 50% Gaussian noise added to the displacement data, the mean shear modulus was accurately estimated with an error less than 2.5%. As expected, the variance in the estimated shear modulus and damping coefficient increased as the amount of Gaussian noise increased.

Similar amounts of noise were then added to the beam displacement data and the FEMU method was used to estimate the shear modulus. The parameters estimated using the FEMU method were the damping coefficient (s), Young's modulus (E) and Poisson's ratio (ν). Since the beam material was isotropic, the shear values shown in Figure 5.4 were calculated as:

$$G = \frac{E}{2(1+\nu)} \tag{5.12}$$

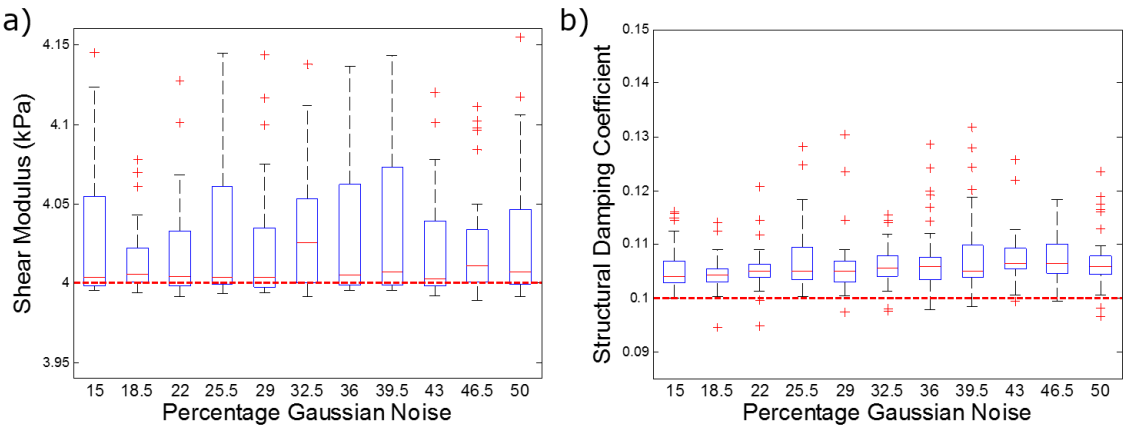

FIGURE 5.4: a) Shear moduli and b) structural damping coefficients (n = 30) estimated with the FEMU method for each amount of Gaussian noise applied to the simulated ground truth displacements. Initial parameter estimates were chosen randomly from a Gaussian distribution centered at the true value with a standard deviation of 25% of the true value.

One primary difference between the analytic VFM and FEMU methods (Figure 5.3 versus Figure 5.4) was the handling of Poisson's ratio. In the VFM, the analytic virtual field was chosen such that the bulk component of the internal stress was zero, thus eliminating the need to estimate Poisson's ratio altogether. However, Poisson's ratio was estimated in the FEMU method within constraints ($\nu < 0.5$). Consequently, shear moduli were overestimated but never greatly underestimated since Poisson's ratios were only allowed to be underestimated. Additionally, estimated parameters were largely dependent on the starting value of Poisson's ratio. To investigate the impact of Poisson's ratio on the estimation of the shear modulus, the FEMU Monte Carlo optimisations were repeated while fixing Poisson's ratio ($\nu = 0.4999$).

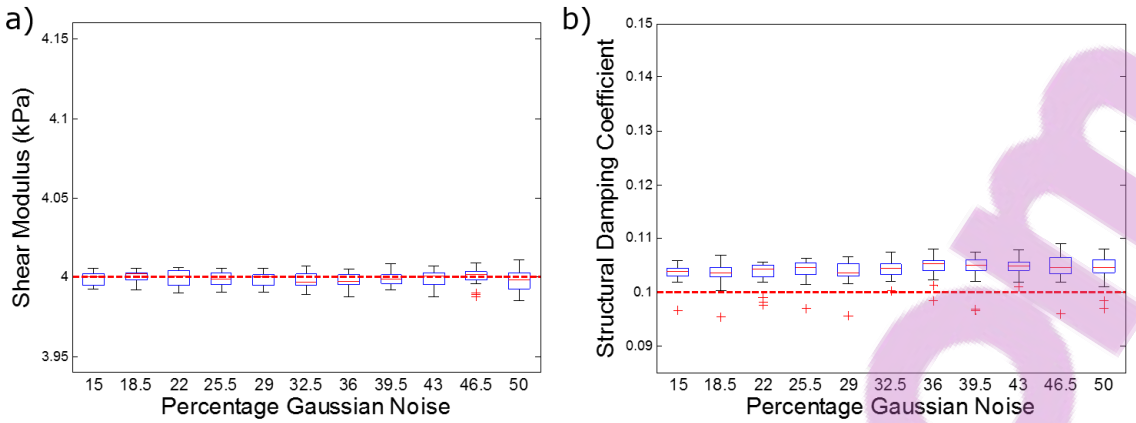

FIGURE 5.5: a) Shear moduli and b) damping coefficients (n = 30) estimated with the FEMU method for each amount of Gaussian noise applied to the simulated ground truth displacements. Initial parameter estimates were chosen randomly from a Gaussian distribution centered at the true value with a standard deviation of 25% of the true value. Poisson's ratio was set to 0.4999.

When the Poisson's ratio was fixed, the shear modulus for the isotropic beam was accurately estimated, even in the presence of large amounts of noise. The values were estimated more accurately and with less variance than the analytic VFM. However, the damping coefficient was consistently overestimated. The reason for this systematic difference is not understood. Despite the accuracy of the FEMU method in estimating shear modulus when the Poisson's ratio is known, the boundary value method is computationally expensive whereas the VFM is a direct (non-iterative) method.

5.1.2.2 Isotropic Phantom MRE

An analytic virtual displacement field was then implemented with the experimental MRE phantom data, which dissociates the bulk and shear components of internal stress while respecting a zero displacement condition on the side walls of the phantom. Since the phantom data were collected from a middle section of the cylindrical phantom, the upper and lower surfaces were assumed to be unconstrained. An analytic virtual displacement field was developed which was null at the boundaries and varied as a function of radial position. Displacements were prescribed in the z direction only, resulting in shear strains: ϵ_{13} and ϵ_{23}.

$$u_z^* = (r - R)\cos\left(\frac{2\pi k r}{R}\right) \qquad u_x^* = 0 \qquad u_y^* = 0 \tag{5.13}$$

where r is the radial position of each node calculated as $\sqrt{x^2 + y^2}$ and R is the maximum radius of the phantom at the boundary (76.2 mm). Virtual wave numbers were sampled around k = 2 [1.5,2.5] since the true phantom displacement data showed approximately two wavelengths across one radius in plots of both real and imaginary displacement. The

resulting shear modulus, damping coefficient and sensitivity were calculated for all values of k.

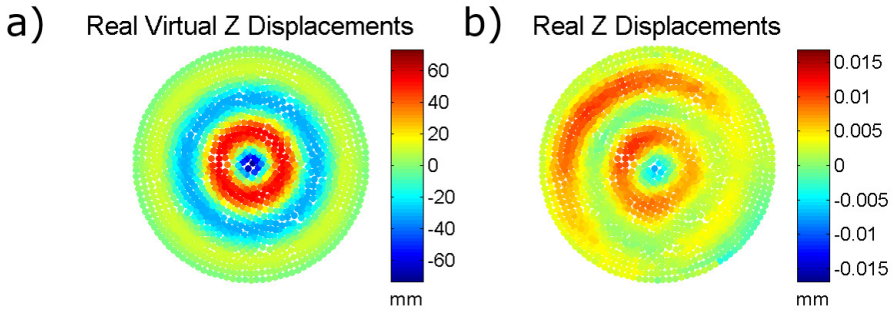

FIGURE 5.6: a) Virtual displacement field with k = 1.7 and b) z-displacement measured from one axial slice in the phantom MRE data.

At k = 1.7, when sensitivity was greatest, the shear modulus and damping coefficient were 5.38 kPa and -0.25, respectively. The estimated shear modulus of the phantom was very similar to those estimated by the FEMU, multi-model direct inversion (MMDI) and directional filter with local frequency estimation (DF-LFE) methods (FEMU: 5.55 kPa, MMDI: 5.45 kPa, DF-LFE: 5.34 kPa). Negative structural damping coefficients are physically impossible since they would represent an increase in energy within the system. Resulting negative damping coefficients may indicate that the model of damping chosen, a structural damping coefficient, does not adequately model the dissipative behaviour in the gel phantom. However, the structural damping model is simple to implement, is commonly used in MRE inversion methods and has, therefore, been used throughout the remainder of this thesis.

Then, the same analytic virtual displacement field was used (k = 1.7) to calculate the shear modulus for each element layer in the phantom, denoted as subzones (Figure 5.7).

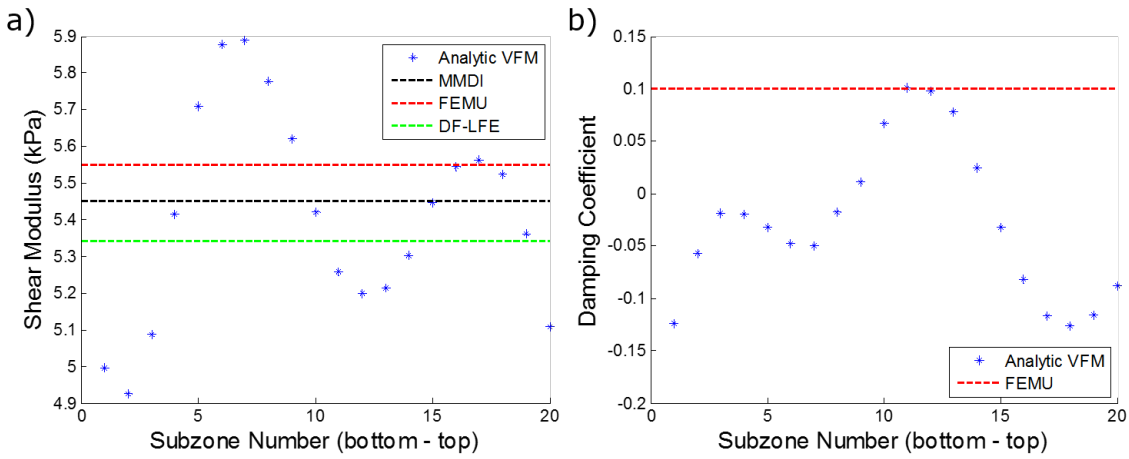

FIGURE 5.7: a) Shear moduli (kPa) and b) structural damping coefficients plotted per subzone. The phantom shear modulus values measured through the MMDI, FEMU and DF-LFE methods are shown by black, red and green lines, respectively in a) and the value of the structural damping coefficient measured using the FEMU method is shown as a red line in b).

The shear moduli estimated for each element layer varied between 4.93 and 5.89 kPa and the resulting mean shear modulus was 5.41 kPa. The mean damping coefficient was -0.0274. Since the virtual displacement field was identical for each slice and only varied with respect to the radial position, the variation in the resulting estimated shear moduli can be attributed to the differences in the measured displacement field in each slice. Figure 5.8 shows the real component of the measured MRE displacement fields at the 2nd and 7th subzones, which correspond to the minimum and maximum estimated shear moduli. Similarly, Figure 5.9 shows the imaginary component of the measured MRE displacements at the 1st and 11th subzones, again at the minimum and maximum estimated damping coefficients.

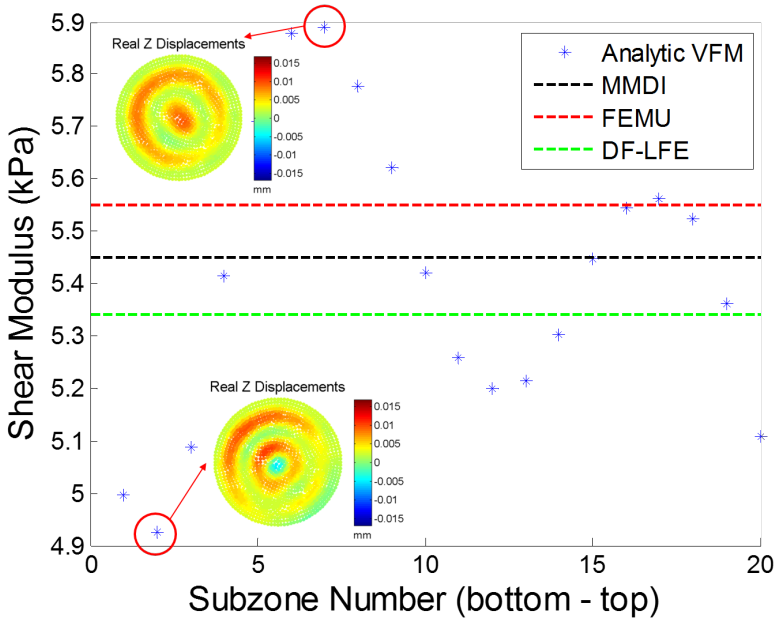

FIGURE 5.8: Shear moduli (kPa) plotted per subzone along with shear moduli estimated through the MMDI, FEMU and DF-LFE methods. MRE (through-plane) measured real displacement fields are shown for the 2nd and 7th subzones.

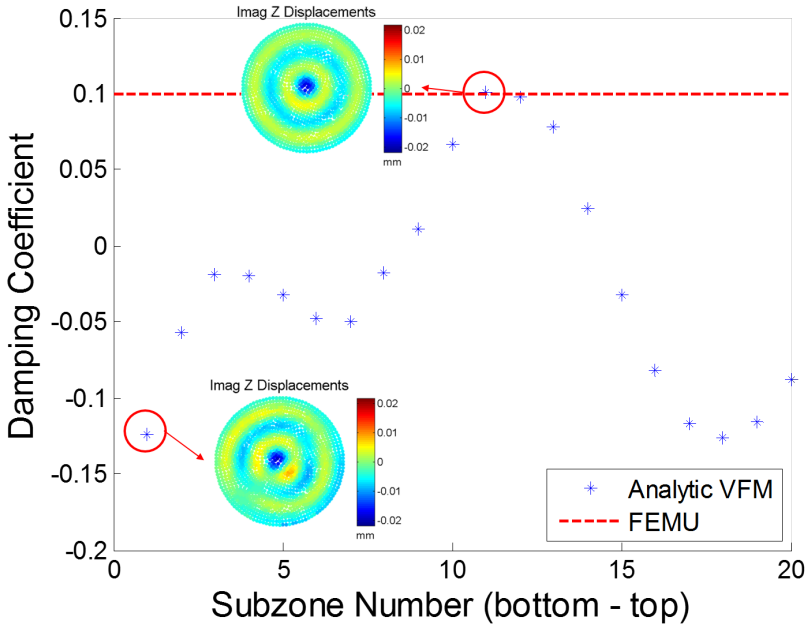

FIGURE 5.9: Damping coefficient plotted per subzone along with structural damping estimated through the FEMU methods. MRE (through-plane) measured imaginary displacement fields are shown for the 1st and 11th subzones.

The number of wavelengths was roughly estimated from the MRE measured through-plane displacement fields by counting the number of peaks (or troughs) between the centre and the periphery. In the second subzone, there were approximately two full wavelengths shown in the real component of displacement, whereas, in the seventh subzone, there were only one and a half wavelengths. When viewing all of the slice displacement fields, an inverse relationship can be seen between the estimated shear modulus and the approximate number of wavelengths in the MRE displacement field. As the number of wavelengths increased, the estimated shear modulus (using virtual wave number: k = 1.7) decreased. Slices with approximately 1.7 wavelengths resulted in estimated shear values closest to the reference values. Conversely, structural damping did not appear to depend on the number of wavelengths in the imaginary component of the measured displacement field as seen in Figure 5.9. In fact, the approximate number of wavelengths in the imaginary displacement field remained relatively constant with around two wavelengths in all slices. However, the estimated damping coefficient varied widely. The coefficient of variation, calculated as the ratio of the standard deviation to the mean, for the estimated shear modulus over the entire region (0.05) was significantly less than that for the damping coefficient (2.64). This indicates that estimation of the damping coefficient may be more sensitive to noise within the signal than the shear modulus when using the analytic VFM.

The analytic VFM was most accurate when the virtual displacement field matched the wave pattern of the measured, or ground truth, displacements. In the beam, parameter estimates were most accurate at k = 9 since there were approximately 9 wavelengths along the length of the beam. In the phantom, the regions with the most accurately estimated shear moduli corresponded to those which had approximately 1.7 wavelengths between the centre and periphery, the same as the virtual wave number, k. This method, which provided accurate identification of an isotropic shear modulus in both a cantilever beam model and a cylindrical phantom experiment, becomes cumbersome when both the geometry of the structure and wave patterns increase in complexity. To deal with this, the optimised virtual fields method, which calculates the virtual displacement field numerically, was then implemented.

5.2 Optimised Virtual Fields Method

5.2.1 Formulation

”Optimised” and ”special” virtual fields have been formulated to estimate the shear modulus in irregularly shaped structures in the presence of noisy MRE data [29]. The same linear elastic constitutive model was used as in [117], separating the bulk from the shear stress. Additionally, a constraint, which requires that all virtual displacements on boundary

nodes be zero, was applied, thus eliminating the traction term. Therefore, incorporating the constitutive equation into Equation (5.3) resulted in the following equation:

$$K\int_V Tr(\boldsymbol{\epsilon})Tr(\boldsymbol{\epsilon}^*)dV + 2G\int_V (\boldsymbol{\epsilon}:\boldsymbol{\epsilon}^* - \frac{1}{3}Tr(\boldsymbol{\epsilon})Tr(\boldsymbol{\epsilon}^*))dV = \int_V \rho\omega^2\mathbf{u}\cdot\mathbf{u}^*dV \quad (5.14)$$

It should be noted that this step assumes constant bulk and shear moduli over the region of interest. To simplify the notation, Equation (5.14) was written as:

$$Kf_K(\boldsymbol{\epsilon},\boldsymbol{\epsilon}^*) + Gf_G(\boldsymbol{\epsilon},\boldsymbol{\epsilon}^*) = \int_V \rho\omega^2\mathbf{u}\cdot\mathbf{u}^*dV \quad (5.15)$$

It is also useful to write the measured displacement field as a sum of the displacements due to the bulk and shear waves, $\mathbf{u} = \mathbf{u}_K + \mathbf{u}_G$. This assumes that displacement components of the bulk and shear waves are independent and can be linearly superimposed. The separation of $\mathbf{u}_K$ and $\mathbf{u}_G$ will prove useful when deriving equations for the optimised virtual displacement field.

$$\begin{aligned} Kf_K(\boldsymbol{\epsilon},\boldsymbol{\epsilon}^*) &= \int_V \rho\omega^2\mathbf{u}_K\cdot\mathbf{u}^*dV \\ Gf_G(\boldsymbol{\epsilon},\boldsymbol{\epsilon}^*) &= \int_V \rho\omega^2\mathbf{u}_G\cdot\mathbf{u}^*dV \end{aligned} \quad (5.16)$$

Special Virtual Fields In order to directly solve for the shear modulus while neglecting the effect of the bulk modulus, special constraints on the virtual field were applied so that:

$$\begin{aligned} f_K(\boldsymbol{\epsilon},\boldsymbol{\epsilon}^*) &= 0 \\ f_G(\boldsymbol{\epsilon},\boldsymbol{\epsilon}^*) &= 1 \end{aligned} \quad (5.17)$$

Incorporating these conditions into Equation (5.15), the shear modulus was simply calculated as:

$$G = \int_V \rho\omega^2\mathbf{u}\cdot\mathbf{u}^*dV \quad (5.18)$$

Optimised Virtual Fields There are an infinite number of possible virtual displacement fields that satisfy these constraints ($f_K = 0$, $f_G = 1$). Therefore, the method was extended to solve for the virtual displacement field that minimised the variance in the estimated shear modulus. The variance of the identified shear modulus can be written as:

$$V(G_{app}) = E\Big(\big[G_{app} - E(G_{app})\big]^2\Big) \quad (5.19)$$

where $E(X)$ is the expectation of X. Estimates of the isotropic shear modulus were assumed to be unbiased, which allowed one to replace $\big[G_{app} - E(G_{app})\big]$ by $\big[G_{app} - G\big]$.

Appendix B, following steps in [29], shows that $\left[G_{app} - G\right]$ can be written solely in terms of the shear stress, which is a function of the noise in the measured strain field and the virtual strain field: $f_G(\boldsymbol{\epsilon}_{no}, \boldsymbol{\epsilon}^*)$. The resulting equation for the variance in estimated shear moduli was written as:

$$V(G_{app}) = G^2 E\Big(f_G^2\big(\boldsymbol{\epsilon}_{no}, \boldsymbol{\epsilon}_G^*\big)\Big) \tag{5.20}$$

By expanding Equation (5.20) and assuming that noise in the displacement field, with standard deviation γ_u, has an unbiased (zero-centred) Gaussian distribution, it was shown that the final equation for variance in the estimated shear modulus was explicitly written as:

$$\begin{aligned} V(G_{app}) \propto \gamma_{\mathbf{u}}^2 \Delta V^2 \sum_{voxels \subset V} \Big[&\Big(\frac{1}{\Delta x^2}\Big)\Big(\boldsymbol{\epsilon}_{11}^* - \frac{1}{3}\mathrm{Tr}(\boldsymbol{\epsilon}^*)\Big)^2 \\ &+\Big(\frac{1}{\Delta y^2}\Big)\Big(\boldsymbol{\epsilon}_{22}^* - \frac{1}{3}\mathrm{Tr}(\boldsymbol{\epsilon}^*)\Big)^2 \\ &+\Big(\frac{1}{\Delta z^2}\Big)\Big(\boldsymbol{\epsilon}_{33}^* - \frac{1}{3}\mathrm{Tr}(\boldsymbol{\epsilon}^*)\Big)^2 \\ +\Big(\frac{4}{\Delta x^2} + \frac{4}{\Delta y^2}\Big)\boldsymbol{\epsilon}_{12}^{*2} + \Big(\frac{4}{\Delta x^2} + \frac{4}{\Delta z^2}\Big)\boldsymbol{\epsilon}_{13}^{*2} + \Big(\frac{4}{\Delta y^2} + \frac{4}{\Delta z^2}\Big)\boldsymbol{\epsilon}_{23}^{*2}\Big] \end{aligned} \tag{5.21}$$

where ΔV was the voxel volume, $\Delta x \cdot \Delta y \cdot \Delta z$. The step by step derivation of Equations (5.20) and (5.21) and their equivalence in the case of complex parameters can be found in Appendix B. The estimated parameter variance can also be written as:

$$V(G_{app}) = \gamma_{\mathbf{u}}^2 \mathbf{u}^{*T}[H]\mathbf{u}^* \tag{5.22}$$

where H is the matrix of derivatives used to compute Equation (5.21), dependent on the chosen material model and element shape functions. H is dependent on the material model as well as the chosen basis functions, but is independent from the measured displacement field. Then, an optimised virtual field was found such that Equation (5.21) was minimised while adhering to the specified constraints. Since H is positive-definite [10], the virtual displacement field vector is in fact the saddle point of the Lagrangian:

$$\mathcal{L} = \gamma^2 \mathbf{u}^{*T}[H]\mathbf{u}^* + \boldsymbol{\Lambda}^T([\mathrm{A}]\mathbf{u}^* - \mathbf{Z}) \tag{5.23}$$

$\boldsymbol{\Lambda}$ is a vector of Lagrangian multipliers, $\mathbf{Z}$ is a vector of right hand side constraint values and A is the matrix constructed from the following constraints (discussed in detail in Appendix B) in the presence of Gaussian noise:

- $f_K(\boldsymbol{\epsilon}, \boldsymbol{\epsilon}^*) + f_K(\boldsymbol{\epsilon}_{no}, \boldsymbol{\epsilon}^*) = 0$ (Equation (B.2))

- $f_G(\boldsymbol{\epsilon}, \boldsymbol{\epsilon}^*) + f_G(\boldsymbol{\epsilon}_{no}, \boldsymbol{\epsilon}^*) = 1$ (Equation (B.2))
- $\int_V \mathbf{u}_x^* dV = 0, \quad \int_V \mathbf{u}_y^* dV = 0, \quad \int_V \mathbf{u}_z^* dV = 0$ (Equation (B.9))
- $\mathbf{u}^*(\Omega) = 0$ (displacement on the boundaries is null)

Implementation of constraints is shown in greater detail in Appendix C. The virtual displacement field was obtained by solving the following linear system of equations:

$$\begin{bmatrix} [H] & [A]^T \\ [A] & [0] \end{bmatrix} \begin{Bmatrix} \mathbf{u}^* \\ \boldsymbol{\Lambda} \end{Bmatrix} = \begin{Bmatrix} \mathbf{0} \\ \mathbf{Z} \end{Bmatrix} \tag{5.24}$$

In [29], this method was applied to simulated harmonic displacements with added Gaussian noise as well as experimental MRE displacements from a gel cube. In the simulations, independent distributions of Gaussian noise were added to each displacement frame (8 frames in total) and the standard deviation of the noise added to the displacements was 0.2% of the loading amplitude. The first harmonic amplitude was extracted using a temporal Fourier analysis and the harmonic displacement field was interpolated at discrete time points (n = 50) over one harmonic cycle. If needed, spatial smoothing was applied (a subjective decision of the operator). Finally, a material map of the parameters was calculated over a moving volume of interest using the optimised VFM at each discrete time point. The number of voxels in each subregion was varied as well as the voxel size in order to determine the optimal region size for accurately determining heterogeneous material properties over the cube. The method was also extended to estimate viscoelastic parameters from time discretised harmonic displacements, including both a storage (G') and a loss (G'') modulus.

Findings When the relative error in the storage shear modulus, G', expressed as a percentage of the true shear modulus, was plotted against the number of voxels per wavelength (λ), Connesson et al. [29, 30] showed that approximately 5 voxels per wavelength resulted in a relative error of 10%. It was also shown that, as the displacement amplitude decreased along the length of the cube (due to material damping), the time-dependency (on n) increased. In addition, a bias appeared on the identified modulus. As the SNR decreased, the identified storage shear moduli converged to the acceleration noise, which was close to zero. It was also shown that using one individual frame would be insufficient to adequately identify the material parameters. A higher number of free nodes in the subregion allowed for better noise robustness. Additionally, a smaller number of free nodes increased time dependency.

The recommendations based on their findings were as follows: 1) images should be acquired to obtain at least 8 voxels per wavelength, 2) the mobile subregion should be chosen so that it is at least half of one wavelength, and 3) the most accurate identified material

parameters arose when the amplitude of the virtual displacement field was minimal. The conclusions for the identification of the loss shear modulus (G'') were mainly similar to those for the storage shear modulus except for 1) a lack of bias and 2) a greater relative error in the estimated moduli.

Sensitivity In this thesis, parameter sensitivity values (η) were also calculated [10] for various loading conditions. It can be seen from Equation (5.22) the the standard deviation of noise in the measured displacement field can can be factored out of the equation for estimated parameter variance. Generally, $V(G_{app})$ can be understood as the uncertainty in the identification procedure and $\gamma_{\boldsymbol{u}}$ as the uncertainty in the displacement measurements. Therefore, the variance is proportional to the displacement noise and can be written as:

$$V(G_{app}) = \gamma_u^2 \eta^2 \tag{5.25}$$

η, then, describes the sensitivity of the method to noise in the measured displacement field. Unlike sensitivity values discussed and reported in [117], low values of η are preferable since they indicate a low sensitivity of the method to noise.

5.2.2 Results

The optimised VFM was implemented with a cantilever beam geometry, experimental phantom MRE data as well as simulated harmonic displacements in a left ventricular (LV) model.

5.2.2.1 Beam Simulations

The beam model used for the analytic VFM (Figure 5.1) was also used to test the optimised VFM. With the same loading condition and in the absence of Gaussian noise, the estimated shear modulus and damping coefficient were precisely 4.0003 kPa and 0.1, respectively. Just as analytic virtual displacement fields that matched the pattern in the reference displacement fields led to accurate estimation of the shear modulus in Section 5.1, the optimised VFM naturally produces a virtual displacement field mimicking the wave pattern in the reference displacement field (Figure 5.10).

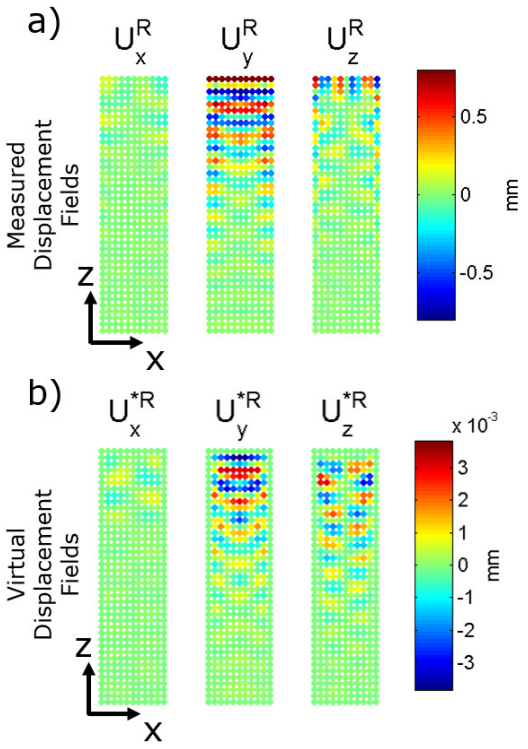

FIGURE 5.10: a) Ground truth displacement fields (x, y and z) and b) virtual displacement fields (x, y and z) from one slice through the beam (x-z plane).

Complex Displacements vs. Discretisation Previous studies discretised the complex displacement field into 50 time points [29, 30, 117] and noted the time dependence of the estimated shear moduli. However, in the studies mentioned, there were no comparisons between estimated shear moduli obtained from complex displacement fields and shear moduli estimated from time discretised displacement fields. Therefore, as a comparison, complex displacements were discretised at 20 time points, and the optimised VFM was used to estimate a shear modulus at each time point. These results were then compared with complex shear moduli estimated from a single complex displacement field.

Over the 20 discretised time points, shear moduli ranged between 3.02 kPa and 4.95 kPa, excluding two values. At n = 6 and n = 16, shear moduli were estimated to be -53.70 kPa. Likely reasons for this gross underestimation are discussed below. These points were not shown in Figure 5.11. Excluding these two time points, the mean estimated shear modulus was 3.963 kPa.

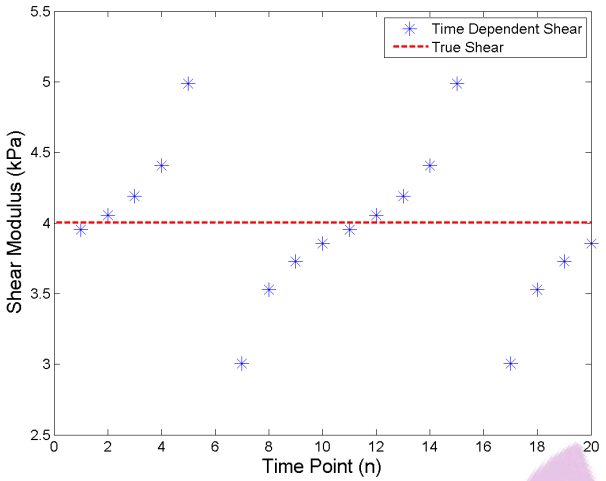

FIGURE 5.11: Shear moduli were calculated using the optimised VFM at 20 individual time points over one harmonic cycle for the beam model. Reference values are shown by red dotted lines..

Compared with the complex displacement method, estimates varied largely over one harmonic cycle. Using the optimised VFM with time discretised displacements returns the storage modulus and does not give information about material damping. Therefore, the viscoelastic time discretised method, presented in [29], was then implemented with the beam model in order to estimate the damping coefficient (G"/G'). The resulting estimated shear moduli and damping coefficients for 20 time points are shown in Figure 5.12.

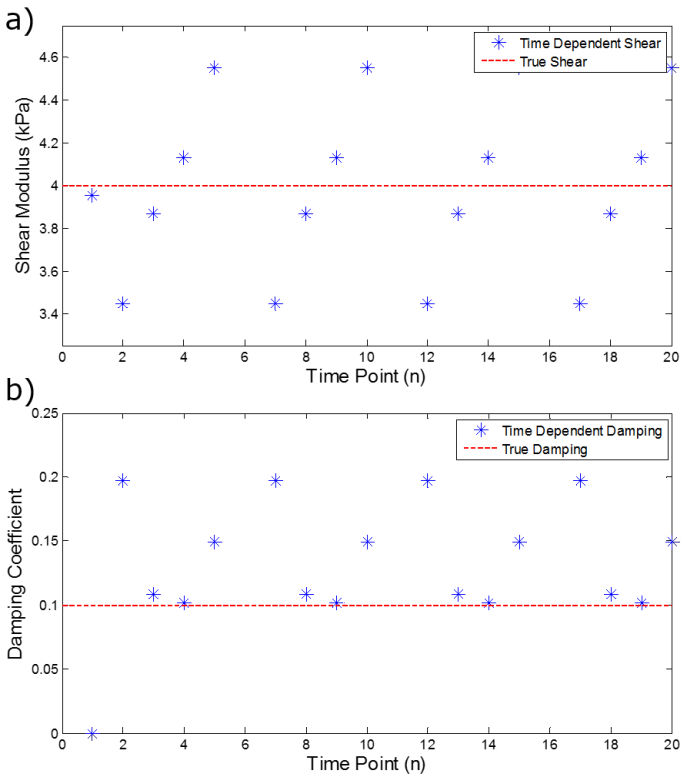

FIGURE 5.12: Shear moduli and viscoelastic damping coefficients were calculated using the optimised VFM at 20 time points over one harmonic cycle for the beam model. The red dotted lines indicate the ground truth parameters.

In the viscoelastic and time discretised method, large errors in the estimted shear moduli were seen at three time points (6, 11 and 16): G_6 = -2.719e15 kPa, G_{11} = -1.308e15 kPa and G_{16} = 5.729e15 kPa. These points were not shown in Figure 5.12. Likewise, estimated values of the structural damping coefficient also erred the most at time points 6, 11 and 16.

Connesson et al. [29] reported that estimated shear values erred the most when the displacement magnitudes at a given time point were close to zero. Therefore, box plots of both the real and imaginary components of displacement (containing all three orthogonal components) are shown in Figure 5.13. The real and imaginary components are used in the viscoelastic formulation. It is apparent that at time points 0, 6, 11 and 16, either the real or imaginary component of displacement is close to zero. The lack of displacement information resulted in incorrect estimates of the shear modulus and damping coefficient at these time points.

It should be noted that at time point n = 1, the amplitude of the imaginary component of the measured displacement field was precisely zero. Therefore, rather than obtaining large errors in estimated shear and damping coefficients, the imaginary component of the complex shear modulus was zero and the real component of the shear modulus was only dependent on the amplitude of the real displacements. When the three outlying values

were omitted from the viscoelastic time discretised method, the mean shear estimate of the remaining time points was 3.998 kPa. The mean damping coefficient was 0.113.

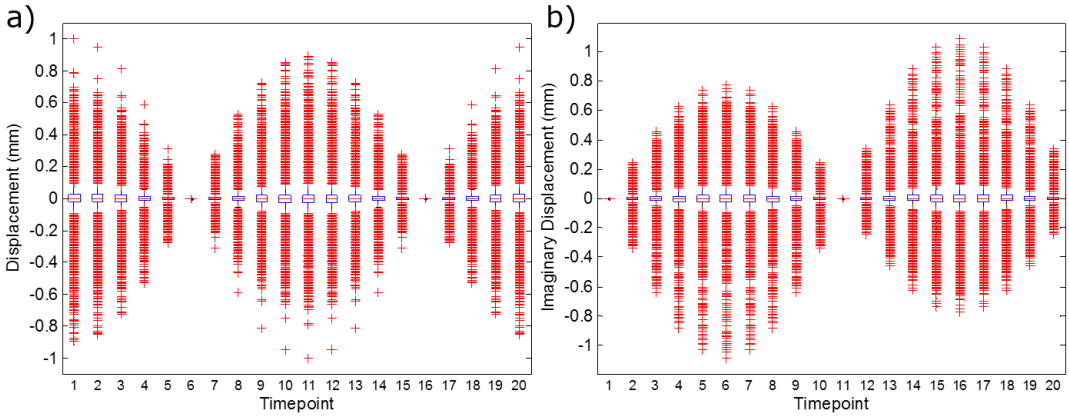

FIGURE 5.13: Boxplots of a) real and b) imaginary displacements at 20 time points.

For three reasons, the time discretised method was not pursued further. The time discetised method requires more computational resources than the method utilising complex displacement fields, since a value is estimated at each individual time point, rather than only once for the complex displacement method. Additionally, with the complex displacement method, a complex shear modulus is estimated, providing estimates of both the shear modulus and the structural damping coefficient in one step. Additionally, the complex optimised VFM resulted in a more accurate estimate of the shear modulus in this cantilever beam problem. Overall, the complex VFM was more accurate than the time discretised viscoelastic method and was less computationally expensive. From this point forward, only the complex VFM is investigated.

Beam Loading Test With the cantilever beam model, simulations were run in Abaqus 6.13 in order to examine the effects of the loading configuration and resulting wave propagation on isotropic shear estimation. Figure 5.14 shows the cantilever beam model highlighting three faces (top, side, end) upon which loads were prescribed. An x, y and/or z displacement was applied on either, one, two or all three faces. These combinations resulted in 511 loading configurations.

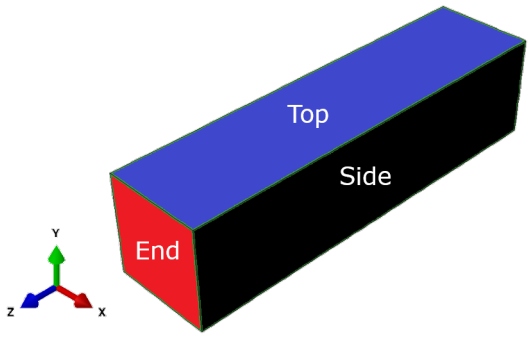

FIGURE 5.14: A cantilever beam FE model showing the end (red), top (blue) and side (black) faces.

The optimised VFM analysis, estimating a complex shear modulus, was run with each of the 511 reference displacement fields. The estimated shear moduli ranged between 4.0000 - 4.0004 kPa, with the ground truth value at 4.0003 kPa. Estimated damping coefficients ranged between 0.0999 - 0.1001, while the reference value was 0.1000. There were minimal differences in the estimated parameters due to the loading conditions. Both parameters were estimated within 0.1% of the true values for all simulations.

Figure 5.15 plots sensitivity values, normalised by the complex shear modulus and illustrates that not all loading conditions had equal sensitivity to noise. It is apparent that as η/G increased, the estimated parameters also diverged from the reference values. Additionally, when the loading configurations were ordered by sensitivity (data not shown), from least to greatest, it became apparent that the loading cases with an x-displacement applied on the top face and a y-displacement applied on the side face led to the lowest sensitivity to noise values.

A z-displacement on the end face did not result in low sensitivity values, which could be due to the geometry of the beam. For example, x- prescribed displacements on the top face of the beam induced a shear wave which was polarised in the x-direction and propagated in the y-direction. Similarly, y- prescribed displacements on the side face resulted in a shear wave which was polarised in the y-direction and propagated in the x-direction. Both the x- and y- dimensions of the beam are less than the z-dimension (50 mm versus 200 mm). The waves induced by these two loads do not damp out quickly since a) there is no pinned boundary condition on the faces opposite the loading and b) the dimensions of the beam are short enough that the waves do not have space to damp out. Conversely, a shear wave travelling along the length of the beam, induced by a z- prescribed displacement on the end face would damp out along the length of the beam, partially due to the length and partially due to the pinned boundary condition on the opposite face. One possible explanation is that the damping of the wave results in smaller displacements and, consequently, a higher sensitivity to noise.

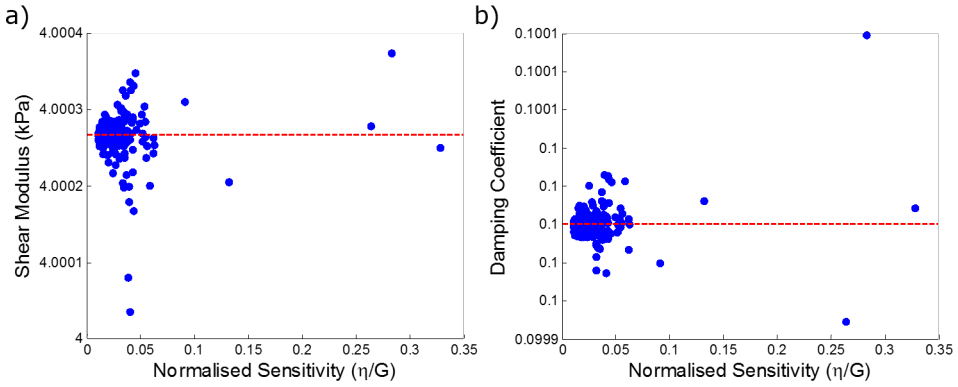

FIGURE 5.15: Estimated a) shear moduli and b) damping coefficients are plotted versus η/G for each of the 511 loading simulations.

Beam Loading Test with Gaussian Noise A Monte Carlo experiment was run (n = 10) in which random, independent sets of Gaussian noise, calculated according to Equation 5.11 (N = 15%), were added to the reference displacement fields for each loading condition. In total, 5,110 isotropic material parameter estimations were run, 10 for each loading configuration. Scatter plots of resulting estimated shear moduli and damping coefficients are shown in Figures 5.16 and 5.17, respectively.

A beam model is shown on the left of every row of scatter plots to illustrate the displacement boundary conditions applied on the side face (only). In each row of scatter plots, the loading on the side face is similar whereas the loads on the top and end faces differ along the row. Each scatter plot in Figure 5.16 and Figure 5.17 then contains results from 64 loading combinations where the boundary conditions differ on the end and top faces.

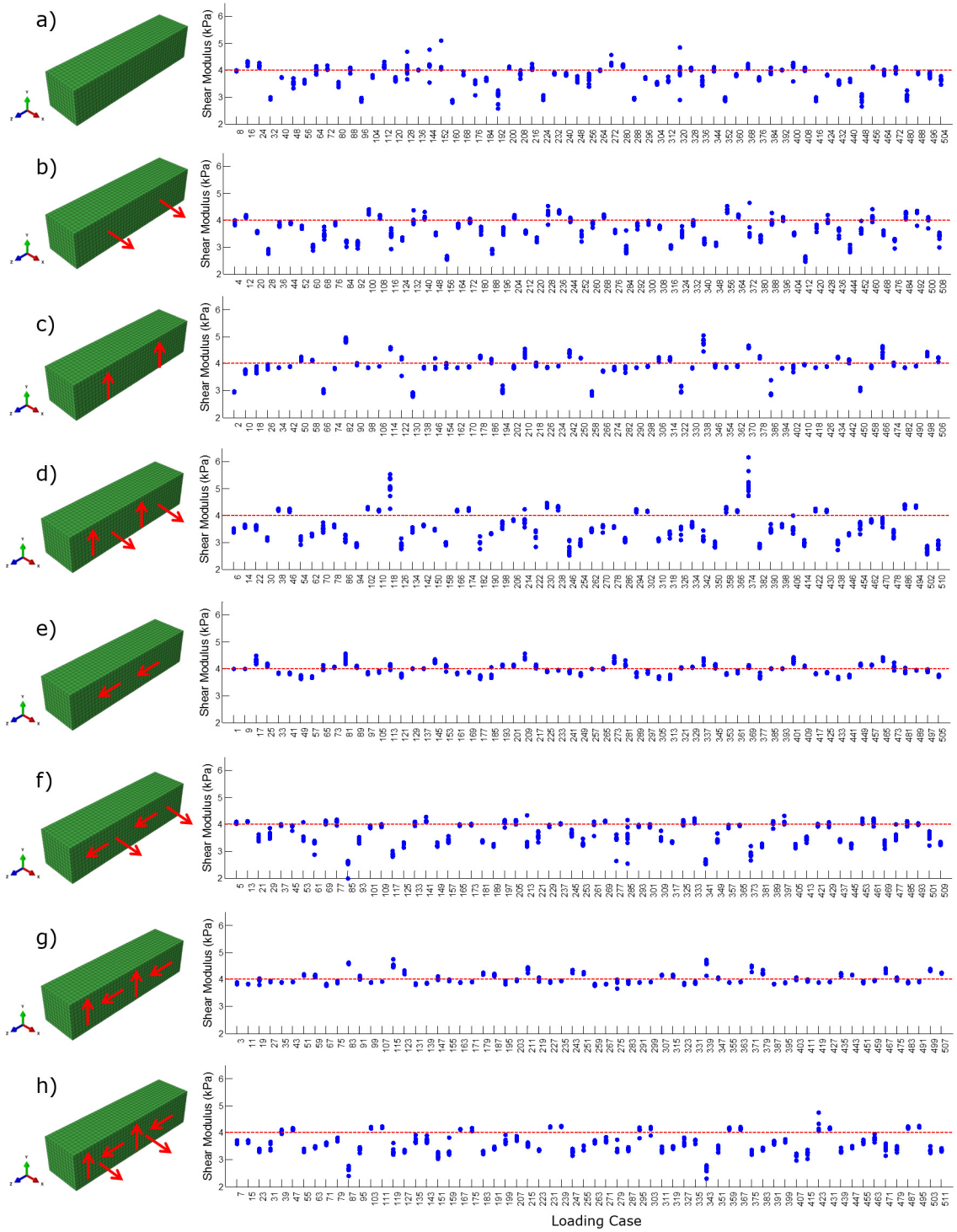

FIGURE 5.16: The eight scatter plots show the resulting estimated shear moduli from Monte Carlo simulations (n = 10) for all 511 loading cases. On the left hand side, a beam is shown with the loading applied to the side face which is common to all simulations in the corresponding row of scatter plots. Red lines represent the ground truth shear modulus (4.0003 kPa).

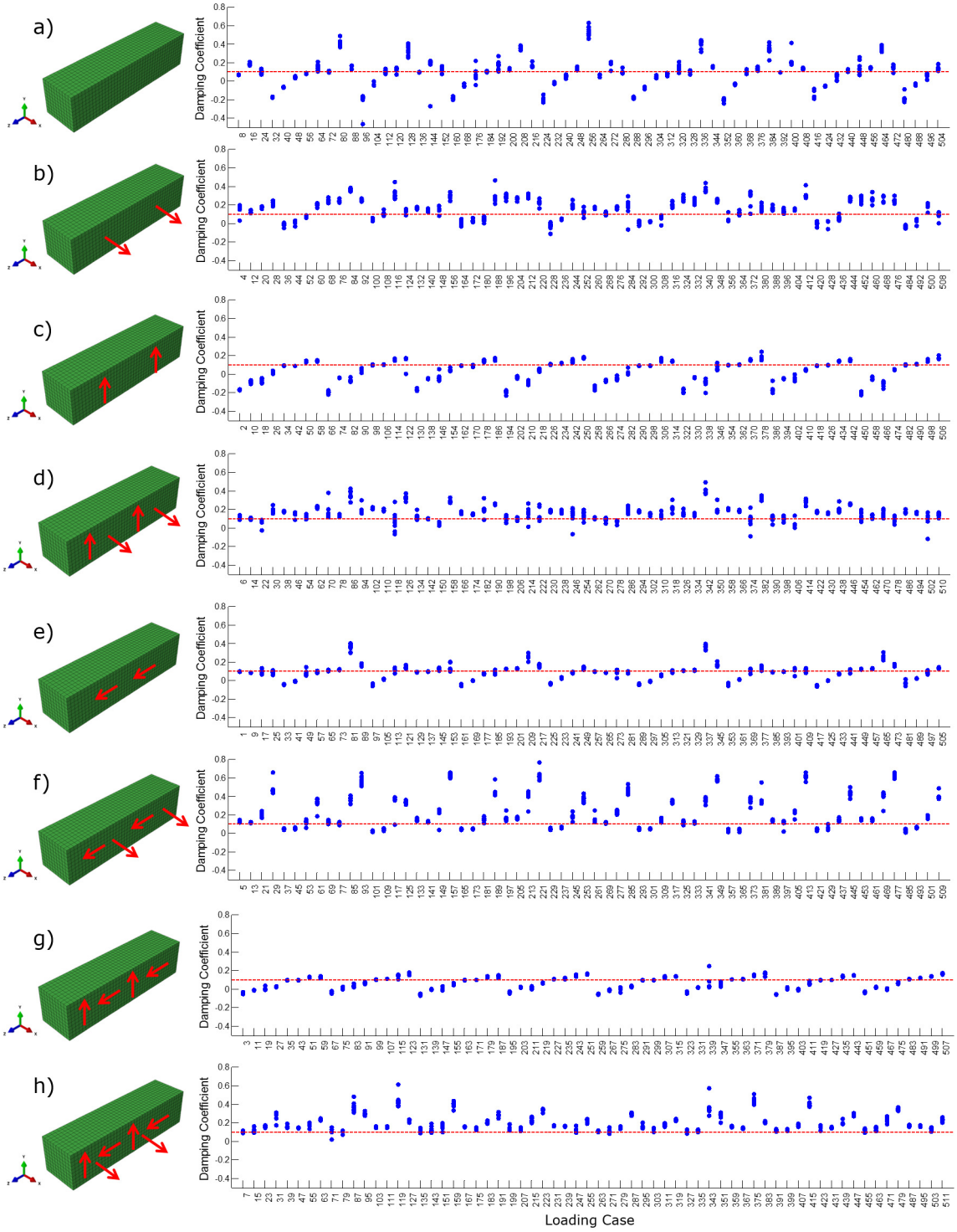

FIGURE 5.17: The eight scatter plots show the resulting estimated damping coefficients from Monte Carlo simulations (n = 10) for all 511 loading cases. On the left hand side, a beam is shown with the loading applied to the side face which is common to all simulations in the corresponding row of scatter plots. Red lines represent the ground truth damping coefficient (0.1 kPa).

The results illustrate that, in the presence of Gaussian noise, the accurate estimation of both the shear modulus and the damping coefficient in this beam model is highly dependent on the loading applied. For 438 out of 511 loading configurations, the standard deviations of estimated shear moduli were very small ($<$ 0.1 kPa). Similarly, more than half of all simulations resulted in standard deviations of estimated damping coefficients below 0.01. However, the addition of Gaussian noise did not have a uniform effect on all simulations. Depending on the wave field present, the inclusion of noise in the signal caused an offset of the estimated shear modulus from the reference values. For some loading configurations, this offset remained minimal. However for others, the shear modulus was underestimated by up to 37%.

The loading configurations that resulted in the lowest sensitivity (η/G) values did not necessarily result in the simulations with estimated shear moduli closest to the reference value (Figure 5.18). The simulations with lowest sensitivity resulted in mean estimated shear moduli which were offset slightly from the reference value. However, a general trend can be seen that as the sensitivity values increased, the mean estimated shear modulus diverged from the reference value and was often underestimated. Conversely, as the parameter sensitivity to noise increased, mean values of estimated damping coefficients were often overestimated.

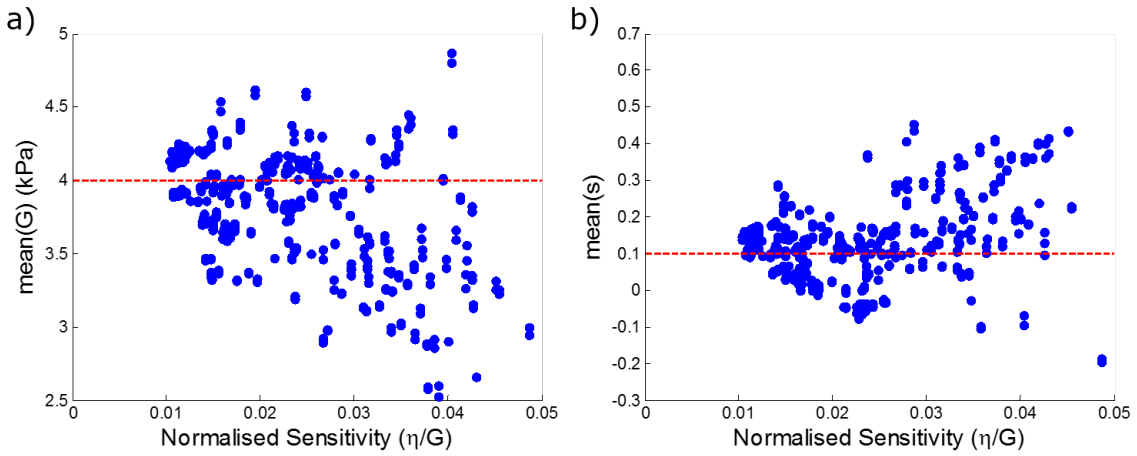

FIGURE 5.18: Mean estimated a) shear moduli and b) damping coefficients for all 511 loading configurations with added Gaussian noise are plotted versus normalised sensitivity values. Reference values are shown by red dotted lines.

Conversely, in Figure 5.19, it can be seen that the simulations with low sensitivity values resulted in the lowest standard deviations of estimated values in the Monte Carlo experiment. Therefore, if a loading configuration is chosen that has a low sensitivity value, it will not necessarily ensure accuracy of estimated parameters in the presence of noise using the optimised VFM, but it is likely to result in estimated values with small variance.

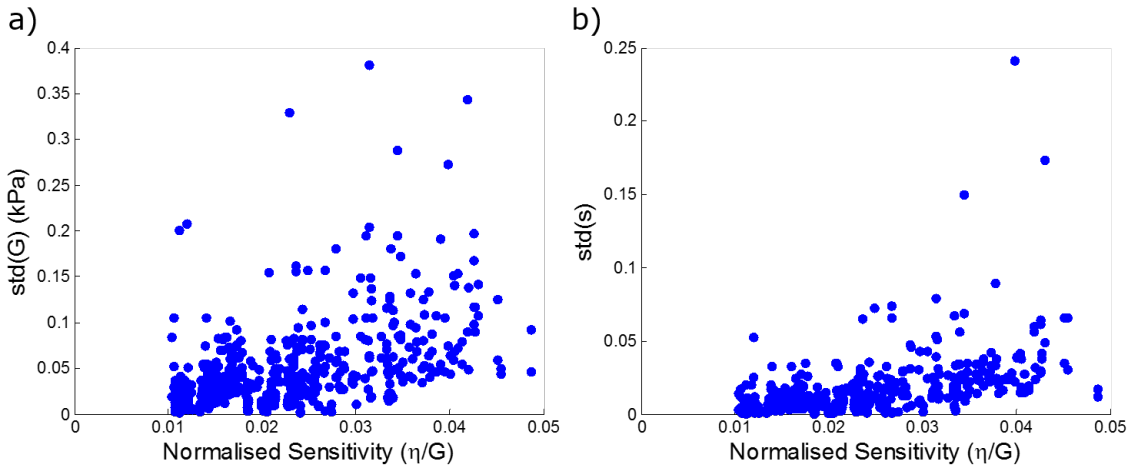

FIGURE 5.19: Standard deviations of estimated a) shear moduli and b) damping coefficients for all 511 loading configurations with added Gaussian noise are plotted versus normalised sensitivity values.

5.2.2.2 Isotropic Phantom MRE

The optimised VFM was used to estimate the shear modulus of the isotropic phantom from the experimental MRE displacements. When all nodes from the phantom mesh were included in the optimised VFM estimation, the resulting shear modulus and damping coefficient were: 5.41 kPa and 0.073, respectively. The shear moduli estimated with FEMU, MMDI and DF-LFE methods were 5.55 kPa, 5.45 kPa and 5.34 kPa, respectively. The shear modulus was also calculated for non-overlapping subzones comprised of three node layers. The phantom finite element model was composed of repeating disc-shaped node layers so each subzone was uniform in size and number of nodes. The mean shear modulus estimated using subzones was 5.32 kPa and the estimated damping coefficient was 0.07. All shear moduli estimated for all subzones ranged between 5.04 - 5.49 kPa. Figure 5.20 illustrates estimated shear moduli and damping coefficients for all subzones.

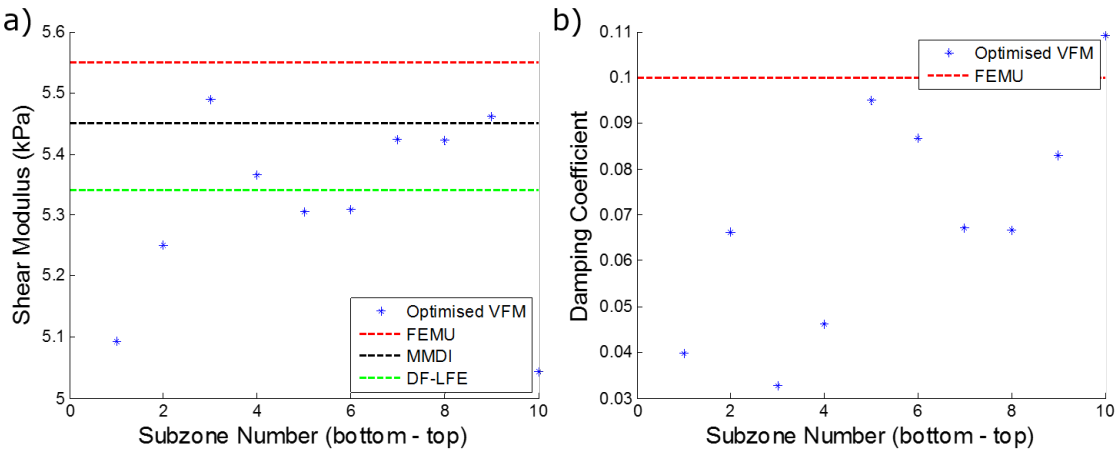

FIGURE 5.20: Estimated a) shear moduli and b) damping coefficients for each non-overlapping subzone (bottom to top) in the cylindrical phantom. Each subzone consists of three node layers. Shear moduli estimated using the MMDI, FEMU and DF-LFE methods are shown for comparison.

Sensitivity values were evaluated for each subzone of the phantom and ranged between 20.6 - 30.5. There was no observed relationship between the sensitivity value for each subzone and the relative accuracy of the shear parameter estimation.

5.2.2.3 Left Ventricle Simulations

Simulations of steady-state harmonic motion were performed in an anatomically realistic canine left ventricular geometry. An isotropic Young's modulus of 8.0 kPa [31] was assigned to the model and the Poisson's ratio was set to 0.4999 since myocardium is nearly incompressible. The corresponding reference shear modulus was, therefore, 2.667 kPa. A structural damping coefficient of 0.1 was applied to obtain realistic dissipation of energy. Following a similar procedure as that for the beam model, 63 different loading configurations were tested to determine the effect of different wave patterns on the identification of the shear modulus and damping coefficient. Loads in the form of nodal displacements were prescribed on the anterior and apical surfaces in the x, y and/or z directions. Anterior surface and apical node sets are shown in Figure 5.21

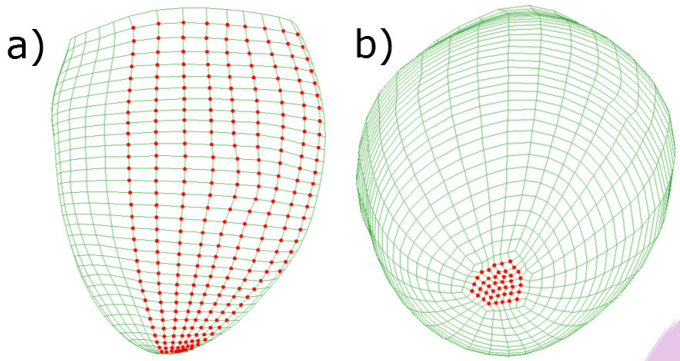

FIGURE 5.21: LV reference model with a) anterior surface and b) apical node sets highlighted

Without Gaussian noise added to the reference displacements, estimated shear moduli ranged between 2.666 - 2.671 kPa and estimated damping coefficients ranged between 0.099 - 0.101. Therefore, all estimated values were close to the reference parameters. Sensitivity values from all 63 LV simulations, normalised by the complex shear modulus, are plotted in Figure 5.22. Generally, sensitivity values were (approximately 3x) larger in the LV model than in the cantilever beam.

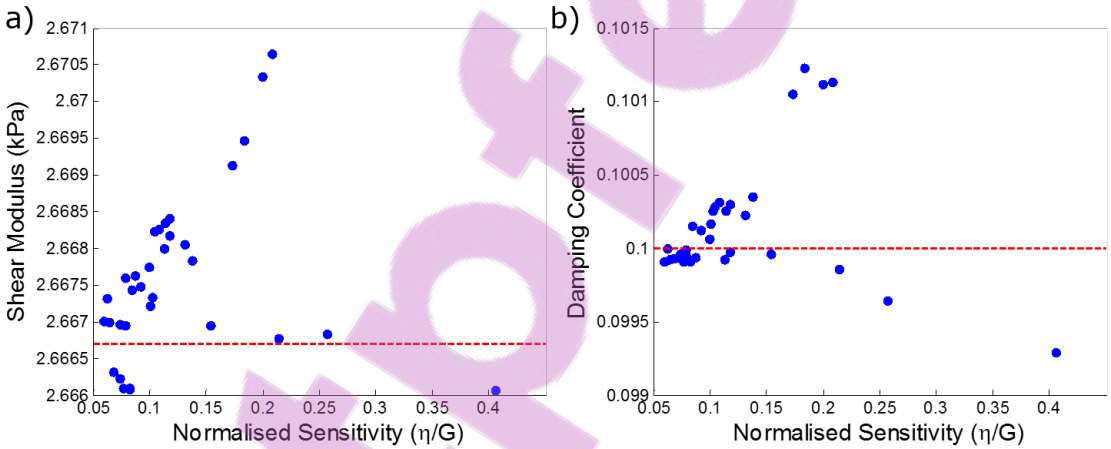

FIGURE 5.22: Scatter plots of estimated a) shear moduli and b) damping coefficients plotted versus normalised parameter sensitivity values for all 63 loading configurations. Red lines correspond to reference values for the shear modulus (4.0003 kPa) and damping coefficient (0.1).

Gaussian noise ($\sigma_N = 15\% \cdot \sigma_{disp}$) was added to the reference displacements for all 63 loading configurations and 10 simulations were run. Scatter plots of the resulting estimated shear moduli and damping coefficients are shown in Figure 5.23.

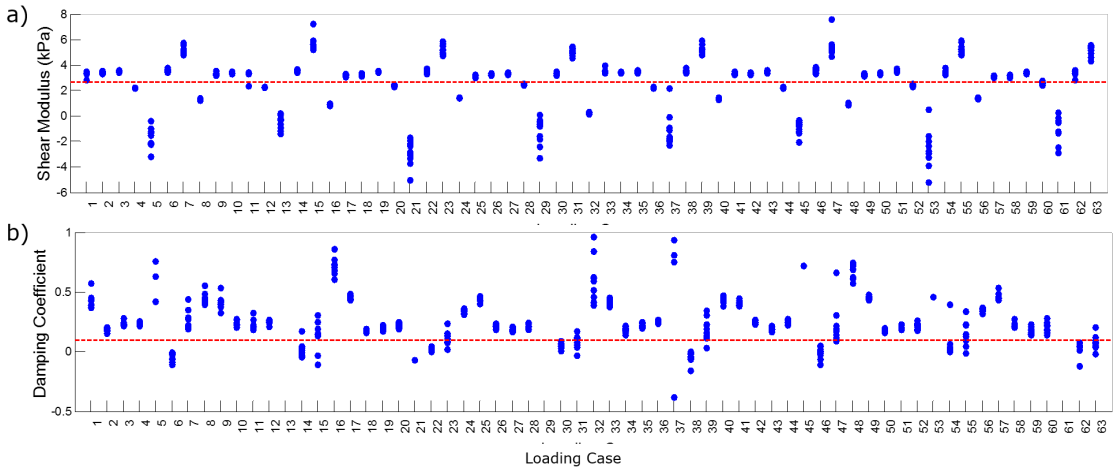

FIGURE 5.23: Estimated a) shear moduli and b) damping coefficients from simulated harmonic displacements in an LV model with 63 different loading configurations. 15% Gaussian noise was added to the reference displacements. Reference values are shown by red dotted lines.

It is apparent that, with the addition of noise, the estimated shear moduli, generally, had means which were offset from the reference value but showed small standard deviations. Simulation numbers 4, 12, 20, 28, 36, 44, 52 and 60 resulted in the most accurate mean estimated shear values (error $< 16\%$). The simulations that resulted in the most accurate estimates of the shear modulus had one loading condition in common: an x-displacement applied to the anterior face. Interestingly, when displacements were prescribed in the x-, y- and z-directions on the anterior face, the shear modulus was always overestimated by nearly 200% (in the presence of Gaussian noise). It can be concluded that inducing a displacement field with a complex set of waves does not necessarily improve the estimation of an isotropic shear modulus using the isotropic optimised VFM with a complex geometry such as the LV. At some loading configurations, estimated damping coefficients exhibited large variances. Overall, the results showed a clear dependence of accurate estimation of shear moduli and damping coefficients on the loading condition applied using this method.

Like the beam experiment, the loading configurations that resulted in the lowest sensitivity (η/G) values did not necessarily correspond to the simulations with the most accurate estimated shear moduli (Figure 5.24). Conversely, in Figure 5.25, it is apparent that as η/G increased, the standard deviation of estimated parameters also increased.

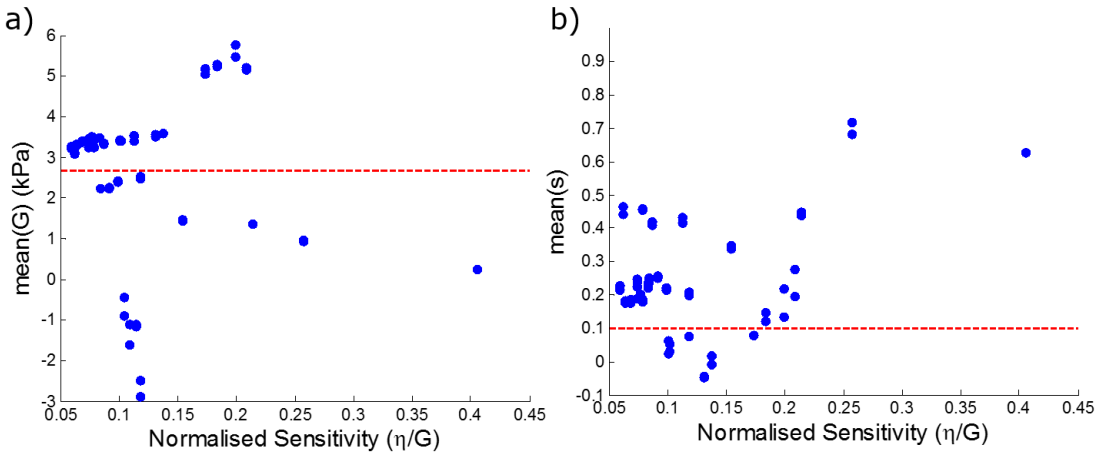

FIGURE 5.24: Mean estimated a) shear moduli and b) damping coefficients for all 63 loading configurations with added Gaussian noise are plotted versus normalised sensitivity values. Red lines correspond to reference values for the shear modulus (4.0003 kPa) and damping coefficient (0.1).

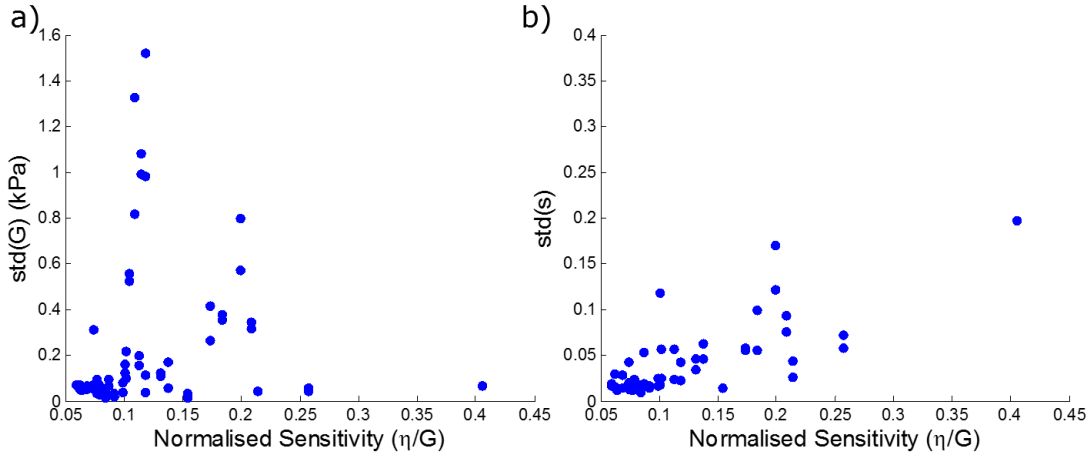

FIGURE 5.25: Standard deviations of estimated a) shear moduli and b) damping coefficients for all 63 loading configurations with added Gaussian noise are plotted versus normalised sensitivity values.

To further test the idea that loading configurations with lower sensitivity values are less sensitive to noise, two loading configurations (#58 and #60) were chosen and a Monte Carlo simulation (n = 3300) was run in which varying amounts of noise (N = 15% - 50%) were added to the reference displacements. Loading case #60 was chosen since it resulted in the most accurate estimation of the shear modulus when 15% Gaussian noise was added to the reference displacements and loading case #58 was chosen since it resulted in the lowest parameter sensitivity to noise. Results for loading case #60 are shown in Figure 5.26 and results for #58 are shown in Figure 5.27.

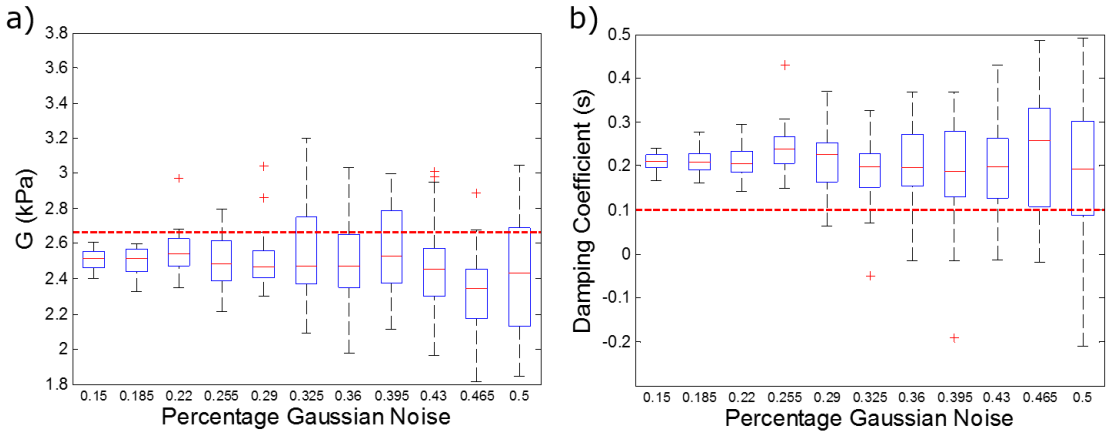

FIGURE 5.26: Estimated a) shear moduli and b) damping coefficients from simulated harmonic displacements in an LV model with varying amounts of Gaussian noise added to the reference displacements (for loading case #60). Reference values are shown by red dotted lines.

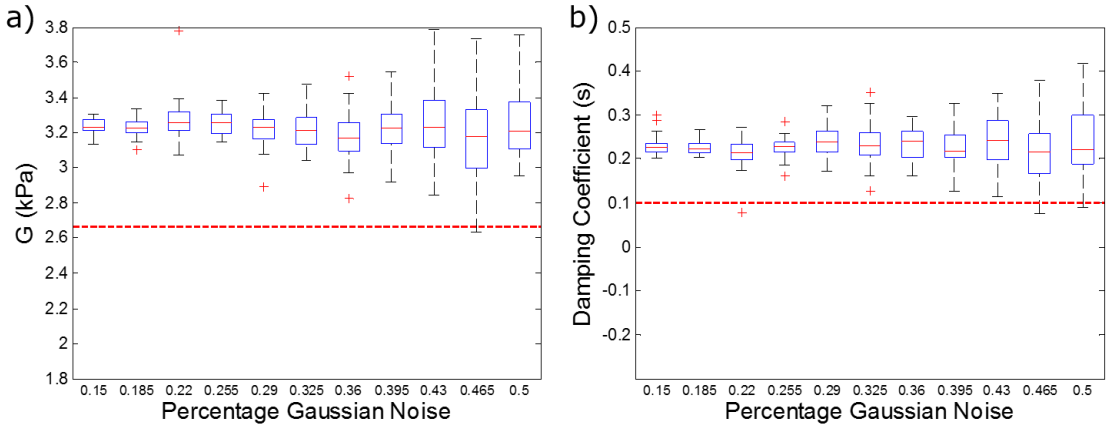

FIGURE 5.27: Estimated a) shear moduli and b) damping coefficients from simulated harmonic displacements in an LV model with varying amounts of Gaussian noise added to the reference displacements (for loading case #58). Reference values are shown by red dotted lines.

Simulations for loading case #60 resulted in shear moduli which were slightly underestimated whereas shear moduli for loading case #58 were overestimated. The damping coefficient was consistently overestimated for both simulations. The standard deviations, calculated over the 30 Monte Carlo runs for each amount of Gaussian noise, were plotted versus the amount of added Gaussian noise in Figure 5.28. Plots are shown with linear regression fits. The standard deviation of estimated shear moduli and damping coefficients increased linearly as the amount of Gaussian noise increased. It is apparent that the standard deviation in estimated values increased at a slower rate for case #58 than for case #60 with increasing amounts of Gaussian noise. This result was expected since case #58 resulted in a lower sensitivity value.

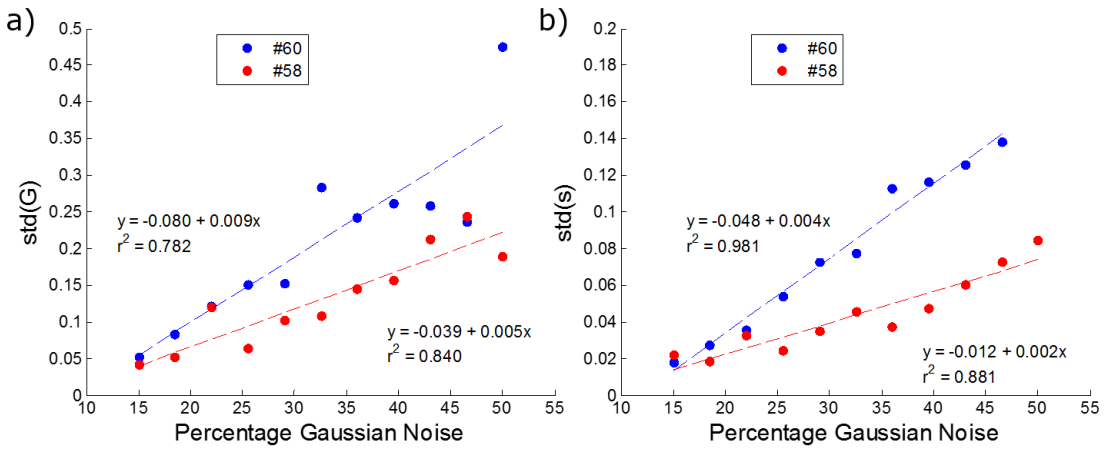

FIGURE 5.28: Standard deviation of estimated a) shear moduli and b) damping coefficients from simulated harmonic displacements in two LV loading conditions (#60, #58) versus the percent Gaussian noise added to the reference displacements.

The LV results with added Gaussian noise differed somewhat from those seen in the cantilever beam model. Each of the 63 loading cases with 15% Gaussian noise added to the reference displacements either over- or underestimated both the shear modulus and damping coefficient. For the LV, no loading condition resulted in precisely accurate material properties. This could be due to effects of the irregular geometry on the wave propagation. Additionally, in the LV model, there were fewer unconstrained nodes with which to estimate the wavelength than there were in the beam model, which may have led to bias in the estimation of both the shear modulus and the damping coefficient since it was previously shown that parameter estimates improved as the number of free nodes increased [29].

5.3 Discussion

In this chapter, the isotropic VFM was developed for use with analytic as well as numerically derived optimised virtual displacement fields. The method addresses the three primary disadvantages of the boundary value FEMU method, as outlined in Chapter 4:

- It is a direct method (computationally inexpensive)
- All data points are weighted equally
- The method bypasses the need to estimate the longitudinal wavelength by using specialised constraints on the virtual displacement field ($f_K = 0$)

There are numerous inversion methods, which were discussed in Chapter 2, to estimate isotropic material properties directly (e.g. direct inversion, LFE, etc.). These methods primarily assume that the tissue is incompressible. Additionally, the optimised VFM is advantageous over direct inversion since it does not require computation of high order

derivatives of the measured displacement field. Compared with LFE, the optimised VFM returns a complex shear modulus. The development of an optimised virtual displacement field which minimises the variance in the estimated shear modulus also provides motivation for the development of this method since phase contrast MRI images which encode elastography displacement fields are inherently noisy.

It was shown in both the cantilever beam and LV geometric models that, even in the isotropic case, accurate estimation of a complex shear modulus in the presence of Gaussian noise is dependent on the loading condition applied. Using the optimised VFM, not all loading conditions were equally sensitive to the addition of Gaussian noise. Using this information along with the sensitivity values could help to guide the placement of drivers in clinical MRE scans to enable the most reliable stiffness estimates.

Compared to the previous implementation of the optimised VFM [29], this study implemented a formulation in which a complex shear modulus was estimated by using a complex displacement field as the input. In a simple cantilever beam model, the complex results were more accurate than those measured for time harmonic displacement fields, which were largely dependent on the time point in the harmonic cycle. Additionally, since the complex form only requires one direct solve, it was more computationally efficient than the time discretised method.

One potential disadvantage of the method used is the constraint to set boundary node virtual displacements to zero. Although this greatly simplifies the equation for the principle of virtual work, it also, particularly in the LV model, reduces the number of free nodes with which to define the virtual displacement field. It was shown in [29] that accuracy of the parameter estimate in a subregion was largely dependent on the number of free nodes within that region. Therefore, to utilise the the boundary constraint, a higher spatial resolution is needed in order to not lose accuracy.

One large disadvantage of this method was the offset in estimated parameter values seen in both the cantilever beam and LV models when Gaussian noise was added to the reference displacement fields. The magnitude and direction of the offsets were not predicted by the sensitivity values and were only dependent on the loading configuration (see Figures 5.16, 5.17 and 5.23). As the amount of noise increased, the offset remained stationary (see Figures 5.26 and 5.27). These results differ from those presented in [29] in which the estimated storage modulus diverged from the true value as the amount of Gaussian noise increased. At low levels of noise, there was no offset observed. Additionally, the storage modulus was always underestimated whereas in this study, depending on the loading configuration, the shear modulus was either over- or underestimated. Numerous tests were done in an attempt to explain this offset including investigating two methods of adding Gaussian noise to the displacements, both directly onto the complex displacement field and onto the discretised ”phase offset” displacement fields. Additionally, various forms of the optimisation matrix,

H, were also tested. However, the offset was observed in all tests when Gaussian noise was added. In [29], displacements were spatially smoothed using a Gaussian filter prior to analysis using the optimised VFM. In this study, no spatial smoothing was performed. Additional smoothing may have resulted in smaller, or non-existent, offsets in the estimated shear moduli and damping coefficients in the presence of Gaussian noise. In the formulation of Equation (5.21), an assumption of unbiased measurements was made in order to simplify the equation for parameter variance: $\big[G_{app} - E(G_{app})\big] = \big[G_{app} - G\big]$. However, the offsets observed in the presence of noise indicate that this assumption may not be valid.

Despite this, the optimised VFM accurately estimated the shear modulus (5.41 kPa) from the MRE phantom data which is inherently noisy when compared to values estimated using three other common inversion methods: FEMU (5.45 kPa), MMDI (5.55 kPa) and DF-LFE (5.34 kPa), providing some confidence in the method. This method was subsequently used as a building block to develop the optimised VFM to estimate anisotropic material properties from MRE data.

6

Anisotropic Optimised Virtual Fields Method

Aspects of this chapter have been published in:

1. Miller R, Kolipaka A, Nash MP, Young AA. Estimating transversely isotropic material parameters from MR elastography using optimised virtual fields. In: Proceedings of 5th International Conference on Computation and Mathematical Biomedical Engineering. Pittsburgh; 2017.

2. Miller R, Kolipaka A, Nash MP, Young AA. Identification of transversely isotropic properties from magnetic resonance elastography using the optimised virtual fields method. In: Functional Imaging and Modeling of the Heart. 2017. p. 421431.

The isotropic optimised virtual fields method, discussed in the Chapter 5, was developed further to estimate transversely isotropic material parameters in simulated harmonic displacements as well as MRE data from an isotropic phantom. Two material models were implemented with the optimised VFM, one which estimated all five independent parameters of the elasticity matrix and one which estimated three parameters, thereby eliminating the need to estimate the longitudinal wavelength, which is dependent on Poisson's ratio. Similarly to results from the previous chapter, the accurate estimation of transversely isotropic parameters was shown to be highly dependent on the applied loading. Transversely isotropic parameters were estimated in the phantom data with two arbitrarily assigned material orientations. In the left ventricular (LV) and cantilever beam models, parameters were estimated from simulated displacement fields. The impact of varying loading conditions, initial parameter estimates and loading frequency were investigated.

6.1 Formulation and Implementation

Like the isotropic VFM, the anisotropic VFM also utilises the principle of virtual work in order to solve for the material properties from a st of full-field displacements (or strains):

$$-\int_V \boldsymbol{\sigma} : \boldsymbol{\epsilon}^* dV + \int_S \mathbf{T} \cdot \mathbf{u}^* dS + \int_V \mathbf{b} \cdot \mathbf{u}^* dV = \int_V \rho \mathbf{a} \cdot \mathbf{u}^* dV \tag{6.1}$$

There are an infinite number of complex-valued virtual displacement fields ($\mathbf{u}^*$) which satisfy the principle of virtual work in Equation (6.1). In the optimised VFM, the optimal virtual displacement field is calculated numerically by finding the field which minimises an objective function while satisfying a number of prescribed constraints. To simplify the problem, the virtual displacement field was set to zero on the boundaries, eliminating the boundary traction term ($\int_S \mathbf{T} \cdot \mathbf{u}^* dS$) and providing the first constraint. Body forces ($\mathbf{b}$) were assumed to be negligible and the forcing frequency was assumed to be the same as the resulting displacement frequency. Thus, Equation (6.1) was simplified to:

$$-\int_V \boldsymbol{\sigma} : \boldsymbol{\epsilon}^* dV = \int_V \rho \omega^2 \mathbf{u} \cdot \mathbf{u}^* dV \tag{6.2}$$

where $\boldsymbol{\sigma}$ is the internal stress, $\boldsymbol{\epsilon}^*$ is the virtual strain field, ρ is the material density, ω is the loading frequency and $\mathbf{u}^*$ is the virtual displacement field. Therefore, Equation (6.1) relies on four quantities: the internal stress field (which depends on the unknown material parameters), density, frequency of excitation and the resulting displacement field.

6.1.1 Five Parameter Model

The internal stress term was expanded to introduce terms of the symmetric elasticity matrix.

$$\begin{aligned}\int_V \boldsymbol{\sigma} : \boldsymbol{\epsilon}^* dV = \int_V \big(& C_{11}\boldsymbol{\epsilon}_{11}\boldsymbol{\epsilon}_{11}^* + C_{22}\boldsymbol{\epsilon}_{22}\boldsymbol{\epsilon}_{22}^* + C_{12}\boldsymbol{\epsilon}_{22}\boldsymbol{\epsilon}_{11}^* + C_{12}\boldsymbol{\epsilon}_{11}\boldsymbol{\epsilon}_{22}^* + \\ & C_{13}\boldsymbol{\epsilon}_{33}\boldsymbol{\epsilon}_{11}^* + C_{13}\boldsymbol{\epsilon}_{11}\boldsymbol{\epsilon}_{33}^* + C_{23}\boldsymbol{\epsilon}_{33}\boldsymbol{\epsilon}_{22}^* + C_{23}\boldsymbol{\epsilon}_{22}\boldsymbol{\epsilon}_{33}^* + C_{33}\boldsymbol{\epsilon}_{33}\boldsymbol{\epsilon}_{33}^* + \\ & 2C_{44}\boldsymbol{\epsilon}_{12}\boldsymbol{\epsilon}_{12}^* + 2C_{55}\boldsymbol{\epsilon}_{13}\boldsymbol{\epsilon}_{13}^* + 2C_{66}\boldsymbol{\epsilon}_{23}\boldsymbol{\epsilon}_{23}^* \big) dV\end{aligned} \tag{6.3}$$

Using equalities for a transversely isotropic material, with the preferred direction oriented in the C_{33} direction, and a modified Voigt notation: $C_{11} = C_{22}$, $C_{12} = C_{11} - 2C_{44}$, $C_{13} = C_{23}$ and $C_{55} = C_{66}$. Grouping terms with similar material constants, Equation (6.3) was substituted into Equation (6.2) to give:

$$\begin{aligned}C_{11}f_{C_{11}}(\boldsymbol{\epsilon}, \boldsymbol{\epsilon}^*) + C_{33}f_{C_{33}}(\boldsymbol{\epsilon}, \boldsymbol{\epsilon}^*) + C_{44}f_{C_{44}}(\boldsymbol{\epsilon}, \boldsymbol{\epsilon}^*) + C_{66}f_{C_{66}}(\boldsymbol{\epsilon}, \boldsymbol{\epsilon}^*) + C_{13}f_{C_{13}}(\boldsymbol{\epsilon}, \boldsymbol{\epsilon}^*) \\ = \int_V \rho \omega^2 \mathbf{u} \cdot \mathbf{u}^* dV\end{aligned} \tag{6.4}$$

where the functions $f_{C_{11}}$, $f_{C_{33}}$, $f_{C_{44}}$, $f_{C_{66}}$ and $f_{C_{13}}$ are linear functions of the strain fields and can be written explicitly as:

$$
\begin{aligned}
f_{C_{11}}(\boldsymbol{\epsilon}, \boldsymbol{\epsilon}^*) &= \int_V (\boldsymbol{\epsilon}_{11}\boldsymbol{\epsilon}^*_{11} + \boldsymbol{\epsilon}_{22}\boldsymbol{\epsilon}^*_{22} + \boldsymbol{\epsilon}_{22}\boldsymbol{\epsilon}^*_{11} + \boldsymbol{\epsilon}_{11}\boldsymbol{\epsilon}^*_{22})dV \\
f_{C_{33}}(\boldsymbol{\epsilon}, \boldsymbol{\epsilon}^*) &= \int_V \boldsymbol{\epsilon}_{33}\boldsymbol{\epsilon}^*_{33}dV \\
f_{C_{44}}(\boldsymbol{\epsilon}, \boldsymbol{\epsilon}^*) &= \int_V (\boldsymbol{\epsilon}_{12}\boldsymbol{\epsilon}^*_{12} - 2\boldsymbol{\epsilon}_{22}\boldsymbol{\epsilon}^*_{11} - 2\boldsymbol{\epsilon}_{11}\boldsymbol{\epsilon}^*_{22})dV \\
f_{C_{66}}(\boldsymbol{\epsilon}, \boldsymbol{\epsilon}^*) &= \int_V (\boldsymbol{\epsilon}_{13}\boldsymbol{\epsilon}^*_{13} + \boldsymbol{\epsilon}_{23}\boldsymbol{\epsilon}^*_{23})dV \\
f_{C_{13}}(\boldsymbol{\epsilon}, \boldsymbol{\epsilon}^*) &= \int_V (\boldsymbol{\epsilon}_{33}\boldsymbol{\epsilon}^*_{11} + \boldsymbol{\epsilon}_{33}\boldsymbol{\epsilon}^*_{22} + \boldsymbol{\epsilon}_{11}\boldsymbol{\epsilon}^*_{33} + \boldsymbol{\epsilon}_{22}\boldsymbol{\epsilon}^*_{33})dV
\end{aligned}
\tag{6.5}
$$

In the VFM, a different virtual displacement field is required to solve for each unknown material parameter. Thus, for five parameters, five separate virtual displacement fields, noted by the superscripts 1-5 (e.g. $\mathbf{u}^{*1}$), are required to solve for the five unknown material parameters: C_{11}, C_{33}, C_{44}, C_{66} and C_{13}. The resulting system of equations is:

$$
\begin{bmatrix}
f_{C_{11}}(\boldsymbol{\epsilon}, \boldsymbol{\epsilon}^{*1}) & f_{C_{33}}(\boldsymbol{\epsilon}, \boldsymbol{\epsilon}^{*1}) & f_{C_{44}}(\boldsymbol{\epsilon}, \boldsymbol{\epsilon}^{*1}) & f_{C_{66}}(\boldsymbol{\epsilon}, \boldsymbol{\epsilon}^{*1}) & f_{C_{13}}(\boldsymbol{\epsilon}, \boldsymbol{\epsilon}^{*1}) \\
f_{C_{11}}(\boldsymbol{\epsilon}, \boldsymbol{\epsilon}^{*2}) & f_{C_{33}}(\boldsymbol{\epsilon}, \boldsymbol{\epsilon}^{*2}) & f_{C_{44}}(\boldsymbol{\epsilon}, \boldsymbol{\epsilon}^{*2}) & f_{C_{66}}(\boldsymbol{\epsilon}, \boldsymbol{\epsilon}^{*2}) & f_{C_{13}}(\boldsymbol{\epsilon}, \boldsymbol{\epsilon}^{*2}) \\
f_{C_{11}}(\boldsymbol{\epsilon}, \boldsymbol{\epsilon}^{*3}) & f_{C_{33}}(\boldsymbol{\epsilon}, \boldsymbol{\epsilon}^{*3}) & f_{C_{44}}(\boldsymbol{\epsilon}, \boldsymbol{\epsilon}^{*3}) & f_{C_{66}}(\boldsymbol{\epsilon}, \boldsymbol{\epsilon}^{*3}) & f_{C_{13}}(\boldsymbol{\epsilon}, \boldsymbol{\epsilon}^{*3}) \\
f_{C_{11}}(\boldsymbol{\epsilon}, \boldsymbol{\epsilon}^{*4}) & f_{C_{33}}(\boldsymbol{\epsilon}, \boldsymbol{\epsilon}^{*4}) & f_{C_{44}}(\boldsymbol{\epsilon}, \boldsymbol{\epsilon}^{*4}) & f_{C_{66}}(\boldsymbol{\epsilon}, \boldsymbol{\epsilon}^{*4}) & f_{C_{13}}(\boldsymbol{\epsilon}, \boldsymbol{\epsilon}^{*4}) \\
f_{C_{11}}(\boldsymbol{\epsilon}, \boldsymbol{\epsilon}^{*5}) & f_{C_{33}}(\boldsymbol{\epsilon}, \boldsymbol{\epsilon}^{*5}) & f_{C_{44}}(\boldsymbol{\epsilon}, \boldsymbol{\epsilon}^{*5}) & f_{C_{66}}(\boldsymbol{\epsilon}, \boldsymbol{\epsilon}^{*5}) & f_{C_{13}}(\boldsymbol{\epsilon}, \boldsymbol{\epsilon}^{*5})
\end{bmatrix}
\begin{Bmatrix} C_{11} \\ C_{33} \\ C_{44} \\ C_{66} \\ C_{13} \end{Bmatrix} =
\begin{Bmatrix}
\int_V \rho\omega^2 \mathbf{u} \cdot \mathbf{u}^{*1} dV \\
\int_V \rho\omega^2 \mathbf{u} \cdot \mathbf{u}^{*2} dV \\
\int_V \rho\omega^2 \mathbf{u} \cdot \mathbf{u}^{*3} dV \\
\int_V \rho\omega^2 \mathbf{u} \cdot \mathbf{u}^{*4} dV \\
\int_V \rho\omega^2 \mathbf{u} \cdot \mathbf{u}^{*5} dV
\end{Bmatrix}
\tag{6.6}
$$

Specialisation constraints, described in detail in [11, 55], were imposed in the optimised VFM to give a well-posed system of equations with which to solve for the unknown material parameters. For example, in the case of five parameters, specialisation constraints for $\mathbf{u}^{*1}$ were written such that:

$$
\begin{aligned}
f_{C_{11}}(\boldsymbol{\epsilon}, \boldsymbol{\epsilon}^{*1}) &= 1 \\
f_{C_{33}}(\boldsymbol{\epsilon}, \boldsymbol{\epsilon}^{*1}) &= 0 \\
f_{C_{44}}(\boldsymbol{\epsilon}, \boldsymbol{\epsilon}^{*1}) &= 0 \\
f_{C_{66}}(\boldsymbol{\epsilon}, \boldsymbol{\epsilon}^{*1}) &= 0 \\
f_{C_{13}}(\boldsymbol{\epsilon}, \boldsymbol{\epsilon}^{*1}) &= 0
\end{aligned}
\tag{6.7}
$$

Specialisation constraints for each consecutive virtual displacement field ($\mathbf{u}^{*2}$, $\mathbf{u}^{*3}$, $\mathbf{u}^{*4}$ and $\mathbf{u}^{*5}$) were developed by exchanging the place of the one in Equation (6.7). With these constraints, Equation (6.6) was written as:

$$\begin{bmatrix} 1 & 0 & 0 & 0 & 0 \\ 0 & 1 & 0 & 0 & 0 \\ 0 & 0 & 1 & 0 & 0 \\ 0 & 0 & 0 & 1 & 0 \\ 0 & 0 & 0 & 0 & 1 \end{bmatrix} \begin{Bmatrix} C_{11} \\ C_{33} \\ C_{44} \\ C_{66} \\ C_{13} \end{Bmatrix} = \begin{Bmatrix} \int_V \rho\omega^2 \mathbf{u} \cdot \mathbf{u}^{*1} dV \\ \int_V \rho\omega^2 \mathbf{u} \cdot \mathbf{u}^{*2} dV \\ \int_V \rho\omega^2 \mathbf{u} \cdot \mathbf{u}^{*3} dV \\ \int_V \rho\omega^2 \mathbf{u} \cdot \mathbf{u}^{*4} dV \\ \int_V \rho\omega^2 \mathbf{u} \cdot \mathbf{u}^{*5} dV \end{Bmatrix} \tag{6.8}$$

The resulting parameters were simply computed by evaluating each right hand side term of Equation (6.8). Details on the implementation of specialisation and other constraints are described in Appendix C.

In order to numerically calculate an optimised field, an equation was developed that describes the variance in the estimated parameters. The optimal virtual displacement field was one that minimised the variance [10]. To write the variance in terms of each virtual displacement field, Equation (6.4) was rewritten, separating the raw signal ($\boldsymbol{\epsilon}$) and accompanying noise ($\boldsymbol{\epsilon}_{no}$).

$$\begin{aligned} &C_{11}(f_{C_{11}}(\boldsymbol{\epsilon}_{no}, \boldsymbol{\epsilon}^*) + f_{C_{11}}(\boldsymbol{\epsilon}, \boldsymbol{\epsilon}^*)) + C_{33}(f_{C_{33}}(\boldsymbol{\epsilon}_{no}, \boldsymbol{\epsilon}^*) + f_{C_{33}}(\boldsymbol{\epsilon}, \boldsymbol{\epsilon}^*)) + \\ &C_{44}(f_{C_{44}}(\boldsymbol{\epsilon}_{no}, \boldsymbol{\epsilon}^*) + f_{C_{44}}(\boldsymbol{\epsilon}, \boldsymbol{\epsilon}^*)) + C_{66}(f_{C_{66}}(\boldsymbol{\epsilon}_{no}, \boldsymbol{\epsilon}^*) + f_{C_{66}}(\boldsymbol{\epsilon}, \boldsymbol{\epsilon}^*)) + \\ &C_{13}(f_{C_{13}}(\boldsymbol{\epsilon}_{no}, \boldsymbol{\epsilon}^*) + f_{C_{13}}(\boldsymbol{\epsilon}, \boldsymbol{\epsilon}^*)) = \int_V \rho\omega^2 \mathbf{u}_{no} \cdot \mathbf{u}^* dV + \int_V \rho\omega^2 \mathbf{u} \cdot \mathbf{u}^* dV \end{aligned} \tag{6.9}$$

Noise components in the strain fields were assumed to be independent Gaussian distributions with positive standard deviations, γ. Noise in each respective strain field was assumed to have equal variance ($\gamma_{\boldsymbol{\epsilon}_{11}} = \gamma_{\boldsymbol{\epsilon}_{22}} = \gamma_{\boldsymbol{\epsilon}_{33}} = \gamma_{\boldsymbol{\epsilon}_{12}} = \gamma_{\boldsymbol{\epsilon}_{13}} = \gamma_{\boldsymbol{\epsilon}_{23}}$) and it was assumed that measurements were unbiased, and that noise was uncorrelated from one measurement to another. With the specialisation constraints applied to the case with noise, the difference between the estimated and reference parameters ($Q^{app} - Q$ where $Q = [C_{11}, C_{33}, C_{44}, C_{66}, C_{13}]$) was written in terms of solely the noise in the signal and the virtual strain field, $\boldsymbol{\epsilon}^*$. The superscript ^{app} indicates the approximate values of the estimated parameters. The full derivation of Equation (6.10) is shown in Appendix B.

$$\begin{aligned} Q_a^{app} - Q_a = &- C_{11} f_{C_{11}}(\boldsymbol{\epsilon}_{no}, \boldsymbol{\epsilon}^*) - C_{33} f_{C_{33}}(\boldsymbol{\epsilon}_{no}, \boldsymbol{\epsilon}^*) - C_{44} f_{C_{44}}(\boldsymbol{\epsilon}_{no}, \boldsymbol{\epsilon}^*) - \\ &C_{66} f_{C_{66}}(\boldsymbol{\epsilon}_{no}, \boldsymbol{\epsilon}^*) - C_{13} f_{C_{13}}(\boldsymbol{\epsilon}_{13}, \boldsymbol{\epsilon}^*) + \int_V \rho\omega^2 \mathbf{u}_{no} \cdot \mathbf{u}^* dV \end{aligned} \tag{6.10}$$

where $a \in [1, 5]$. For example, $Q_1 = C_{11}$. The noise in the acceleration (right hand side term) was previously shown to be negligible in MRE displacement fields [29]. Therefore,

the final term of Equation 6.10 was omitted. The variance of an estimated parameter can be written as:

$$V(Q^{app}) = E\Big(\big[Q^{app} - E(Q^{app})\big]^2\Big) \tag{6.11}$$

where $E(x)$ represents the expectation of x. If it is assumed that there is no bias in the measurement, then $E\big(Q^{app}\big) = Q$ and it follows that

$$V(Q^{app}) = E\Big(\big[Q^{app} - Q\big]^2\Big). \tag{6.12}$$

Substituting Equation (6.10) into Equation (6.12) resulted in the following generalised equation.

$$V(Q^{app}) = E\Big(\big[Q^{app} - Q)\big]^2\Big) = \gamma^2\big(Q^{app}\big)^T\big[E(N^TN)\big]Q^{app} \tag{6.13}$$

where γ represents the uncertainty in the strain measurements and

$$N = \begin{bmatrix} f_{C_{11}}(\boldsymbol{\epsilon}_{no}, \boldsymbol{\epsilon}^*) \\ f_{C_{33}}(\boldsymbol{\epsilon}_{no}, \boldsymbol{\epsilon}^*) \\ f_{C_{44}}(\boldsymbol{\epsilon}_{no}, \boldsymbol{\epsilon}^*) \\ f_{C_{66}}(\boldsymbol{\epsilon}_{no}, \boldsymbol{\epsilon}^*) \\ f_{C_{13}}(\boldsymbol{\epsilon}_{no}, \boldsymbol{\epsilon}^*) \end{bmatrix}, Q^{app} = \begin{bmatrix} C_{11}^{app} \\ C_{33}^{app} \\ C_{44}^{app} \\ C_{66}^{app} \\ C_{13}^{app} \end{bmatrix}. \tag{6.14}$$

The minimisation matrix, $\mathbf{H}$, was written as:

$$\mathbf{H} = \big(Q^{app}\big)^T\big[E(N^TN)\big]Q^{app} \tag{6.15}$$

Therefore, an optimal virtual field was found such that Equation (6.15) was minimised while adhering to the constraints (Equation (6.7) and $u^* = 0$ on boundaries). Following [10], the virtual displacement field vector turns out to be the saddle point of the Lagrangian:

$$\mathcal{L} = \frac{\gamma^2}{2}\mathbf{u}^{*T}[\mathbf{H}]\mathbf{u}^* + \Lambda^T([\mathbf{A}]\mathbf{u}^* - \mathbf{Z}) \tag{6.16}$$

where $\mathbf{H}$ is the matrix of estimated shear variance to be minimised (Equation (6.15)), $\mathbf{\Lambda}$ is a vector of Lagrangian multipliers, $\mathbf{Z}$ is a vector of right hand side constraint values and $\mathbf{A}$ is a matrix that included specialisation constraints (Equation (6.7)) and boundary constraints, $\mathbf{u}^*(\Omega) = 0$.

Therefore, the virtual displacement field was obtained by solving the following linear system of equations:

$$\begin{bmatrix} [\mathbf{H}] & [\mathbf{A}]^T \\ [\mathbf{A}] & [0] \end{bmatrix} \begin{Bmatrix} \mathbf{u}^* \\ \Lambda \end{Bmatrix} = \begin{Bmatrix} 0 \\ \mathbf{Z} \end{Bmatrix} \tag{6.17}$$

Since the parameters in Q are involved in the minimisation matrix, $\mathbf{H}$, an iterative process was implemented. An initial set of parameters Q^{app} were applied to calculate an initial $\mathbf{H}$ matrix. The resulting $\mathbf{H}$ matrix was used to estimate the material properties. This step was repeated until the maximum change in estimated parameters was less than 0.1% between two consecutive iterations. Additionally, a maximum number of allowable iterations was set to 30. If this value was exceeded, parameters for the given model, or region, were disregarded.

The results from the five-parameter formulation were written in terms of two shear moduli (G_{12} and G_{13}), two Young's moduli (E_1 and E_3) and a Poisson's ratio (ν_{31}) since these parameters have relevant physical meaning (i.e. stiffness in shear, stiffness in tensile stretching and volume change). Conversely, the parameters of the elasticity matrix, C_{11}, C_{33} and C_{13}, represent a combination of tensile stiffness and volume effects and do not have a simple physical meaning. The shear moduli, Young's moduli and Poisson's ratio can be calculated from the compliance matrix, which is the inverse of the elasticity matrix containing C_{11}, C_{33}, etc. (Equation 4.2).

Equation (6.13) can be rewritten to clearly show that the variance in the estimated parameter is proportional to the error in the measured strain field:

$$V(Q_a) = \gamma^2 \eta_a^2 \tag{6.18}$$

If the variance, $V(Q_a)$, is understood as the uncertainty of the method in estimating a given parameter and γ is the uncertainty in the strain measurements, then η_a is the sensitivity of the estimated parameters to noise in the measurements. In this study, parameter sensitivity values were normalised by their respective parameters (e.g. η/C_{11}), which allows for the direct comparison of parameter sensitivity values within each material model formulation. However, this does not allow for the direct comparison of sensitivity values between the two material models (e.g. between η/C_{11} and η/τ).

6.1.2 Three Parameter Model

A second material model formulation, developed in [47], was used which separates the dilatational from the deviatoric properties. The equations were derived from a hyperelastic material formulation at the refernece configuration. The equations in [47] were rewritten as a linear combination of four parameters: κ, G_{12}, G_{13} and τ, where $\tau = G_{12} \cdot E_3/E_1$ and describes the anisotropic tensile ratio equal, and κ is defined as the ratio of the hydrostatic stress to the unit volume change.

$$
\begin{aligned}
C_{11} &= \kappa + \frac{8}{9}G_{12} + \frac{4}{9}\tau & C_{33} &= \kappa - \frac{4}{9}G_{12} + \frac{16}{9}\tau \\
C_{12} &= \kappa - \frac{10}{9}G_{12} + \frac{4}{9}\tau & C_{13} &= \kappa + \frac{2}{9}G_{12} - \frac{8}{9}\tau \\
C_{44} &= G_{12} & C_{66} &= G_{13}
\end{aligned}
\tag{6.19}
$$

Specialisation constraints, like those in Equation (6.7), were applied to the three-parameter model. However, due to the lack of confidence in estimation of the longitudinal wavelength, and hence κ, only G_{12}, G_{13} and τ were estimated. Therefore, with three virtual displacement fields ($\mathbf{u}^{*1}$, $\mathbf{u}^{*2}$, $\mathbf{u}^{*3}$) and corresponding strain fields ($\boldsymbol{\epsilon}^{*1}$, $\boldsymbol{\epsilon}^{*2}$, $\boldsymbol{\epsilon}^{*3}$), the parameters were calculated as:

$$
G_{12} = \int_V \rho\omega^2 \mathbf{u}\cdot\mathbf{u}^{*1} dV \quad G_{13} = \int_V \rho\omega^2 \mathbf{u}\cdot\mathbf{u}^{*2} dV \quad \tau = \int_V \rho\omega^2 \mathbf{u}\cdot\mathbf{u}^{*3} dV \tag{6.20}
$$

6.1.3 Implementation

Beam Simulations To test the implementation of these two methods, simulations of steady-state harmonic motion were run with a cantilever beam model using Abaqus 6.13 (Dassault Systèmes Simulia Corp., Providence, USA). The material orientation was aligned down the longest dimension (z-axis) of the beam. Since it is known that both fast and slow shear waves are necessary for the accurate estimation of transversely isotropic material properties [139, 151], 511 simulations were run in order to illustrate the effect of the loading configuration and resulting wave propagation direction on the estimation of anisotropic material properties. Figure 6.1 shows the beam finite element model with three faces highlighted: the end (red), side (black) and top (blue). An x, y and/or z displacement was applied on either, two or all of the three faces. These combinations resulted in 511 different loading configurations. For this test, initial parameter estimates were set to the reference values. In the figure, element material axes are shown by red arrows pointing along the length of the beam in the +z direction.

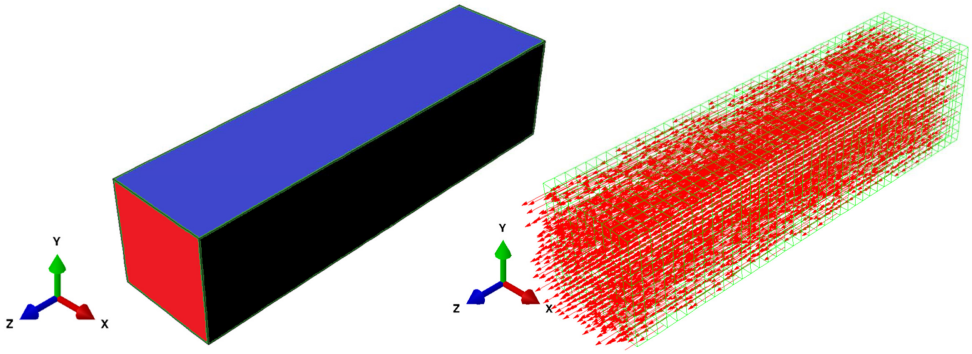

FIGURE 6.1: Beam finite element model illustrating three faces on which displacement boundary conditions were applied as well as the material orientation.

Using six of the 511 loading configurations, a Monte-Carlo simulation (n=30) was run with Gaussian noise ($\sigma_{\text{noise}} = 15\% \cdot \sigma_{\text{disp}}$) added to the reference displacement fields. Reference material properties were assigned to be: E_1 = 12.00 kPa, E_3 = 36.00 kPa, G_{12} = 3.27 kPa, G_{13} = 12.00 kPa and ν_{31} = 0.4999. The structural damping coefficient was set to 0.1 and a density of 1.00 g/cm^3 was used.

Isotropic Phantom MRE The two transversely isotropic inversion methods were then tested with MRE images collected from an isotropic phantom. Performing the inversion on an anisotropic phantom provides a form of validation since shear moduli, and (separately) the two Young's moduli should be equal (i.e. $G_{12} = G_{13}$ and $E_1 = E_3$), whereas values measured estimated for an anisotropic phantom cannot be directly validated.

The MRE images of a PVC cylindrical gel phantom were obtained using a 3T MR scanner (Tim Trio, Siemens Healthcare, Erlangen, Germany) with gradients of 27 mT/m (2.7 G/cm) and a slew rate of 163 μs (TE/TR = 21.27/25 ms). A pneumatic driver system (Resoundant Inc., Rochester, MN) was used to apply a harmonic load to the bottom surface of the phantom at 60 Hz. Phase-contrast images (native resolution = 128 voxels x 63 voxels, reconstructed resolution = 256 voxels x 256 voxels, slice thickness = 5 mm, FOV = 250 mm x 250 mm) were collected at 16 longitudinal locations in the mid-region of the phantom. The cylindrical phantom had a radius of 76.2 mm and a height of 127 mm. At each location, 12 images were collected that encoded phase in three orthogonal directions at four phase offsets relative to the induced harmonic motion. A discrete Fourier transform was used to fit a sinusoid to the four phase offsets at each pixel in each direction. A finite element mesh was developed to represent the geometry of the imaged portion of the cylindrical phantom.

Since the phantom was isotropic, two different arbitrary material orientations were assigned, shown in Figure 6.2. The volume was broken up into 18 equally sized sub-regions and both formulations of the transversely isotropic optimised VFM were used to

analyse each sub-region.

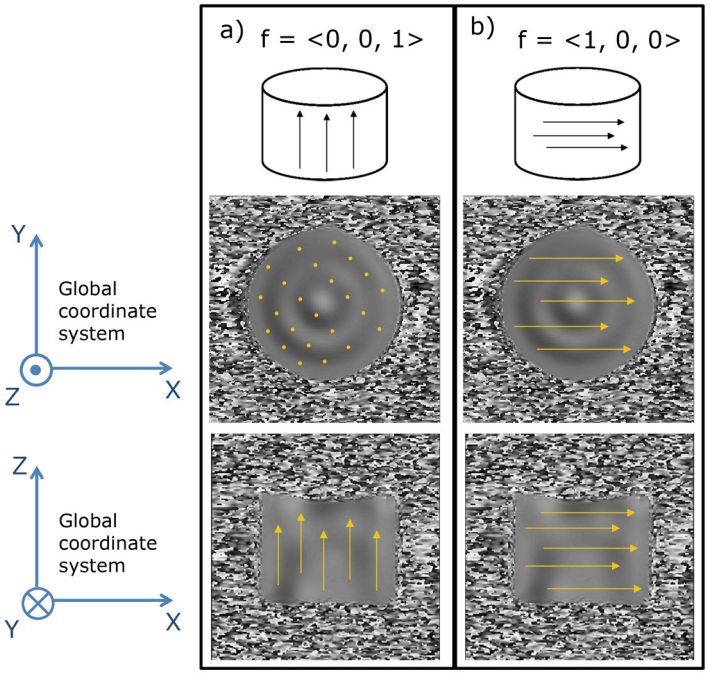

FIGURE 6.2: Sketches of the two arbitrarily assigned material orientations are shown as well as phase images with "fibre" orientations drawn on top. "Fibre" orientations are alligned with the global a) z: <0, 0, 1> and b) x: <1, 0, 0> directions, respectively.

Left Ventricular Simulations Next, both methods were used to estimated transversely isotropic material properties from simulated harmonic displacements in an anatomically realistic canine left ventricle finite element model embedded with fibre orientations measured from histology [88]. In order to guide future cardiac MRE studies, various loading conditions and frequencies were tested to evaluate their impact on the accuracy of parameter estimates as well as the sensitivities of the parameters to noise. Fibre orientations were embedded in the geometric finite element model by interpolating nodal parameters. Reference stiffness values were defined based on cardiac anisotropic shear moduli measured from ultrasound elastography [31]. The fibre direction was assigned a Young's modulus (E_3) of 10.5 kPa. The Young's moduli in the transverse directions (E_1, E_2) were set to 6.5 kPa, and the fibre shear moduli (G_{13}, G_{23}) were set to 2.5 kPa. The structural damping coefficient was set to 0.1; the Poisson's ratio was set to 0.4999 as cardiac tissue is largely incompressible; and a density of 1.06 g/cm^3 was prescribed. The large ratio of the bulk modulus to the transverse shear modulus (κ/G_{12} ¿¿ 100) demonstrates that the fast shear wave is near the incompressible limit [150].

A loading test was carried out in which 63 different loading combinations of x, y and/or z displacements were prescribed on the apical and anterior surfaces (Figure 6.3). These surfaces were chosen since wave propagation observed in cardiac MRE experiments

originates from approximately the anterior and apical surfaces of the LV. Gaussian noise was added to the real and imaginary components for six selected loading cases. Noise in MR images can be adequately modelled as Gaussian, given that the signal-to-noise ratio is above 3 [60]. The Gaussian distribution of noise had a mean of zero and a standard deviation (σ_{noise}) computed as:

$$\sigma_{noise} = 15\% \cdot \sigma_{disp} \tag{6.21}$$

where σ_{disp} was the standard deviation of the ground truth displacement field. Then, for one loading condition, various frequencies were tested in order to assess the impact on parameter identification.

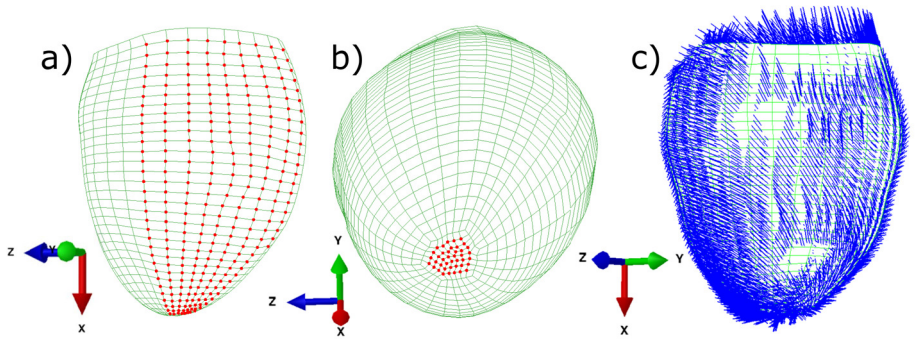

FIGURE 6.3: LV finite element model illustrating a) anterior surface nodes, b) apical surface nodes and c) fibre field measured from histology.

6.2 Results

6.2.1 Beam Simulations

Of the 511 simulations without Gaussian noise, numerous loading cases resulted in accurate parameter estimates for both material model formulations. Variance in estimated shear moduli over the different loading configurations was less for the three-parameter formulation than the five-parameter formulation. Values of E_3 erred up to 25% from the reference value whereas all estimated values of τ were within 5% of the true value. However, τ showed biased estimation with the majority of cases overestimating the parameter. Despite this, the three-parameter formulation resulted in more accurate estimates of transversely isotropic material properties in the cantilever beam geometry. Complex parameters were estimated for both the five- and three-parameter formulations. However, for conciseness, this chapter presents the storage moduli (i.e. the real part of the complex moduli) only. However, damping coefficients, calculated as the ratio of the imaginary part to the real part of each complex modulus, are presented in Appendix D.

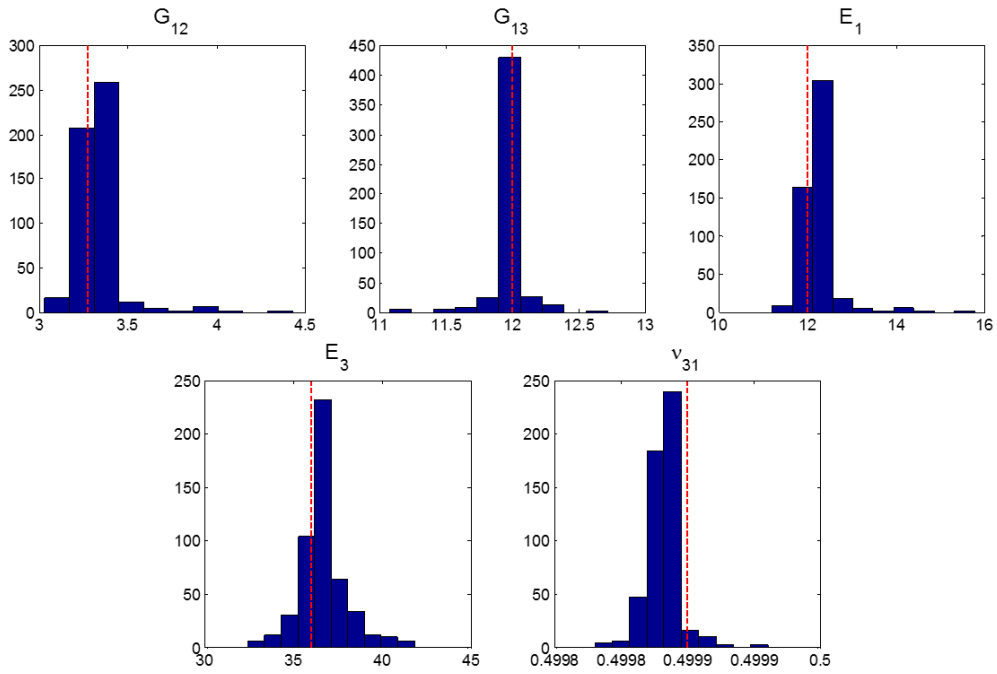

FIGURE 6.4: Histograms of estimated parameters for all 511 loading cases using the five-parameter formulation. Reference values are shown as red dotted lines.

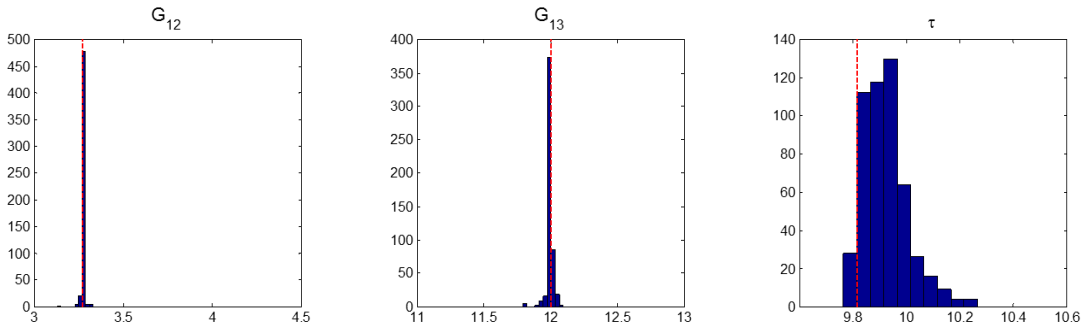

FIGURE 6.5: Histograms of estimated parameters for all 511 loading cases using the three-parameter formulation. Reference values are shown as red dotted lines.

It should be noted that, using the five-parameter formulation, the matrix to solve for the numeric virtual fields (Equation (6.17)) was badly scaled (COND = 1e-20), since, in nearly incompressible media, C_{11}, C_{33} and C_{13} approach infinity while C_{44} and C_{66} generally range between 1 - 10 kPa for biological tissue. Despite the ill-conditioning of the matrix, the method converged in two to three iterations for each loading case. Since the three-parameter formulation does not estimate the Poisson's ratio, the problem was well conditioned. On average, the three-parameter estimation method took three iterations to converge.

Normalised sensitivity values were also calculated for each parameter and are shown in Figures 6.6 and 6.7. Sensitivity values for the five-parameter formulation are shown

with respect to the five independent parameters of the elasticity matrix (C_{11}, C_{33}, C_{13}, C_{44} and C_{66}). Normalising sensitivity values has the effect of putting all values on the same scale, enabling comparisons between the sensitivity of each parameter. Normalisation, however, does not allow for directly comparing sensitivity values between the five- and three-parameter material formulations.

Both Figures 6.6 and 6.7 reveal that the shear moduli were less sensitive to noise, seen by smaller normalised sensitivity values, than all other parameters. C_{11}, C_{33} and C_{13} sensitivity values were nearly equivalent for all loading cases. With the three-parameter formulation, τ resulted in larger parameter sensitivity for some loading cases.

The magnitude of sensitivity values was larger for the five-parameter formulation than the three-parameter formulation since the sensitivity is calculated from the parameter variance matrix ($\eta^2 = (Q^{app})^T E(N^T N) Q^{app}$), which contains the estimated parameters, themselves. In a nearly incompressible material, C_{11}, C_{33} and C_{13} approach infinity, resulting in large values in the variance matrix. Conversely, since all material properties in the three-parameter formulation are between 0-10 kPa, the resulting sensitivity values are within similar ranges. It can be also be seen in Figures 6.6 and 6.7 that, although many loading conditions resulted in accurate estimation of transversely isotropic material parameters, they did not result in equal sensitivity to noise.

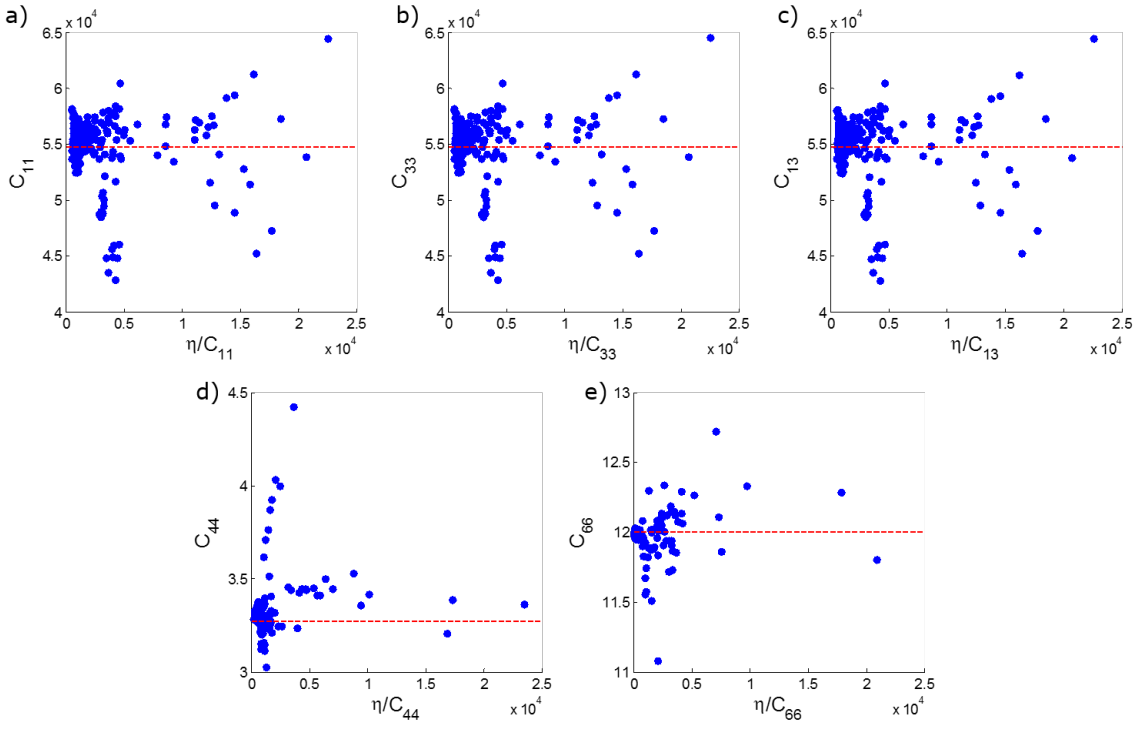

FIGURE 6.6: The estimated parameters from the elasticity matrix plotted versus their respective normalised sensitivity values (e.g. η/C_{11}). Reference values are shown as red dotted lines.

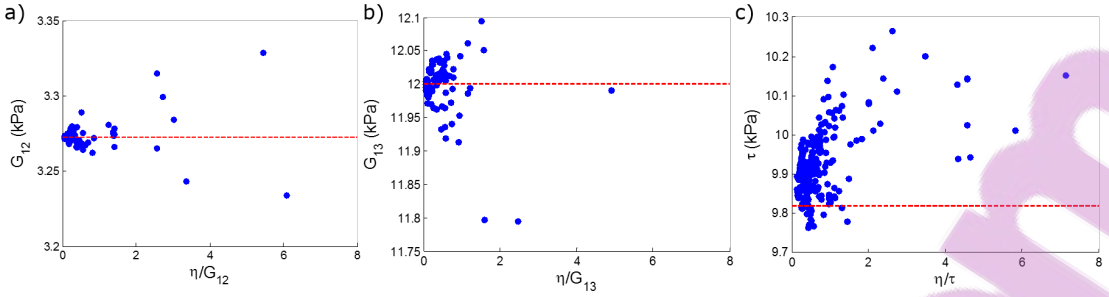

FIGURE 6.7: The estimated parameters (G_{12}, G_{13} and τ) plotted versus their respective normalised sensitivity values (e.g. η/G_{12}). Reference values are shown as red dotted lines.

Six loading configurations were then chosen for analysis with Gaussian noise added to the reference displacements. Six simulations (#113, #189, #211, #412, #447 and #451) were chosen as they resulted in either the most accurate identification of reference parameters (minimum cumulative RMS error) or they resulted in overall low normalised sensitivity values. The loads for these simulations along with their reference displacement fields are shown in Figure 6.8.

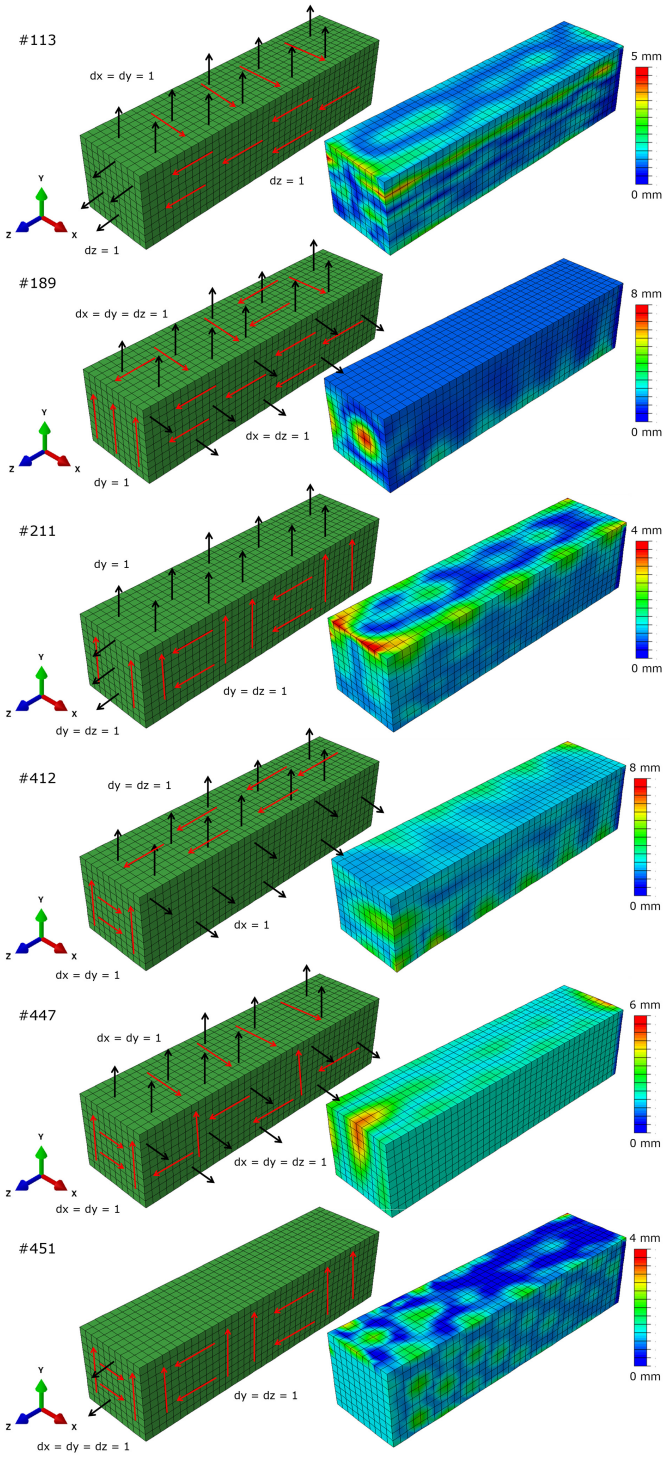

FIGURE 6.8: Beam models showing loading configurations and reference displacements for simulations used in the noise analysis. Red arrows indicate shear and black arrows indicate loads normal to the surface. Reference displacements encode magnitude ($\sqrt{x^2 + y^2 + z^2}$).

A Monte Carlo simulation (n = 30) was run for each of the six loading configurations and independent Gaussian noise copies were added to the reference displacement fields at each run. The initial parameter estimates were varied within a normal distribution centred at the reference value ($\overline{x} = Q_{REF}, \sigma = 20\% \cdot Q_{REF}$). Resulting estimated moduli for all simulations which converged in under 30 iterations are illustrated by box plots in Figures 6.9 and 6.10. G_{13} was the most accurately estimated parameter using both material model formulations. The loading configurations had a large impact on the mean and standard deviation of estimated parameters. Additionally, a loading case which resulted in accurate estimation of material properties in the five-parameter formulation did not necessarily result in accurate estimation with the three-parameter model (e.g. simulation #189). Estimated Poisson's ratios showed large variance and were often outside of physically realistic ranges. With the three-parameter material formulation, loading cases #189, #412 and #447 resulted in large errors in estimated values of G_{12}.

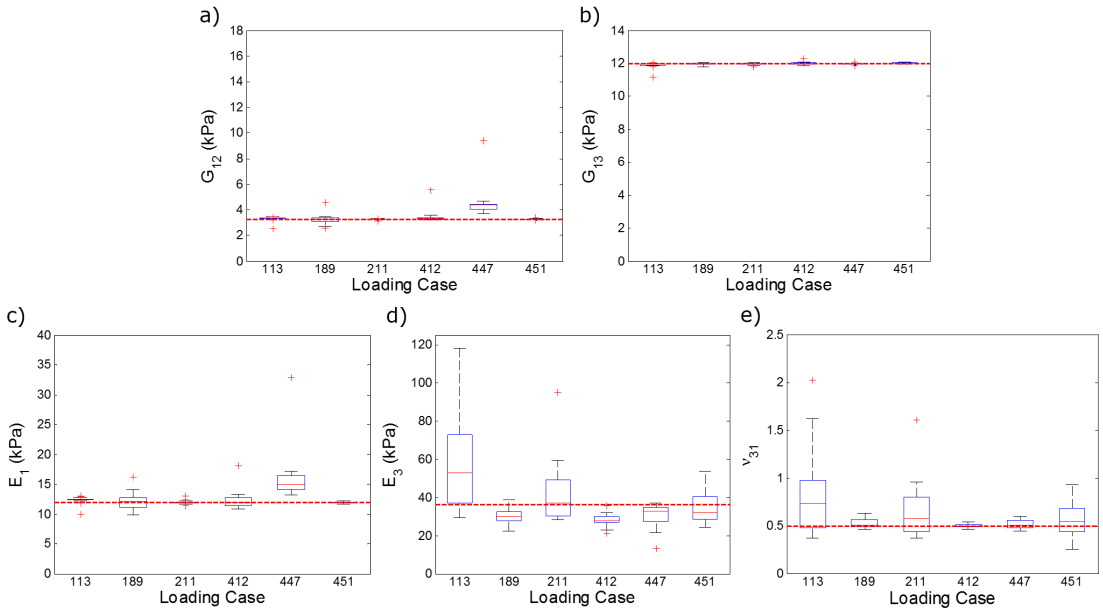

FIGURE 6.9: Results from all converged Monte Carlo simulations, using the five-parameter formulation, for six beam loading cases showing a) transverse shear moduli (G_{12}), b) fibre shear moduli (G_{13}), c) transverse Young's moduli (E_1), d) fibre Young's moduli (E_3) and e) fibre-transverse Poisson's ratio (ν_{31}). Reference values are shown by red dotted lines.

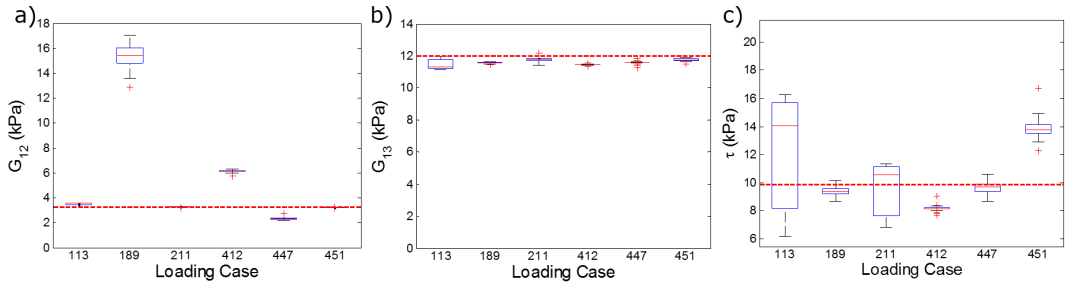

FIGURE 6.10: Results from all converged Monte Carlo simulations, using the three-parameter formulation, for each beam loading case (1-4) showing a) transverse shear moduli (G_{12}), b) fibre shear moduli (G_{13}) and c) anisotropic tensile ratio (τ). Reference values are shown by red dotted lines.

Not all simulations converged in under 30 iterations. Table 6.1 lists the number of simulations which converged as well as the mean number of iterations ($\pm$ one standard deviation) required for convergence for both the three- and five-parameter formulations. In the three-parameter formulation, three loading configurations (#189, #412 and #447) converged in all or nearly all of the Monte Carlo simulations whereas the other three configurations (#113, #211 and #451), converged in only 3, 6 and 12 simulations out of 30, respectively. These latter three simulations showed larger parameter sensitivity to noise values than the former three in Figure 6.7. In the five-parameter formulation, 16 simulations (out of 30) converged on average for the six loading configurations.

TABLE 6.1: The number of simulations in the Monte Carlo experiment (n = 30) which converged for the five- and three-parameter formulations are shown as well as the mean number of iterations for convergence ($\pm$ one standard deviation).

Simulation Number	5 Parameter Method	3 Parameter Method
113	17 (12.2 $\pm$ 6.9)	3 (19.0 $\pm$ 4.4)
189	15 (14.1 $\pm$ 8.4)	30 (9.5 $\pm$ 2.7)
211	19 (12.4 $\pm$ 7.5)	6 (15.7 $\pm$ 7.2)
412	15 (10.0 $\pm$ 5.4)	30 (6.8 $\pm$ 0.7)
447	14 (13.1 $\pm$ 5.9)	27 (13.1 $\pm$ 2.8)
451	17 (11 $\pm$ 5.3)	12 (23.0 $\pm$ 3.6)

6.2.2 Isotropic Phantom MRE

Using the five-parameter formulation, four out of 18 sub-regions did not converge to a solution for both arbitrarily defined material orientations. In the three-parameter formulation, two sub-regions did not converge to a solution when the fibre direction was oriented along the global z-axis (axially) and all sub-regions converged when the material was oriented

along the global x-axis (transverse to the axis of the cylinder). Overall, the three-parameter formulation converged in a greater number of sub-regions, and required fewer iterations (see Table 6.2).

TABLE 6.2: The number of sub-regions of the phantom that converged in less than 30 iterations for the five- and three-parameter formulations are shown together with the mean number of iterations for convergence ($\pm$ one standard deviation). Material orientation labels are illustrated in Figure 6.2.

Material Orientation	5 Parameter Method	3 Parameter Method
<0, 0, 1>	14 (9.71 $\pm$ 6.37)	16 (9.50 $\pm$ 6.93)
<1, 0, 0>	14 (10.86 $\pm$ 6.41)	18 (5.00 $\pm$ 1.91)

Resulting estimated moduli for all sub-regions that converged to a solution are shown in Figures 6.11 and 6.12. The mean shear moduli resulted in values very close to those estimated by three other inversion methods, including a finite element model update method [103] (FEMU: 5.55 kPa), a multi-modal direct inversion method [39] (MMDI: 5.45 kPa), and a directional filter with local frequency estimation method [97] (DF-LFE: 5.34 kPa). Since the phantom was isotropic, the pairs of shear moduli (G_{12} and G_{13}), and Young's moduli (E_1 and E_3), were each expected to be equal. The mean estimated shear moduli from the five-parameter formulation differed by only 0.2 kPa. However, the mean estimated Young's modulus in the material orientation (E_3) was greater than than that in the transverse direction (E_1) for both material orientations. The Poisson's ratios were consistently overestimated. The true value of ν_{31} should be very close to 0.5, since the PVC gel was approximately incompressible. In the three-parameter formulation, the estimated values of G_{12} varied widely across the sub-regions when the material orientation was aligned with the global z-axis (axially), whereas G_{13} values were accurately estimated with little variance for both material orientations. Estimated values of τ were centred at the reference value but showed large variation.

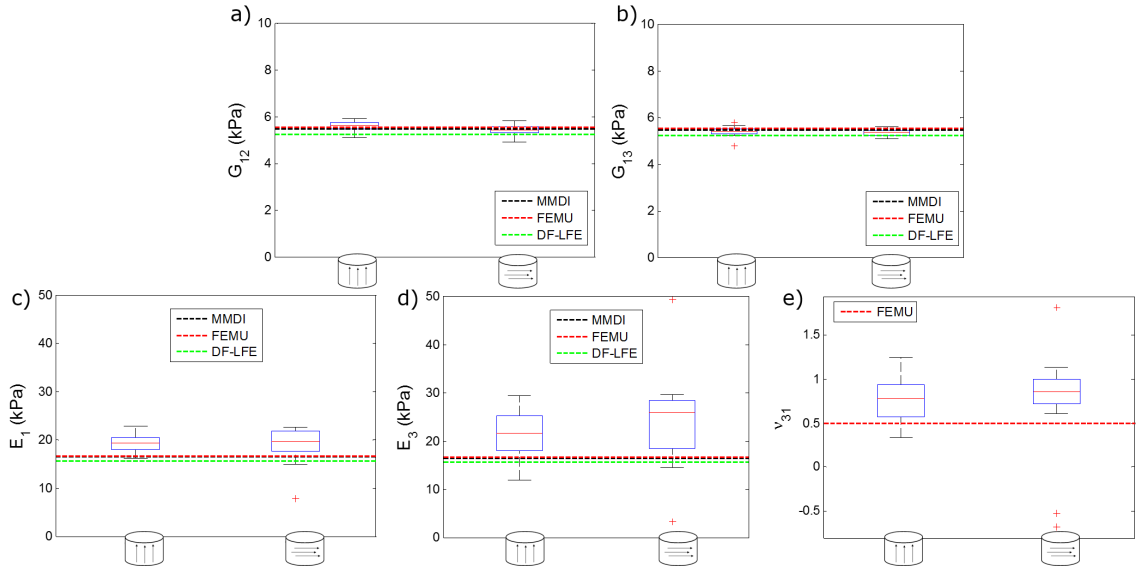

FIGURE 6.11: Results from all converged sub-regions in the isotropic phantom, using the five-parameter formulation, for both material orientations illustrated below each graph, showing a) transverse shear moduli (G_{12}), b) fibre shear moduli (G_{13}), c) transverse Young's moduli (E_1), d) fibre Young's moduli (E_3) and e) fibre-transverse Poisson's ratio (ν_{31}). Values measured by three other methods (MMDI, FEMU and DF-LFE) are shown by dotted lines.

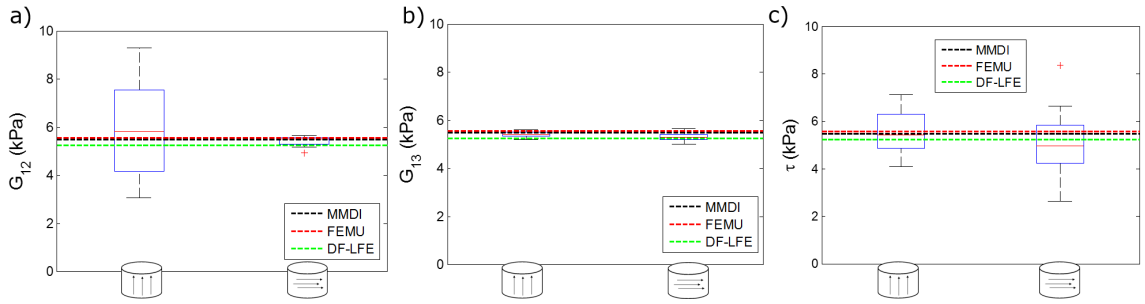

FIGURE 6.12: Results from all converged sub-regions in the isotropic phantom, using the three-parameter formulation, for both material orientations illustrated below each graph, showing a) transverse shear moduli (G_{12}), b) fibre shear moduli (G_{13}) and c) anisotropic tensile ratio (τ). Values measured by three other methods (MMDI, FEMU and DF-LFE) are shown by dotted lines.

Normalised parameter sensitivity values were calculated for each sub-region and are plotted in Figures 6.13 and 6.14. For the five-parameter formulation, it should be noted that the parameter sensitivities are plotted on different scales for C_{11}, C_{33} and C_{13} in comparison to that for the shear moduli, C_{44} and C_{66}. Shear moduli demonstrated much lower sensitivities to noise than the other parameters. Additionally, since there were no constraints on the values of C_{11}, C_{33} and C_{13}, these values can be negative and still result in accurate Young's moduli. Parameter sensitivity values are reported as the absolute value since negative sensitivity does not have an interpretable meaning.

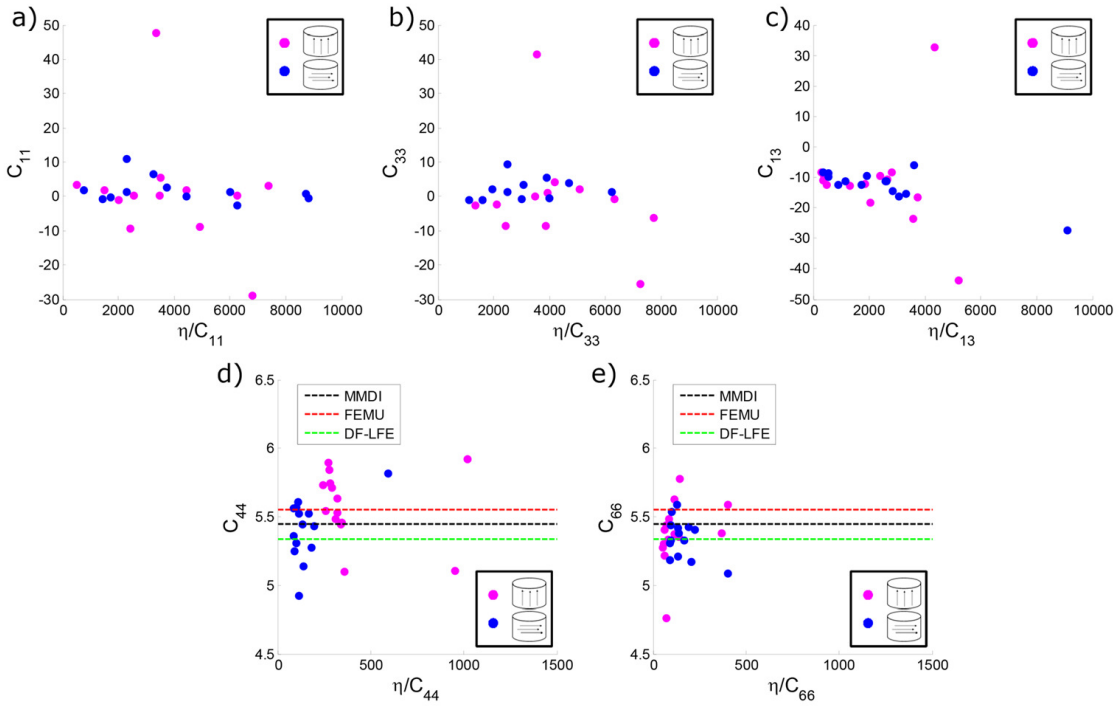

FIGURE 6.13: Resulting estimated moduli: a) C_{11}, b) C_{33}, c) C_{13}, d) C_{44} (= G_{12}) and e) C_{66} (= G_{13}) plotted versus the normalised sensitivity values. Parameters measured by three other methods (MMDI, FEMU and DF-LFE) are shown by dotted lines in plots d) and e).

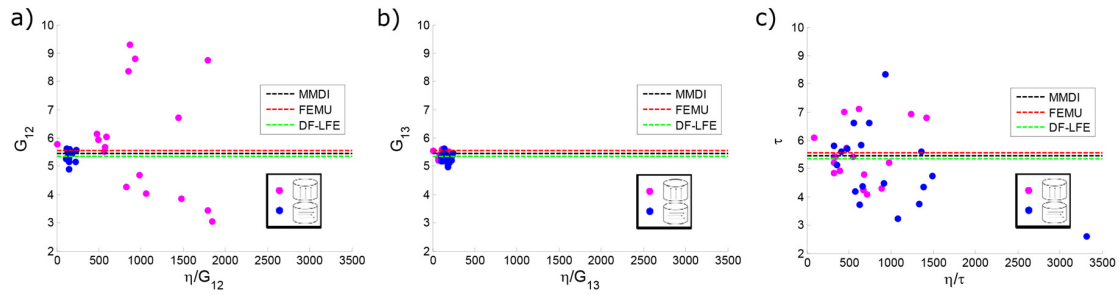

FIGURE 6.14: Resulting estimated moduli: a) G_{12}, b) G_{13} and c) τ plotted versus the normalised sensitivity values. Parameters measured by three other methods (MMDI, FEMU and DF-LFE) are shown by dotted lines.

In the three-parameter formulation, G_{12} resulted in much greater sensitivity to noise when the material was aligned with the global z-axis (axially) than when it was oriented with the global x-axis (transverse). Parameter sensitivities were small for G_{13} irrespective of the chosen material direction. This can be understood by the fact that the relative amplitude of the displacement in the global x- and y- directions was significantly less than the global z-direction displacements. The driver was placed on the bottom of the cylindrical phantom and the largest amplitude displacements occurred in the z-direction. Therefore, when the material orientation was aligned with the global z-axis (axial direction), the esti-

mation of the transverse shear modulus (G_{12}) was solely dependent on small-amplitude displacements in the global x- and y-directions. When the material was in the global x-direction, both shear moduli were accurately estimated with small variances. In this case, the large amplitude through-plane motion contributed to the estimation of G_{12}. The estimated values of τ showed large variance throughout the phantom. τ resulted in large sensitivity values for both material orientations. However, with the three-parameter formulation, the mean values of the estimated shear moduli and τ were close to those estimated using the MMDI, FEMU and DF-LFE methods.

6.2.3 Left Ventricle Simulations

In the LV model loading test without added Gaussian noise, eight of the 63 simulations did not converge within 30 iterations for the three-parameter formulation. The remaining simulations converged in 3 - 20 iterations. The simulations that did not converge were those which had zero displacements applied to the anterior face. All simulations converged within two or three iterations for the five-parameter formulation, and the resulting mean parameters ($\pm$ one standard deviation) were: E_1 = 6.59 $\pm$ 0.24 kPa, E_3 = 10.80 $\pm$ 0.48 kPa, G_{12} = 1.94 $\pm$ 0.07 kPa, G_{13} = 2.52 $\pm$ 0.05 kPa and ν_{31} = 0.4999 $\pm$ 4.4e-6 (note reference values: E_1 = 6.5 kPa, E_3 = 10.5 kPa, G_{12} = 1.92 kPa, G_{13} = 2.5 kPa and ν_{31} = 0.4999). For the three-parameter formulation, the resulting mean parameters ($\pm$ one standard deviation) were: G_{12} = 2.20 $\pm$ 0.29 kPa, G_{13} = 2.79 $\pm$ 0.38 kPa and τ = 3.65 $\pm$ 0.41 kPa (reference: τ = 3.11 kPa). The five-parameter formulation resulted in a more accurate estimation of shear moduli than the three-parameter formulation. In the three-parameter formulation, τ was consistently overestimated and all three moduli erred by up to 33%.

Normalised sensitivity values were calculated for each parameter and are shown in Figures 6.15 and 6.16. Shear parameters resulted in lower sensitivity to noise than C_{11}, C_{33} and C_{13}. In the three parameter formulation, all moduli had comparable sensitivity values.

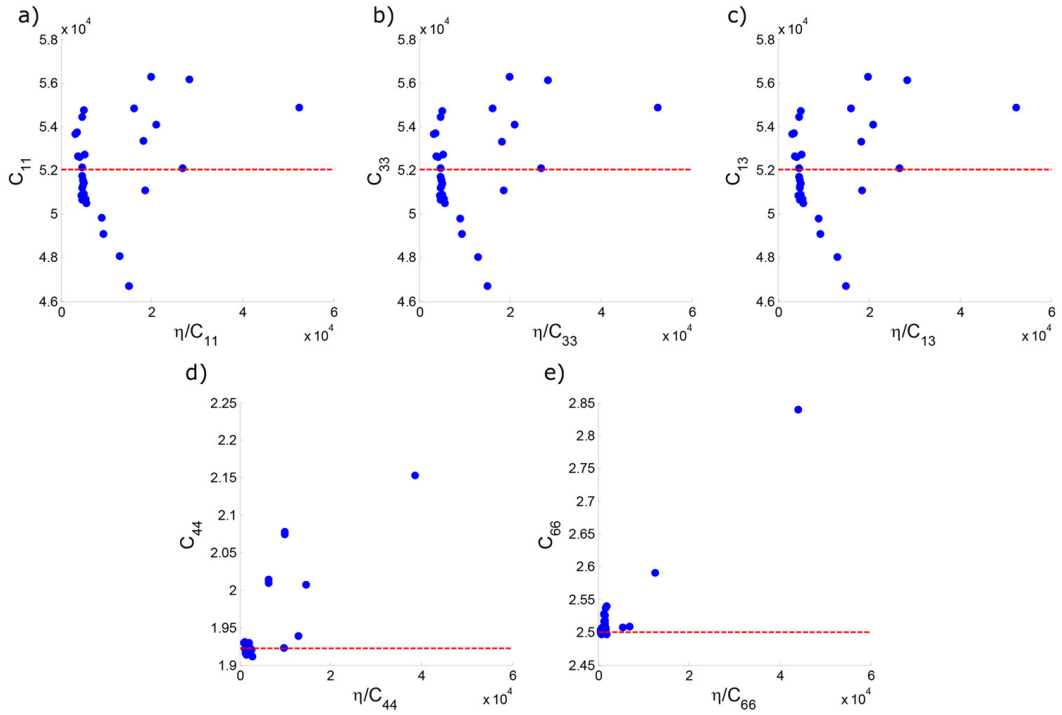

FIGURE 6.15: The estimated parameters from the elasticity matrix are plotted versus their respective normalised sensitivity values (e.g. η/C_{11}). Reference values are shown as red dotted lines.

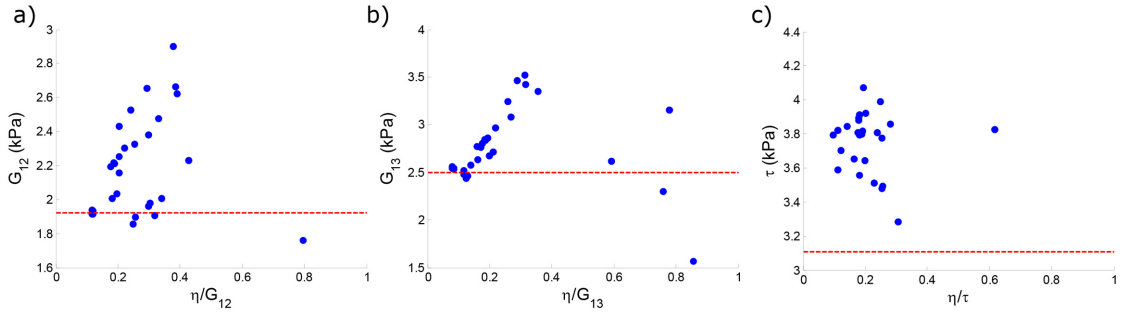

FIGURE 6.16: The estimated parameters (G_{12}, G_{13} and τ) are plotted versus their respective normalised sensitivity values (e.g. η/G_{12}). Reference values are shown as red dotted lines.

Monte Carlo simulations were run (n = 30) using six different loading configurations. Independent distributions of Gaussian noise were added to the reference displacements for each simulation. These six loading configurations were chosen since they resulted in either accurate parameter identification in the loading test or low cumulative sensitivity values. Figure 6.17 illustrates the loads applied as well as the reference displacement fields.

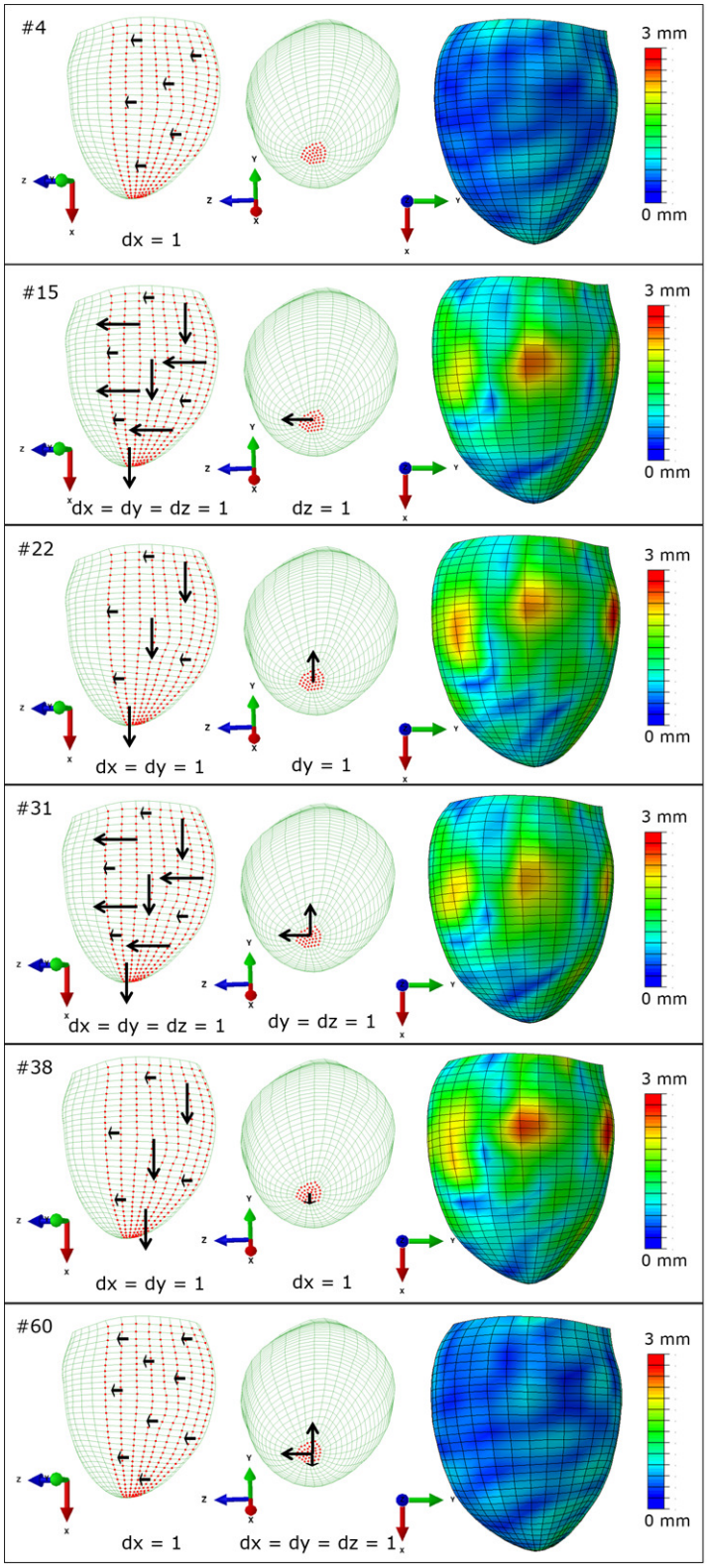

FIGURE 6.17: LV models showing loading configurations and reference displacements for simulations: #4, #15, #22, #31, #38 and #60 used in the noise analysis. Reference displacements encode the magnitudes of displacement ($\sqrt{x^2 + y^2 + z^2}$).

The number of cases that converged in less than 30 iterations, as well as the mean number of iterations ($\pm$ one standard deviation) required for convergence are shown in Table 6.3. Loading cases #60 and #4 resulted in the most accurate estimation of three- and five-parameters (Figure 6.17), respectively, in the loading test without noise. However, these cases also resulted in large normalised sensitivity values for the three-parameter formulation. The other four loading cases chosen (15, 22, 31 and 38, Figure 6.17) resulted in low cumulative sensitivity values for both methods. These four loading cases, with low parameter sensitivity to noise, converged in nearly all three-parameter simulations. Therefore, for the three-parameter formulation, there was a clear relationship between the parameter sensitivity to noise and the convergence. The five-parameter formulation converged in between 13 - 20 simulations out of 30 for these four loading cases. The convergence of the five-parameter formulation appeared to be uncorrelated with the parameter sensitivity to noise.

TABLE 6.3: Number of simulations in the Monte Carlo experiment (n = 30) that converged for the five- and three-parameter formulations, as well as the mean number of iterations for convergence ($\pm$ one standard deviation).

Simulation Number	5 Parameter Formulation	3 Parameter Formulation
4	19 (9.1 $\pm$ 3.8)	5 (16.4 $\pm$ 6.1)
15	20 (9.7 $\pm$ 5.6)	30 (5.1 $\pm$ 2.9)
22	20 (12.8 $\pm$ 7.5)	29 (6.8 $\pm$ 1.3)
31	17 (8.4 $\pm$ 4.7)	30 (4.5 $\pm$ 1.0)
38	13 (12.2 $\pm$ 6.0)	29 (6.1 $\pm$ 0.7)
60	21 (10.9 $\pm$ 6.0)	5 (18.0 $\pm$ 8.1)

Results from the simulations that converged are illustrated as box plots in Figures 6.18 and 6.19. In the five-parameter formulation, estimates of G_{12} and E_1 varied widely for two simulations. G_{13} was consistently estimated accurately with relatively small variance. E_3 values varied widely and were generally overestimated. Poisson's ratios were centred at the reference value (ν_{31} = 0.4999) but varied by up to 40%. In the three-parameter formulation, the resulting estimated parameters for the four loading cases with low sensitivity to noise resulted in estimated values with very little variance but the means were offset from the reference values. Only loading cases #4 and #60 showed large variance in estimated values of τ.

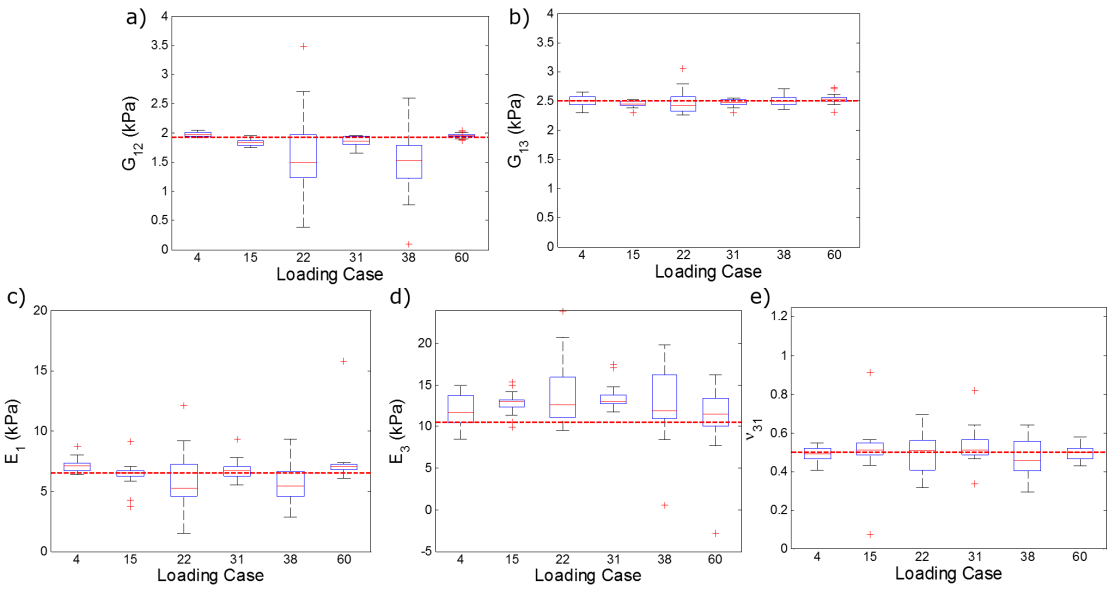

FIGURE 6.18: Results from all converged Monte Carlo simulations, using the five-parameter formulation, for six LV loading cases showing a) transverse shear moduli (G_{12}), b) fibre shear moduli (G_{13}), c) transverse Young's moduli (E_1), d) fibre Young's moduli (E_3) and e) fibre-transverse Poisson's ratio (ν_{31}). Reference values are shown as red dotted lines.

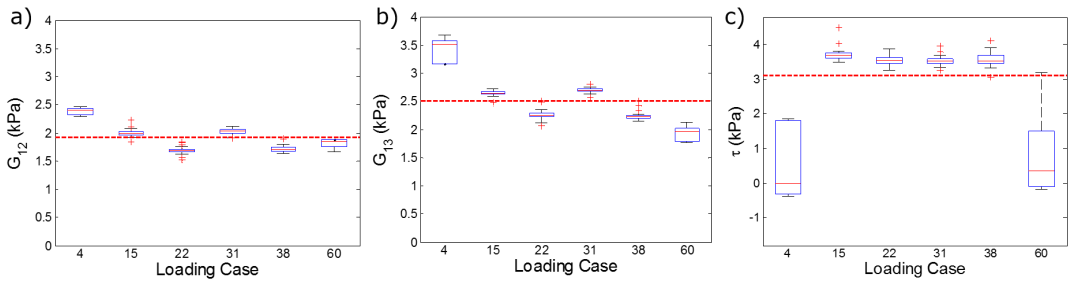

FIGURE 6.19: Results from all converged Monte Carlo simulations, using the three-parameter formulation, for six LV loading cases showing a) transverse shear moduli (G_{12}), b) fibre shear moduli (G_{13}) and c) anisotropic tensile ratio (τ). Reference values are shown as red dotted lines.

Superposition of Loading Cases One previous study on the identification of transversely isotropic material properties from slow and fast shear waves [149] has shown improvement of identification when several displacement fields, corresponding to different excitation boundary conditions, were superimposed. To test this, wave fields which resulted in accurate estimation of single parameters, in either the three- or five-parameter formulation, were superimposed. From these superimposed wave fields, three and five parameters were estimated. Table 6.4 shows simulations which resulted in the most accurate parameter estimates for each parameter shown to its left.

The reference displacement fields were then superimposed (column-wise in Table 6.4) for the three- and five-parameter formulations, respectively, prior to estimating parame-

TABLE 6.4: Loading configurations resulting in the most accurate parameter estimates for the five- and three-parameter formulations.

3 Parameter Formulation		5 Parameter Formulation	
Parameter	Simulation Number	Parameter	Simulation Number
G_{12}	7	G_{12}	25
G_{13}	14	G_{13}	7
τ	28	E_1	57
		E_3	4

ters. In this LV experiment, the superposition of reference displacement fields did improve accuracy of parameter estimates. Results from individual simulations as well as the combined displacement field are shown in Tables 6.5 and 6.6. However, some of the more complicated loading conditions studied also provided good results, so that superposition did not necessarily give any more information than a complex loading case on its own.

TABLE 6.5: Resulting parameter estimates from the three-parameter formulation for simulations #7, #14, #28 and the superimposed combination of those displacement fields.

Displacement Field	G_{12}	G_{13}	τ
Reference	1.92 kPa	2.50 kPa	3.11 kPa
#7	1.92 kPa	2.54 kPa	3.92 kPa
#14	2.01 kPa	2.48 kPa	2.31 kPa
#28	1.91 kPa	2.31 kPa	3.16 kPa
Combined	1.82 kPa	2.30 kPa	3.49 kPa

TABLE 6.6: Resulting parameter estimates from the five-parameter formulation for simulations #4, #7, #25, #57 and the superimposed combination of those displacement fields.

Displacement Field	G_{12}	G_{13}	E_1	E_3	ν_{31}
Reference	1.92 kPa	2.50 kPa	6.50 kPa	10.50 kPa	0.4999
#4	1.93 kPa	2.51 kPa	6.51 kPa	10.55 kPa	0.4999
#7	1.92 kPa	2.50 kPa	6.53 kPa	10.87 kPa	0.4999
#25	1.92 kPa	2.51 kPa	6.51 kPa	10.65 kPa	0.4999
#57	1.92 kPa	2.50 kPa	6.50 kPa	10.65 kPa	0.4999
Combined	1.90 kPa	2.49 kPa	6.43 kPa	10.58 kPa	0.4999

Varying Gaussian Noise Varying amounts of noise were added to the reference displacement field for one loading case (#15) and parameters were estimated using the five- and three-parameter formulations. The percentage, which defines the ratio between the standard deviation of noise (σ_{noise}) to the standard deviation of the displacements (σ_{disp}) as shown in Equation (6.21), was varied between 15% - 50%. As the amount of Gaus-

sian noise was increased, the standard deviation of estimated parameters generally increased and the means remained the same. In the five-parameter formulation, on average, 19 out of 30 simulations in each Monte Carlo experiment converged, and there was no trend seen between the amount of noise and the number of converged simulations. In the three-parameter formulation, either 29 or 30 out of 30 simulations converged, which also illustrated that there was no impact of the additional noise on convergence. τ and E_3 were consistently overestimated for each amount of Gaussian noise in the three- and five-parameter formulations, respectively.

Box plots of the resulting parameter estimates with each amount of noise are shown in Figures 6.20 and 6.21.

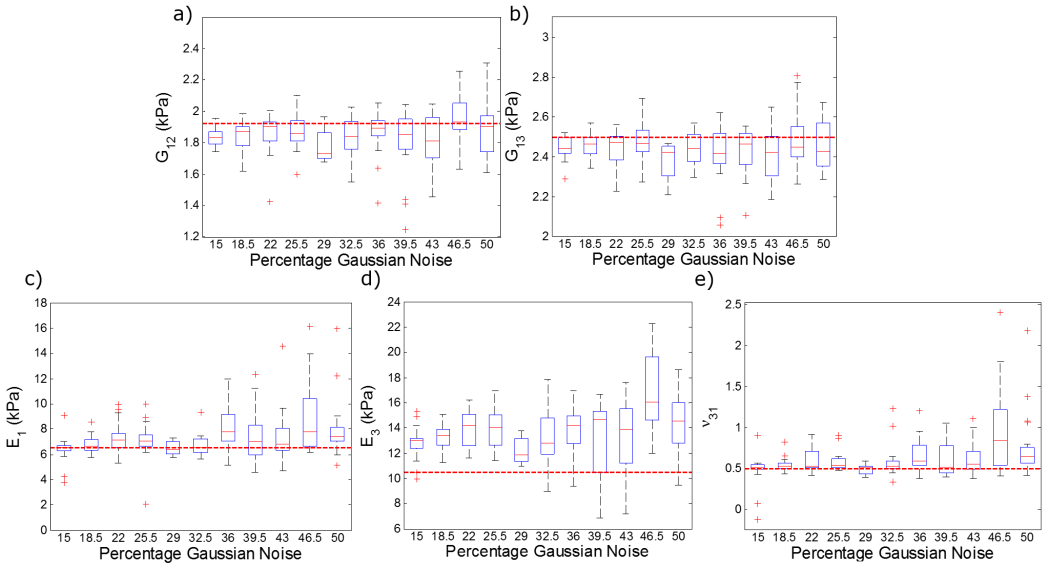

FIGURE 6.20: Resulting estimated values of a) G_{12}, b) G_{13}, c) E_1, d) E_3 and e) ν_{31} using the five-parameter formulation with varying amounts of Gaussian noise (N = 15% - 50%) added to the reference displacements. Reference values are shown as red dotted lines.

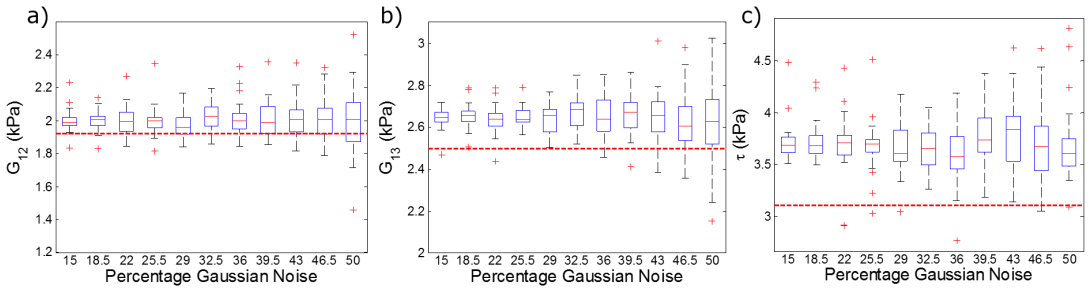

FIGURE 6.21: Resulting estimated values of a) G_{12}, b) G_{13} and c) τ using the three-parameter formulation with varying amounts of Gaussian noise (N = 15% - 50%) added to the reference displacements. Reference values are shown as red dotted lines.

The coefficient of variation, calculated as $\sigma/\overline{x}$, was plotted (Figure 6.22) for each pa-

rameter versus the amount of Gaussian noise added to the reference displacements in order to compare the change in relative variances. Linear regressions were computed for each parameter in order to illustrate the general trend with increasing Gaussian noise.

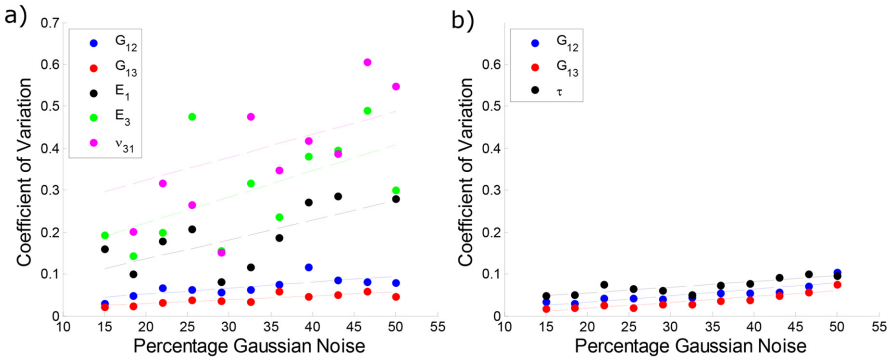

FIGURE 6.22: Coefficients of variation of estimated parameters in the a) five-parameter and b) three-parameter formulation plotted versus amount of Gaussian noise added to the reference displacements (N = 15% - 50%).

G_{12} and G_{13}, estimated by both methods, resulted in small coefficients of variation, which only increased minimally as the amount of Gaussian noise increased. Additionally, τ also resulted in small coefficients of variation over all amounts of noise. Conversely, E_1, E_3 and ν_{31} had larger coefficients of variation, which increased at a greater rate as the amount of noise increased, marked by larger slopes in the linear regressions. These results, in agreement with the parameter sensitivity values shown in Figures 6.15 and 6.16, support the definition of η as a measure of the sensitivity of the method to Gaussian noise in the signal.

Initial Parameter Estimate As was mentioned in the previous section on the formulation and implementation, the anisotropic optimised VFM is an iterative method which requires initial parameter estimates. All results thus far from experiments with Gaussian noise added to the reference displacement fields have utilised a random initial estimate for each parameter which was chosen from a Gaussian distribution centred at the true value with a standard deviation equal to 20% of the reference value. Without noise, the loading test was run using the true parameters as the initial estimates. As a comparison, both five and three parameters were estimated for the LV model without Gaussian noise using all 63 loading conditions. Varying the initial estimate did not have an impact on the number of iterations until convergence for the three-parameter material formulation. However, with the five-parameter material model, varying the initial estimate increased the number of iterations until convergence from two to three. Additionally, all final estimated parameters for both the three- and five-parameter formulations were identical to those estimated when the initial estimates were the true values. Therefore, it can be deduced that varying the

initial parameter estimate had neither an impact on the resulting values nor a significant effect on the number of iterations until convergence.

Frequency Analysis The experiments run to this point have all used reference displacement fields obtained by applying a harmonic displacement at 80 Hz since this frequency has previously been used with *in vivo* cardiac MRE experiments [98, 99]. However, more wavelengths can be obtained in the volume by increasing the frequency of excitation. To test the impact on parameter identification, a sweep of frequencies from 60 Hz - 200 Hz was analysed and both the three- and five-parameter formulations of the optimised VFM were used to estimate anisotropic material properties using the loading condition from simulation #15.

Without added Gaussian noise, the estimated values of the shear moduli and Young's moduli varied over the frequency range but there was no clear difference in parameter estimates with increasing frequency. However, when the normalised parameter sensitivity values were plotted versus frequency (Figure 6.23), it was apparent that the sensitivity of C_{11}, C_{33} and C_{13} decreased significantly for the five-parameter formulation as the frequency of excitation increased. There was no trend in sensitivity values versus frequency in the three-parameter formulation. However, overall sensitivity was lowest at 80 Hz. Since calculation of parameter sensitivity values includes the estimated parameters, Q^{app}, (see Equation (6.13)) normalised parameter sensitivity values cannot be directly compared between the five- and three-parameter formulations.

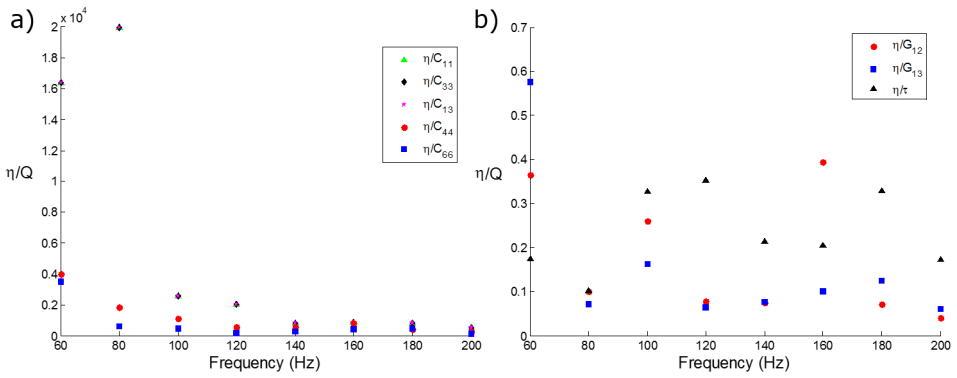

FIGURE 6.23: Normalised parameter sensitivity values are plotted versus the excitation frequency for both the a) five-parameter and b) three-parameter formulation. Note that in a) the sensitivity values are overlapping for η/C_{11}, η/C_{33} and η/C_{13}. Consequently, only those for η/C_{13} can be seen.

Gaussian noise was added to the reference displacements and a Monte Carlo simulation (n = 30) was run for each frequency. Table 6.7 shows the number of simulations that converged, out of 30, as well as the mean number of iterations until convergence ($\pm$ one standard deviation). It can be seen that as the frequency increased, the number of converged

simulations for the five-parameter formulation also increased. Conversely, no simulations converged for the three-parameter formulation at 160 Hz, 180 Hz and 200 Hz.

TABLE 6.7: The number of simulations in the Monte Carlo experiment (n = 30) that converged for the five- and three-parameter formulations are shown as well as the mean number of iterations for convergence ($\pm$ one standard deviation).

Frequency	5 Parameter Method	3 Parameter Method
60 Hz	15 (13.7 $\pm$ 7.5)	27 (12.1 $\pm$ 4.5)
80 Hz	20 (9.7 $\pm$ 5.6)	30 (5.1 $\pm$ 2.9)
100 Hz	16 (11.1 $\pm$ 5.5)	30 (5.2 $\pm$ 1.7)
120 Hz	18 (9.7 $\pm$ 3.9)	20 (10.2 $\pm$ 5.3)
140 Hz	19 (9.1 $\pm$ 2.7)	26 (11.0 $\pm$ 2.9)
160 Hz	17 (8.7 $\pm$ 3.5)	0 (NA)
180 Hz	23 (11.4 $\pm$ 7.2)	0 (NA)
200 Hz	28 (10.2 $\pm$ 5.1)	0 (NA)

Figures 6.24 and 6.25 show box plots of the resulting estimated material parameters for the five- and three-parameter formulations, respectively. With the five-parameter material formulation, G_{13} was most accurately estimated and had the smallest variance at 200 Hz. However, estimated values of E_3 showed the most variation at 200 Hz. At 100 Hz and 160 Hz, G_{12} and E_1 were underestimated. Similar to results when varying loading conditions were applied, estimated Poisson's ratios were centred at the true values yet varied widely. With the three-parameter formulation, loading at 80 Hz resulted in the most accurate estimation of all three parameters: G_{12}, G_{13} and τ. Results at 60 Hz showed the largest variance compared with resulting estimated parameters at other frequencies.

A greater number of wavelengths, induced by applying a higher excitation frequency, resulted in a lower sensitivity to noise in the five-parameter formulation. Conversely, the three-parameter formulation did not converge for any simulations at higher frequencies despite the fact that the sensitivity plots did not reveal any trend in parameter sensitivity values with increasing frequency. This could be due to the fact that the three-parameter formulation does not accurately model the wave propagation in the LV at higher frequencies, suggesting that the bulk modulus may have a greater effect on dynamic deformations at higher frequencies.

At higher frequencies, more wavelengths were present in the LV. However, mesh resolution was not altered. Therefore, there were less elements per wavelength with which to estimate material properties. Although both material parameter formulations would have been affected by low mesh resolution, the three-parameter formulation may have been more sensitive to this. To test this, the same frequency test could be carried out with a finer LV mesh. Inspecting the parameters (G_{12}, G_{13} and τ) during the course of the 30 iterations,

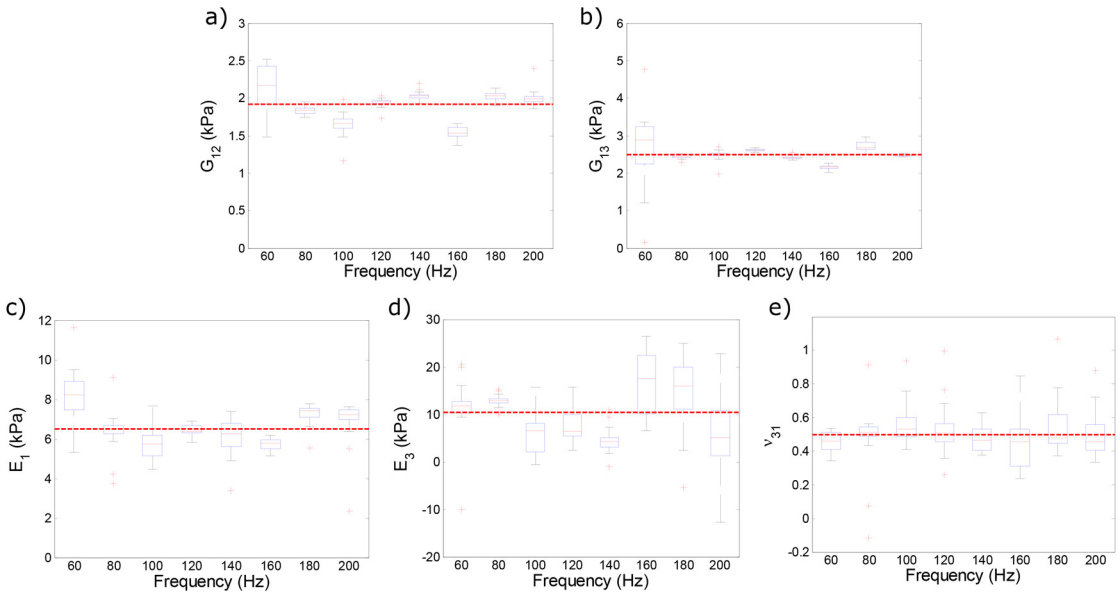

FIGURE 6.24: Results from all converged Monte Carlo simulations, using the five-parameter VFM, for frequencies between 60 Hz - 200 Hz showing a) transverse shear moduli (G_{12}), b) fibre shear moduli (G_{13}), c) transverse Young's moduli (E_1), d) fibre Young's moduli (E_3) and e) fibre-transverse Poisson's ratio (ν_{31}). The reference values are shown by red dotted lines.

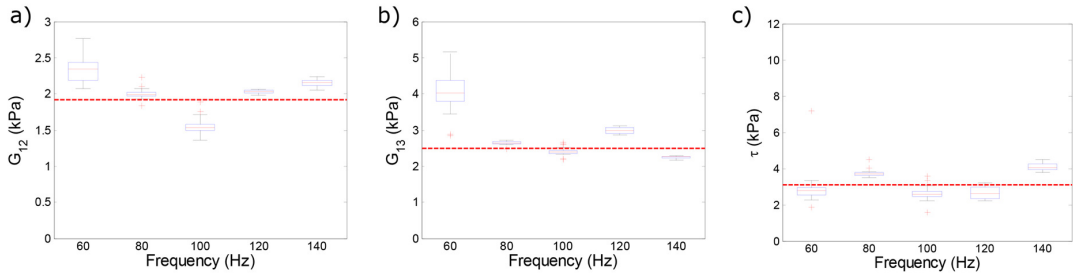

FIGURE 6.25: Results from all converged Monte Carlo simulations, using the three-parameter VFM, for frequencies between 60 Hz - 140 Hz showing a) transverse shear moduli (G_{12}), b) fibre shear moduli (G_{13}) and c) anisotropic tensile ratio (τ). The reference values are shown by red dotted lines.

it was clear that the result would not have been affected by changing the maximum number of iterations (= 30). Parameters varied widely between consecutive iterations and did not appear to be convergent.

6.3 Discussion

In both the five- and three-parameter formulations of the VFM for parameter estimation applied to MRE phantom data, the mean estimated shear moduli were similar to those estimated for the same phantom using the MMDI (5.45 kPa), FEMU (5.55 kPa) and DF-LFE (5.34 kPa) methods. However, variance in estimated parameters over the sub-regions was

dependent on the arbitrarily assigned material orientation, and subsequently, the magnitude of displacements used to calculate each parameter. All estimated values for G_{12}, G_{13} and τ in the phantom were within physical limits and were centred around the reference values, whereas values of E_3 and ν_{31} showed large variance and were sometimes outside of physical ranges. Therefore, with the phantom data, the three-parameter formulation gave the most accurate results. In future studies, multiple experiments will be run with varying loading conditions on the phantom in order to investigate parameter estimation with superposition of multiple displacement fields [149].

Implementation of the anisotropic optimised VFM with the LV model illustrated the capability of its application to cardiac MRE. The heart presents challenges such as its thin-walled geometry and complex fibre architecture. However, it was shown in this study that accurate results can be obtained given knowledge of the material orientations (from DTI, rule based methods or histology), the geometry from MRI images, and an appropriate loading condition.

Without Gaussian noise, the five-parameter material model resulted in more accurate estimation of parameters over all the loading cases. If a Poisson's ratio was chosen closer to 0.5, such as 0.499999999, the three-parameter method may have provided better results. Also, it may be a result of the complex geometry of the left ventricular model. An investigation into the impact of loading was also carried out in a simple cantilever beam geometry (results not shown). In the beam results, the three-parameter formulation resulted in more accurate parameter estimates than the five-parameter formulation. Therefore, the thin-walled LV geometry may have an adverse impact on the estimation of τ (in the three-parameter formulation) due to lack of wavelengths in the transmural direction.

The five-parameter formulation only converged in between 13-20 (out of 30) simulations in each Monte Carlo experiment. Several alternative convergence criteria, such as only measuring change between consecutive estimated shear moduli, were also tested (data not shown). However, none of the methods tested increased the number of simulations that converged. This could be due to the fact that the optimisation matrix (Equation (6.15)) contains each of the approximate parameters, Q^{app}. If one value in Q^{app} varies widely from iteration to iteration (e.g. one that is dependent on Poisson's ratio), then all virtual displacement fields will be affected (i.e. $\mathbf{u}^{*1}$, $\mathbf{u}^{*2}$, $\mathbf{u}^{*3}$, $\mathbf{u}^{*4}$ and $\mathbf{u}^{*5}$). Therefore, one future development could be to formulate the optimisation matrix, H, in a way which does not depend on C_{11}^{app}, C_{33}^{app} and C_{13}^{app}.

Isotropic myocardial shear stiffness has previously been measured from MRE experiments [5, 44, 77, 98, 99, 163] and so it is assumed that sufficient wave propagation in the heart can be achieved experimentally. Additionally, it is known that the heart undergoes nonlinear deformation throughout the cardiac cycle. However, with an 80 Hz excitation frequency, it can be assumed that the myocardium is stationary since motion of the heart due

to the cardiac cycle is on the order of 1 Hz. Therefore, only the small amplitude harmonic deformations are taken into account. The loading conditions applied to the LV model in this experiment do not necessarily represent the exact harmonic motion that would occur in the LV during cardiac MRE. However, the anterior and apical surfaces were chosen since, in cardiac MRE experiments, waves generally propagate from the anterior surface through the myocardium to the posterior free wall. Depending on driver placement, waves have also been observed travelling from the apex towards the base. This was an initial test of feasibility to estimate transversely isotropic properties in a realistic LV geometry with a physiological fibre field in the presence of noise.

Current methods for estimating myocardial stiffness in-vivo require invasive pressure measurements to estimate hyperelastic non-linear quasi-static material parameters by matching modelled inflation to the cardiac geometry measured from MR images given the pressure loading conditions [162, 166]. Despite measuring linear elastic versus hyperelastic material properties, MR elastography provides a non-invasive means of measuring linear dynamic cardiac tissue stiffness, eliminating the need for invasive LV pressure measurements. This study shows the feasibility of non-invasively estimating linearly elastic transversely isotropic material properties from harmonic displacement fields in an LV model.

Two recent studies [149, 150] estimated transversely isotropic properties using simulated harmonic displacements. Tweten et al. [149] estimated anisotropic parameters to within 25% without added noise in a simple cubic geometry. Our study aimed to verify that similar results could be obtained in an LV geometry with complex fibre architecture. In the absence of noise, all parameters were identified to within 33% of the reference values. In this study, when Gaussian noise was added to the reference displacement fields, moduli estimated with the three-parameter formulation in the LV model were consistently either over- or underestimated. One possible cause may be the limited mesh resolution in the LV model. A previous study [29] reported that the accuracy of isotropic parameter estimates using the optimised VFM is dependent on the number of elements per wavelength. Eight elements per wavelength resulted in approximately 5% error in the estimation of an isotropic shear modulus. In some regions of the LV model, there are as few as four elements per wavelength, depending on the loading configuration. Additionally, any nodes on the boundary of the FE model were prescribed a virtual displacement of zero since traction forces were unknown. Thus, in the LV model, there were only three free nodes in the transmural direction with which to estimate the wavelength, which may not be sufficient.

It is known that both fast and slow shear waves must be present to accurately identify transversely isotropic material properties. However, with the complex fibre distribution in the LV, it may be that fast (or slow) shear waves do not exist in all regions of the myocardium for a given loading condition, which may give rise to errors in parameter estimation. One previous study used superposition of fast and slow shear waves to test

anisotropic inversion methods [149]. Similarly, further tests could be carried out in which displacement fields from the 63 loading conditions in the LV model could be superimposed to estimate the transversely isotropic material properties. *In vivo*, however, complex and multiple loading cases may be difficult to acquire as there are limited options for passive driver placement on the chest wall. However, superposition of displacement fields may provide more accurate parameter estimates.

The results from this study showed that the accurate identification of material parameters using MRE data interpreted with the optimised VFM is largely dependent on the loading configuration as well as the formulation of the constitutive relation. Both the three- and five-parameter formulations were affected differently by the waves present in the material, as is illustrated by the parameter sensitivities to noise for each loading condition. In general, the parameters C_{11}, C_{33} and C_{13}, and subsequently E_1, E_3 and ν_{31}, were much more sensitive to noise than the shear moduli using the five-parameter material formulation. This was expected since the parameters in the upper left quadrant of the elasticity matrix (C_{11}, C_{33} and C_{13}) are dependent on accurate estimation of the longitudinal wavelength, which is much longer than the object of interest in nearly incompressible media. In the three-parameter formulation, all three parameters showed relatively similar parameter sensitivities to noise. When loading conditions that resulted in low parameter sensitivity values were selected, all or nearly all simulations converged in the presence of Gaussian noise. Conversely, the five-parameter formulation converged in just over half of the Monte Carlo runs, and convergence appeared to be less dependent on the parameter sensitivity. As frequency increased, there was a significant decrease in parameter sensitivity to noise of C_{11}, C_{33} and C_{13} in the five-parameter formulation. The decrease in parameter sensitivity at higher frequencies resulted in a greater number of converged runs in the Monte Carlo test with Gaussian noise.

Overall, these results show the feasibility of estimating transversely isotropic material properties from simulated harmonic displacements in the LV model as well as from MRE displacements measured from an isotropic phantom using the anisotropic optimised VFM. Unlike other inversion methods, the optimised VFM does not assume that the medium is isotropic and infinite and does not require calculation of high order derivatives of the displacement field, compared to direct inversion methods. Additionally, the three-parameter formulation bypasses the need to estimate the longitudinal wavelength. In future studies, these methods will be applied to estimate *in vivo* anisotropic myocardial mechanical properties non-invasively, given diffusion tensor MRI as well as MRE images.

7

CONCLUSIONS

7.1 Summary

IN this thesis, two anisotropic inversion methods were investigated, a boundary value finite element model update (FEMU) method as well as an optimised virtual fields method (VFM), to estimate global transversely isotropic material properties from magnetic resonance elastography (MRE) data given knowledge of the local material orientations.

Firstly, Chapter 4 quantified the relative identifiability of transversely isotropic material parameters and showed that, despite the error function having a unique minimum, not all parameters were equally identifiable. The fibre Poisson's ratio (ν_{31}) was least identifiable whereas the fibre shear modulus (G_{13}) was most identifiable. However, setting the Poisson's ratio did not significantly improve the accuracy of identified parameters in the presence of Gaussian noise.

Secondly, analytic and optimised virtual fields methods were implemented in conjunction with a constitutive relation that separated contributions of the bulk and shear stresses (Equation (5.12)). Chapter 5 showed that, even in the isotropic case, the sensitivity of the method to Gaussian noise was dependent on the loading condition applied. The analytic VFM resulted in accurate shear moduli estimates for the isotropic phantom when compared with results from the FEMU, MMDI (multi-model direct inversion) and DF-LFE (directional filter and local frequency estimation) methods. However, resulting damping coefficients were often negative, illustrating that the model of damping used (a complex modulus carrying a loss coefficient) may not accurately describe the damping behaviour within the phantom. With the analytic VFM, it was shown that accurate estimates of the complex shear modulus were obtained when the chosen virtual displacement field pattern closely matched the measured displacement field.

Analytic virtual fields are difficult to develop for complex geometries such as the heart. Therefore, the optimised VFM [291] was investigated in order to directly solve for a virtual

displacement field, which minimises the variance in the estimated shear modulus. One primary difference between the VFM implemented in this thesis and previous studies [29, 117] is that, in this study, complex measured displacement fields were used in order to estimate a single complex shear modulus rather than viscoelastic material properties at discretised time points. Estimating complex parameters is faster since it requires solving the inverse problem only once. For both the cantilever beam and LV models, the optimised VFM accurately estimated the complex shear modulus over a range of loading conditions. However, in the presence of Gaussian noise, accurate estimation was dependent on the loading configuration. Each loading configuration showed a different parameter sensitivity to noise and the standard deviation of estimated parameters, not the error, was correlated with the parameter sensitivity.

When applying the complex optimised VFM to the phantom MRE data, estimated values over each subzone agreed well with shear moduli estimated using three other inversion methods: FEMU, MMDI and DF-LFE. Compared to the cantilever beam geometry, estimated shear moduli and damping coefficients, in the presence of Gaussian noise, showed more variation in the LV model, which is most likely due to there being fewer free nodes in the LV compared to the beam geometry. Overall, Chapter 6 showed that the optimised VFM could be used to estimate a complex isotropic shear modulus for a) simulated displacements in a cantilever beam geometry, b) experimental phantom MRE data and c) simulated harmonic displacements in a realistic canine LV geometry.

Finally, Chapter 6 extended the optimised VFM to estimate transversely isotropic material properties from complex harmonic displacement fields using two different material models, estimating either five or three parameters. Similar to Chapter 5, both material formulations were used to estimate transversely isotropic properties in a) a cantilever beam geometry with fibres aligned down the length of the beam, b) experimental phantom MRE data with two arbitrarily assigned material orientations and c) a canine LV geometry with fibre orientations measured from histology. Loading tests were performed with both the cantilever and LV geometric models in order to compare parameter sensitivity to noise for each loading case. It was shown that parameter sensitivity did not predict estimation error.

In nearly all simulations, a driving frequency of 80 Hz was specified since previous cardiac MRE experiments have been performed at this frequency. In addition, a frequency sweep was performed and transversely isotropic parameters were estimated at frequencies between 60 Hz - 200 Hz. The five-parameter estimation method improved with increasing frequency, most likely due to the fact that more wavelengths were included in the volume with increasing frequency. Tests also showed that the optimised VFM was insensitive to the initial parameter estimates.

In summary, accuracy as well as variance in the estimated parameters is largely dependent on the loading configuration applied. Estimation using the three-parameter model

seems more robust at 80 Hz, but the five-parameter formulation may perform better at higher frequencies. Results from Chapter 6 show that estimating transversely isotropic material parameters in the LV is feasible given knowledge of the fibre orientations (e.g. using DTI) and a sufficient loading condition. However, the LV presents challenges since it has a complex geometry as well as varying fibre orientation. Therefore, inducing both fast and slow shear waves *in vivo* may be challenging.

7.2 Contributions to the Field

Although numerous other inversion methods exist, both for isotropic and anisotropic materials, many make assumptions, such as incompressibility and waves travelling in an infinite medium. In this thesis, the boundary value FEMU method avoided both of these assumptions since it took into account the boundary of the structure and included estimation of a Poisson's ratio. To the author's knowledge, this was the first study to quantify identifiability of transversely isotropic parameters from simulated and measured MRE data.

Chapter 5 provided a robust analysis of various loading conditions applied to a cantilever beam as well as a LV model. These results could be used to drive future studies and provide suggestions on optimal driver design and placement for cardiac MRE studies. The optimal load, resulting in the most accurate parameter estimation, contained a longitudinal displacement on the anterior face of the LV (in the x-direction). Current pneumatic drivers in cardiac MRE induce a compression load, which displaces the tissue in the radial direction on the anterior face. This study showed that shear parameter estimates could be improved by altering the loading delivered to the myocardium.

In Chapter 6, an anisotropic inversion method was introduced that a) does not rely on high order derivatives of the displacement field, b) takes into account complex fibre architecture (such as in myocardium) and c) weights all data points equally. Two material model formulations were implemented. The first estimated all five independent terms of the elasticity matrix for a transversely isotropic material. Each of the terms was complex and carried an associated damping coefficient. The second constitutive relation was organised in a way that dissociated the bulk term. It was shown that the optimised VFM shows promise as a fast, accurate inversion method for estimating anisotropic material properties from *in vivo* MRE displacement fields.

7.3 Limitations

One limitation is that MRE provides an estimate of material properties at an instance by measuring harmonic displacements about a deformed state. In myocardiu, the deformed state is nonlinearly dependent on the loading condition (i.e. cavity pressure). Therefore, in-

terpreting the parameters requires knowledge of, and controlling for, the state of ventricular loading. At this point, material parameters estimated from MRE provide only "effective" stiffness.

It was noted that for the isotropic and anisotropic optimised VFM results, parameter sensitivity to noise was correlated with the standard deviation of the estimated values from the Monte Carlo simulation, but was not correlated with error. Therefore, loading configurations that have little sensitivity to noise may not produce accurate results with the optimised VFM yet will have small variance. This could be due to the derivation of the parameter sensitivity matrix, for which it is assumed that $E(X) = X$. If estimated parameters in the presence of noise are not centred around the true value, then this assumption is no longer valid and presents a major limitation to this method.

Another limitation of the VFM is the necessity of having full-field deformation measurements. Cardiac MRE experiments generally obtain between 1 - 6 short axis MRE slices, which do not provide displacement fields over the entire LV volume. Therefore, either the optimised VFM must be applied over a portion of the volume that contains displacement information or displacements must be interpolated at all points in the model. It was shown in [29] that the acccuracy of the isotropic VFM increased with a greater number of free nodes. Reducing the amount of displacement information reduces the specificity of the method. High resolution *in vivo* MRE images are difficult to obtain due to long scan times. However, with improvements in MRE sequences, higher resolution images (with potentially isotropic voxel sizes [5]) can be obtained, providing enough information to make the optimised VFM a reliable inversion method for estimating anisotropic properties of myocardium.

An additional limitation is that the methods tested to this point have assumed knowledge of the fibre orientations. *In vivo* DTMRI is being developed but is not yet available in clinical practice. Advances in DTMRI sequences will be necessary in order to acquire the information needed to estimate anisotropic material properties. Conversely, a rule-based fibre model could be used, assuming that the patient has no pathologies that alter the fibre orientations.

7.4 Future Work

In future studies, an anisotropic phantom (e.g. [25, 109]) as well as biological anisotropic media, such as bovine muscle, could be used to further validate these results and other inversion methods utilising MRE, DTI and SSFP data. Additionally, the methods can be applied for the estimation of both isotropic and anisotropic material properties from *in vivo* porcine MRE images.

A

FINITE ELEMENT STRAIN FORMULATIONS

TRILINEAR hexahedral (brick) elements were used in all FE models in this thesis. A Cartesian natural coordinate system (ξ, η, ζ) was used and linear shape functions ($\mathbf{N}$) were applied to relate element displacement to nodal displacements. For this thesis, three different element types were implemented and investigated: C3D8F, C3D8R and C3D8. The defining differences between them are the ways that nodal displacements are mapped to element strains at either the element centroid or the Gauss points.

C3D8F Elements For C3D8F elements, the shape functions, $\mathbf{N}$, can be summarised in a single expression by:

$$N_i^e = \frac{1}{8}(1 + \xi\xi_i)(1 + \eta\eta_i)(1 + \zeta\zeta_i) \tag{A.1}$$

where ξ, η and ζ ([-1,1]) represent the coordinates of the integration points in the natural coordinate system.

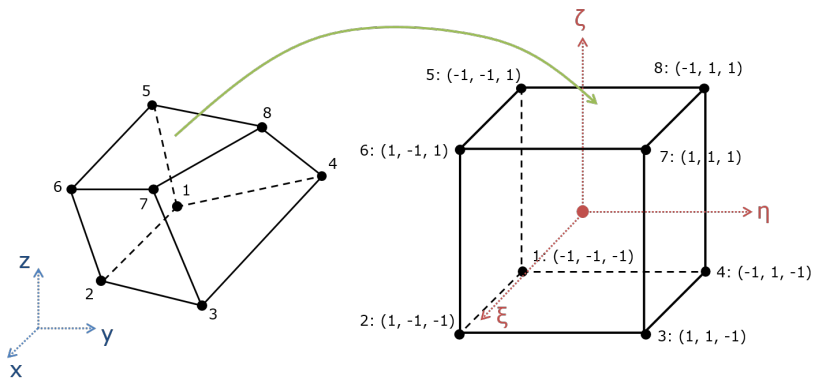

FIGURE A.1: Illustration of a hexahedral element with eight nodes in the global coordinate system and the natural coordinate system.

In this element formulation, Gaussian quadrature is used to define locations of integration points. Therefore, the FE equations are solved at either 1, 8 or 27 integration points within the element. Individually, the shape functions are written as:

$$
\begin{aligned}
N_1 &= \frac{1}{8}(1-\xi)(1-\eta)(1-\zeta) \\
N_2 &= \frac{1}{8}(1+\xi)(1-\eta)(1-\zeta) \\
N_3 &= \frac{1}{8}(1+\xi)(1+\eta)(1-\zeta) \\
N_4 &= \frac{1}{8}(1-\xi)(1+\eta)(1-\zeta) \\
N_5 &= \frac{1}{8}(1-\xi)(1-\eta)(1+\zeta) \\
N_6 &= \frac{1}{8}(1+\xi)(1-\eta)(1+\zeta) \\
N_7 &= \frac{1}{8}(1+\xi)(1+\eta)(1+\zeta) \\
N_8 &= \frac{1}{8}(1-\xi)(1+\eta)(1+\zeta)
\end{aligned}
\tag{A.2}
$$

The matrix of shape functions is:

$$
\mathbf{N} = \begin{bmatrix} \mathbf{N_1} & \mathbf{N_2} & \mathbf{N_3} & \mathbf{N_4} & \mathbf{N_5} & \mathbf{N_6} & \mathbf{N_7} & \mathbf{N_8} \end{bmatrix} \tag{A.3}
$$

where

$$
\mathbf{N_i} = \begin{bmatrix} N_i & 0 & 0 \\ 0 & N_i & 0 \\ 0 & 0 & N_i \end{bmatrix} \tag{A.4}
$$

The element strain, for any element type, is generally calculated as:

$$\boldsymbol{\epsilon} = \mathbf{B}\mathbf{u}_e \tag{A.5}$$

where $\mathbf{B}$ is the strain matrix which relates nodal displacements to element strain and $\mathbf{u}_e$ is a vector of nodal displacements in the orthogonal directions of the global coordinate system. The matrix is composed of the partial derivatives of the shape functions with respect to the global Cartesian directions:

$$\mathbf{B_i} = \begin{bmatrix} \partial N_i/\partial x & 0 & 0 \\ 0 & \partial N_i/\partial y & 0 \\ 0 & 0 & \partial N_i/\partial z \\ \partial N_i/\partial y & \partial N_i/\partial x & 0 \\ \partial N_i/\partial z & 0 & \partial N_i/\partial x \\ 0 & \partial N_i/\partial z & \partial N_i/\partial y \end{bmatrix} \tag{A.6}$$

and

$$\mathbf{B} = \begin{bmatrix} \mathbf{B_1} & \mathbf{B_2} & \mathbf{B_3} & \mathbf{B_4} & \mathbf{B_5} & \mathbf{B_6} & \mathbf{B_7} & \mathbf{B_8} \end{bmatrix} \tag{A.7}$$

Since the partial derivatives of the shape functions with respect to the global Cartesian coordinates are not known directly, they can be calculated using the chain rule. The partial derivatives of the shape functions with respect to the natural coordinates (ξ, η, ζ) as well as the partial derivatives of the global nodal coordinates with respect to the natural coordinates can both be calculated.

The derivatives of shape functions with respect to the global coordinates are derived as follows:

$$\begin{Bmatrix} \partial N_i/\partial x \\ \partial N_i/\partial y \\ \partial N_i/\partial z \end{Bmatrix} = [J]^{-1} \begin{Bmatrix} \partial N_i/\partial \xi \\ \partial N_i/\partial \eta \\ \partial N_i/\partial \zeta \end{Bmatrix} \tag{A.8}$$

where the Jacobian matrix, J, is:

$$[J] = \begin{bmatrix} \partial x/\partial \xi & \partial y/\partial \xi & \partial z/\partial \xi \\ \partial x/\partial \eta & \partial y/\partial \eta & \partial z/\partial \eta \\ \partial x/\partial \zeta & \partial y/\partial \zeta & \partial z/\partial \zeta \end{bmatrix} \tag{A.9}$$

The Jacobian matrix represents the linear transformation of the element from global coordinates to natural coordinates. The partial derivatives of x, y and z with respect to ξ, η and ζ are found by differentiation of coordinate locations expressed through shape functions and nodal coordinate values:

$$\begin{aligned}
\frac{\partial x}{\partial \xi} &= \sum \frac{\partial N_i}{\partial \xi} x_i, & \frac{\partial x}{\partial \eta} &= \sum \frac{\partial N_i}{\partial \eta} x_i, & \frac{\partial x}{\partial \zeta} &= \sum \frac{\partial N_i}{\partial \zeta} x_i \\
\frac{\partial y}{\partial \xi} &= \sum \frac{\partial N_i}{\partial \xi} y_i, & \frac{\partial y}{\partial \eta} &= \sum \frac{\partial N_i}{\partial \eta} y_i, & \frac{\partial y}{\partial \zeta} &= \sum \frac{\partial N_i}{\partial \zeta} y_i \\
\frac{\partial z}{\partial \xi} &= \sum \frac{\partial N_i}{\partial \xi} z_i, & \frac{\partial z}{\partial \eta} &= \sum \frac{\partial N_i}{\partial \eta} z_i, & \frac{\partial z}{\partial \zeta} &= \sum \frac{\partial N_i}{\partial \zeta} z_i
\end{aligned} \tag{A.10}$$

The Matlab code to calculate the strain matrix for C3DF elements is shown below.

```
% Evaluate the derivative of the shape functions at m, n, o
dN = 0.125*[-1*(1-n)*(1-o) (1-n)*(1-o) (1+n)*(1-o) -1*(1+n)*(1-o) ...
    -1*(1-n)*(1+o) (1-n)*(1+o) (1+n)*(1+o) -1*(1+n)*(1+o);...
-1*(1-m)*(1-o) -1*(1+m)*(1-o) (1+m)*(1-o) (1-m)*(1-o) ...
    -1*(1-m)*(1+o) -1*(1+m)*(1+o) (1+m)*(1+o) (1-m)*(1+o);
-1*(1-m)*(1-n) -1*(1+m)*(1-n) -1*(1+m)*(1+n) -1*(1-m)*(1+n) ...
    (1-m)*(1-n) (1+m)*(1-n) (1+m)*(1+n) (1-m)*(1+n)];

% Calculate Jacobian for current element
jac = dN*[X Y Z];

% Multiply inverse of jacobian times the derivative of shape ...
    functions
dNdXYZ = jac\dN;

% Determinant of Jacobian
detJ = det(jac);

% Calculate B matrix (strain matrix)
B = [];
for c = 1:nodesPerElem %Loop through number of nodes per element
    Bi = [dNdXYZ(1,c)     0              0; ...
          0            dNdXYZ(2,c)       0; ...
          0               0          dNdXYZ(3,c); ...
          dNdXYZ(2,c)  dNdXYZ(1,c)       0; ...
          dNdXYZ(3,c)     0          dNdXYZ(1,c); ...
          0            dNdXYZ(3,c)  dNdXYZ(2,c)];
    B = [B Bi];
end
```

C3D8R Elements Reduced integration elements (i.e. C3D8R elements) utilise a uniform strain formulation [48] so that the strain calculated is constant over the entire element. The FE equations are only solved once over for the element, rather than at multiple Gauss points.

The shape functions for the uniform strain element are written as:

$$N = \frac{1}{8}\Sigma + \frac{1}{4}\xi\Lambda_1 + \frac{1}{4}\eta\Lambda_2 + \frac{1}{4}\zeta\Lambda_3 + \frac{1}{2}\eta\zeta\Gamma_1 + \frac{1}{2}\xi\zeta\Gamma_2 + \frac{1}{2}\eta\xi\Gamma_3 + \frac{1}{2}\xi\eta\zeta\Gamma_4 \tag{A.11}$$

where

$$\begin{aligned}
\Sigma &= [+1,+1,+1,+1,+1,+1,+1,+1] \\
\Lambda_1 &= [-1,+1,+1,-1,-1,+1,+1,-1] \\
\Lambda_2 &= [-1,-1,+1,+1,-1,-1,+1,+1] \\
\Lambda_3 &= [-1,-1,-1,-1,+1,+1,+1,+1] \\
\Gamma_1 &= [+1,+1,-1,-1,-1,-1,+1,+1] \\
\Gamma_2 &= [+1,-1,-1,+1,-1,+1,+1,-1] \\
\Gamma_3 &= [+1,-1,+1,-1,+1,-1,+1,-1] \\
\Gamma_4 &= [-1,+1,-1,+1,+1,-1,+1,-1]
\end{aligned} \tag{A.12}$$

The strain matrix, $\mathbf{B}$, is calculated over the element as:

$$\mathbf{B} = \begin{bmatrix} x_J z_K \\ z_J x_K \\ x_J y_K \end{bmatrix} \mathbf{C} \tag{A.13}$$

where

$$\mathbf{C} = e_{ijk} \int\int\int \frac{\partial N_I}{\partial \xi} \frac{\partial N_J}{\partial \eta} \frac{\partial N_K}{\partial \zeta} d\xi d\eta d\zeta \tag{A.14}$$

.

Uppercase subscripts range from [1,8] and lowercase subscripts range from [1,3]. e_{ijk} represents the determinant of the 3 x 3 Jacobian matrix. It can be noted that $\mathbf{C}$ is the same for all hexahedra. Practically, this was implemented by solving for values in one column of the $\partial N_I / \partial X_i$ matrix and then permuting the nodal ordering to obtain the values for each subsequent column.

```
% Nodal permutations
np = [1 2 3 4 5 6 7 8; ...
      2 3 4 1 6 7 8 5; ...
      3 4 1 2 7 8 5 6; ...
      4 1 2 3 8 5 6 7; ...
      5 8 7 6 1 4 3 2; ...
      6 5 8 7 2 1 4 3; ...
      7 6 5 8 3 2 1 4; ...
```

```
9         8 7 6 5 4 3 2 1];
10
11 % Compile matrix of derivatives of shape functions with respect ...
       to X, Y and Z
12 dNdXYZ = zeros(3,8);
13 for i = 1:8
14     % Row 1
15     dNdXYZ(1,i) = 1/12 * ( y(np(i,2))* ((z(np(i,6)) - z(np(i,3))) ...
           - (z(np(i,4)) - z(np(i,5)))) + y(np(i,3)) * (z(np(i,2)) - ...
           z(np(i,4))) + y(np(i,4)) * ((z(np(i,3)) - z(np(i,8))) - ...
           (z(np(i,5)) - z(np(i,2)))) + y(np(i,5)) * ((z(np(i,8)) - ...
           z(np(i,6))) - (z(np(i,2)) - z(np(i,4)))) + y(np(i,6)) * ...
           (z(np(i,5)) - z(np(i,2))) + y(np(i,8)) * (z(np(i,4)) - ...
           z(np(i,5))) );
16
17     % Row 2
18     dNdXYZ(2,i) = 1/12 * ( z(np(i,2))* ((x(np(i,6)) - x(np(i,3))) ...
           - (x(np(i,4)) - x(np(i,5)))) + z(np(i,3)) * (x(np(i,2)) - ...
           x(np(i,4))) + z(np(i,4)) * ((x(np(i,3)) - x(np(i,8))) - ...
           (x(np(i,5)) - x(np(i,2)))) + z(np(i,5)) * ((x(np(i,8)) - ...
           x(np(i,6))) - (x(np(i,2)) - x(np(i,4)))) + z(np(i,6)) * ...
           (x(np(i,5)) - x(np(i,2))) + z(np(i,8)) * (x(np(i,4)) - ...
           x(np(i,5))) );
19
20     % Row 3
21     dNdXYZ(3,i) = 1/12 * ( x(np(i,2))* ((y(np(i,6)) - y(np(i,3))) ...
           - (y(np(i,4)) - y(np(i,5)))) + x(np(i,3)) * (y(np(i,2)) - ...
           y(np(i,4))) + x(np(i,4)) * ((y(np(i,3)) - y(np(i,8))) - ...
           (y(np(i,5)) - y(np(i,2)))) + x(np(i,5)) * ((y(np(i,8)) - ...
           y(np(i,6))) - (y(np(i,2)) - y(np(i,4)))) + x(np(i,6)) * ...
           (y(np(i,5)) - y(np(i,2))) + x(np(i,8)) * (y(np(i,4)) - ...
           y(np(i,5))) );
22 end
23
24 % Calculate B matrix (strain matrix)
25 B = [];
26 for c = 1:size(dNdXYZ,2) %Loop through number of nodes per element
27     Bi = [dNdXYZ(1,c)     0              0; ...
28           0            dNdXYZ(2,c)      0; ...
29           0               0          dNdXYZ(3,c); ...
30           dNdXYZ(2,c)  dNdXYZ(1,c)      0; ...
31           dNdXYZ(3,c)     0          dNdXYZ(1,c); ...
32           0            dNdXYZ(3,c)  dNdXYZ(2,c)];
33     B = [B Bi];
34 end
```

C3D8 Elements C3D8 elements are also known as "selectively reduced" integration elements. The deviatoric components of the strain tensor are calculated using full integration (8/27 Gauss points) and the dilatational (volumetric) components are calculated using the uniform strain method (discussed in the previous section). Therefore, it is a combination of the previous two methods discussed. In Matlab, two strain vectors are calculated using both the uniform strain, or reduced integration, $\mathbf{B_r}$ matrix and the full integration $\mathbf{B_f}$ matrix as shown below.

```
% Calculate strain: B*U
eV_f = Bf*Ue; % Strain of measured displacements using full ...
    integration
eV_r = Br*Ue; % Strain of measured displacements using reduced ...
    integration
```

Then, the fully integrated strain was used to compute the deviatoric stress (and corresponding constraints) while the reduced integration strain was used to compute the dilatational stress (and corresponding constraints).

In all three element formulations of the strain matrix, the transformation of integrals from the global coordinate system to the natural coordinate system was performed with the use of the determinant of the Jacobian matrix, which represents the change in volume at the current Gauss point.

$$dV = dxdydz = |J|d\xi d\eta d\zeta \tag{A.15}$$

All three element strain formulations were tested with the virtual fields method. With harmonic displacements simulated in (cantilever beam and LV) finite element models, results from the VFM were most accurate when the element type used in the VFM matched the element type used in the original FE model to generate the reference displacements. Conversely, if C3D8R elements were used in the analysis and C3D8 elements in the generation of reference displacements, additional errors arose. C3D8F elements were not used since they were not available in Abaqus to generate reference displacement fields. When each element strain formulation was tested with the MRE phantom data, only slight differences were observed in the resulting shear parameter estimates. Figure A.2 illustrates resulting estimated shear moduli for each subzone of the phantom for both C3D8 and C3D8R element strain formulations.

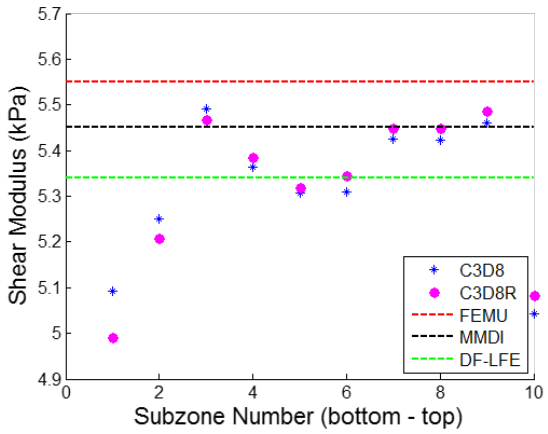

FIGURE A.2: Plot of estimated shear moduli for C3D8 and C3D8R element types.

Although all three element types were tested with the virtual fields method, results in Chapters 5 and 6 show results from analysis using the C3D8 strain formulation only. This element strain formulation was chosen since simulated harmonic displacements were generated in Abaqus and C3D8 elements were used. This type was then used with the phantom data for consistency. In Chapter 3, it was also shown that C3D8R elements resulted in hourglassing.

B

PARAMETER VARIANCE MATRICES

THE novelty and primary benefit of the optimised VFM is the ability to solve directly for a set of virtual displacement fields that adhere to constraints as well as minimise the variance in the estimated parameters. The theory and derivation for obtaining the parameter variance matrices will be explored.

Isotropic Parameter Variance The derivation, leading to Equations (5.21) and (5.20), is provided in this section. First, the measured displacement and strain fields were written as a sum of the noise-free displacement/strain and noise in the signal ($\mathbf{u}_{meas} = \mathbf{u} + \mathbf{u}_{no}$ and $\boldsymbol{\epsilon}_{meas} = \boldsymbol{\epsilon} + \boldsymbol{\epsilon}_{no}$). With the addition of noise in the displacement and strain fields, the approximate shear and bulk moduli were written as: G_{app} and K_{app}, respectively. Equation (5.15) was rewritten as:

$$\begin{aligned} K_{app}\big(f_K(\boldsymbol{\epsilon}, \boldsymbol{\epsilon}_G^*) + f_K(\boldsymbol{\epsilon}_{no}, \boldsymbol{\epsilon}_G^*)\big) + G_{app}\big(f_G(\boldsymbol{\epsilon}, \boldsymbol{\epsilon}_G^*) + f_G(\boldsymbol{\epsilon}_{no}, \boldsymbol{\epsilon}_G^*)\big) = \\ \int_V \rho\omega^2 \mathbf{u} \cdot \mathbf{u}_G^* dV + \int_V \rho\omega^2 \mathbf{u}_{no} \cdot \mathbf{u}_G^* dV \end{aligned} \tag{B.1}$$

Then, the specialisation constraints with data in the presence of noise were written as:

$$\begin{aligned} f_K(\boldsymbol{\epsilon}, \boldsymbol{\epsilon}_G^*) + f_K(\boldsymbol{\epsilon}_{no}, \boldsymbol{\epsilon}_G^*) = 0 \\ f_G(\boldsymbol{\epsilon}, \boldsymbol{\epsilon}_G^*) + f_G(\boldsymbol{\epsilon}_{no}, \boldsymbol{\epsilon}_G^*) = 1 \end{aligned} \tag{B.2}$$

Substituting these new specialisation conditions into Equation (B.1) resulted in the following equation:

$$\begin{aligned} K_{app}(0) + G_{app}(1) &= \int_V \rho\omega^2 \mathbf{u} \cdot \mathbf{u}_G^* dV + \int_V \rho\omega^2 \mathbf{u}_{no} \cdot \mathbf{u}_G^* dV \\ G_{app} &= \int_V \rho\omega^2 \mathbf{u} \cdot \mathbf{u}_G^* dV + \int_V \rho\omega^2 \mathbf{u}_{no} \cdot \mathbf{u}_G^* dV \end{aligned} \tag{B.3}$$

Next, the equation for virtual work in the noise-free case was substituted into Equation (B.3) in place of $\int_V \rho\omega^2 \mathbf{u} \cdot \mathbf{u}_G^* dV$.

$$G_{app} = K f_K(\boldsymbol{\epsilon}, \boldsymbol{\epsilon}_G^*) + G f_G(\boldsymbol{\epsilon}, \boldsymbol{\epsilon}_G^*) + \int_V \rho\omega^2 \mathbf{u}_{no} \cdot \mathbf{u}_G^* dV \tag{B.4}$$

Then, the specialisation conditions in the case with noise (Equation (B.2)) were rearranged and written as:

$$\begin{aligned} f_K(\boldsymbol{\epsilon}, \boldsymbol{\epsilon}_G^*) &= -f_K(\boldsymbol{\epsilon}_{no}, \boldsymbol{\epsilon}_G^*) \\ f_G(\boldsymbol{\epsilon}, \boldsymbol{\epsilon}_G^*) &= 1 - f_G(\boldsymbol{\epsilon}_{no}, \boldsymbol{\epsilon}_G^*) \end{aligned} \tag{B.5}$$

Substituting the right hand side terms from Equation (B.5) into Equation (B.4) resulted in the expression:

$$G_{app} = -K f_K(\boldsymbol{\epsilon}_{no}, \boldsymbol{\epsilon}_G^*) + G\big(1 - f_G(\boldsymbol{\epsilon}_{no}, \boldsymbol{\epsilon}_G^*)\big) + \int_V \rho\omega^2 \mathbf{u}_{no} \cdot \mathbf{u}_G^* dV \tag{B.6}$$

Finally, Equation (B.6) was rearranged to write an expression for the error in the estimated shear modulus, $G_{app} - G$, which was a linear combination of the the noise from the bulk, shear and acceleration terms. Note that the identification error is independent of the measured strain field, $\boldsymbol{\epsilon}$.

$$G_{app} - G = -K f_K(\boldsymbol{\epsilon}_{no}, \boldsymbol{\epsilon}_G^*) - G f_G(\boldsymbol{\epsilon}_{no}, \boldsymbol{\epsilon}_G^*) + \int_V \rho\omega^2 \mathbf{u}_{no} \cdot \mathbf{u}_G^* dV \tag{B.7}$$

In [29], tests showed that the acceleration noise was negligible compared to the noise in the bulk and shear components. Therefore, no efforts were put into minimising the noise in the acceleration term ($\int_V \rho\omega^2 \mathbf{u}_{no} \cdot \mathbf{u}_G^* dV$). To evaluate the bulk strain noise, the specialisation constraint for the bulk term in Equation (B.2) was used along with the bulk term in Equation (5.16) to show that:

$$K f_K(\boldsymbol{\epsilon}, \boldsymbol{\epsilon}_G^*) = -K f_K(\boldsymbol{\epsilon}_{no}, \boldsymbol{\epsilon}_G^*) = \int_V \rho\omega^2 \mathbf{u}_K \cdot \mathbf{u}_G^* dV \tag{B.8}$$

where $\mathbf{u}_K$ represents displacements due to the bulk wave. Therefore, in the case with noise, a new condition on the virtual field, $\mathbf{u}_G^*$, was chosen to set the right-hand side of Equation (B.8) to equal zero so that the bulk wave strain noise would also be zero. By assuming that the density was constant and the wavelength of the bulk wave was much longer than the integration volume, the condition was written as:

$$\int_V u_{xG}^* dV = 0, \quad \int_V u_{yG}^* dV = 0, \quad \int_V u_{zG}^* dV = 0 \tag{B.9}$$

where u_{xG}^*, u_{yG}^* and u_{zG}^* were the three orthogonal components of the virtual displacement field. In other words, the summed displacements in the three orthogonal directions should

be zero. Then, with this additional constraint and neglecting the noise due to acceleration, the equation to estimate error in the resulting shear modulus was reduced to:

$$G_{app} - G = -G f_G(\boldsymbol{\epsilon}_{no}, \boldsymbol{\epsilon}_G^*) \tag{B.10}$$

This estimation of error in the shear modulus was used to develop the optimised virtual fields. Generally, the variance in an estimated parameter, in this case G_{app}, can be written as:

$$V(G_{app}) = E\Big(\big[G_{app} - E(G_{app})\big]^2\Big) \tag{B.11}$$

where $E(X)$ is the expectation of X. Estimates of the isotropic shear modulus were assumed to be unbiased, which allowed one to replace $\big[G_{app} - E(G_{app})\big]$ by $\big[G_{app} - G\big]$. Then, Equation (B.10) was substituted into Equation (B.11), resulting in an equation for the variance in estimated shear moduli, which was related to the strain noise, $\boldsymbol{\epsilon}_{no}$, and the virtual strain field, $\boldsymbol{\epsilon}_G^*$.

$$V(G_{app}) = G^2 \cdot E\Big(f_G^2\big(\boldsymbol{\epsilon}_{no}, \boldsymbol{\epsilon}_G^*\big)\Big) \tag{B.12}$$

In this thesis, complex moduli were estimated. The distribution of a set of random complex variables can be interpreted as the joint distribution of two random real variables. The variance of a distribution of a complex parameter is real-valued and can be written as the sum of the variances of the real and imaginary components.

$$V(G_{app}) = V(\mathbb{R}(G_{app})) + V(\mathbb{I}(G_{app})) \tag{B.13}$$

In [29] (Appendix), it was also shown that the variance in the real and imaginary components of the isotropic shear modulus were equivalent and equal to:

$$V\big(\mathbb{R}(G_{app})\big) = V\big(\mathbb{I}(G_{app})\big) = \frac{1}{2}\big((\mathbb{R}(G_{app}))^2 + (\mathbb{I}(G_{app}))^2\big) E\Big[f_G^2(\boldsymbol{\epsilon}_{no}, \boldsymbol{\epsilon}_G^*)\Big] \tag{B.14}$$

where $f_G(\boldsymbol{\epsilon}_{no}, \boldsymbol{\epsilon}_G^*)$ is calculated identically to the case of a real-valued shear modulus. Then, summing the variance for the real and imaginary parts provides the final equation for variance in the complex shear modulus, which can be written as:

$$V\big(G_{app}\big) = \big((\mathbb{R}(G_{app}))^2 + (\mathbb{I}(G_{app}))^2\big) E\Big[f_G^2(\boldsymbol{\epsilon}_{no}, \boldsymbol{\epsilon}_G^*)\Big] \tag{B.15}$$

The optimised virtual field was one which minimised the variance in the identified shear modulus, which was equivalent to directly minimising $E\big(f_G^2(\boldsymbol{\epsilon}_{no}, \boldsymbol{\epsilon}_G^*)\big)$. All six components of strain noise, $\boldsymbol{\epsilon}_{no}$, can be substituted by $\gamma_{\boldsymbol{\epsilon}_i} N_i$ where i ranges from 1 to 6. γ represents the standard deviation of N, the independent Gaussian noise copy. Making this

substitution, shear stress as a function of noise in the strain signal and the virtual strain field ($f_G(\boldsymbol{\epsilon}_{no}, \boldsymbol{\epsilon}_G^*)$) can then be expanded and written as:

$$\begin{aligned} & f_G\big(\boldsymbol{\epsilon}_{no}, \boldsymbol{\epsilon}_G^*\big) = \\ & 2\int_V \big(\boldsymbol{\epsilon}_{no} : \boldsymbol{\epsilon}^* - \frac{1}{3}\mathrm{Tr}(\boldsymbol{\epsilon}_{no})\mathrm{Tr}(\boldsymbol{\epsilon}^*)\big)dV \\ & 2\int_V \big((\gamma_{\boldsymbol{\epsilon}_1} N_1 \boldsymbol{\epsilon}_1^* + \gamma_{\boldsymbol{\epsilon}_2} N_2 \boldsymbol{\epsilon}_2^* + \gamma_{\boldsymbol{\epsilon}_3} N_3 \boldsymbol{\epsilon}_3^* + 2\gamma_{\boldsymbol{\epsilon}_4} N_4 \boldsymbol{\epsilon}_4^* + 2\gamma_{\boldsymbol{\epsilon}_5} N_5 \boldsymbol{\epsilon}_5^* + 2\gamma_{\boldsymbol{\epsilon}_6} N_6 \boldsymbol{\epsilon}_6^*) \\ & - \frac{1}{3}(\gamma_{\boldsymbol{\epsilon}_1} N_1 + \gamma_{\boldsymbol{\epsilon}_2} N_2 + \gamma_{\boldsymbol{\epsilon}_3} N_3) \cdot (\boldsymbol{\epsilon}_1^* + \boldsymbol{\epsilon}_2^* + \boldsymbol{\epsilon}_3^*)\big)dV \end{aligned} \tag{B.16}$$

Grouping terms, according to the Gaussian noise copy (e.g. N_1) results in the following equation:

$$\begin{aligned} & f_G\big(\boldsymbol{\epsilon}_{no}, \boldsymbol{\epsilon}_G^*\big) = 2\int_V \big(\gamma_{\boldsymbol{\epsilon}_1} N_1(\boldsymbol{\epsilon}_1^* - \frac{1}{3}\mathrm{Tr}(\boldsymbol{\epsilon}^*)) + \gamma_{\boldsymbol{\epsilon}_2} N_2(\boldsymbol{\epsilon}_2^* - \frac{1}{3}\mathrm{Tr}(\boldsymbol{\epsilon}^*)) + \\ & \gamma_{\boldsymbol{\epsilon}_3} N_3(\boldsymbol{\epsilon}_3^* - \frac{1}{3}\mathrm{Tr}(\boldsymbol{\epsilon}^*)) + 2\gamma_{\boldsymbol{\epsilon}_4} N_4 \boldsymbol{\epsilon}_4^* + 2\gamma_{\boldsymbol{\epsilon}_5} N_5 \boldsymbol{\epsilon}_5^* + 2\gamma_{\boldsymbol{\epsilon}_6} N_6 \boldsymbol{\epsilon}_6^*\big)dV \end{aligned} \tag{B.17}$$

As Equation (B.17) is inserted back into (B.15) and $E\big[f_G^2(\boldsymbol{\epsilon}_{no}, \boldsymbol{\epsilon}^*)\big]$ is evaluated, it is helpful to refer back to Weiner's theory of integrating stochastic variables, which shows that the expectation of the product of two independent noise copies results in zero (i.e. $E[N_1 N_2] = 0$). Formally, this is written:

$$\begin{aligned} & E\Big(\Big(\sum \gamma_1 N_{f1} f_1^* \Delta V\Big)\Big(\sum \gamma_1 N_{f1} f_2^* \Delta V\Big)\Big) = \gamma_1^2\Big(\sum f_1^* f_2^* \Delta V^2\Big) \\ & E\Big(\Big(\sum \gamma_1 N_{f1} f_1^* \Delta V\Big)\Big(\sum \gamma_2 N_{f2} f_2^* \Delta V\Big)\Big) = 0 \end{aligned} \tag{B.18}$$

where f_1^* and f_2^* represent two functions which are independent from the noise copies. Therefore, only terms which contain similar Gaussian noise copies remain in the final equation. The integral in Equation (B.17) can be replaced by a discrete sum over the volume to obtain the final equation:

$$\begin{aligned} V(G_{app}) = 4\big((\mathbb{R}(G_{app}))^2 + (\mathbb{I}(G_{app}))^2\big)\Delta V^2 \sum_{voxels \subset V} \Big[& \gamma_{\boldsymbol{\epsilon}_{11}}^2 \big(\boldsymbol{\epsilon}_{11}^* - \frac{1}{3}\mathrm{Tr}(\boldsymbol{\epsilon}^*)\big)^2 \\ & + \gamma_{\boldsymbol{\epsilon}_{22}}^2 \big(\boldsymbol{\epsilon}_{22}^* - \frac{1}{3}\mathrm{Tr}(\boldsymbol{\epsilon}^*)\big)^2 \\ & + \gamma_{\boldsymbol{\epsilon}_{33}}^2 \big(\boldsymbol{\epsilon}_{33}^* - \frac{1}{3}\mathrm{Tr}(\boldsymbol{\epsilon}^*)\big)^2 \\ & + 4\gamma_{\boldsymbol{\epsilon}_{12}}^2 \boldsymbol{\epsilon}_{12}^{*2} + 4\gamma_{\boldsymbol{\epsilon}_{13}}^2 \boldsymbol{\epsilon}_{13}^{*2} + 4\gamma_{\boldsymbol{\epsilon}_{23}}^2 \boldsymbol{\epsilon}_{23}^{*2}\Big] \end{aligned} \tag{B.19}$$

Next, noise was modelled as standard centred Gaussian white noise on the displacement, rather than strain, fields.

$$\mathbf{u}_{meas} = \mathbf{u} + \mathbf{u}_{no} = \begin{Bmatrix} U_1 \\ U_2 \\ U_3 \end{Bmatrix} + \gamma_u \begin{Bmatrix} N_1 \\ N_2 \\ N_3 \end{Bmatrix} \tag{B.20}$$

where $\gamma_{\mathbf{u}}$ was the standard deviation of the displacement noise, which was assumed to be identical for each displacement direction. The strain noise was computed from the displacement noise by numerical centred differentiation (Equation (B.21)).

$$\begin{aligned}
\boldsymbol{\epsilon}_{11}^{meas} &= \boldsymbol{\epsilon}_{11} + \gamma_{\boldsymbol{\epsilon}11} N_{11} = \boldsymbol{\epsilon}_{11} + \frac{\gamma_u}{\sqrt{2}\Delta x} N_{11} \\
\boldsymbol{\epsilon}_{22}^{meas} &= \boldsymbol{\epsilon}_{22} + \gamma_{\boldsymbol{\epsilon}22} N_{22} = \boldsymbol{\epsilon}_{22} + \frac{\gamma_u}{\sqrt{2}\Delta y} N_{22} \\
\boldsymbol{\epsilon}_{33}^{meas} &= \boldsymbol{\epsilon}_{33} + \gamma_{\boldsymbol{\epsilon}33} N_{33} = \boldsymbol{\epsilon}_{33} + \frac{\gamma_u}{\sqrt{2}\Delta z} N_{33} \\
\boldsymbol{\epsilon}_{12}^{meas} &= \boldsymbol{\epsilon}_{12} + \gamma_{\boldsymbol{\epsilon}12} N_{12} = \boldsymbol{\epsilon}_{12} + \frac{\gamma_u}{\sqrt{2}} \sqrt{\frac{1}{\Delta y^2} + \frac{1}{\Delta z^2}} N_{12} \\
\boldsymbol{\epsilon}_{13}^{meas} &= \boldsymbol{\epsilon}_{13} + \gamma_{\boldsymbol{\epsilon}13} N_{13} = \boldsymbol{\epsilon}_{13} + \frac{\gamma_u}{\sqrt{2}} \sqrt{\frac{1}{\Delta x^2} + \frac{1}{\Delta z^2}} N_{13} \\
\boldsymbol{\epsilon}_{23}^{meas} &= \boldsymbol{\epsilon}_{23} + \gamma_{\boldsymbol{\epsilon}23} N_{23} = \boldsymbol{\epsilon}_{23} + \frac{\gamma_u}{\sqrt{2}} \sqrt{\frac{1}{\Delta x^2} + \frac{1}{\Delta y^2}} N_{23}
\end{aligned} \tag{B.21}$$

Replacing each standard deviation of strain noise, $\gamma_{\boldsymbol{\epsilon}_i}$, with the corresponding standard deviation in displacement noise, $\gamma_{\mathbf{u}}$, results in the following equation for variance in the estimated shear modulus.

$$\begin{aligned}
V(G_{app}) = 4\big((\mathbb{R}(G_{app}))^2 + (\mathbb{I}(G_{app}))^2\big)\Delta V^2 \gamma_u^2 \sum_{voxels \subset V} \Big[&\Big(\frac{1}{\Delta x^2}\Big)\big(\boldsymbol{\epsilon}_{11}^* - \frac{1}{3}\mathrm{Tr}(\boldsymbol{\epsilon}^*)\big)^2 \\
&+ \Big(\frac{1}{\Delta y^2}\Big)\big(\boldsymbol{\epsilon}_{22}^* - \frac{1}{3}\mathrm{Tr}(\boldsymbol{\epsilon}^*)\big)^2 \\
&+ \Big(\frac{1}{\Delta z^2}\Big)\big(\boldsymbol{\epsilon}_{33}^* - \frac{1}{3}\mathrm{Tr}(\boldsymbol{\epsilon}^*)\big)^2 \\
+ \Big(\frac{4}{\Delta x^2} + \frac{4}{\Delta y^2}\Big)\boldsymbol{\epsilon}_{12}^{*2} + \Big(\frac{4}{\Delta x^2} + \frac{4}{\Delta z^2}\Big)\boldsymbol{\epsilon}_{13}^{*2} + \Big(\frac{4}{\Delta y^2} + \frac{4}{\Delta z^2}\Big)\boldsymbol{\epsilon}_{23}^{*2} &\Big]
\end{aligned} \tag{B.22}$$

Omitting constants, the variance in the estimated shear modulus, to be minimised by the optimal virtual displacement field, is proportional to the element volume squared multiplied by the discrete sum of components which are only dependent on the virtual strain field.

$$
\begin{aligned}
V(G_{app}) \propto \Delta V^2 \sum_{voxels \subset V} \Big[\Big(\frac{1}{\Delta x^2}\Big) \big(\boldsymbol{\epsilon}^*_{11} - \frac{1}{3}\mathrm{Tr}(\boldsymbol{\epsilon}^*)\big)^2 \\
+ \Big(\frac{1}{\Delta y^2}\Big) \big(\boldsymbol{\epsilon}^*_{22} - \frac{1}{3}\mathrm{Tr}(\boldsymbol{\epsilon}^*)\big)^2 \\
+ \Big(\frac{1}{\Delta z^2}\Big) \big(\boldsymbol{\epsilon}^*_{33} - \frac{1}{3}\mathrm{Tr}(\boldsymbol{\epsilon}^*)\big)^2 \\
+ \Big(\frac{4}{\Delta x^2} + \frac{4}{\Delta y^2}\Big) \boldsymbol{\epsilon}^{*2}_{12} + \Big(\frac{4}{\Delta x^2} + \frac{4}{\Delta z^2}\Big) \boldsymbol{\epsilon}^{*2}_{13} + \Big(\frac{4}{\Delta y^2} + \frac{4}{\Delta z^2}\Big) \boldsymbol{\epsilon}^{*2}_{23} \Big]
\end{aligned}
\tag{B.23}
$$

Equation (B.23), identical to Equation (5.21), is the final form which was used to calculate the optimal virtual displacement field.

Anisotropic Parameter Variance Like the isotropic method, in the anisotropic optimised VFM, the virtual displacement field corresponding to each parameter was calculated which minimised the variance in each respective parameter. The formulation is shown for developing the parameter variance matrix in the optimised VFM for anisotropic material models. Consider a general set of parameters:

$$
Q = \begin{bmatrix} Q_1 \\ Q_2 \\ Q_3 \end{bmatrix} \tag{B.24}
$$

and the equation

$$
Q_1 F_1 \mathbf{u}^{*1} + Q_2 F_2 \mathbf{u}^{*1} + Q_3 F_3 \mathbf{u}^{*1} = F_4 \mathbf{u}^{*1} \tag{B.25}
$$

where $\mathbf{u}^{*1}$ represents a single virtual displacement field and F_i are independent functions, each containing components of the measured strain field. Similarly to specialisation constraints described in Chapters 5 and 6, the following constraints are applied to $\mathbf{u}^{*1}$:

$$
F_1 \mathbf{u}^{*1} = 1 \qquad F_2 \mathbf{u}^{*1} = 0 \qquad F_3 \mathbf{u}^{*1} = 0 \tag{B.26}
$$

Specialisation constraints for each consecutive virtual displacement field ($\mathbf{u}^{*2}$ and $\mathbf{u}^{*3}$) were developed by exchanging the place of the one in Equation (B.26). Equation (B.25) in the presence of noise can be written as:

$$
\begin{aligned}
Q_1\big(F_1 + \gamma_1 F_1^{No}\big)\mathbf{u}^{*1} + Q_2\big(F_2 + \gamma_2 F_2^{No}\big)\mathbf{u}^{*1} + Q_3\big(F_3 + \gamma_3 F_3^{No}\big)\mathbf{u}^{*1} = \\
\big(F_4 + \gamma_4 F_4^{No}\big)\mathbf{u}^{*1}
\end{aligned}
\tag{B.27}
$$

F_i^{No} represents the noise in the measured strain field with a standard deviation, γ. Similarly, the constraints in Equation (B.26) can be rewritten as:

$$\begin{aligned}\left(F_1+\gamma_1 F_1^{No}\right)\mathbf{u}^{*1}&=1\\ \left(F_2+\gamma_2 F_2^{No}\right)\mathbf{u}^{*1}&=0\\ \left(F_3+\gamma_3 F_3^{No}\right)\mathbf{u}^{*1}&=0\end{aligned} \tag{B.28}$$

Substituting the noisy constraints (Equation (B.28)) on the virtual displacement field, into Equation (B.27) results in:

$$Q_1^{app}=(F_4+\gamma_4 F_4^{No})\mathbf{u}^{*1}=F_4\mathbf{u}^{*1}+\gamma_4 F_4^{No}\mathbf{u}^{*1} \tag{B.29}$$

The superscript ^{app} is applied since the parameter, Q_1 is estimated in the presence of noise and is approximate. The entire left-hand side of Equation (B.25) can be substituted into the noise-free part of Equation (B.29).

$$Q_1^{app}=Q_1F_1\mathbf{u}^{*1}+Q_2F_2\mathbf{u}^{*1}+Q_3F_3\mathbf{u}^{*1}+\gamma_4 F_4^{No}\mathbf{u}^{*1} \tag{B.30}$$

Next, it can be seen that each of the constraints in Equation (B.28) can be rearranged so that the noise-free part is written in terms of the strain noise (i.e. $F_1\mathbf{u}^{*1}=1-\gamma_1 F_1^{No}\mathbf{u}^{*1}$, $F_2\mathbf{u}^{*1}=-\gamma_2 F_2^{No}\mathbf{u}^{*1}$ and $F_3\mathbf{u}^{*1}=-\gamma_3 F_3^{No}\mathbf{u}^{*1}$). Substituting the strain noise components in place of the noise-free functions, it follows that Equation (B.30) can be written as:

$$Q_1^{app}=Q_1\left(1-\gamma_1 F_1^{No}\mathbf{u}^{*1}\right)-Q_2\gamma_2 F_2^{No}\mathbf{u}^{*1}-Q_3\gamma_3 F_3^{No}\mathbf{u}^{*1}+\gamma_1 F_4^{No}\mathbf{u}^{*1} \tag{B.31}$$

If all strain noise standard deviations are assumed to be equal, $\gamma_1=\gamma_2=\gamma_3=\gamma$, then the identification error of Q_1, in the presence of Gaussian noise, can be written as:

$$Q_1^{app}-Q_1=-\gamma\left[Q_1F_1^{No}\mathbf{u}^{*1}-Q_2F_2^{No}\mathbf{u}^{*1}-Q_3F_3^{No}\mathbf{u}^{*1}+F_4^{No}\mathbf{u}^{*1}\right] \tag{B.32}$$

It was previously stated that the variance in a parameter estimate, assuming unbiased estimates, can be written as:

$$vV(Q_1)=E[Q_1^{app}-Q_1]. \tag{B.33}$$

Therefore, an expression for the variance in the estimated parameter, Q_1, can be written by simply substituting Equation (B.32) into Equation (B.33). It should be noted that the parameters, Q_1, Q_2 and Q_3, are included in the expression for the parameter variance. However, in practice, the true values of each parameter are unknown. Therefore, the expression can be written utilising the approximate parameter values: Q_1^{app}, Q_2^{app} and Q_3^{app}. Additionally, F_4^{No} can be assumed negligible, as was done for the acceleration term

in Chapter 6. Substituting Equation (B.32) into the equation for variance results in the following expression:

$$V(Q_1) = \gamma^2 E\Big(\left[Q_1^{app} F_1^{No}\mathbf{u}^{*1} + Q_2^{app} F_2^{No}\mathbf{u}^{*1} + Q_3^{app} F_3^{No}\mathbf{u}^{*1}\right]^2\Big) \tag{B.34}$$

Generally, (B.34) can be written as:

$$V(Q_1) = (Q^{app})^T E(N^T N) Q^{app} \tag{B.35}$$

In the five parameter-formulation, N and Q^{app} can be written as:

$$N = \begin{bmatrix} f_{C_{11}}(\boldsymbol{\epsilon}_{no}, \boldsymbol{\epsilon}^*) \\ f_{C_{33}}(\boldsymbol{\epsilon}_{no}, \boldsymbol{\epsilon}^*) \\ f_{C_{44}}(\boldsymbol{\epsilon}_{no}, \boldsymbol{\epsilon}^*) \\ f_{C_{66}}(\boldsymbol{\epsilon}_{no}, \boldsymbol{\epsilon}^*) \\ f_{C_{13}}(\boldsymbol{\epsilon}_{no}, \boldsymbol{\epsilon}^*) \end{bmatrix}, Q^{app} = \begin{bmatrix} C_{11}^{app} \\ C_{33}^{app} \\ C_{44}^{app} \\ C_{66}^{app} \\ C_{13}^{app} \end{bmatrix}. \tag{B.36}$$

It should be noted that, in the anisotropic formulation of the optimised VFM, the noise in the strain fields, not the displacement fields, were assumed to be independent with equal variance (i.e. $\gamma_{\boldsymbol{\epsilon}_{11}} = \gamma_{\boldsymbol{\epsilon}_{22}} = \gamma_{\boldsymbol{\epsilon}_{33}} = \gamma_{\boldsymbol{\epsilon}_{12}} = \gamma_{\boldsymbol{\epsilon}_{13}} = \gamma_{\boldsymbol{\epsilon}_{23}} = \gamma$). This assumption is not entirely valid since, for example, $\boldsymbol{\epsilon}_{12}$ and $\boldsymbol{\epsilon}_{13}$, are related by the displacement $\mathbf{u}_1$. Similarly, noise components will also be related. However, it is presumed that this assumption does not have a large impact on the optimised virtual field calculation. The assumption was made due to the resulting simplification of the implementation. In the future, a formulation of the anisotropic VFM will be implemented while assuming only that noise in the displacement fields are independent with equal variance. Looking at the first term in N, $f_{C_{11}}(\boldsymbol{\epsilon}_{no}, \boldsymbol{\epsilon}^*)$ can be expanded and written in terms of the standard deviation, γ, Gaussian noise copies in the strain field, N_i, and the virtual strain field, $\boldsymbol{\epsilon}^*$.

$$f_{C_{11}}(\boldsymbol{\epsilon}_{no}, \boldsymbol{\epsilon}^*) = \gamma N_1 \boldsymbol{\epsilon}_1^* + \gamma N_2 \boldsymbol{\epsilon}_2^* + \gamma N_1 \boldsymbol{\epsilon}_2^* + \gamma N_2 \boldsymbol{\epsilon}_1^* \tag{B.37}$$

Each term in N can be expanded similarly. Next, expanding $E(N^T N)$ leads to a square matrix. For conciseness, each term $f_{C_{ij}}(\boldsymbol{\epsilon}_{no}, \boldsymbol{\epsilon}^*)$ is simply written as $f_{C_{ij}}^{no}$.

$$N^T N = \begin{bmatrix} f_{C_{11}}^{no} f_{C_{11}}^{no} & f_{C_{11}}^{no} f_{C_{33}}^{no} & f_{C_{11}}^{no} f_{C_{44}}^{no} & f_{C_{11}}^{no} f_{C_{66}}^{no} & f_{C_{11}}^{no} f_{C_{13}}^{no} \\ f_{C_{33}}^{no} f_{C_{11}}^{no} & f_{C_{33}}^{no} f_{C_{33}}^{no} & f_{C_{33}}^{no} f_{C_{44}}^{no} & f_{C_{33}}^{no} f_{C_{66}}^{no} & f_{C_{33}}^{no} f_{C_{13}}^{no} \\ f_{C_{44}}^{no} f_{C_{11}}^{no} & f_{C_{44}}^{no} f_{C_{33}}^{no} & f_{C_{44}}^{no} f_{C_{44}}^{no} & f_{C_{44}}^{no} f_{C_{66}}^{no} & f_{C_{44}}^{no} f_{C_{13}}^{no} \\ f_{C_{66}}^{no} f_{C_{11}}^{no} & f_{C_{66}}^{no} f_{C_{33}}^{no} & f_{C_{66}}^{no} f_{C_{44}}^{no} & f_{C_{66}}^{no} f_{C_{66}}^{no} & f_{C_{66}}^{no} f_{C_{13}}^{no} \\ f_{C_{13}}^{no} f_{C_{11}}^{no} & f_{C_{13}}^{no} f_{C_{33}}^{no} & f_{C_{13}}^{no} f_{C_{44}}^{no} & f_{C_{13}}^{no} f_{C_{66}}^{no} & f_{C_{13}}^{no} f_{C_{13}}^{no} \end{bmatrix} \tag{B.38}$$

Again, using Weiner's theory of integration of stochastic variables leads to some simplifications when evaluating each term in $E(N^T N)$. For example, $f_{C_{66}}(\boldsymbol{\epsilon}_{no}, \boldsymbol{\epsilon}^*) \cdot f_{C_{33}}(\boldsymbol{\epsilon}_{no}, \boldsymbol{\epsilon}^*)$ can be written out:

$$f_{C_{66}}(\boldsymbol{\epsilon}_{no}, \boldsymbol{\epsilon}^*) \cdot f_{C_{33}}(\boldsymbol{\epsilon}_{no}, \boldsymbol{\epsilon}^*) = \left(\gamma N_5 \boldsymbol{\epsilon}_5^* + \gamma N_6 \boldsymbol{\epsilon}_6^*\right)\left(\gamma N_3 \boldsymbol{\epsilon}_3^*\right) \tag{B.39}$$

Since the expectation of the product of independent sets of noise is equal to zero, according to Wiener's theory of integration of stochastic variables ($E(N_1 N_2) = 0$), then, the $E(f_{C_{66}}(\boldsymbol{\epsilon}_{no}, \boldsymbol{\epsilon}^*) f_{C_{33}}(\boldsymbol{\epsilon}_{no}, \boldsymbol{\epsilon}^*))$ must equal zero. Therefore, numerous terms in the matrix in Equation (B.38) reduce to zero.

$$N^T N = \begin{bmatrix} f_{C_{11}}^{no} f_{C_{11}}^{no} & 0 & f_{C_{11}}^{no} f_{C_{44}}^{no} & 0 & f_{C_{11}}^{no} f_{C_{13}}^{no} \\ 0 & f_{C_{33}}^{no} f_{C_{33}}^{no} & 0 & 0 & f_{C_{33}}^{no} f_{C_{13}}^{no} \\ f_{C_{44}}^{no} f_{C_{11}}^{no} & 0 & f_{C_{44}}^{no} f_{C_{44}}^{no} & 0 & f_{C_{44}}^{no} f_{C_{13}}^{no} \\ 0 & 0 & 0 & f_{C_{66}}^{no} f_{C_{66}}^{no} & 0 \\ f_{C_{13}}^{no} f_{C_{11}}^{no} & f_{C_{13}}^{no} f_{C_{33}}^{no} & f_{C_{13}}^{no} f_{C_{44}}^{no} & 0 & f_{C_{13}}^{no} f_{C_{13}}^{no} \end{bmatrix} \tag{B.40}$$

Each term in Equation (B.40) was evaluated in order to implement the parameter variance matrix for the five-parameter formulation of the optimised VFM. Similar steps were followed for the three-parameter formulation in order to develop an expression for the estimated parameter variance (Chapter 6).

C

CONSTRAINTS ON VIRTUAL DISPLACEMENTS

THE strain matrix (discussed in detail in Appendix A), was used in the numeric calculation of the the virtual displacement fields. The implementations, in Matlab 2012b, of both isotropic and anisotropic constraints are presented in this section.

Isotropic Virtual Fields Constraints Specialisation constraints were used in both the isotropic and anisotropic formulations to solve for a single parameter, given a unique virtual displacement field. In the isotropic case, these constraints were:

$$\begin{aligned} f_K(\boldsymbol{\epsilon}, \boldsymbol{\epsilon}^*) &= 0 \\ f_G(\boldsymbol{\epsilon}, \boldsymbol{\epsilon}^*) &= 1 \end{aligned} \tag{C.1}$$

where

$$\begin{aligned} f_K(\boldsymbol{\epsilon}, \boldsymbol{\epsilon}^*) &= \int_V \mathrm{Tr}(\boldsymbol{\epsilon})\mathrm{Tr}(\boldsymbol{\epsilon}^*)dV \\ f_G(\boldsymbol{\epsilon}, \boldsymbol{\epsilon}^*) &= 2\int_V \big(\boldsymbol{\epsilon} : \boldsymbol{\epsilon}^* - \frac{1}{3}\mathrm{Tr}(\boldsymbol{\epsilon})\mathrm{Tr}(\boldsymbol{\epsilon}^*)\big)dV \end{aligned} \tag{C.2}$$

The virtual strain field can be written as the product of the strain matrix, $\mathbf{B}$ and the virtual displacement field, $\boldsymbol{\epsilon}^* = \mathbf{B}\mathbf{u}^*$. Therefore, a constraint can be constructed such that: $[\mathbf{A_K}]\mathbf{u}^* = 0$ and $[\mathbf{A_G}]\mathbf{u}^* = 1$. Then, $[\mathbf{A_K}]$ can be explicitly written as:

$$\mathbf{A_K} = \mathrm{Tr}(\boldsymbol{\epsilon}) \begin{bmatrix} \partial N_1/\partial x & \partial N_1/\partial y & \partial N_1/\partial z & ... \end{bmatrix} |J| d\xi d\eta d\zeta \tag{C.3}$$

The partial derivative components of Equation (C.3) are components of the strain matrix, $\mathbf{B}$ (see Equation (A.6)). It can similarly be shown that all constraints on the virtual

displacement field can be written in terms of the measured displacement field, $\mathbf{u}$ (or strain field, $\boldsymbol{\epsilon}$), and the strain matrix, $\mathbf{B}$. In Matlab, Equation (C.3) was written as:

```
% Ak term for current element (row vector)
% fk = ak * UeVF = 0
ak = trace(e)*sum(B(1:3,:),1)*detJ;
```

The constraint $f_G(\boldsymbol{\epsilon}, \boldsymbol{\epsilon}^*_G) = 1$ can similarly be constructed as:

```
% Ag term for current element (row vector)
% fg = ag * UeVF = 1
% tmp = e:e*
tmp = eV(1)*B(1,:) + eV(2)*B(2,:) + eV(3)*B(3,:) + ...
    2*0.5*eV(4)*0.5*B(4,:) + 2*0.5*eV(5)*0.5*B(5,:) + ...
    2*0.5*eV(6)*0.5*B(6,:); % e:eVF
% ag = 2 * (e:e* - 1/3 * Tr(e) * Tr(e*)) * dV
ag = 2*(tmp - (1/3)* trace(e)* sum(B(1:3,:),1)) * detJ;
```

The matrix of parameter variances, derived in Appendix B (Equation (B.23)), was implemented similarly using components of the $\mathbf{B}$ matrix:

```
% Minimise var(G)

% tmp = 1/3 * Tr(e*)
tmp = 1/3 * sum(B(1:3,:),1);

% Calculate each component of h
h1 = (1/(delX^2))*(B(1,:) - tmp)'*(B(1,:) - tmp);
h2 = (1/(delY^2))*(B(2,:) - tmp)'*(B(2,:) - tmp);
h3 = (1/(delZ^2))*(B(3,:) - tmp)'*(B(3,:) - tmp);
h12 = (4/delX^2 + 4/delY^2)*(0.5*B(4,:))'*(0.5*B(4,:));
h13 = (4/delX^2 + 4/delZ^2)*(0.5*B(5,:))'*(0.5*B(5,:));
h23 = (4/delY^2 + 4/delZ^2)*(0.5*B(6,:))'*(0.5*B(6,:));

h = (detJ^2)*(h1 + h2 + h3 + h12 + h13 + h23); %Hg
```

Anisotropic Virtual Fields Constraints The simplest form of the equation for the principle of virtual work, used in both Chapters 5 and 6, is:

$$\int \boldsymbol{\sigma} : \boldsymbol{\epsilon}^* dV = \rho\omega^2 \int \mathbf{u} \cdot \mathbf{u}^* dV \tag{C.4}$$

If $\mathbf{D}$ is defined as the elasticity matrix, then Equation (C.4) can be rewritten as:

$$\int \left(\mathbf{D}\boldsymbol{\epsilon}\right) : \boldsymbol{\epsilon}^* dV = \rho\omega^2 \int \mathbf{u} \cdot \mathbf{u}^* dV \tag{C.5}$$

As described in the section above, $\boldsymbol{\epsilon}$ is calculated as $\mathbf{Bu}$ where $\mathbf{B}$ is the strain matrix. Additionally, the right-hand side term requires the conversion of nodal displacements to element displacements using the shape function, $\mathbf{N}$ (Equation (A.2)). Then, (C.5) becomes:

$$\int \left(\mathbf{DBu}\right) : \left(\mathbf{Bu}^*\right) dV = \rho\omega^2 \int \left(\mathbf{Nu}\right) \cdot \left(\mathbf{Nu}^*\right) dV \tag{C.6}$$

In the case of a locally varying coordinate system, the strain tensors need to be rotated to the local coordinate system from the global coordinate system. Incorporating the rotation matrix, $\mathbf{L}$, into Equation (C.6) gives:

$$\int \left(\mathbf{DL}\left(\mathbf{Bu}\right)\mathbf{L}^T\right) : \left(\mathbf{L}\left(\mathbf{Bu}^*\right)\mathbf{L}^T\right) dV = \rho\omega^2 \int \left(\mathbf{LNu}\right) \cdot \left(\mathbf{LNu}^*\right) dV \tag{C.7}$$

In the previous section, it was shown that the constraints on the virtual displacement field can be formulated using the measured nodal displacements along with the $\mathbf{B}$ matrix. Likewise, in the anisotropic case, the constraints can be derived from the nodal displacements, $\mathbf{B}$ matrix and the rotation matrix, $\mathbf{L}$. First, the rotated $\mathbf{B}$ matrix was calculated.

```
% Calculate rotated B matrix
eVF11r = L(1,1)*L(1,1)*B(1,:) + L(1,2)*L(1,1)*0.5*B(4,:) + ...
    L(1,1)*L(1,3)*0.5*B(5,:) + L(1,1)*L(1,2)*0.5*B(4,:) + ...
    L(1,2)*L(1,2)*B(2,:) + L(1,3)*L(1,2)*0.5*B(6,:) + ...
    L(1,1)*L(1,3)*0.5*B(5,:) + L(1,2)*L(1,3)*0.5*B(6,:) + ...
    L(1,3)*L(1,3)*B(3,:);
eVF12r = L(2,1)*L(1,1)*B(1,:) + L(2,2)*L(1,1)*0.5*B(4,:) + ...
    L(2,3)*L(1,1)*0.5*B(5,:) + L(2,1)*L(1,2)*0.5*B(4,:) + ...
    L(2,2)*L(1,2)*B(2,:) + L(2,3)*L(1,2)*0.5*B(6,:) + ...
    L(2,1)*L(1,3)*0.5*B(5,:) + L(2,2)*L(1,3)*0.5*B(6,:) + ...
    L(2,3)*L(1,3)*B(3,:);
eVF13r = L(3,1)*L(1,1)*B(1,:) + L(3,2)*L(1,1)*0.5*B(4,:) + ...
    L(3,3)*L(1,1)*0.5*B(5,:) + L(3,1)*L(1,2)*0.5*B(4,:) + ...
    L(3,2)*L(1,2)*B(2,:) + L(3,3)*L(1,2)*0.5*B(6,:) + ...
    L(3,1)*L(1,3)*0.5*B(5,:) + L(3,2)*L(1,3)*0.5*B(6,:) + ...
    L(3,3)*L(1,3)*B(3,:);
eVF22r = L(2,1)*L(2,1)*B(1,:) + L(2,2)*L(2,1)*0.5*B(4,:) + ...
    L(2,3)*L(2,1)*0.5*B(5,:) + L(2,1)*L(2,2)*0.5*B(4,:) + ...
    L(2,2)*L(2,2)*B(2,:) + L(2,3)*L(2,2)*0.5*B(6,:) + ...
    L(2,1)*L(2,3)*0.5*B(5,:) + L(2,2)*L(2,3)*0.5*B(6,:) + ...
    L(2,3)*L(2,3)*B(3,:);
eVF23r = L(3,1)*L(2,1)*B(1,:) + L(3,2)*L(2,1)*0.5*B(4,:) + ...
    L(3,3)*L(2,1)*0.5*B(5,:) + L(3,1)*L(2,2)*0.5*B(4,:) + ...
```

```
    L(3,2)*L(2,2)*B(2,:) + L(3,3)*L(2,2)*0.5*B(6,:) + ...
    L(3,1)*L(2,3)*0.5*B(5,:) + L(3,2)*L(2,3)*0.5*B(6,:) + ...
    L(3,3)*L(2,3)*B(3,:);
eVF33r = L(3,1)*L(3,1)*B(1,:) + L(3,2)*L(3,1)*0.5*B(4,:) + ...
    L(3,3)*L(3,1)*0.5*B(5,:) + L(3,1)*L(3,2)*0.5*B(4,:) + ...
    L(3,2)*L(3,2)*B(2,:) + L(3,3)*L(3,2)*0.5*B(6,:) + ...
    L(3,1)*L(3,3)*0.5*B(5,:) + L(3,2)*L(3,3)*0.5*B(6,:) + ...
    L(3,3)*L(3,3)*B(3,:);

% Rotated B matrix - used to derive constraints
B_rot = [eVF11r; eVF22r; eVF33r; 2*eVF12r; 2*eVF13r; 2*eVF23r];
```

Then, constraints on the anisotropic virtual displacement fields (Equation (6.7)) were implemented using the rotated $\mathbf{B}$ matrix. For the five-parameter formulation, these constraints were:

$$\begin{aligned}
[A_{C_{11}}]\mathbf{u}_1^* &= 1 \\
[A_{C_{33}}]\mathbf{u}_1^* &= 0 \\
[A_{C_{44}}]\mathbf{u}_1^* &= 0 \\
[A_{C_{66}}]\mathbf{u}_1^* &= 0 \\
[A_{C_{13}}]\mathbf{u}_1^* &= 0
\end{aligned} \tag{C.8}$$

Constraints for each consecutive virtual displacement field were developed by exchanging the place of the one in Equation (C.8). Equation (6.5) was used to write each constraint in terms of solely the measured strain and the rotated $\mathbf{B}$ matrix. In Matlab, these constraints matrices were written as:

```
% Calculate constraints: c1, c2, c3, c4 and c5
A_c11 = detJ*( eV(1)*B_rot(1,:) + eV(2)*B_rot(2,:) +  ...
    eV(1)*B_rot(2,:) + eV(2)*B_rot(1,:) );
A_c33 = detJ*( eV(3)*B_rot(3,:) );
A_c44 = detJ*( eV(4)*B_rot(4,:) - 2*eV(1)*B_rot(2,:) - ...
    2*eV(2)*B_rot(1,:) );
A_c66 = detJ*( eV(5)*B_rot(5,:) + eV(6)*B_rot(6,:) );
A_c13 = detJ*( eV(1)*B_rot(3,:) + eV(3)*B_rot(1,:) + ...
    eV(2)*B_rot(3,:) + eV(3)*B_rot(2,:) );
```

Finally, the parameter variance matrix to be minimised, discussed in Appendix B, was written in terms of the rotated strain matrix as:

```
% 5 Parameter: H matrix

```

```
% Calculate each term in the H matrix  (N11 corresponds to N(1,1))
% N => E(N'N)
N11 = (detJ^2)*( 2*B_rot(1,:).'*B_rot(1,:) + ...
    4*B_rot(1,:).'*B_rot(2,:) + 2*B_rot(2,:).'*B_rot(2,:) );
N22 = (detJ^2)*( B_rot(3,:).'*B_rot(3,:) );
N33 = (detJ^2)*( B_rot(4,:).'*B_rot(4,:) + ...
    4*B_rot(1,:).'*B_rot(1,:) + 4*B_rot(2,:).'*B_rot(2,:));
N44 = (detJ^2)*( B_rot(5,:).'*B_rot(5,:) + B_rot(6,:).'*B_rot(6,:));
N55 = (detJ^2)*( 2*B_rot(3,:).'*B_rot(3,:) + ...
    2*B_rot(1,:).'*B_rot(2,:) + B_rot(1,:).'*B_rot(1,:) + ...
    B_rot(2,:).'*B_rot(2,:) );
N13 = (detJ^2)*( -2*B_rot(1,:).'*B_rot(1,:) - ...
    2*B_rot(2,:).'*B_rot(2,:) - 4*B_rot(1,:).'*B_rot(2,:) );
N15 = (detJ^2)*( 2*B_rot(1,:).'*B_rot(3,:) + ...
    2*B_rot(2,:).'*B_rot(3,:) );
N25 = (detJ^2)*( B_rot(1,:).'*B_rot(3,:) + ...
    B_rot(2,:).'*B_rot(3,:) );
N35 = (detJ^2)*( -2*B_rot(1,:).'*B_rot(3,:) - ...
    2*B_rot(2,:).'*B_rot(3,:) );

% Multiply in approximate parameters: Q' E(N'N) Q
h = C11_app^2 * N11 + C33_app^2 * N22 + C44_app^2 * N33 + ...
    C66_app^2 * N44 + C13_app^2 * N55 + 2*C11_app*C44_app * N13 + ...
    2*C11_app*C13_app * N15 + 2*C33_app*C13_app * N25 + ...
    2*C44_app*C13_app * N35;
```

The constraints along with the parameter variance matrix were used to numerically calculate each virtual displacement field in Chapter 6.

D

ANISOTROPIC DAMPING COEFFICIENTS

WITH the anisotropic optimised VFM implemented in Chapter 6, all estimated moduli were complex values, comprised of both real and imaginary parts. However, for conciseness, only real components of moduli were presented in Chapter 6. The structural damping coefficients (s), calculated as the ratio of the imaginary over the real part of each modulus, are presented here. The structure of this section follows closely the structure of Chapter 6.

In a noise-free and ideal case, the resulting Poisson's ratio estimated from the five-parameter formulation has only a real component. However, E_1, E_3, G_{12} and G_{13} are all complex-valued. For the three-parameter formulation, all estimated moduli, G_{12}, G_{13} and τ, are complex-valued. Therefore, for the five-parameter formulation, four damping coefficients (s_{E_1}, s_{E_3}, $s_{G_{12}}$ and $s_{G_{13}}$) were reported and for the three-parameter formulation, three were given ($s_{G_{12}}$, $s_{G_{13}}$ and s_τ).

Simulated Displacements in a Cantilever Beam The resulting damping coefficients from the beam loading test are shown in Figures D.1 and D.2. For the five parameter method, estimated damping coefficients were most accurately estimated for the two shear moduli for all 511 loading conditions and least accurately estimated for the fibre Young's modulus (s_{E_3}). In fact, even without noise, some damping coefficients associated with the fibre Young's modulus were negative, which is physically impossible.

Similarly to the resulting storage moduli reported in Chapter 6, damping coefficients were more accurately estimated with the three-parameter formulation than the five-parameter formulation, as seen by the narrow range of estimated values, centred at the reference parameter (0.1) for $s_{G_{12}}$ and $s_{G_{13}}$. s_τ showed a larger range of estimated values than both shear moduli yet varied less than s_{E_1} and s_{E_3}.

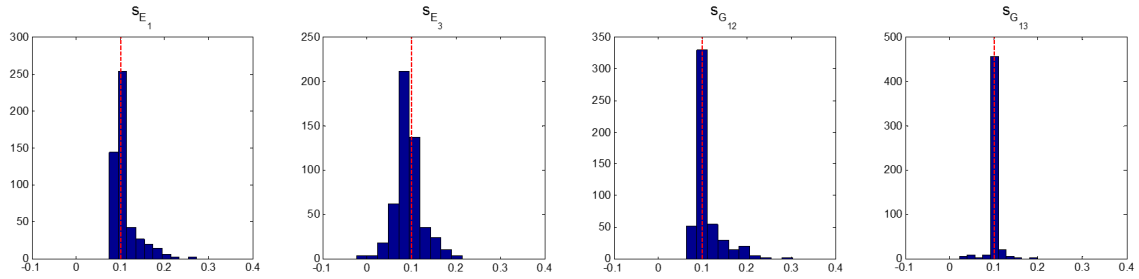

FIGURE D.1: Histograms of estimated damping coefficients (s_{E_1}, s_{E_3}, $s_{G_{12}}$, $s_{G_{13}}$) for all 511 loading cases using the five-parameter formulation. Reference values are shown as red dotted lines (s = 0.1). Corresponding storage moduli are shown in Figure 6.4.

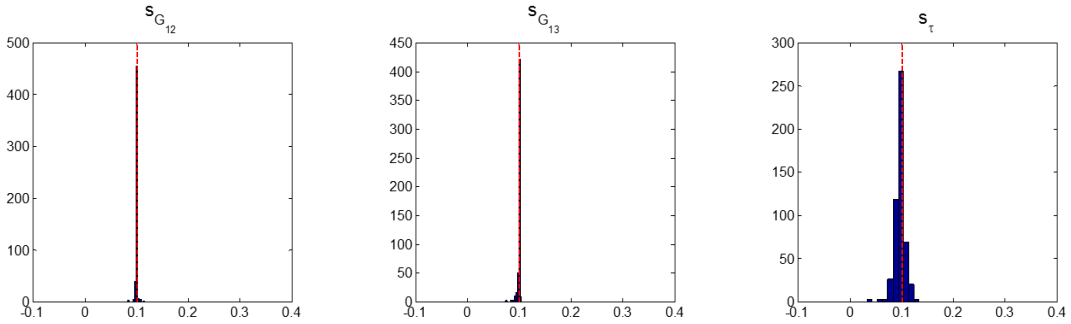

FIGURE D.2: Histograms of estimated damping coefficients ($s_{G_{12}}$, $s_{G_{13}}$, s_{τ}) for all 511 loading cases using the three-parameter formulation. Reference values are shown as red dotted lines (s = 0.1). Corresponding storage moduli are shown in Figure 6.5.

Monte Carlo simulations (n = 30) were run for each of the six loading configurations and Figures D.3 and D.4 illustrate box plots of the estimated damping coefficients when Gaussian noise was added to the reference displacements. Damping coefficients are grouped by their respective modulus (e.g. s_{E_1}) and the horizontal axis lists the six loading configuration numbers. It is apparent that in both material formulations, the damping coefficients associated with G_{13} were most accurately estimated with the smallest variance. s_{E_3} values estimated from the five-parameter formulation exhibited the largest variation. The variances were greater for loading cases #113, #211 and #451 than for loading cases #189, #412 and #447. Similarly, values of s_{τ} were consistently underestimated for loading configurations #113, #211 and #451.

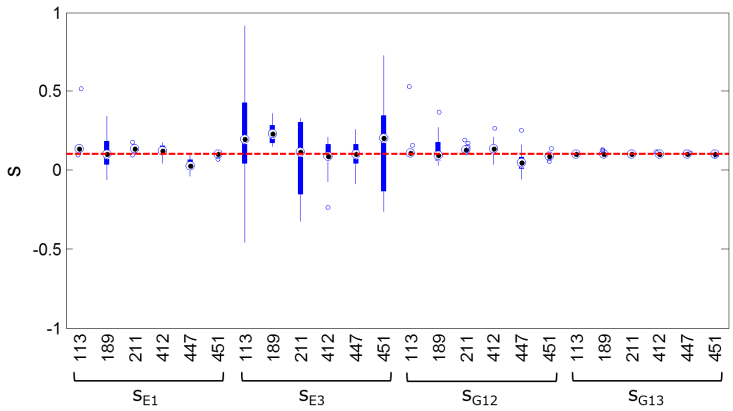

FIGURE D.3: Box plots of estimated damping coefficients (s_{E_1}, s_{E_3}, $s_{G_{12}}$, $s_{G_{13}}$) from all Monte-Carlo simulations (n = 30) for each beam loading case. Corresponding storage moduli are shown in Figure 6.9. The reference value is shown as a red dotted line.

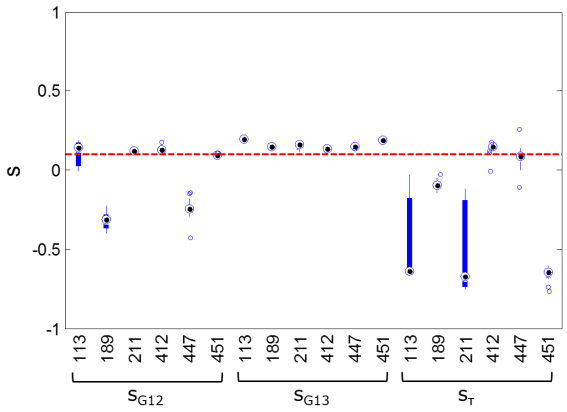

FIGURE D.4: Box plots of estimated damping coefficients ($s_{G_{12}}$, $s_{G_{13}}$ and s_τ) from all Monte-Carlo simulations (n = 30) for each beam loading case. Corresponding storage moduli are shown in Figure 6.10. The reference value is shown as a red dotted line.

Cylindrical Phantom MRE For the cylindrical phantom MRE data, box plots of resulting estimated damping coefficients are shown in Figures D.5 and D.6 for both arbitrarily assigned material orientations: <0, 0, 1> and <1, 0, 0> (see Figure 6.2). Again, the results are grouped according to the associated parameter (e.g. s_{E_3}) and the horizontal axis shows the material orientation, either <0, 0, 1> or <1, 0, 0>. Like the beam results, estimated damping coefficients associated with shear moduli (G_{12} and G_{13}) showed the least variance and were most accurate estimated. Conversely, damping coefficients associated with Young's moduli and τ showed large variance and were often negative.

Similarly to storage moduli presented in Chapter 6, estimated values of $s_{G_{12}}$ showed larger variation when the material was oriented along the global <0, 0, 1> direction compared to when it was aligned with the global <1, 0, 0> direction. Again, this result is most likely due to the lack of signal provided in the image plane, in the global x- and global

y-directions, with which to estimate the shear in the image plane.

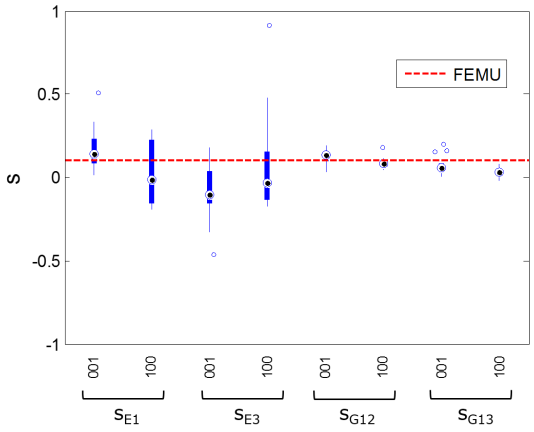

FIGURE D.5: Box plots of estimated damping coefficients (s_{E_1}, s_{E_3}, $s_{G_{12}}$, $s_{G_{13}}$) from all converged subzones in the isotropic phantom. The reference value is shown as a red dotted line. Corresponding storage moduli are shown in Figure 6.11.

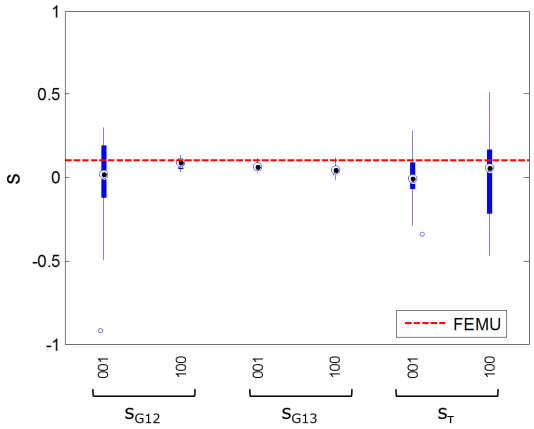

FIGURE D.6: Box plots of estimated damping coefficients ($s_{G_{12}}$, $s_{G_{13}}$ and τ) from all converged subzones in the isotropic phantom. The reference value is shown as a red dotted line. Corresponding storage moduli are shown in Figure 6.12.

Simulated Displacements in a Left Ventricle For the loading test utilising the left ventricular model, estimated damping coefficients are shown in Figures D.7 and D.8. Conversely to the beam, but showing similar trends to the storage moduli presented in Chapter 6, damping coefficients estimated with the five-parameter formulation were more accurate and showed less variance than those estimated using the three-parmeter formulation. The three-parameter formulation resulted in a wide variation of estimated damping coefficients, illustrating that the LV geometry had a profound impact on the estimation of damping coefficients when using the three-parameter formulation.

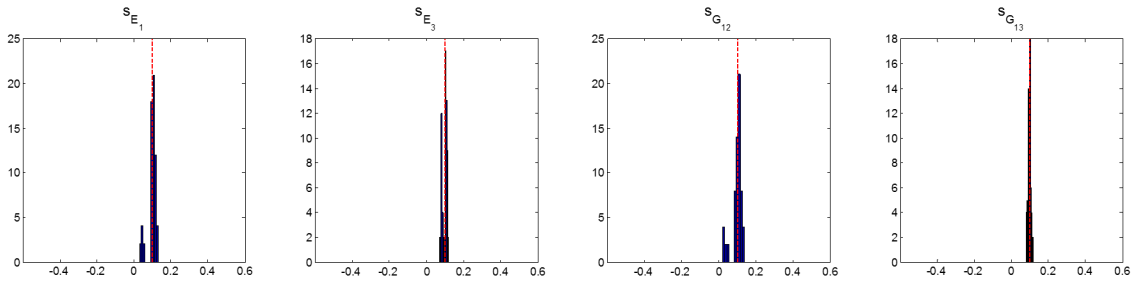

FIGURE D.7: Histograms of estimated damping coefficients (s_{E_1}, s_{E_3}, $s_{G_{12}}$, $s_{G_{13}}$) for all 63 loading cases using the five-parameter formulation. The reference values are shown as red dotted lines (s = 0.1).

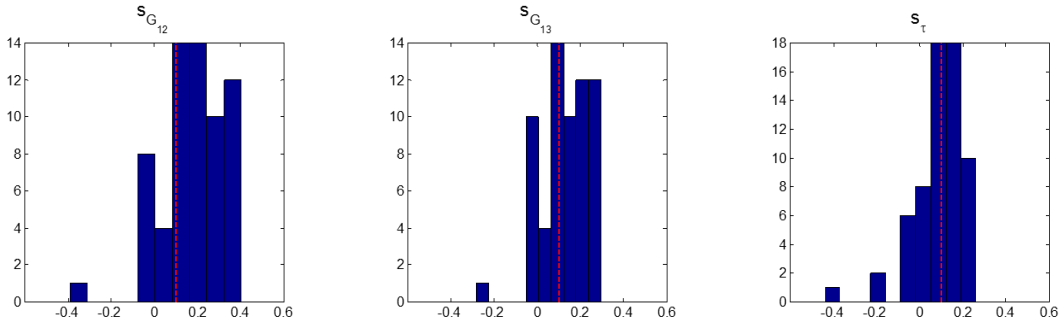

FIGURE D.8: Histograms of estimated damping coefficients ($s_{G_{12}}$, $s_{G_{13}}$, s_{τ}) for all 63 loading cases using the three-parameter formulation. The reference values are shown as red dotted lines (s = 0.1).

The damping coefficients estimated for each modulus in the Monte Carlo test with 15% added Gaussian noise (Equation (6.21)) are plotted in Figures D.9 and D.10 for all six loading cases. Estimated damping coefficients showed large variance and the means were not always centred on the true values. Again, damping coefficients associated with G_{13} in the five-parameter formulation were most accurate.

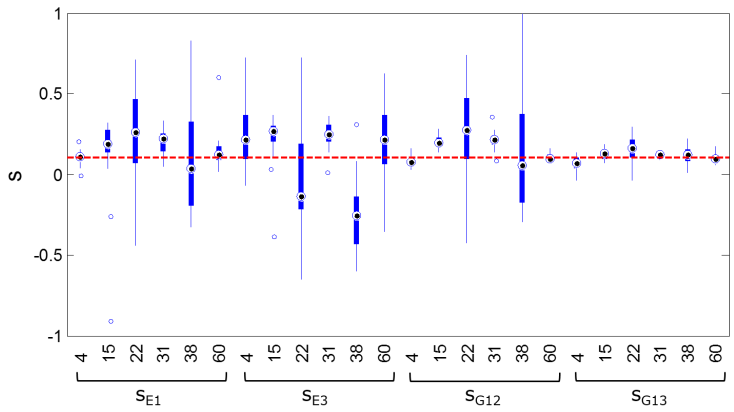

FIGURE D.9: Box plots of estimated damping coefficients (s_{E_1}, s_{E_3}, $s_{G_{12}}$, $s_{G_{13}}$) from Monte-Carlo experiments for six LV loading cases. The reference value is shown as a red dotted line. Corresponding storage moduli are shown in Figure 6.18.

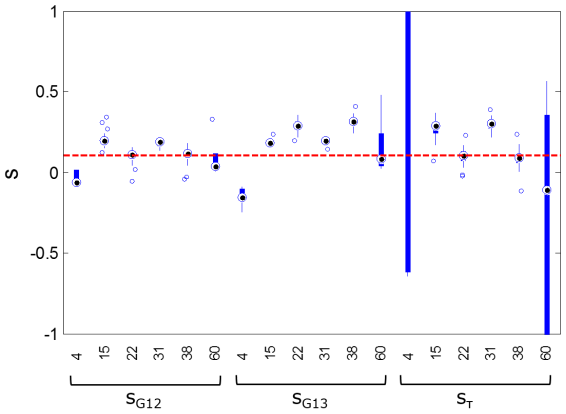

FIGURE D.10: Box plots of estimated damping coefficients ($s_{G_{12}}$, $s_{G_{13}}$ and s_τ) from Monte-Carlo experiments for six LV loading cases. The reference value is shown as a red dotted line. Corresponding storage moduli are shown in Figure 6.19.

Results are shown in Figures D.11 and D.12 for estimated damping coefficients when varying amounts of noise were added to the reference displacement field for one loading configuration.

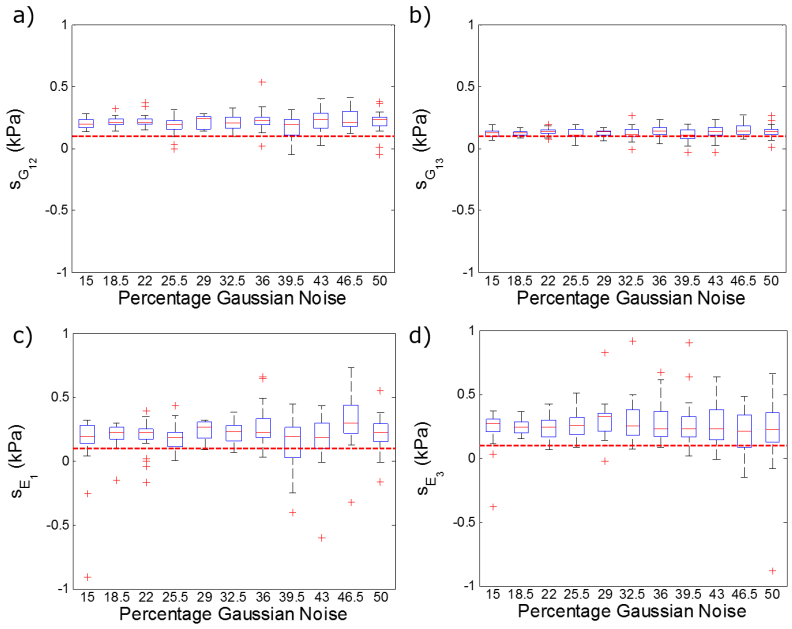

FIGURE D.11: Box plots of estimated values of a) a) $s_{G_{12}}$, b) $s_{G_{13}}$, c) s_{E_1} and d) s_{E_3} using the five-parameter formulation with varying amounts of Gaussian noise (N = 15% - 50%) added to the reference displacements. Reference values are shown as red dotted lines. Corresponding storage moduli are shown in Figure 6.20.

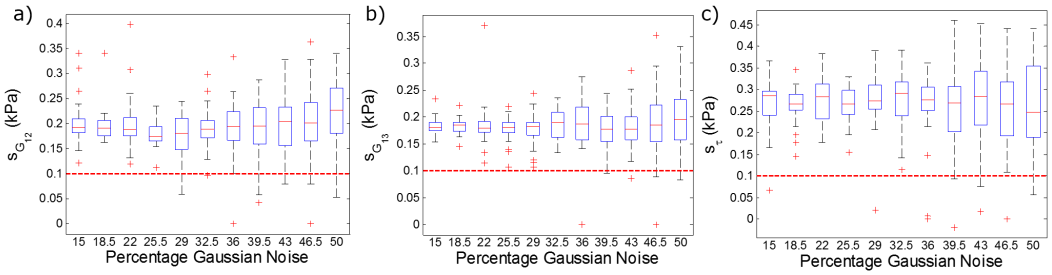

FIGURE D.12: Box plots of estimated values of a) $s_{G_{12}}$, b) $s_{G_{13}}$ and c)s_τ using the three-parameter formulation with varying amounts of Gaussian noise (N = 15% - 50%) added to the reference displacements. Reference values are shown as red dotted lines. Corresponding storage moduli are shown in Figure 6.20.

In Figure D.13, the coefficients of variation are plotted for damping coefficients estimated with both the five- and three-parameter formulations. Note the difference in scale between subplots a) and b). The addition of increasing amounts of Gaussian noise resulted in overall smaller increases in variance when using the three-parameter formulation than the five-parameter formulation. Variance in estimated damping coefficients, s_{E_1} and s_{E_3}, did not increase linearly with increasing noise.

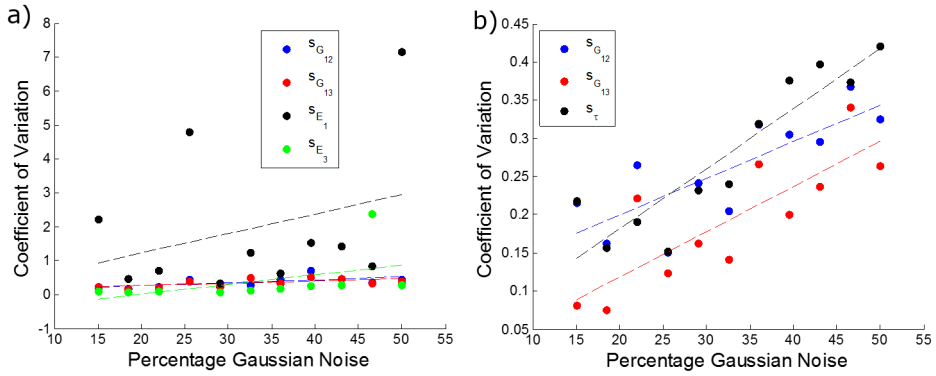

FIGURE D.13: Coefficients of variation of damping coefficients in the a) five-parameter and b) three-parameter formulation plotted versus amount of Gaussian noise added to the reference displacements (N = 15% - 50%). Note the difference in scales between a) and b). Corresponding plot of coefficient of variation of storage moduli is shown in Figure 6.22.

Damping coefficients estimated from the Monte Carlo experiment when varying the frequency of excitation between 60 Hz and 200 Hz are shown in Figures D.14 and D.15. Like previous results, $s_{G_{13}}$ was most accurately estimated when using the five-parameter formulation. One interesting result to note is that, despite the higher rate of convergence of the five-parameter formulation at higher frequencies (see Table 6.7), estimated values of s_{E_3} vary more at higher frequencies. Therefore, convergence of the method does not necessarily ensure accuracy, at least with the imaginary part of the moduli.

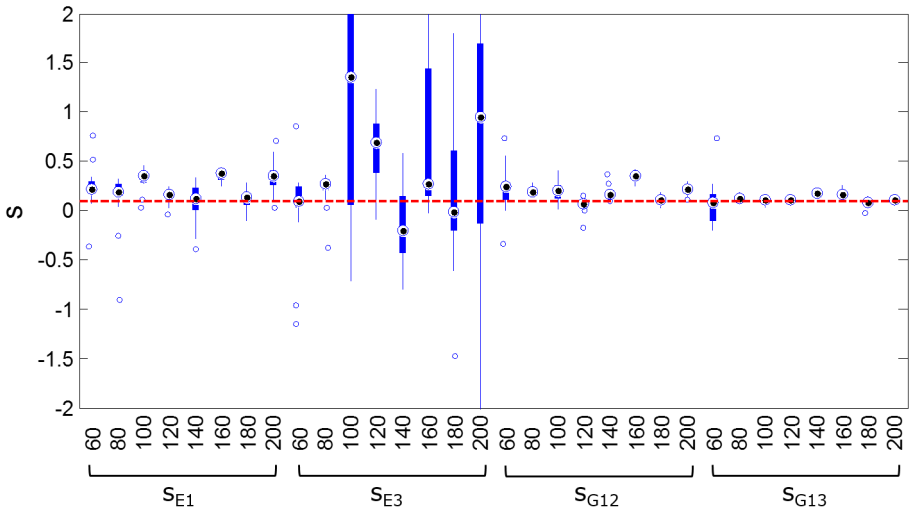

FIGURE D.14: Box plots of estimated damping coefficients (s_{E_1}, s_{E_3}, $s_{G_{12}}$ and $s_{G_{13}}$) from all converged Monte Carlo simulations, using the five-parameter formulation, for frequencies between 60 Hz - 200 Hz. The reference value is shown as a red dotted line. Corresponding storage moduli are shown in Figure 6.24.

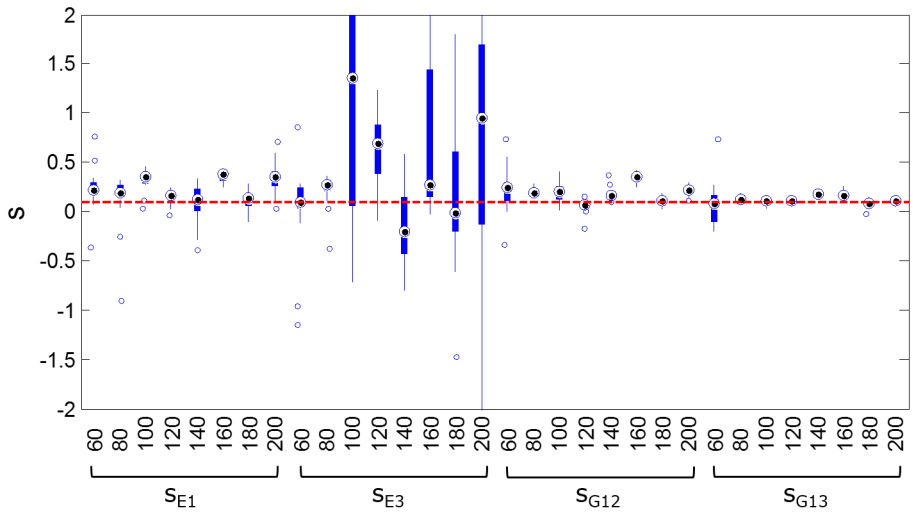

FIGURE D.15: Box plots of estimated damping coefficients ($s_{G_{12}}$, $s_{G_{13}}$ and s_τ) from all converged Monte Carlo simulations, using the three-parameter formulation, for frequencies between 60 Hz - 140 Hz. The reference value is shown by a red dotted line. Corresponding storage moduli are shown in Figure 6.25.

Overall, trends in damping coefficients estimated from the anisotropic optimised VFM follow closely those seen in the storage moduli presented in Chapter 6. Damping coefficients were estimated accurately for G_{13} in the presence of noise for the cantilever beam, phantom and LV modelsl. Conversely, s_{E_3} was consistenly inaccurate and showed large variance. Errors (expressed as a percentage) were much larger for damping coefficients than for estimated storage moduli. Therefore, the implementation of the optimised VFM, which produces complex moduli, may not accurately estimate damping coefficients in the presence of Gaussian noise, except for that of G_{13}.

REFERENCES

[1] T. P. Abraham and R. A. Nishimura. "Myocardial strain: Can we finally measure contractility?" In: *Journal of the American College of Cardiology* 37.3 (2001), pp. 731–734.

[2] A. H. Aletras et al. "DENSE: displacement encoding with stimulated echoes in cardiac functional MRI". In: *Journal of Magnetic Resonance* 137.1 (1999), pp. 247–252. eprint: NIHMS150003.

[3] A. T. Anderson et al. "Observation of direction-dependent mechanical properties in the human brain with multi-excitation MR elastography". In: *Journal of the Mechanical Behavior of Biomedical Materials* 59 (2016), pp. 538–546.

[4] A. Arani et al. "In vivo, high-frequency three-dimensional cardiac MR elastography: Feasibility in normal volunteers". In: *Magnetic Resonance in Medicine* 77.1 (2017), pp. 351–360.

[5] S. P. Arunachalam et al. "Regional assessment of in vivo myocardial stiffness using 3D magnetic resonance elastography in a porcine model of myocardial infarction". In: *Magnetic Resonance in Medicine* (2017), Published online.

[6] S. M. Atay and C. D. Kroenke. "Measurement of the dynamic shear modulus of mouse brain tissue in vivo by magnetic resonance elastography". In: *Journal of Biomechanical Engineering* 130.2 (2008), pp. 1–30.

[7] K. F. Augenstein et al. "Method and Apparatus for Soft Tissue Material Parameter Estimation Using Tissue Tagged Magnetic Resonance Imaging". In: *Journal of Biomechanical Engineering* 127.1 (2005), pp. 148–157.

[8] D. Augustine et al. "Global and regional left ventricular myocardial deformation measures by magnetic resonance feature tracking in healthy volunteers: comparison with tagging and relevance of gender". In: *Journal of Cardiovascular Magnetic Resonance* 15.1 (2013), p. 8.

[9] S. Avril, P. Badel, and A. Duprey. "Anisotropic and hyperelastic identification of in vitro human arteries from full-field optical measurements". In: *Journal of Biomechanics* 43.15 (2010), pp. 2978–2985.

[10] S. Avril, M. Grédiac, and F. Pierron. "Sensitivity of the virtual fields method to noisy data". In: *Computational Mechanics* 34.6 (2004), pp. 439–452.

[11] S. Avril et al. "Overview of identification methods of mechanical parameters based on full-field measurements". In: *Experimental Mechanics* 48.4 (2008), pp. 381–402.

[12] T. P. Babarenda Gamage et al. "Identification of mechanical properties of heterogeneous soft bodies using gravity loading". In: *International Journal for Numerical Methods in Biomedical Engineering* 27.3 (2011), pp. 391–407.

[13] S. F. Bensamoun et al. "Determination of thigh muscle stiffness using magnetic resonance elastography". In: *Journal of Magnetic Resonance Imaging* 23.2 (2006), pp. 242–247.

[14] S. F. Bensamoun et al. “Estimation of Muscle Force Derived From in Vivo MR Elastography Tests: A Preliminary Study”. In: *Journal of Musculoskeletal Research* 16.3 (2013), p. 1350015.

[15] S. F. Bensamoun et al. “Thigh muscle stiffness assessed with magnetic resonance elastography in hyperthyroid patients before and after medical treatment”. In: *Journal of Magnetic Resonance Imaging* 26.3 (2007), pp. 708–713.

[16] B. C. Berk, K. Fujiwara, and S. Lehoux. “Review series ECM remodeling in hypertensive heart disease”. In: *Journal of Clinical Investigation* 117.3 (2007), pp. 568–575.

[17] M. A. Bernstein, K. F. King, and X. J. Zhou. *Handbook of MRI Pulse Sequences*. Elsevier, 2004.

[18] O. Bernus et al. “Comparison of diffusion tensor imaging by cardiovascular magnetic resonance and gadolinium enhanced 3D image intensity approaches to investigation of structural anisotropy in explanted rat hearts”. In: *Journal of Cardiovascular Magnetic Resonance* 17.1 (2015), p. 31.

[19] Hamparsum Bozdogan. “Model selection and Akaike’s Information Criterion (AIC): The general theory and its analytical extensions”. In: *Psychometrika* 52.3 (1987), pp. 345–370.

[20] D. Burkhoff, I. Mirsky, and H. Suga. “Assessment of systolic and diastolic ventricular properties via pressure-volume analysis: a guide for clinical, translational, and basic researchers.” In: *American Journal of Physiology - Heart and Circulatory Physiology* 289.2 (2005), H501–H512.

[21] M. Carfagni, E. Lenzi, and M. Pierini. “The loss factor as a measure of mechanical damping”. In: *Proceedings of the International Society for Optics and Photonics*. Vol. 1. 1998, pp. 580–584.

[22] M. K. Chakouch et al. “Viscoelastic shear properties of in vivo thigh muscles measured by MR elastography”. In: *Journal of Magnetic Resonance Imaging* 43.6 (2016), pp. 1423–1433.

[23] S. K. Chamarthi et al. “Rapid acquisition technique for MR elastography of the liver”. In: *Journal of Magnetic Resonance Imaging* 32.6 (2014), pp. 679–683.

[24] S. Chatelin et al. “An automatic differentiation-based gradient method for inversion of the shear wave equation in magnetic resonance elastography: specific application in fibrous soft tissues”. In: *Physics in Medicine and Biology* 61.13 (2016), pp. 5000–5019.

[25] S. Chatelin et al. “Anisotropic polyvinyl alcohol hydrogel phantom for shear wave elastography in fibrous biological soft tissue: a multimodality characterization”. In: *Physics in Medicine and Biology* 59.22 (2014), pp. 6923–6940.

[26] Q. Chen, J. Basford, and K. N. An. “Ability of magnetic resonance elastography to assess taut bands”. In: *Clinical Biomechanics* 23.5 (2008), pp. 623–629.

[27] Q. Chen et al. “Identification and quantification of myofascial taut bands with magnetic resonance elastography”. In: *Archives of Physical Medicine and Rehabilitation* 88.12 (2007), pp. 1658–1661.

[28] E. H. Clayton et al. “Comparison of dynamic mechanical testing and MR elastography of biomaterials”. In: *Proceedings of the SEM Annual Conference*. Ed. by Tom Proulx. Vol. 4. Conference Proceedings of the Society for Experimental Mechanics Series. New York, NY: Springer New York, 2010, pp. 143–150.

[29] N. Connesson et al. “Extension of the optimised virtual fields method to estimate viscoelastic material parameters from 3D dynamic displacement fields”. In: *Strain* 51.2 (2015), pp. 110–134.

[30] N. Connesson et al. “The effects of noise and spatial sampling on identification of material parameters by magnetic resonance elastography”. In: *Mechanics of Biological Systems and Materials*. Vol. 5. 2013, pp. 161–168.

[31] M. Couade et al. “In vivo quantitative mapping of myocardial stiffening and transmural anisotropy during the cardiac cycle”. In: *IEEE Transactions on Medical Imaging* 30.2 (2011), pp. 295–305.

[32] L. L. Demer and F. C . P. Yin. “Passive biaxial mechanical properties of isolated canine myocardium”. In: *Journal of Physiology* 339.1 (1983), pp. 615–630.

[33] M. Destrade, P. A. Martin, and T. C. T. Ting. “The incompressible limit in linear anisotropic elasticity, with applications to surface waves and elastostatics”. In: *Journal of the Mechanics and Physics of Solids* 50.7 (2002), pp. 1453–1468.

[34] S. Dokos et al. “Shear properties of passive ventricular myocardium”. In: *American Journal of Physiology - Heart and Circulatory Physiology* 283.6 (2002), H2650–H2659.

[35] M. M. Doyley, P. M. Meaney, and J. C. Bamber. “Evaluation of an iterative reconstruction method for quantitative elastography”. In: *Physics in Medicine and Biology* 45.6 (2000), pp. 1521–1540.

[36] M. M. Doyley et al. “Shear modulus estimation using parallelized partial volumetric reconstruction”. In: *IEEE Transactions on Medical Imaging* 23.11 (2004), pp. 1404–1416.

[37] M. A. Dresner et al. “Functional MR elastography of human skeletal muscle”. In: *Proceedings of the 6th Conference of the International Society of Magnetic Resonance in Medicine*. 1998, p. 463.

[38] M. A. Dresner et al. “Magnetic resonance elastography of skeletal muscle”. In: *Journal of Magnetic Resonance Imaging* 13.2 (2001), pp. 269–276.

[39] B. Dzyubak et al. “Automated liver elasticity calculation for MR elastography”. In: *Journal of Magnetic Resonance Imaging* 43.5 (2015), pp. 1055–1063.

[40] T. Edvardsen et al. “Quantitative assessment of intrinsic regional myocardial deformation by Doppler strain rate echocardiography in humans: Validation against three-dimensional tagged magnetic resonance imaging”. In: *Circulation* 106.1 (2002), pp. 50–56.

[41] T. Elgeti et al. “Cardiac magnetic resonance elastography: Toward the diagnosis of abnormal myocardial relaxation”. In: *Investigative Radiology* 45.12 (2010), pp. 782–787.

[42] T. Elgeti et al. “Cardiac MR elastography: Comparison with left ventricular pressure measurement”. In: *Journal of Cardiovascular Magnetic Resonance* 11.44 (2009).

[43] T. Elgeti et al. “Elasticity-based determination of isovolumetric phases in the human heart”. In: *Journal of Cardiovascular Magnetic Resonance* 12.60 (2010).

[44] T. Elgeti et al. “Shear-wave Amplitudes Measured with Cardiac MR Elastography for Diagnosis of Diastolic Dysfunction”. In: *Radiology* 271.3 (2014), pp. 681–687.

[45] T. Elgeti et al. “Vibration-synchronized magnetic resonance imaging for the detection of myocardial elasticity changes”. In: *Magnetic Resonance in Medicine* 67.4 (2012), pp. 919–924.

[46] H. Eskandari et al. “Viscoelastic characterization of soft tissue from dynamic finite element models”. In: *Physics in Medicine and Biology* 53.22 (2008), pp. 6569–6590.

[47] Y. Feng et al. “Measurements of mechanical anisotropy in brain tissue and implications for transversely isotropic material models of white matter”. In: *Journal of the Mechanical Behavior of Biomedical Materials* 23 (2013), pp. 117–132.

[48] D. P. Flanagan and A. T. Belytschko. “A uniform strain hexahedron and quadrilateral with orthogonal hourglass control”. In: *International Journal for Numerical Methods in Engineering* 17.5 (1981), pp. 679–706.

[49] D. Fu et al. “Non-invasive quantitative reconstruction of tissue elasticity using an iterative forward approach”. In: *Physics in Medicine and Biology* 45.6 (2000), pp. 1495–1509.

[50] M. Genet et al. “Distribution of normal human left ventricular myofiber stress at end-diastole and end-systole–a target for in silico studies of cardiac procedures”. In: *Journal of Applied Physiology* 117.2 (2014), pp. 142–152.

[51] J. L. Gennisson et al. “Transient elastography in anisotropic medium: application to the measurement of slow and fast shear wave speeds in muscles”. In: *The Journal of the Acoustical Society of America* 114.1 (2003), pp. 536–541.

[52] J. L. Gennisson et al. “Viscoelastic and anisotropic mehcanical properties of in-vivo muscle tissue assessed by supersonic shear imaging”. In: *Ultrasound in Medicine and Biology* 36.5 (2010), pp. 789–801.

[53] H. Ghaemi, K. Behdinan, and A. D. Spence. “In vitro technique in estimation of passive mechanical properties of bovine heart. Part I. Experimental techniques and data”. In: *Medical Engineering and Physics* 31.1 (2009), pp. 76–82.

[54] K. F. Graff. *Wave Motion in Elastic Solids*. Courier Corporation, 1975.

[55] M. Grédiac, E. Toussaint, and F. Pierron. “Special virtual fields for the direct determination of material parameres with the virtual fields method. 1–principle and definition”. In: *International Journal of Solids and Structures* 39.10 (2002), pp. 2691–2705.

[56] A. E. Green, R. S. Rivlin, and R. T. Shield. “General theory of small elastic deformations superposed on finite elastic deformations”. In: *Proceedings of the Royal Society of London. Series A, Mathematical and Physical Sciences*. Vol. 211. 1104. The Royal Society, 1952, pp. 128–154.

[57] M. A. Green et al. “Measuring anisotropic muscle stiffness properties using elastography”. In: *NMR in Biomedicine* 26.11 (2013), pp. 1387–1394.

[58] M. A. Green et al. “Measuring changes in muscle stiffness after eccentric exercise using elastography”. In: *NMR in Biomedicine* 25.6 (2012), pp. 852–858.

[59] J. M. Guccione, A. D. McCulloch, and L. K. Waldman. “Passive material properties of intact ventricular myocardium determined from a cylindrical model”. In: *Journal of Biomechanical Engineering* 113.1 (1991), pp. 42–55.

[60] H. Gudbjartsson and S. Patz. “The Rician distribution of noisy MRI data”. In: *Magnetic Resonance in Medicine* 34.6 (1995), pp. 910–914.

[61] J. Guo et al. “Three-parameter shear wave inversion in MR elastography of incompressible transverse isotropic media: Application to in vivo lower leg muscles”. In: *Magnetic Resonance in Medicine* 75.4 (2015), pp. 1537–1545.

[62] P. Helm et al. “Measuring and mapping cardiac fiber and laminar architecture using diffusion tensor MR imaging”. In: *Annals of the New York Academy of Sciences* 1047.1 (2005), pp. 296–307.

[63] M. Honarvar, R. Rohling, and S. E. Salcudean. “A comparison of direct and iterative finite element inversion techniques in dynamic elastography”. In: *Physics in Medicine and Biology* 61.8 (2016), pp. 3026–3048.

[64] M. Honarvar et al. “A comparison of FEM-based inversion algorithms, Local frequency estimation and direct inversion approach used in MR elastography”. In: *IEEE Transactions on Medical Imaging* (2017), Published online.

[65] M. Honarvar et al. “Direct vibro-elastography FEM inversion in Cartesian and cylindrical coordinate systems without the local homogeneity assumption”. In: *Physics in Medicine and Biology* 60.9 (2015), pp. 3847–3868.

[66] M. Honarvar et al. “Sparsity regularization in dynamic elastography”. In: *Physics in Medicine and Biology* 57.19 (2012), pp. 5909–5927.

[67] P. J. Hunter. “Myocardial constitutive laws for continuum mechanics models of the heart”. In: *Molecular and Subcellular Cardiology: Effects of Structure and Function*. Springer US, 1995, pp. 303–318.

[68] L. Huwart et al. “Liver fibrosis: non-invasive assessment with MR elastography”. In: *NMR in Biomedicine* 19.2 (2006), pp. 173–179.

[69] F. Kallel and M. Bertrand. “Tissue elasticity reconstruction using linear perturbation method”. In: *Medical Imaging, IEEE Transactions on Medical Imaging* 15.3 (1996), pp. 299–313.

[70] H. Kanai. “Propagation of spontaneously actuated pulsive vibration in human heart wall and in vivo viscoelasticity estimation”. In: *IEEE Transactions on Ultrasonics, Ferroelectrics, and Frequency Control* 52.11 (2005), pp. 1931–1942.

[71] R. Karimi et al. “Estimation of nonlinear mechanical properties of vascular tissues via elastography”. In: *Cardiovascular Engineering* 8.4 (2008), pp. 191–202. eprint: NIHMS150003.

[72] D. A. Kass et al. “Determination of left ventricular end-systolic pressure-volume relationships by the conductance (volume) catheter technique”. In: *Circulation* 73.3 (1986), pp. 586–595.

[73] J. Kemper et al. “MR elastography of the prostate: Initial in-vivo application”. In: *RoFo Fortschritte auf dem Gebiet der Rontgenstrahlen und der Bildgebenden Verfahren* 176.8 (2004), pp. 1094–1099.

[74] R. S. Kirton et al. “Strain softening behaviour in nonviable rat right-ventricular trabeculae, in the presence and the absence of butanedione monoxime.” In: *Experimental Physiology* 89.5 (2004), pp. 593–604.

[75] D. Klatt et al. “Viscoelasticity-based MR elastography of skeletal muscle”. In: *Physics in Medicine and Biology* 55.21 (2010), pp. 6445–6459.

[76] H. Knutsson, C. F. Westin, and G. Granlund. “Local multiscale frequency and bandwidth estimation”. In: *Proceedings of 1st International Conference on Image Processing*. Vol. 1. 1994, pp. 36–40.

[77] A. Kolipaka et al. “Evaluation of a rapid, multiphase MRE sequence in a heart-simulating phantom”. In: *Magnetic Resonance in Medicine* 62.3 (2009), pp. 691–698.

[78] A. Kolipaka et al. “In vivo assessment of MR elastography-derived effective end-diastolic myocardial stiffness under different loading conditions”. In: *Journal of Magnetic Resonance Imaging* 33.5 (2011), pp. 1224–1228.

[79] A. Kolipaka et al. “Magnetic resonance elastography as a method for the assessment of effective myocardial stiffness throughout the cardiac cycle”. In: *Magnetic Resonance in Medicine* 64.3 (2010), pp. 862–870.

[80] A. Kolipaka et al. “Magnetic resonance elastography as a method to estimate myocardial contractility”. In: *Journal of Magnetic Resonance Imaging* 36.1 (2012), pp. 120–127.

[81] A. Kolipaka et al. “Magnetic resonance elastography: Inversions in bounded media”. In: *Magnetic Resonance in Medicine* 62.6 (2009), pp. 1533–1542.

[82] A. Kolipaka et al. “MR elastography as a method for the assessment of myocardial stiffness: comparison with an established pressure-volume model in a left ventricular model of the heart”. In: *Magnetic Resonance in Medicine* 62.1 (2009), pp. 135–140.

[83] A. Krishnamurthy et al. “Patient-specific models of cardiac biomechanics”. In: *Journal of Computational Physics* 244 (2013), pp. 4–21.

[84] S. A. Kruse, G. H. Rose, and K. J. Glaser. “Magnetic resonance elastography of the brain”. In: *Neuroimage* 39.1 (2008), pp. 231–237.

[85] S. A. Kruse et al. “Tissue characterization using magnetic resonance elastography: preliminary results”. In: *Physics in Medicine and Biology* 45.6 (2000), pp. 1579–1590.

[86] G. E. Leclerc et al. “Characterization of a hyper-viscoelastic phantom mimicking biological soft tissue using an abdominal pneumatic driver with Magnetic Resonance Elastography (MRE)”. In: *Journal of Biomechanics* 18.9 (2013), pp. 1199–1216.

[87] G. E. Leclerc et al. “Identification process based on shear wave propagation within a phantom using finite element modelling and magnetic resonance elastography”. In: *Computer Methods in Biomechanics and Biomedical Engineering* 18.5 (2013), pp. 485–491.

[88] I. J. LeGrice et al. “Laminar structure of the heart: ventricular myocyte arrangement and connective tissue architecture in the dog”. In: *American Journal of Physiology* 269.2 (1995), H571–H582.

[89] I. J. LeGrice et al. “Progression of myocardial remodeling and mechanical dysfunction in the spontaneously hypertensive rat”. In: *American Journal of Physiology - Heart and Circulatory Physiology* 303.11 (2012), H1353–H1365.

[90] B. M. Lempriere. “Poisson’s ratio in orthotropic materials”. en. In: *AIAA Journal* 6.11 (1968), pp. 2226–2227.

[91] Y. Liu, T. Yasar, and T. J. Royston. “Interpreting magnetic resonance elastography measurements using finite element analysis”. In: *Proceedings of the ASME 2013 International Mechanical Engineering Congress and Exposition*. 2013, pp. 1–6.

[92] E. L. Madsen, H. J. Sathoff, and J. A. Zagzebski. “Ultrasonic shear wave properties of soft tissues and tissue-like materials”. In: *The Journal of the Acoustical Society of America* 74.5 (1983), pp. 1346–1355.

[93] A. Manduca. “Magnetic resonance elastography: non-invasive mapping of tissue elasticity”. In: *Medical Image Analysis* 5.4 (2001), pp. 237–254.

[94] A. Manduca and R. Muthupillai. “Local wavelength estimation for magnetic resonance elastography”. In: *Proceedings of the International IEEE Conference on Image Processing*. Vol. 3. 1996, pp. 527–530.

[95] A. Manduca et al. “Characterization and Evaluation of Inversion Algorithms for MR Elastography”. In: *Proceedings from the International Society for Optics and Photonics*. Ed. by Milan Sonka and J. Michael Fitzpatrick. Vol. 4684. 2002, pp. 1180–1185.

[96] A. Manduca et al. “Reconstruction of elasticity and attenuation maps in shear wave imaging: An inverse approach”. In: *Proceedings from Medical Image Computing and Computer-Assisted Intervention*. Vol. 1496. 1998, pp. 606–613.

[97] A. Manduca et al. “Spatio-temporal directional filtering for improved inversion of MR elastography images”. In: *Medical Image Analysis* 7.4 (2003), pp. 465–473.

[98] R. Mazumder et al. “In vivo magnetic resonance elastography to estimate left ventricular stiffness in a myocardial infarction induced porcine model”. In: *Journal of Magnetic Resonance Imaging* 45.4 (2016), pp. 1024–1033.

[99] R. Mazumder et al. “In vivo quantification of myocardial stiffness in hypertensive porcine hearts using MR elastography”. In: *Journal of Magnetic Resonance Imaging* 45.3 (2016), pp. 813–820.

[100] R. Mazumder et al. “In-vivo waveguide cardiac magnetic resonance elastography”. In: *Journal of Cardiovascular Magnetic Resonance*. Vol. 17. 2015, pp. 35–36.

[101] M. D. J. McGarry et al. “Comparison of iterative and direct inversion MR elastography algorithms”. In: *Conference Proceedings of the Society for Experimental Mechanics*. Vol. 2. 2011, pp. 49–56.

[102] A. L. McKnight et al. “MR elastography of breast cancer: preliminary results”. In: *American Journal of Roentgenology* 178.6 (2002), pp. 1411–1417.

[103] R. Miller et al. “Determining Anisotropic Myocardial Stiffness from Magnetic Resonance Elastography: A Simulation Study”. In: *Functional Imaging and Modeling of the Heart*. 2015, pp. 346–354.

[104] J. M. Millward et al. “Tissue structure and inflammatory processes shape viscoelastic properties of the mouse brain”. In: *NMR in Biomedicine* 28.7 (2015), pp. 831–839.

[105] C. C. Moore et al. “Calculation of threedimensional left ventricular strains from biplanar tagged MR images”. In: *Journal of Magnetic Resonance Imaging* 2.2 (1992), pp. 165–175. eprint: NIHMS150003.

[106] R. Muthupillai et al. “Magnetic resonance elastography by direct visualization of propagating acoustic strain waves”. In: *Science* 269.5232 (1995), pp. 1854–1857.

[107] R. Muthupillai et al. “Magnetic resonance imaging of transverse acoustic strain waves”. In: *Magnetic Resonance in Medicine* 36.2 (1996), pp. 266–274.

[108] R. Namani and P. V. Bayly. “Shear wave propagation in anisotropic soft tissues and gels”. In: *Conference Proceedings of IEEE Engineering in Medicine and Biology Society*. 2009, pp. 1117–1122.

[109] R. Namani et al. “Anisotropic mechanical properties of magnetically aligned fibrin gels measured by magnetic resonance elastography”. In: *Journal of Biomechanics* 42.13 (2009), pp. 2047–2053.

[110] M. H. Nathanson and G. M. Saidel. “Multiple-objective criteria for optimal experimental design: application to ferrokinetics”. In: *American Journal of Physiology* 248.3 (1985), R378–R386.

[111] R. J. Okamoto, E. H. Clayton, and P. V. Bayly. “Viscoelastic properties of soft gels: comparison of magnetic resonance elastography and dynamic shear testing in the shear wave regime”. In: *Physics in Medicine and Biology* 56.19 (2011), pp. 6379–6400. eprint: NIHMS150003.

[112] T. E. Oliphant and J. L. Mahowald. “Complex-valued quantitative stiffness estimation using dynamic displacement measurements and local inversion of conservation of momentum”. In: *IEEE Ultrasonics Symposium*. 1999, pp. 1641–1644.

[113] T. E. Oliphant et al. “An error analysis of Helmholtz inversion for incompressible shear, vibration elastography with application to filter-design for tissue characterization”. In: *IEEE Ultrasonics Symposium*. 2000, pp. 1795–1798.

[114] T. E. Oliphant et al. “Complex-valued stiffness reconstruction for magnetic resonance elastography by algebraic inversion of the differential equation”. In: *Magnetic Resonance in Medicine* 45.2 (2001), pp. 299–310.

[115] S. Papazoglou et al. “Shear wave group velocity inversion in MR elastography of human skeletal muscle”. In: *Magnetic Resonance in Medicine* 56.3 (2006), pp. 489–497.

[116] S. Papazoglou et al. “Two-dimensional waveform analysis in MR elastography of skeletal muscles”. In: *Physics in Medicine and Biology* 50.6 (2005), pp. 1313–1325.

[117] F. Pierron, P. V. Bayly, and R. Namani. “Application of the virtual fields method to magnetic resonance elastography data”. In: *Application of Imaging Techniques to Mechanics of Materials and Structures*. Vol. 4. Springer New York, 2013, pp. 135–142.

[118] F. Pierron and M. Grediac. *The Virtual Fields Method: Extracting Constitutive Mechanical Parameters from Full-field Deformation Measurements*. 2012, pp. 1–531.

[119] C. Pislaru et al. “Ultrasound strain imaging of altered myocardial stiffness: Stunned versus infarcted reperfused myocardium”. In: *Circulation* 109.23 (2004), pp. 2905–2910.

[120] M. J. D. Powell. “A direct search optimization method that models the objective and constraint functions by linear interpolation”. In: *Advances in Optimization and Numerical Analysis*. Springer Netherlands, 1994, pp. 51–67.

[121] M. J. D. Powell. “A view of algorithms for optimization without derivatives”. In: *Mathematics Today-Bulletin of the Institute of Mathematics and its Applications* 43.5 (2007), pp. 170–174.

[122] A. Prasad et al. “Characterization of static and dynamic left ventricular diastolic function in patients with heart failure with a preserved ejection fraction”. In: *Circulation: Heart Failure* 3.5 (2010), pp. 617–626.

[123] B. Qiang et al. “Modeling transversely isotropic, viscoelastic, incompressible tissue-like materials with application in ultrasound shear wave elastography”. In: *Physics in Medicine and Biology* 60.3 (2015), pp. 1289–1306.

[124] E. C. Qin. “Investigating the anisotropic mechanical properties of skeletal muscle using magnetic resonance elastography and diffusion tensor imaging”. Doctor of Philosophy. University of New South Wales, 2012, p. 182.

[125] E. C. Qin et al. “Combining MR elastography and diffusion tensor imaging for the assessment of anisotropic mechanical properties: a phantom study”. In: *Journal of Magnetic Resonance Imaging* 37.1 (2013), pp. 217–226.

[126] E. C. Qin et al. “In vivo anisotropic mechanical properties of dystrophic skeletal muscles measured by anisotropic MR elastographic imaging: The MDX mouse model of muscular dystrophy”. In: *Radiology* 273.3 (2014), pp. 726–735.

[127] S. I. Ringleb et al. “Applications of magnetic resonance elastography to healthy and pathologic skeletal muscle”. In: *Journal of Magnetic Resonance Imaging* 25.2 (2007), pp. 301–309.

[128] S. I. Ringleb et al. “Quantitative shear wave magnetic resonance elastography: comparison to a dynamic shear material test”. In: *Magnetic Resonance in Medicine* 53.5 (2005), pp. 1197–1201.

[129] A. Romano et al. “In vivo waveguide elastography: Effects of neurodegeneration in patients with amyotrophic lateral sclerosis”. In: *Magnetic Resonance in Medicine* 72.6 (2014), pp. 1755–1761.

[130] A. Romano et al. “In vivo waveguide elastography of white matter tracts in the human brain”. In: *Magnetic Resonance in Medicine* 68.5 (2012), pp. 1410–1422.

[131] A. J. Romano. “Evaluation of a material parameter extraction algorithm using MRI-based displacement measurements”. In: *IEEE Transactions on Ultrasonics, Ferroelectrics, and Frequency Control* 47.6 (2000), pp. 1575–1581.

[132] A. J. Romano, J. J. Shirron, and J. A. Bucaro. “On the noninvasive determination of material parameters from a knowledge of elastic displacements: theory and numerical simulation”. In: *IEEE Transactions on Ultrasonics, Ferroelectrics, and Frequency Control* 45.3 (1998), pp. 751–759.

[133] A. J. Romano et al. “Determination and analysis of guided wave propagation using magnetic resonance elastography”. In: *Magnetic Resonance in Medicine* 54.4 (2005), pp. 893–900.

[134] A. J. Romano et al. “Waveguide magnetic resonance elastography of the heart”. In: *Proceedings of the 21st International Society of Magnetic Resonance in Medicine*. 2013, p. 2431.

[135] N. C. Rouze et al. “Finite element modeling of impulsive excitation and shear wave propagation in an incompressible, transversely isotropic medium”. In: *Journal of Biomechanics* 46.16 (2013), pp. 2761–2768.

[136] D. Royer et al. “On the elasticity of transverse isotropic soft tissues (L)”. In: *Journal of the Acoustical Society of America* 129.5 (2011), pp. 2757–2760.

[137] I. Sack, J. Bernarding, and J. Braun. “Analysis of wave patterns in MR elastography of skeletal muscle using coupled harmonic oscillator simulations”. In: *Magnetic Resonance Imaging* 20.1 (2002), pp. 95–104.

[138] I. Sack et al. “MR elastography of the human heart: noninvasive assessment of myocardial elasticity changes by shear wave amplitude variations”. In: *Magnetic Resonance in Medicine* 61.3 (2009), pp. 668–677.

[139] J. L. Schmidt et al. “Magnetic resonance elastography of slow and fast shear waves illuminates differences in shear and tensile moduli in anisotropic tissue”. In: *Journal of Biomechanics* 49.7 (2016), pp. 1042–1049.

[140] R. Sinkus. “Elasticity of the heart, problems and potentials”. In: *Current Cardiovascular Imaging Reports* 7.9 (2014), p. 9288.

[141] R. Sinkus et al. “Imaging anisotropic and viscous properties of breast tissue by magnetic resonance-elastography”. In: *Magnetic Resonance in Medicine* 53.2 (2005), pp. 372–387.

[142] R. Sinkus et al. “Viscoelastic shear properties of in vivo breast lesions measured by MR elastography”. In: *Magnetic Resonance Imaging* 23.2 (2005), pp. 159–165.

[143] Ji. Song, O. I. Kwon, and Ji. K. Seo. “Anisotropic elastic moduli reconstruction in transversely isotropic model using MRE”. In: *Inverse Problems* 28.11 (2012), p. 115003.

[144] P. Song et al. “Quantitative assessment of left ventricular diastolic stiffness using cardiac shear wave elastography: A pilot study”. In: *Journal of Ultrasound in Medicine* 35.7 (2016), pp. 1419–1427.

[145] W. W. Soroka. “Note on the relations between viscous and structural damping coefficients”. In: *Journal of the Aeronautical Sciences* 16.7 (1949), pp. 409–410.

[146] C. Sun, B. Standish, and V. X. D. Yang. “Optical coherence elastography: current status and future applications”. In: *Journal of Biomedical Optics* 16.4 (2011), p. 043001.

[147] L. M. Taylor and D. P. Flanagan. *PRONTO 3D: A three-dimensional transient solid dynamics program*. 1989.

[148] S. Tomita et al. “Numerical simulations of magnetic resonance elastography using finite element analysis with a linear heterogeneous viscoelastic model”. In: *Journal of Visualization* (2017), pp. 1–13.

[149] D. J. Tweten, R. J. Okamoto, and P. V. Bayly. “Requirements for accurate estimation of anisotropic material parameters by magnetic resonance elastography: A computational study”. In: *Magnetic Resonance in Medicine* (2017).

[150] D. J. Tweten et al. “Estimation of material parameters from slow and fast shear waves in an incompressible, transversely isotropic material”. In: *Journal of Biomechanics* 48.15 (2015), pp. 4002–4009.

[151] D. J. Tweten et al. “Identification of anisotropic material parameters in elastic tissue using magnetic resonance imaging of shear waves”. In: *Proceedings of the ASME 2015 International Design Engineering Technical Conferences & Compuers and Information in Engineering Conference*. 2015, pp. 1–8.

[152] K. Uffmann et al. “In vivo elasticity measurements of extremity skeletal muscle with MR elastography”. In: *NMR in Biomedicine* 17.4 (2004), pp. 181–190.

[153] M. W. Urban et al. “Measurement of viscoelastic properties of in vivo swine myocardium using Lamb Wave Dispersion Ultrasound Vibrometry (LDUV)”. In: *IEEE Transactions on Medical Imaging* 32.2 (2013), pp. 247–261. eprint: NIHMS150003.

[154] S. Urheim et al. “Myocardial Strain by Doppler Echocardiography Validation of a New Method to Quantify Regional Myocardial Function”. In: *Circulation* 102.10 (2000), pp. 1158–1164.

[155] E. Van Houten et al. “An overlapping subzone technique for MR-based elastic property reconstruction”. In: *Magnetic Resonance in Medicine* 42.4 (1999), pp. 779–786.

[156] E. E. W. Van Houten et al. “Subzone based magnetic resonance elastography using a Rayleigh damped material model”. In: *Medical Physics* 38.4 (2011), pp. 1993–2004.

[157] E. E. W. Van Houten et al. “Three dimensional subzone based reconstruction algorithm for MR elastography”. In: *Magnetic Resonance in Medicine* 45.5 (2001), pp. 827–837.

[158] E. D. Verdonk, S. A. Wickline, and J. G. Miller. “Anisotropy of ultrasonic velocity and elastic properties in normal human myocardium”. In: *Journal of the Acoustical Society of America* 92.6 (1992), pp. 3039–3050.

[159] J. C. Walker et al. “MRI-based finite-element analysis of left ventricular aneurysm”. In: *American Journal of Physiology-Heart and Circulatory Physiology* 289.2 (2005), H692–H700.

[160] V. Y. Wang, H. I. Lam, and D. B. Ennis. “Cardiac active contraction parameters estimated from magnetic resonance imaging”. In: *Statistical Atlases and Computational Models of the Heart*. 2010, pp. 194–203.

[161] V. Y. Wang, P. M. F. Nielsen, and M. P. Nash. “Image-based predictive modeling of heart mechanics”. In: *Annual Review of Biomedical Engineering* 17 (2015), pp. 351–383.

[162] V. Y. Wang et al. “Modelling passive diastolic mechanics with quantitative MRI of cardiac structure and function”. In: *Medical Image Analysis* 13.5 (2009), pp. 773–784.

[163] P. A. Wassenaar et al. “Measuring age-dependent myocardial stiffness across the cardiac cycle using MR elastography: A reproducibility study”. In: *Magnetic Resonance in Medicine* 75.4 (2016), pp. 1586–1593.

[164] J. Wuerfel et al. “MR-elastography reveals degradation of tissue integrity in multiple sclerosis”. In: *NeuroImage* 49.3 (2010), pp. 2520–2525.

[165] J. Xi et al. “Myocardial transversely isotropic material parameter estimation from in-silico measurements based on a reduced-order unscented Kalman filter”. In: *Journal of the Mechanical Behavior of Biomedical Materials* 4.7 (2011), pp. 1090–1102.

[166] J. Xi et al. “The estimation of patient-specific cardiac diastolic functions from clinical measurements”. In: *Medical Image Analysis* 17.2 (2013), pp. 133–146.

[167] Y. Yamakoshi, J. Sato, and T. Sato. “Ultrasonic imaging of internal vibration of soft tissue under forced vibration”. In: *IEEE Transactions on Ultrasonics, Ferroelectrics, and Frequency Control* 37.2 (1990), pp. 45–53.

[168] F. C. P. Yin et al. “Quantification of the mechanical properties of noncontracting canine myocardium under simultaneous biaxial loading”. In: *Journal of Biomechanics* 20.6 (1987), pp. 577–589.

[169] M. Yin et al. “Dynamic postprandial hepatic stiffness augmentation assessed with MR elastography in patients with chronic liver disease”. In: *American Journal of Roentgenology* 197.1 (2011), pp. 64–70.

[170] M. R. Zile, C. F. Baicu, and W. H. Gaasch. “Diastolic heart failure–abnormalities in active relaxation and passive stiffness of the left ventricle”. In: *The New England Journal of Medicine* 350.19 (2004), pp. 1953–1959.